THÈSE

En vue de l'obtention du

DOCTORAT DE L'UNIVERSITÉ DE TOULOUSE

Délivré par : *l'Université Toulouse 3 Paul Sabatier (UT3 Paul Sabatier)*

Présentée et soutenue le *13 Decembre 2013* **par :**

ARMIN RAJABZADEH

Etude expérimentale et théorique de la migration de joints de grains, couplée à un cisaillement

---

JURY

SYLVIE LARTIGUE-KORINEK	Chargé de Recherche	ICMPE-Paris EST
SABINE LAY-DIETRICH	Directeur de Recherche	SIMAP-Grenoble
JOSEPH MORILLO	Professeur	CEMES-Toulouse
LAURENT PIZZAGALLI	Directeur de Recherche	Institu P'-Poitiers
ANNA SERRA-TORT	Professeur	Polytecnica de Catalunya-Barcelone
BERNARD VIGUIER	Professeur	CIRIMAT-Toulouse
MARC LEGROS	Directeur de Recherche	CEMES-Toulouse
FRÉDÉRIC MOMPIOU	Chargé de Recherche	CEMES-Toulouse
NICOLAS COMBE	Maître de conférences	CEMES-Toulouse

École doctorale et spécialité :
SDM : Sciences et génie des matériaux - CO034

Unité de Recherche :
Centre d'Elaboration de Matériaux et d'Etudes Structurales - CEMES-CNRS UPR 8011

Directeur(s) de Thèse :
Marc LEGROS, *Frédéric MOMPIOU* et *Nicolas COMBE*

Rapporteurs :
Sabine LAY-DIETRICH et *Laurent PIZZAGALLI*

À mes parents,

Rahim Rajabzadeh
et
Parivash Azarpisheh

REMERCIEMENTS

Tout d'abord je tiens à exprimer ma profonde reconnaissance à mes directeurs de thèse : Frédéric, Marc et Nicolas. Merci pour votre encadrement, disponibilité, patience, vos conseils et l'aide que vous m'avez apportée pendant ces trois années de travail.
Ensuite, je voudrais remercier Sabine Lay-Dietrich et Laurent Pizzagalli d'avoir accepté la tâche de rapporteurs de ce manuscrit. Mes remerciements vont également à Anna Serra, Bernard Viguier et Joseph Morillo d'avoir accepté de faire partie de mon jury de thèse et pour leurs remarques instructives.
Je tiens également à adresser un remerciement spécial à Sylvie Lartigue-Korinek, avec qui j'ai eu l'occasion de travailler. Ses précieux conseils m'ont éclairé sur la partie de l'analyse des défauts structuraux des joint de grains de ma thèse. Sylvie, merci pour ta générosité et ton enthousiasme scientifique et bien sûr merci d'avoir participé à mon jury de thèse. Je remercie tous les chercheurs du CEMES, surtout les membres de l'équipe MC2 pour leur accueil chaleureux. Plus particulièrement, je remercie Daniel Caillard, Lise Durand, Alain Couret, Jean-Philippe Monchoux. J'ai toujours apprécié votre convivialité et les petits échanges intéressants devant la machine à café qui rendaient les jours au CEMES plus agréables. Je remercie aussi Joël Douin, pour ces aides dans la procédure administratives avec l'école doctorale de sciences de la matière. Je pense aussi aux membres de l'équipe de simulation de MC2, à Magali Benoît, Nathalie Tarrat, Joseph Morillo et Hao Tang et je les remercie pour les discussions intéressantes lors des réunions de simulations qui m'ont aidé à faire avancer la partie théorique de ma thèse.
Je tiens aussi à remercier les membre des services de préparation, microscopie, mécanique et informatique du CEMES.
Un immense merci à tous les doctorants et post-doctorants du CEMES (passés et présents) avec qui j'ai partagé cette aventure : Thomas, Ludwig, Romain (Garbage et Dupuis), Roman, Agnès, Robin, Zofia, Miguel, Sviatlana, Aniket, Hermann, Alexandre, Mathilde, Rémi, Olivier, Florian, Christophe, Zohreh, Jiangfeng, Loranne, Maxime, Lama, ...
Enfin j'ai quelques remerciements plus personnels à exprimer à ma famille.
À mes parents que j'admire. Je les remercie pour l'amour pure et inconditionnelle qu'ils m'ont toujours offert et pour leur soutien incessant durant ma vie. À ma sœur, Shaghayegh que j'aime de tout mon cœur et qui est ma meilleure amie de tous les temps.
Merci à mes autres amis, surtout à Nikrooz Nasr et Alireza Amyari.
Et je remercie enfin et surtout Salimeh, qui pour mon plus grand bonheur partage ma vie. Elle a assisté quotidiennement à l'avancement de cette thèse et n'a pas cessé de me soutenir. Je la remercie d'avoir été à mon écoute et notamment de m'avoir encouragé lors des moments difficiles que j'ai affrontés en travaillant sur cette thèse.

TABLE OF CONTENTS

1 INTRODUCTION AND THEORY REVIEW

Plastic deformation, i.e. the ability of a crystal to deform permanently, is an important feature of metals and alloys. In conventional coarse-grained metals, plastic deformation is determined by the nucleation, multiplication and interactions of dislocations between themselves or with the microstructure. The ability of a material to sustain a critical stress before deforming plastically (the strength) is then a consequence of the difficulty to create and move dislocations.
Grain refinement is one of the possible strategies of strengthening. Indeed, grain boundaries that delimit two crystals of different orientations, are known to be generally strong obstacles to the motion of dislocations. Increasing the density of grain boundaries yields then to a strength increase, a conclusion which has been drawn empirically by Hall and Petch in the 50's [1, 2]. For this reason, small grain metals $100nm < d <\sim 1\mu$m, usually exhibit enhanced mechanical properties compared to their coarse-grained counterparts.
In the case of nanocrystalline (NC) metals ($d < 100nm$) however, this conclusion is not so clear and some works claim even a softening of the materials with excessive decrease of grain size ($d < 10nm$) [3, 4], a phenomena coined "inverse Hall-Petch" relationship.
Intragranular dislocations are usually not present in NC metals suggesting that grain boundaries play themselves a crucial role in the plasticity mechanisms. Among different possible grain boundary mechanisms, shear-coupled grain boundary migration, i.e. grain growth assisted by a mechanical stress, has rapidly attracted a great attention. The understanding of this mechanism is at the heart of this thesis and accordingly the manuscript presented here is constructed as follows :

- The first chapter is an introduction to general concepts of plastic deformation, grain boundary description and their defects, and a literature overview of the grain boundary deformation mechanisms with an emphasis on shear coupled grain boundary migration.
- The second chapter presents results of shear-coupled grain boundary migration in Al bicrystals by means of in-situ Transmission Electron Microscopy (TEM) straining experiments.
- The third chapter deals with the characterization of elementary structural defects of a grain boundary by High resolution TEM (HRTEM) observations and their possible formation through lattice dislocation/grain boundary interactions.
- The fourth chapter finally presents the results of atomistic simulations of grain boundary shear coupled migration.

1.1 Deformation and dislocations

A single crystal subjected to tensile or compression stress initially deforms elastically according to Hooke's law. This means that up to a certain limit, the deformation of the crystal is linearly proportional to the applied load. At a critical stress, called yield stress, the crystal deforms plastically by shearing along definite planes called slip planes. These slip planes are generally the closest packed planes of the crystallographic systems, i.e. the planes with highest density of atoms, and slip directions are parallel to the shortest lattice translation vectors along which the atoms are most closely spaced. For face centred cubic (fcc) crystals, the principal slip plane is of type $\{111\}$ and the direction is of type $< 110 >$. It was found that experimental values of yield stress in single crystals are considerably less than the stress required to shear a single crystal plane, which is related to the cohesive forces between atoms along the plane. For the first time in 1934, Egon Orowan, Michael Polanyi and Geoffrey Ingram Taylor [5, 6, 7], nearly at the same time introduced linear lattice imperfections, called dislocations, to explain the measurement discrepancies in yield strength of crystals. According to this explanation, during deformation, atomic planes do not slip over each other as rigid bodies. But instead, the slip starts at localized mis-alignments in the periodic perfect lattice points in the crystal and then spreads over the plane.
A dislocation can be formally constructed by using the Volterra process [8]. It consists in cutting the crystal along an arbitrary line, then moving the two lips of the cut by a lattice translation vector $\vec{b}$, called the Burgers vector, and eventually in gluing the two lips back together. In this last step, extra material has to be added if $\vec{b}$ is not in the cut plane in order to fill the gap after the two lips have been displaced. Figure 1.1a shows two particular cases of straight dislocations : the edge dislocation corresponds to the situation where the line (defined by $\vec{l}$) is perpendicular to $\vec{b}$. The screw dislocation (figure 1.1b) corresponds to $\vec{l}$ parallel to $\vec{b}$. However in real materials, dislocations have usually a curved line and thus are neither perfect screw or edge.

The deformation is predominantly carried by the motion of dislocations, called dislocation glide, along a slip plane that contains both the line and the Burgers vector. This motion doesn't require any transport of matter but only atomic rearrangement in the core of the dislocation. The amount of shear caused by individual dislocations is characterized by their Burgers vector $\vec{b}$.

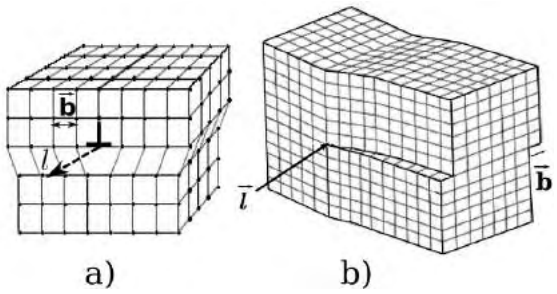

Figure 1.1: Two special geometries of dislocations : a) Edge dislocation with Burgers vector $\vec{b}$ perpendicular to the line vector $\vec{l}$ of the dislocation. b) Screw dislocation with the Burgers vector parallel to line vector. (after [9])

According to Schmid's law [10], dislocation slip is initiated in response to an uniaxial tensile stress, when the resolved shear stress attains a critical value τ_c :

$$\tau_c = \sigma_y \cos\phi \cos\lambda \tag{1.1}$$

with σ_y being the yield stress and ϕ and λ the angles of the slip plane normal and the slip direction with respect to the tensile axis. $\cos\phi\cos\lambda$ is the Schmid factor whose maximum value corresponds to the favourable slip system (the combination of slip plane and Burgers vector) in the crystal.
Dislocations, except screw ones, can also move out of their slip plane by climb process, a process that requires the vacancies or interstitial diffusion at the dislocation core. This process usually takes place at high homologous temperatures (i.e. $T >\sim 0.5T_m$, where T_m is the melting temperature).

The material strengthening techniques consist mainly in creating obstacles against dislocations in order to hinder their glide in crystals. Grain size reduction, strain hardening, precipitation, dispersion strengthening are some examples of these methods.
In the next section we will concentrate on strengthening by grain refinement.

1.2 Grain size effect and Hall-Petch relation

The strength of polycrystalline materials depends on their grain sizes. In the early 50's Hall [1] and Petch [2] suggested an empirical equation relating the yield stress (σ_y) of a polycrystalline material to the inverse square of its grain diameter ($d^{-1/2}$) :

$$\sigma_y = \sigma_0 + kd^{-1/2} \tag{1.2}$$

Here σ_0 is the minimum friction stress for dislocations motion in a single crystal and k the Hall-Petch coefficient depending on the material, strain rate, grain boundaries type, etc.
This phenomenon has been first explained by the dislocation pile-up theory : when dislocations arrive at grain boundaries, the boundary acts as an obstacle against their motion, causing dislocations to pile-up against the boundary. There are two main reasons for this blocking : the difficulty for a dislocation to be transmitted directly (because of the non-continuity of slip systems across the interface) and the decomposition of dislocations in the grain boundary [11]. (We will discuss lattice dislocation/grain boundary interactions in more details in Chapter 3).
Nevertheless, deformation can be transferred from one grain to another when the stress at the head of the pile-up is sufficient to activate sources of dislocations in adjacent grains, a process called indirect transmission [11].
In small grains however, the calculation of the pile-up stress is not valid for a small number of dislocations and the pile-up theory fails to explain the Hall-Petch law. More elaborated models that rely on intragranular plasticity can be derived to capture the Hall-Petch relationship [12].
Indeed, numerous experimental works report a deviation from the Hall-Petch law in very small grain size regime ($d < 100nm$), some of them even suggesting an inverse Hall-Petch relation where the material is softened with decreasing the grain size [13, 14, 15, 16, 17]. However as pointed out by Saada, an accurate measurement of the plastic strain is mandatory to reach the domain of validity of the Hall-Petch law [18].
Moreover, the NC metals have been found usually to be free of lattice dislocations, implying that either the intragranular plasticity is suppressed, and/or the dislocations are nucleated from the grain boundary and absorbed rapidly in the adjacent grains. While early theoretical studies have focused on the second possibility [19], more recent works have envisaged grain boundary-mediated mechanisms such as grain boundary sliding [20], grain boundary diffusional creep [21] grain rotation [22] or shear coupled grain boundary migration [23]. A great deal of attention has been paid to the last mechanism, since several experimental evidence stress assisted grain growth in small grain metals have been observed either during indentation [24, 25], compression [26, 27] or tensile tests [28, 29, 30, 31, 32].

However, before describing this particular mechanism in more details, some fundamental concepts about grain boundaries and their defects are necessary and will be developed in the next section.

1.3 Fundamental concepts on grain boundaries

A grain boundary is a planar lattice defect which separates two regions of the same composition and structure but of different orientations. Macroscopically to fully characterize a grain boundary, there are 5 parameters, known as geometric degrees of freedom (DOF) that need to be identified : the relative rotation of the adjoining grains is given by a misorientation angle θ (1 DOF). The rotation axis [uvw] between two crystals is defined by its direction cosines (2 DOF). Also the orientation of the grain boundary plane is specified by the normal $\vec{n}$ to the grain boundary plane (2 DOF).
Furthermore, there are 4 more degrees of freedom at the atomic scale : rigid body translations of

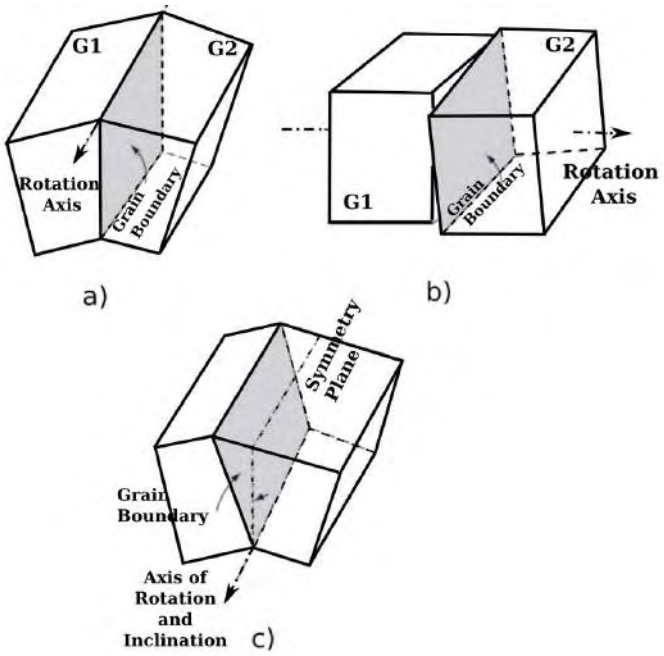

Figure 1.2: Different geometries of grain boundaries : tilt (a) and twist (b) grain boundaries with the rotation axis respectively parallel and perpendicular to the grain boundary plane ; c) A representation of asymmetrical tilt grain boundaries (after [33]).

the two crystals relative to each other and the volume expansion (3 DOF) and the position of the grain boundary plane indicated be the vector $\vec{d}$ normal to the grain boundary plane ($|\vec{d}| < |\vec{n}|$). According to the relations between the rotation axis and the grain boundary plane the grain boundaries can be categorized into different groups :
If the rotation axis belongs to the boundary plane, as in figure1.2a, we have a *tilt* grain boundary. In *twist* grain boundaries however, the rotation axis is perpendicular to the boundary plane (Figure 1.2b). The grain boundaries which do not fit in any of these cases are mixed grain boundaries. For two adjacent crystals positioned as mirror images of each other relative to boundary plane,

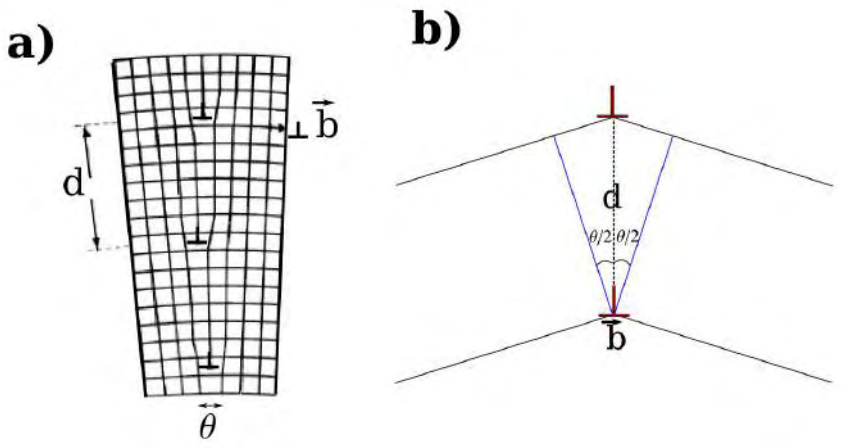

Figure 1.3: a) Array of discrete dislocations with $\vec{b}$ as their Burgers vector, accommodating the misorientation θ between two grains in low angle grain boundaries. b) According to Read and Shockley [34], the spacing distance d between two dislocations is geometrically related to the misorientation angle θ : $d = \frac{|\vec{b}|}{2\sin\frac{\theta}{2}}$

the grain boundary is symmetric. In asymmetric grain boundaries however, as in figure 1.2c, the grain boundary plane is inclined about an axis contained in the symmetry plane. However it should be noted that clear distinctions between different types of grain boundaries are generally observed in model materials with engineered interfaces rather than in real polycrystalline materials.

1.3.1 Dislocation and Grain boundary

According to the Read and Shockley model [34], grain boundaries with small rotation angles ($< 15°$) known as *low angle grain boundaries* (LAGB), can be considered as distorted structures with respect to a perfect crystal. In this deviated structure the misorientation is thus accommodated by arrays of lattice dislocations rearranged periodically along the interface. According to this model, a twist boundary can be produced by a crossed grid of two arrays of screw dislocations, whereas a simple symmetric tilt grain boundary is composed of a single array of edge dislocations. These dislocations of Burgers vector $\vec{b}$, indicated schematically for a tilt grain boundary in figure 1.3a, are the *primary intrinsic grain boundary dislocations* that are periodically distributed along the interface. In a symmetrical tilt grain boundary, the spacing d between the dislocations can be geometrically determined as a function of the rotation angle θ and the Burgers vector $\vec{b}$ according to figure 1.3b :

$$d = \frac{|\vec{b}|}{2\sin\frac{\theta}{2}} \tag{1.3}$$

For small misorientation angles θ we have :

$$d \cong \frac{|\vec{b}|}{\theta} \tag{1.4}$$

At atomic scale the structure of a grain boundary is however more easily captured by using the structural units model [35]. In this model a grain boundary structure is defined as configurations

of small groups of atoms, called the structural units which are distributed periodically along the interface. The structural units, in the shape of simple or complicated polyhedra, can be regarded as spaces where the lattice orientation of one grain changes to the other.
Grain boundaries consisting of a single type or short periods of structural units are called *singular*

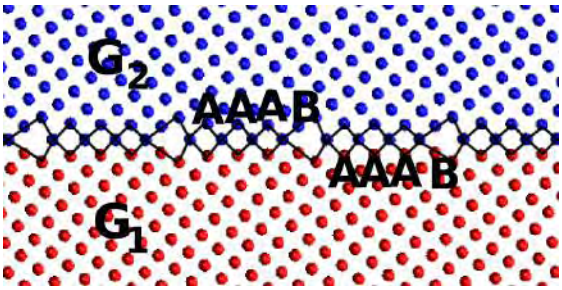

Figure 1.4: The A and B structural units in a $\theta = 77.32°$ [001] (540)symmetrical grain boundary with repetition period as $|AAAB.AAAB|$, in a fcc lattice.

grain boundaries [36]. Singular grain boundaries have the lowest interfacial energies compared to general boundaries. The general boundaries are composed of a complex combination of A and B type structural units, described as $|A_xB_y|$, where x and y are number of each unit for a period of repetition. For instance the sequence of structural units in figure 1.4 corresponds to a symmetric grain boundary in fcc lattice with the misorientation angle of $\theta = 77.32°$ around [001] direction. The repetition period of the structural units in this boundary is described as $|AAAB|$.
In analogy with the description of a grain boundary in terms of dislocations, each structural unit of type B corresponds to the position of the primary dislocations. It is worth noting in figure 1.4 that a large number of atoms per grain boundary area unit are common to both grains G_1 and G_2 i.e. they are coincident. This coincidence is an important feature of low interfacial energy grain boundaries and will be discussed in the following.

1.3.2 Coincidence site grain boundaries

Particular misorientation angles and grain boundary planes correspond to periodic coincident atomic positions in both adjacent grains. The resulting grain boundaries are then called, coincident grain boundaries. The network formed by the translation vectors joining the coincident positions is called the Coincident Site Lattice (CSL).
The inverse ratio of the volume of the coincidence unit cell to the volume of the primitive unit cell of the crystal is the coincidence index, denoted by Σ. The smaller the Σ value, the higher the density of coincidence sites would be for the interpenetrating lattices. Thus $\Sigma = \infty$ means two completely not coincident grains and $\Sigma = 1$ corresponds to a perfect crystal. For cubic structures, Σ is always an odd integer and for the misorientation angle θ is determined by the Miller indices of the rotation axis $< uvw >$ or by indices of the grain boundary plane (hkl). In the latter case for instance Σ is given by [11] :

$$\Sigma = n(h^2 + k^2 + l^2) \tag{1.5}$$

with n being 1 or 1/2.
In figure1.5, the CSL lattice is drawn on the dichromatic pattern of a Σ13(320) (θ=67.38° around [001]). The dichromatic pattern corresponds to the superposition of the two adjacent lattices projected on a plane perpendicular to the misorientation axis. In the dichromatic pattern [37] the lattice sites of each grain are represented with different geometric shapes e.g in figure1.5

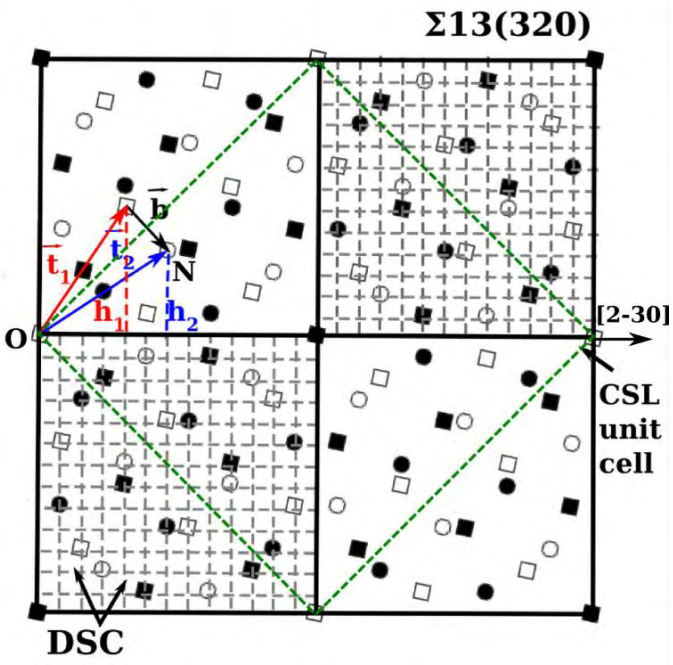

Figure 1.5: Coincidence site (CSL) and DSC lattice for Σ13(320) in cubic system. Lattice sites for grains G1 and G2 are shown by □ and ◯ respectively and filled and empty shapes represent different depths along the rotation axis ([001]). $\vec{t}_1$ and $\vec{t}_2$ are translation vectors corresponding to each grain and h_1 and h_2 are their associated step height. $\vec{b} = \vec{t_2} - \vec{t_1}$ is the Burgers vector of the secondary intrinsic dislocation of the corresponding intergranular structure.

□ for grain G_1 and ◯ for G_2, where filled and empty shapes represent the sites with different depths according to the rotation axis. The unit cell of the Σ13(320) CSL lattice indicated by green dashed lines, encloses indeed 13 lattice sites of G_1 and G_2.
A sub-lattice of the CSL, called the Displacement Shift Complete (DSC) lattice can also be drawn (dashed line in figure 1.5) which corresponds to the lattice formed by all possible translations $\vec{t} = \vec{t}_1 - \vec{t}_2$, where $\vec{t}_1$ and $\vec{t}_2$ are the lattice vectors of grains G_1 and G_2 respectively. This lattice which has been rigorously formalized by Bollmann [38], is very important as we will see in the following because any translation of one grain by a DSC vector preserves the CSL lattice. However it should be underlined that the CSL lattice is defined only for certain grain boundary misorientations, thus Bollmann extends this concept by introducing the O-lattice [38] which is the locus of all points in good fit of two superimposed crystal lattices, between the regions of bad fit. This latter concept may also be used to consider the structure of interphase interfaces.

1.3.3 Structural defects in CSL grain boundaries

The main type of structural defects in grain boundaries are called disconnections [39, 40] which are analogous to lattice dislocations. Indeed, as lattice dislocations are perturbations of the perfect lattice that preserve the translational symmetry of the crystal (their Burgers vector is a lattice translation), the disconnections are perturbations of the grain boundary structure that preserve the translational invariance of the grain boundary structure (i.e. the CSL). In this context, as an array of periodically spaced lattice dislocations in a perfect crystal can accom-

modate a lattice rotation, an array of disconnections in a CSL boundary also accommodates a small extra rotation with respect to the coincidence misorientation of two grains. In this case, the disconnections are called intrinsic secondary dislocations and their Burgers vector is a vector of the DSC lattice.
Isolated disconnections, called extrinsic dislocation, can arise from the decomposition of a lattice dislocation in the grain boundary as it will be shown in Chapter 3.
As said before, the Burgers vector of a disconnection is defined by the difference between translational vectors $\vec{t_1}$ and $\vec{t_2}$ in each grain :

$$\vec{b} = \vec{t_1} - \vec{t_2} \tag{1.6}$$

Moreover, a disconnection can correspond to a step on the boundary. This corresponds to the case where the Burgers vector may not be contained in the grain boundary plane. Indeed, if a disconnection of vector $\vec{b}$ as shown in figure 1.5, is introduced in the $(2\bar{3}0)$ plane (seen here edge on), the old coincident position O (the origin of the translation vector $\vec{t_1}$ and $\vec{t_2}$) will be shifted to the new coincident position N. The step height h, which can be defined in each grain is then (see figure 1.5) [41] :

$$h_{1,2} = \vec{t}_{1,2} \cdot \vec{n} \tag{1.7}$$

with $\vec{n}$ being the unit vector of the grain boundary plane normal. The overall step height for

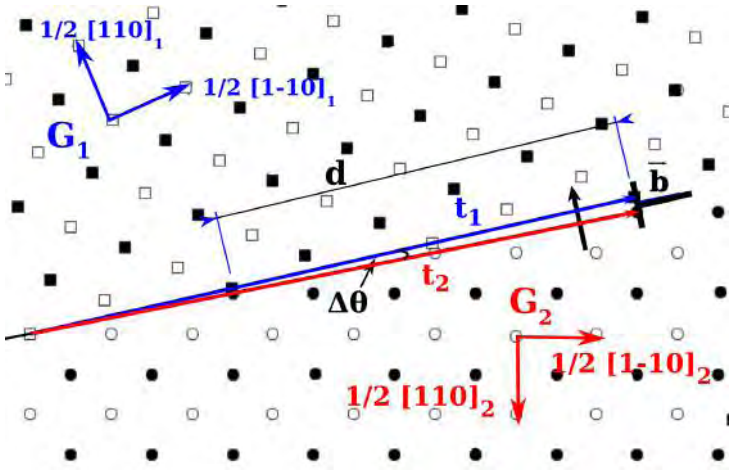

Figure 1.6: Schematic representation of a disconnection accommodating the deviation $\Delta\theta = 1.38°$ from coincidence angle $\theta = 67.38°$ in a $\Sigma13(320)$ grain boundary. $\vec{t_1}$ and $\vec{t_2}$ are the equivalent translation vectors from a coincidence site in each grain.

the grain boundary would be the average of the step heights measured in each grain :

$$h = \frac{h_1 + h_2}{2} \tag{1.8}$$

Different cases of disconnections can be defined :
Disconnection without step character $\vec{b} \neq 0$, $h = 0$: This case arises when the CSL grain boundary structure deviates by a small tilt angle. In figure 1.6 the grain boundary is a near-coincidence grain boundary close to $\Sigma13(320)$ in which the misorientation angle is $\theta = 66°$ instead of $\theta = 67.38°$. This difference can be accommodated for example by an array of disconnections separated by a distance d, with a Burgers vector $\vec{b}$. According to Read and Shockley (cf. equation

1.4) the extra misorientation angle will be : $\Delta\theta \approx \vec{b}/d$

Pure steps $h \neq 0$ **,** $\vec{b} = \vec{0}$ **:** This case corresponds to a grain boundary step with no dislocation character. In pure steps as it is represented schematically in figure 1.7 for a Σ13(320) tilt grain boundary, the translation vectors $\vec{t_1} = \vec{t_2}$ connect two coincidence sites together and h_1=$h_2 \neq 0$, thus $h \neq 0$, $\vec{b} = \vec{0}$.

General disconnection $\vec{b} \neq 0$**,** $h \neq 0$ **:** Here is the general case of the interrelation of the

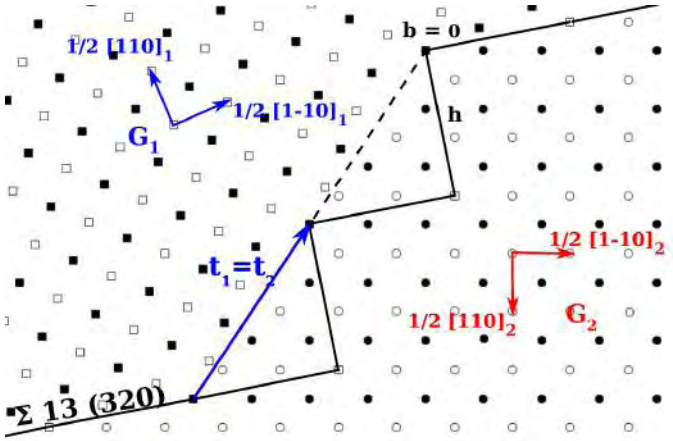

Figure 1.7: Representation of a pure step in the in a Σ13(320) *grain boundary between two grains G1 (□) and G2 (◯). Here two equal translation vectors* ($\vec{t_1} = \vec{t_2}$) *connect two coincidence sites together, giving* $\vec{b} = 0$ *and* $h \neq 0$.

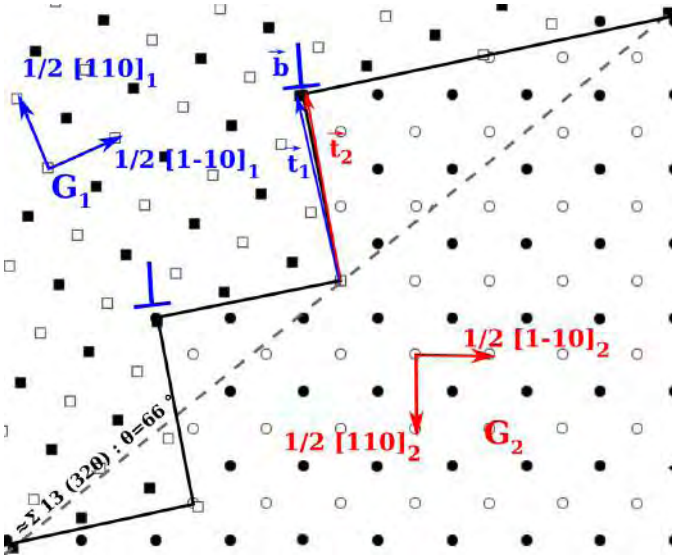

*Figure 1.8: A schematic representation of disconnections in a near-*Σ13(320) *grain boundary with* $\theta = 66°$ *misorientation angle (Instead of* $\theta = 67.38°$ *as in ideal coincidence). This deviation from coincidence angle is accommodated by dislocation* $\vec{b}$ *as the difference of the translation vectors in each lattice. Step height* h *is the average of the step heights in each each grain.*

translation vectors of each grain in the DSC lattice where $\vec{t_1} \neq \vec{t_2}$ and $h_1 \neq h_2$. This case is the combination of two previous cases in which the intergranular defect has dual dislocation/step character. Figure 1.8 representing this case, as in figure1.6 corresponds to a near-CSL grain boundary with $\theta = 66°$. The translation vectors $\vec{t_1}$ and $\vec{t_2}$ connect a coincidence site to two lattice sites of G_1 and G_2. Similarly to the previous case, $\vec{b} = \vec{t_2} - \vec{t_1}$ and the overall step height is the average of the steps corresponding to $\vec{t_1}$ and $\vec{t_2}$.

After having introduced the general concepts about grain boundaries and their defects, we will now review some important examples of grain boundary deformation and relaxation mechanisms in more details.

1.4 Deformation mechanisms in NC materials

1.4.1 Deformation twinning

Twin grain boundaries are special coincident grain boundaries with highly symmetrical structures often with one grain the mirror image of the other and with high misorientation angle [42]. Deformation twinning, i.e. the formation and growth of twins under stress, results from the nucleation and the motion of disconnections, called twinning dislocations, along a particular plane called the twinning plane. In face centred cubic metals, it corresponds to the motion of $\frac{1}{6}[112]$ edge twinning dislocation on successive $(11\bar{1})$ planes. Several mechanisms of twin growth have been developed in the literature and are reviewed in [42].
Generally, deformation twinning is not favoured compared to lattice dislocation motion because it requires the creation of a twin interface, also called stacking fault. Thus in coarse-grained materials, deformation twinning mostly tends to happen in metals with low stacking fault energy. However recent Molecular Dynamics (MD) simulations [43, 44] and TEM observations [45, 46, 47] suggest a favoured operation of deformation twinning in NC metals with high stacking fault energies, such as Al.
Simulations indicate that twinning dislocations can be nucleated from grain boundary before being absorbed in the adjacent grains. Thus the role of grain boundaries and dislocation emission from boundaries is predominant in this mechanism. Based on this, Chen et al. [45] give a possible explanation for the higher tendency of twinning in NC materials by comparing the nucleation possibilities of twinning and lattice dislocations in grain boundaries. In this model the required stress for nucleating twinning dislocations τ_t and lattice dislocations τ_l from a source in grain boundary is related to the dislocations source size d. By approximating d with grain sizes, the critical stress for nucleation of lattice dislocations in this source can be given by :

$$\tau_l = \frac{2\alpha\mu b_l}{d} \tag{1.9}$$

where μ is the shear modulus, $\vec{b_l}$ the Burgers vector corresponding to the lattice dislocations. The parameter α depends on the character (edge or screw) of the dislocation and contains the scaling factor between the length of the dislocation source and the grain size.
Similarly the required stress for nucleation of twinning dislocation would be :

$$\tau_t = \frac{2\alpha\mu b_t}{d} + \frac{\gamma}{b_t} \tag{1.10}$$

with $\vec{b_t}$ being the Burgers vector of the twinning dislocation and γ the stacking fault energy.
Generally $\tau_t > \tau_l$ and lattice dislocations are more likely generated than the partial ones. However

for a critical grain size the corresponding required stress would be :

$$d_c = \frac{2\alpha\mu(b_l - b_t)b_t}{\gamma} \tag{1.11}$$

So for grain sizes lower than this critical grain size d_c, the nucleation of twinning dislocations would be easier than the lattice dislocations and this can indicate the higher potential of deformation twinning for fine grained materials. Taking $\alpha = 1$ the estimated d_c is approximately 10 to 15 nm for Aluminium. However this model does not take into account the influence of elastic anisotropy, the small Peierls-Nabarro stress, localized stress concentrations, and the interactions of dislocations with grain boundaries.

1.4.2 Grain boundary creep

Grain boundary creep which is a deformation mechanism occurring usually at high homologous temperatures ($T > 0.5T_m$, with T_m the melting temperature), under constant loads, appears as a plausible mechanism at room temperature in NC materials with very small grains ($d < 10$ nm).
In classical diffusion creep model, such as Coble creep [48], macroscopic deformation is carried out by a flux of vacancies in the grain boundary from regions in tension to ones in compression. Since the diffusion of vacancies is faster along the grain boundaries and considering the limited diffusion distance in NC materials, according to Coble, the experimentally measured creep rate is expected to be given by :

$$\dot{\epsilon} = A\frac{\sigma\Omega}{kT}\frac{D_{GB}}{d^3} \tag{1.12}$$

with σ the typical applied stress, Ω the atomic volume, D_{GB} the grain boundary diffusion coefficient, T the temperature, d the grain size and A a constant.
However there is not enough experimental verification of this model at room temperature [3] and the estimation of the grain boundary diffusivity at room temperature, which is an extrapolation of values measured at higher temperature, has been rejected recently [49]. Also the creep rate proportionality to d^{-3} in Coble creep was contradicted by experimental results reporting a creep resistance much greater than the Coble prediction in NC materials [50]. Several more refined models have been proposed to explain these discrepancies. In some of them the role of non conservative disconnections motion (see paragraph 1.4.3) as source and sink of vacancies have been considered [51, 52], while other include diffusion along triple junctions [53].

1.4.3 Grain boundary sliding

The rigid-body translation of two adjoining grains in response to local shearing is known as grain boundary sliding. Sliding is considered as the main deformation mechanism during superplasticity, i.e. a phenomenon of extraordinary ductility of fine-grained materials deformed at high temperatures [54]. Differences in grain boundary sliding rates along different grain boundaries or sliding along curved interfaces lead to grain rotation [55, 56].
The role of disconnections in grain boundary sliding has been highlighted in several experimental studies [57, 58, 59, 60]. These disconnections can be related to the structure of the grain boundary or the result of interactions and decompositions of lattice dislocations in the grain boundary. To that respect, grain boundary acts as a sink for dislocations. In singular grain boundaries, the decomposition of the lattice dislocations will lead to disconnections with DSC Burgers vectors with both glissile component, i.e. a Burgers vector parallel to the grain boundary plane, and a climb component. Grain boundary sliding by pure disconnection glide is thus unlikely to occur

as far as curved grain boundaries are concerned and thus sliding is controlled by the climb of disconnections. Based on this, numerous models of grain boundary sliding that account for superplasticity, have been proposed and are reviewed in details in [61].

1.4.4 Grain migration coupled with shear deformation

Grain growth has been considered traditionally to be driven either by capillarity forces in order to reduce the grain boundary surface or by the strain energy differences between grains, as observed during recrystallization. Early observations of near Σ5 grain boundary migration at high temperature by Babcock and Baluffi [62] had shown erratic motion of the grain boundaries that was not correlated to the motion of dislocations. More recent experiments on small rounded-shape grains island shrinking under capillarity forces at high temperatures, have revealed that grain boundaries migrate in absence of stress without any sliding/rotation or deformation [63, 64]. This type of motion is attributed to a pure shuffling mechanism that occurs by the collective and stochastic rearrangement of atoms at the grain boundary [65]. In singular grain boundary, the shuffling mechanism is expected to occur by the lateral motion of pure steps accompanied by atomic columns rotation [64]. This process is illustrated schematically in figure 1.9 for a Σ13(320) grain boundary.

In contrast, the stress-induced migration of grain boundary, although known for a long time in

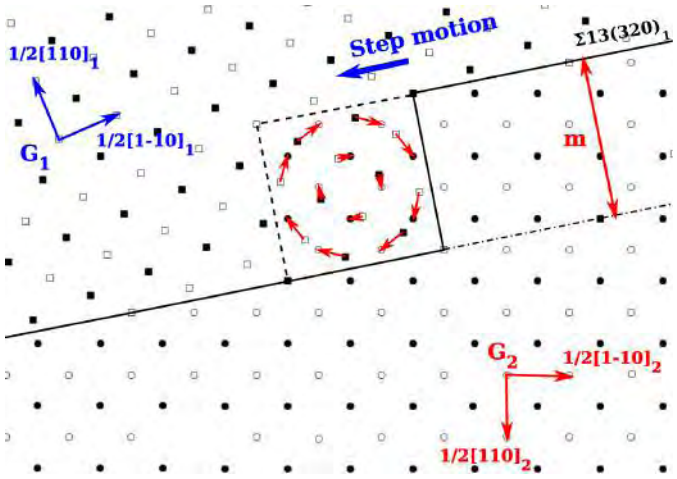

Figure 1.9: Schematic representation of the migration of a Σ13(320) grain boundary by pure shuffling. The downward lateral motion of the pure step of height m, gives rise to the collective atomic rearrangement from the lattice corresponding to G1 into G2 lattice.

low angle grain boundaries [66, 67] or in twin boundaries [68], has never been recognized as a plasticity mechanism in nanograined materials before recent observations by experimental [28] and atomistic simulations [69] methods. Since then, the stress assisted grain growth has been evidenced experimentally or by molecular dynamic simulations in different materials and under various mechanical solicitations :

Legros et al. [30] report fast grain boundary motion in crack tip zones of NC aluminium films during in-situ transmission electron microscopy (TEM) straining experiments. Similarly, Mompiou et al. [58] observe stress-induced grain growth, together with inter- and intragranular dislocation motion and grain boundary sliding, operating during deformation of ultrafine-grained Al thin films. Other experimental methods such as cold rolling experiments on nanocrystalline palladium

[70], compression of bulk nanocrystalline nickel and copper [27] and micro-hardness indentation in nanocrystalline copper [71], provide more experimental evidence about operation of this mechanism.
Apart from NC metals, the response of a grain boundary to a mechanical stress has been evidenced in experiments on near-coincident grain boundaries [72, 73, 74] and more recently for arbitrary high angle grain boundaries [32, 75, 76, 77]. Both molecular dynamic simulations [23, 78] and experimental methods either in bicrystals (see for instance [76]) or polycrystals [75] have shown that a normal grain boundary displacement over a distance m is usually accompanied by a relative translation d of the grains parallel to the grain boundary plane for both low- and high-angle grain boundaries. This shear-coupled grain boundary migration is characterized by a coupling factor $\beta = \frac{d}{m}$ which represents the induced shear strain (figure 1.10) [23, 79].
More extensive numerical simulations have been performed in the recent years, looking in more details at different aspects of this mechanism. Mishin et al. have focused for instance on the stick-slip grain boundary migration under a constant shear velocity [23, 80]. Or the work of Schafer et al. have highlighted that in pure NC metals, sliding is rapidly hindered by coupling mechanism in neighbouring grain boundaries with different associated coupling factors. This is because it suppresses the major prerequisite of the sliding mechanism which is presence of aligned subsets of neighbouring grain boundaries in these materials [81]. In another theoretical approach Homer et al. [82] have analyzed the dependence of the temperature on the shear-coupled grain boundary migration. Accordingly they suggest three different trends in the temperature dependence of the shear-coupled mechanism in different grain boundaries that they have examined : The boundaries that shear-couple over the entire temperature ranges, the boundaries that shear-couple at higher temperatures but with a decreasing magnitude and finally the boundaries that completely change their shear coupling directions at certain temperatures.
In the work of Gianola et al. [28], 3D molecular dynamics simulations have revealed how shear-coupled grain boundary migration operates in a realistic network of NC grains, highlighting especially the role of free surfaces.
Numerous theoretical studies, that will be presented in the next section, have been proposed to explain the shear-coupled mechanism and especially the relation between the coupling factor and the grain boundary geometry.

Read and Shockley model for migration of LAGBs

Shear-coupled migration of symmetrical tilt grain boundaries was first experimentally observed in low angle boundaries in Zn [66, 67]. Theoretically, LAGBs can move entirely by simultaneous motion of their primary intrinsic dislocations [34, 83]. Being subjected to a uniform shear stress τ, the work for a dislocation of the Burgers vector $\vec{b}$ to move by $\vec{\delta r}$ is given by [8] :

$$\delta W = \vec{F} \cdot \vec{\delta r} = [\tau \cdot (\vec{l} \times \vec{\delta r}]) \cdot \vec{b} \tag{1.13}$$

where $\vec{l}$ is the line vector of the dislocation and $\vec{F}$ is the Peach-Koehler forces. Accordingly application of a shear stress, τ on a symmetric tilt LAGB, as schematically represented in figure 1.11a, would extract a force (per unit length) of $\vec{F_g} = \tau\vec{b}$ exerted on each dislocation, that makes it glide over its slip plane.
This force causes the grain boundary to move forward by means of the collective motion of the dislocations without any change in their local distribution. Hereby the uniform motion of the boundary will induce a shape change in the bicrystal (figure 1.11b).
For a more complex tilt boundary containing two sets of edge dislocations with the Burgers vector $\vec{b_1}$ and $\vec{b_2}$, ($\vec{b} = \vec{b_1} + \vec{b_2}$), the applied shear stress will exert a climb force $\vec{F_c}$ and a glide

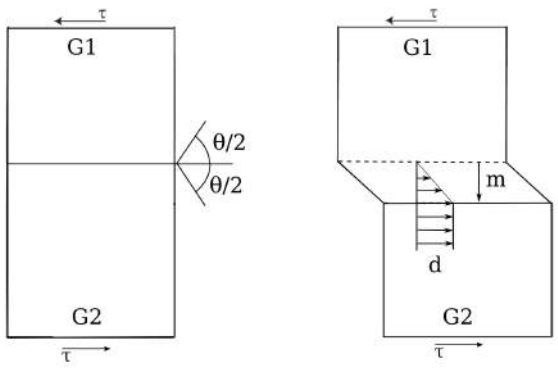

Figure 1.10: The grain boundary of two grains G1 and G2 misoriented of the angle θ relative to each other is sheared by τ. The shear strain causes the grain boundary to move in normal direction to its plane of a distance m. The region swept by the boundary undergoes a deformation which increases linearly until d at the next position of the grain boundary. The coupling factor β is the ratio of the deformation to migration distance.

force $\vec{F}_g$ on each dislocation as indicated in figure 1.11c. Upon application of the stress τ, each dislocation would move normal to the boundary plane simultaneously by combined glide and climb while mutual forces between them will keep them at regular spacings (figure 1.11d).

Cahn model

As an extension for the Read and Shockley model, Cahn et al. generalize it to high angle symmetrical and asymmetrical grain boundaries [84, 85]. Cahn model is a purely geometrical model that assumes that the grain boundary migration, induced by applied stresses or a capillary or any other driving force, produces a shear deformation in the lattice swept by the grain boundary motion [23, 86]. In this theory, the coupling factor β depends only on the density of the dislocations which varies continuously with the misorientation angle θ. As a consequence, the coupling factor is a continuous function of θ.
According to the Cahn model, the shear deformation coupled with grain boundary migration involves two steps (figure 1.12) : (1) plastic deformation of the lattice by the motion of the primary grain boundary dislocations (d_p) along slip planes of the receding grain, without changing its lattice orientation similarly to Read and Shockley model, and (2) a rotation of the lattice of the receding grain into the orientation of the growing grain.
The shear deformation produced at the first step depends on the dislocation density of the boundary and in the second step, to ensure continuity of the lattice left behind the moving boundary, the lattice rotates around the rotation axis of the boundary by the misorientation angle θ. The rotation step depends on the crystal rotational symmetry that produces physically identical states of the lattice. For the particular case of $< 001 >$ tilt grain boundaries in materials in face centred crystal system, there are four equivalent coincidence grain boundaries obtained for misorientation angle $k\pi/2 - \theta$ for $k = 0..3$. This generates four possible coupling modes :

$$\beta = 2\tan(\theta/2 + \pi k/4), k = 0, 1, 2, 3 \tag{1.14}$$

Among the four possible coupling factors, two of them which correspond to the smallest magnitudes of $\vec{b}$, have been evidenced in MD simulations [23, 80] and experimentally [87, 77, 88] :

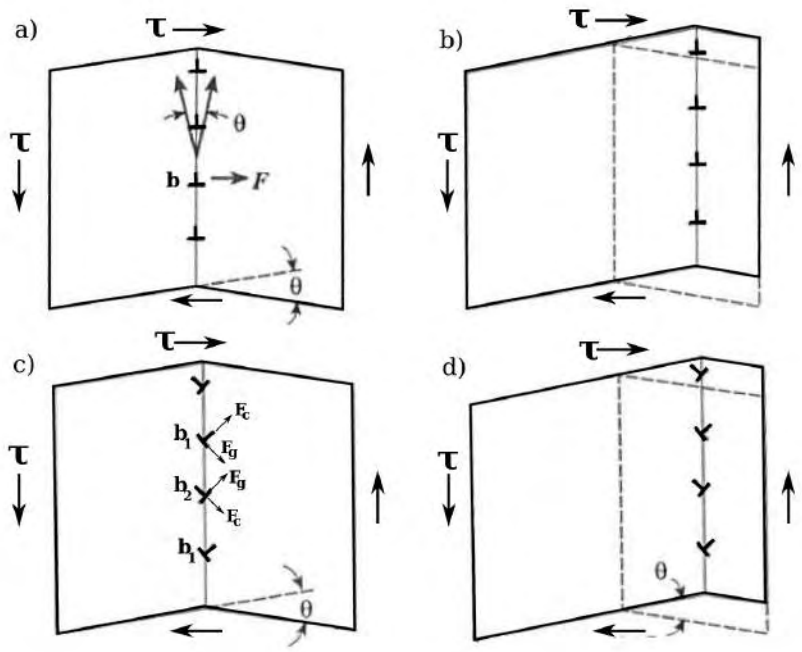

Figure 1.11: a)- b) Motion of low angle symmetric tilt grain boundaries coupled by applied shear stresses, τ, according to the Read-Shockley model [34]. $\vec{F}$ is the glide drive force applied on dislocation due to shear stress. c)- d) Shear-coupled motion of a grain boundary consisting of two sets of edge dislocations, when the applied stress exerts a climb force, $\vec{F}$, on each dislocation. This results in the movement of the entire regularly separated dislocations to move in normal direction to the boundary

The $< 100 >$ mode as it is the case for a $\Sigma 13(510)$ shown in figure 1.12a, in response of the application of a shear τ, the dislocations with $a[100]_{G_1}$ Burgers vector move parallel to $< 100 >_{G_1}$ direction in the (100) slip plane of the receding grain. Due to the coupling mode a counter-clockwise rotation rearranges the lattice points of grain G_1 into G_2 causing the boundary move upward. The coupling factor in this mode is given by

$$\beta_{<100>} = 2\tan(\frac{\theta}{2}) \tag{1.15}$$

The $< 110 >$ mode : This coupling mode corresponds to motion of dislocations with $a/2[110]_{G_1}$ Burgers vector move parallel to $< 110 >_{G_1}$ direction in the (110) slip plane of the receding grain as represented in figure 1.12b for $\Sigma 13(320)$ grain boundary. The shear deformation coupled with the downward motion of the grain boundary in this mode is characterized by :

$$\beta_{<110>} = 2\tan(\frac{\pi}{4} - \frac{\theta}{2}) \tag{1.16}$$

Similarly for low-angle grain boundaries with two arrays of dislocations in Read and Shockley model, the migration of asymmetrical high-angle grain boundaries with two sets of dislocations ($\vec{b}_1$ and $\vec{b}_2$) involves their cooperative motion.

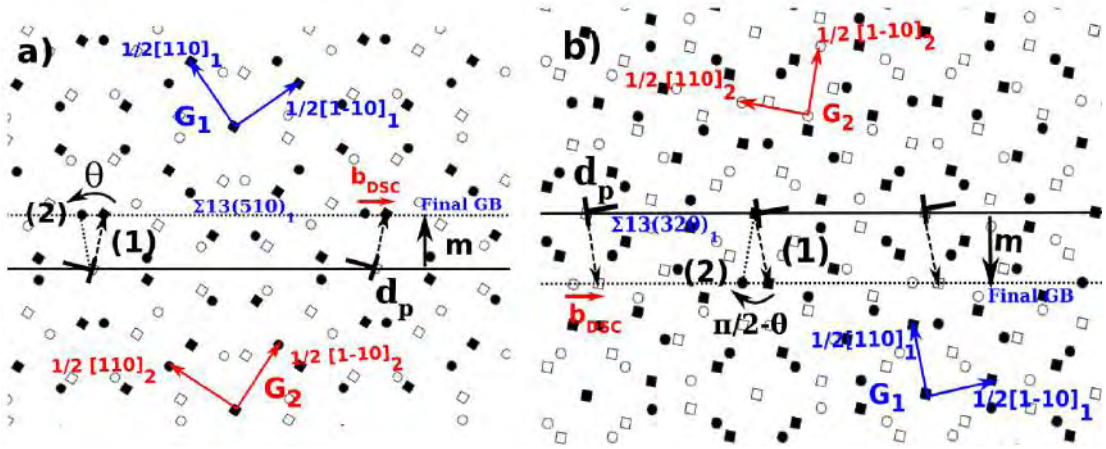

Figure 1.12: The coupling modes according to the Cahn model for two grain boundaries with equivalent $\Sigma 13$ *coincidence : a)* $< 100 >$ *mode in the* $\Sigma 13(510)$*, corresponding to the motion of the primary dislocations* d_p*, parallel to* $< 100 >_{G1}$ *direction in the* $\{100\}$ *plane. Simultaneously with dislocations motion, a counter-clockwise rotation by* θ *around the rotation axis, rearranges the lattice points of* G_1 *into* G_2 *making the grain boundary move upward by* m *; b)* $< 110 >$ *mode in a* $\Sigma 13(320)$ *: the primary dislocations move parallel to* $< 110 >_{G1}$ *in the* $\{110\}$ *slip plane and the grain boundary moves downward by* m *as the a clockwise rotation by* $\frac{\pi}{2} - \theta$ *rearranges the lattice points of* G_1 *into* G_2*.*

The disconnection model

Movement of disconnections with a non-zero step height (cf Figure 1.8) along the grain boundary provides a mechanism for grain boundary migration [89].
Considering the angle between the disconnection and grain boundary plane, its motion can be through glide and/or climb process. Thus the passage of an array of disconnections along the interface involves shearing of the matrix and/or long-range diffusion. In any case the lattice continuity during this motion requires atomic rearrangements i.e the pure shuffling in the wake of the step [72]. Similar conclusions can be drawn in case of twinning, as proposed by Bilby and Crocker [90] and confirmed by atomistic simulations in Zr [91].
Hence according to this model the coupling factor due to the motion of grain boundary induced by the motion of a disconnection is measured by the ratio of its Burgers vector to the step height h.
Also it should be noted that the disconnection model can be regarded as a more general case of the previously described Cahn model. In the Cahn model, following the motion of grain boundary dislocations normal to the plane, there is a local grain translation process due to the coupling mode, to which a line defect similar to grain boundary step can be associated. In other words the translation vector in this process, as it is shown in the figures 1.12a and b corresponding respectively to $< 100 >$ and $< 110 >$ coupling modes of the migration of a $\Sigma 13$ boundary in Cahn model, is equivalent to the motion of a disconnection parallel to the boundary. However, contrary to the Cahn model considering two coupling modes for a grain boundary, the possibility of several coupling modes is conceivable for a grain boundary. This is of course due to multiplicity of disconnections in a grain boundary.
However it should be underlined that both Cahn and disconnection models correspond to coincidence or near-coincidence tilt boundaries and hence not applicable to general non-coincident

high angle grain boundaries, like those that can be found in polycrystals.

More recently, in the Shear Migration Geometrical (SMIG) model, Caillard et al. [93], [92]

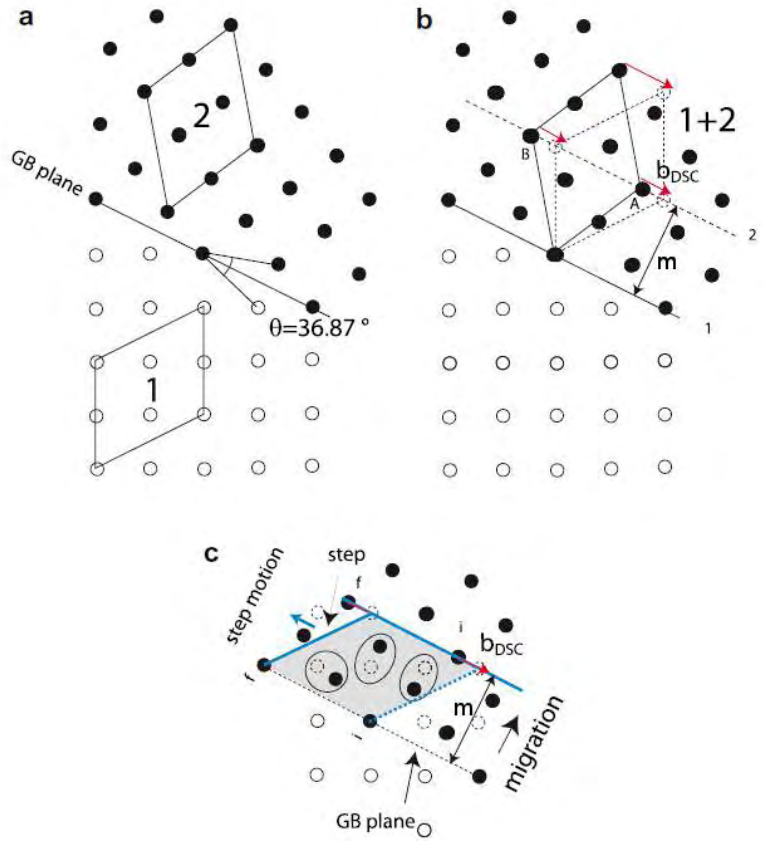

Figure 1.13: (a)-(b) In a given lattice normal to the plane of a coincident grain boundary, two parallelograms (1 and 2) enclosing the same number of atoms are defined in the two adjacent lattices representing each grain. The two parallelograms can be defined in the reference lattice of the first parallelogram by rotating the second parallelogram by the misorientation angle θ along an axis perpendicular to the lattice plane. The pair of rotation and shear transformation that brings two parallelograms, into coincidence define a coupling mode. (c) This process is equivalent to dislocation glide between equivalent positions along the grain boundary plane leading to the motion of the step parallel to the grain boundary and a migration perpendicular to the grain boundary. This glide is accompanied by atomic shuffling inside the gray area, which is the size of the parallelograms [92].

adopt an approach which allows the computation of several coupling modes for any arbitrary grain boundary. In the SMIG model as represented schematically in figure1.13, the two adjoining grains are considered like two different phases but with identical atom types and lattice volume. These different phases can be defined in the plane perpendicular to grain boundary plane and to the rotation axis by selecting two distinct parallelogram motives with the same area and number of lattice sites for each grain (figure1.13a). By finding pairs of shear and rotation values (figure 1.13b-c), one lattice orientation can be transferred into the other and according the choice of these pairs we can have different modes of coupling.

For coincident grain boundaries the shear propagation is done by the glissile movement of the

disconnections with a DSC lattice Burgers vector $\vec{b}_{DSC}$, in the interface plane. The associated steps to these vectors, induce a grain boundary displacement of the distance m, simultaneously rotating the atoms inside the parallelograms from one grain to the other (Figure 1.13c). This rotation corresponds to the shuffling process that was described before. The corresponding coupling factor in this case would be $\beta = \vec{b}_{DSC}/m$

For general grain boundaries on the other hand, no DSC lattice can be defined since there is no displacement vector that repeats periodically along the grain boundary plane. However a dislocation associated with a step can be imagined with Burgers vector of $\vec{b}$. Although $\vec{b}$ have irrational coordinates in both lattices, the disconnection may glide according to Pond et al. [94, 95] along terraces which follow in average the grain boundary plane and would make grain boundary migration of distance m. The corresponding coupling factor in this case would be $\beta = \vec{b}/m$.

Due to the diversity of the choices to define the parallelograms and pairs of shear-rotation transformations to convert them to one another, this purely geometric model predicts several coupling modes for a given grain boundary. The SMIG model, is particularly suitable for asymmetrical grain boundaries and for grain boundary-mediated plasticity in polycrystals where collective grain boundary migrations involving a large variety of coupling modes are needed to accommodate the strain.

1.5 Objectives

Among different models presented for the shear-coupled grain boundary migration, the disconnection model (and as a particular case the Cahn model) has shown good agreement with experimental results on bicrystals experiments in Al [73, 88, 87], Zn [74], cubic zirconia [96] and Au [62]. However, in other experiments on polycrystalline and bicrystalline Al samples [97, 32, 75], much more complicated coupling modes, frequently associated with small coupling factor and sometimes with grain rotation, have been observed. The disconnection model allows a large variety of defects associated to the shear-coupled grain boundary migration and hence are expected to capture more easily the variations of the results. Although the disconnection model potentially explains different modes of coupling for a given grain boundary, a detailed analysis of the operation of these mechanisms is not available yet.
The understanding of the atomic-scale mechanisms associated to the operation of the disconnections during deformation, as the elementary mechanisms of shear-coupled grain boundary migration is indispensable in giving a comprehensive explanation of the observed results at microscopic and macroscopic scales.
Accordingly the main objective of this project is the study of the elementary mechanisms of the shear-coupled grain boundary migration by achieving following goals :

- Investigation of the disconnection dynamics during deformation and identification of the coupling modes :
  This question is dealt in the second chapter of this manuscript where the results of in-situ transmission electron microscopy straining experiments on Al (bicrystals and polycrystalline samples) are reported in details.
- Investigation of structural defects in grain boundaries :
  Preexisting defects and the defects created due to the lattice/grain boundary interactions are analyzed in the third chapter. Their relation to possible coupling modes and comparison with results obtained in Chapter 2 are discussed
- Identification of the atomic processes underlying the coupling :
  In the last chapter the shear-coupled migration of a $\Sigma 13(320)$ is modelled at 0 K in a Copper bicrystal. The minimum energy path of the migration and the corresponding structural evolution is then determined.

2 EVIDENCE OF GRAIN BOUNDARY DISLOCATION STEP MOTION ASSOCIATED TO SHEAR-COUPLED GRAIN BOUNDARY MIGRATION

In this chapter we will use in-situ transmission electron microscopy (TEM) straining experiments to qualitatively and quantitatively probe grain boundary shear-coupled migration in both polycrystals and bicrystals.
In-situ tensile experiments in TEM, provide a unique way to directly investigate the microstructural evolution of materials in real time. It consists of deforming microsamples by application of a uniaxial loading inside a TEM thanks to dedicated holders. Since several years, the use of in-situ TEM straining experiments has proven to be efficient to probe the elementary mechanisms at suitable time and length scales, especially in small grained materials where intergranular plasticity are difficult to capture by post-mortem observations. However, determining grain boundaries characteristics in NC metals is a tedious and difficult task in the best case, and almost impossible, if several grains overlap in the film thickness. To avoid this problem, we have used samples with larger grain sizes (in the ultrafine grain range $100nm < d < 1\mu m$) and bicrystals. Also in order to preferentially activate intergranular plasticity, we have conducted experiments at high temperatures.
Bicrystal as a model material allows the investigation of deformation mechanisms in a grain boundary with controlled characteristics (both misorientation and plane) which avoid the complexity of a network of curved grain boundaries and triple junctions. Moreover, their use allows a direct comparison with in-situ creep tests performed in bulk bicrystals [88]. In order to investigate possible collective grain boundary behaviour induced by shear-migration coupling and/or under capillarity forces, in-situ experiments performed in polycrystals are considered in a second time.
After a description of the methodology of the experiments in the section 2.1, the experimental results will be reported in details in section 2.2. Finally the results will be discussed in section 2.3.

2.1 Experiment Methodology

2.1.1 Samples

Two types of high purity (99.9%) Al samples were used during the in situ TEM straining experiments :

- Bicrystal samples with a symmetrical 76.4° < 001 > tilt grain boundary (near to Σ41(540)) ;
- The ultra-fine grained (UFG) polycrystalline samples ;

The bicrystal samples, provided by D. Molodov from Aachen University, were produced by the Bridgman technique [98]. In this technique a quartz crucible filled with material is pulled horizontally through a furnace tube in which the material is heated above its melting point. Two seed crystals are placed in the heated zone in the desired orientations corresponding to the relative orientations of the grains in the bicrystal. As the crucible is drawn slowly from the heated region into a colder region, the seed crystals induce crystal growth. The newly created material will accurately replicate the crystal structure of the seed crystal. The orientations of the adjacent grains across the boundary and deviations of the normal directions with an ideal [001] axis normal to the boundary plane in the investigated bicrystal are given in Table 2.1. The created bicrystal presents a grain boundary with a tilt angle of 76.4° which nearly corresponds to the one 77.32° of a Σ41(540) grain boundary. More details of the processing steps of the bicrystal sample are explained in [88].

Tilt Angle	Grain 1			Grain 2		
$\lvert\Delta z\rvert_1 + \lvert\Delta z\rvert_2$	$\lvert\Delta x\rvert_1$	$\lvert\Delta y\rvert_1$	$\lvert\Delta z\rvert_1$	$\lvert\Delta x\rvert_2$	$\lvert\Delta y\rvert_2$	$\lvert\Delta z\rvert_2$
76.4°	−0.9°	−0.5°	38.7°	−0.2°	−0.4°	37.7°

Table 2.1: Orientations and misorientations of adjoining grains in the investigated bicrystalline specimen. Δx and Δy are deviations of the $< hkl >$ directions from the sheet normal, Δz is the rotation angle around the z axis. $\theta = \lvert\Delta z\rvert_1 + \lvert\Delta z\rvert_1$ is the misorientation of the grain boundary.

The UFG samples are fabricated by equal channel angular pressing (ECAP). ECAP is one of the severe plastic deformation techniques for processing bulk fine-grained materials. In this method, massive billets of material is repetitively pressed through a die consisting of two channels with identical cross sections.The deformation occurs by simple shear parallel to the intersecting plane of the channels.

Sample Preparation

The as-received bicrystal and polycrystalline bulk samples are first cut and sectioned precisely into rectangular 2.5 mm × 1 mm samples with a nearly 500-800 μm thickness. In the case of bicrystal samples, prior to the cutting, the exact position of the grain boundary is marked on the surface of the bulk material. The position of the boundary is revealed using a chemical etch with a solution of 50%HCl, 47% HNO3 and 3%HF. The mark of the grain boundary position should be preserved on at least one side of the sample surfaces all through the preparation procedure. These samples are cut perpendicularly to the misorientation axis of the grain boundary.
The sectioned specimens are then thinned mechanically down to a 30-40 μm, keeping two sides of the slices as parallel as possible. Electrochemical polishing using a methanol solution with 33% of nitric acid at T=-10°C is finally the last step of the preparation to obtain a thin observable area in the sample, around the edge of a hole created by perforation.

In addition to the general requirements for preparation of the samples to be observed by conventional TEM, special care must be taken for TEM straining sample, so that the perforation is circular and at the center of the specimen, with an edge free of cracks. This is important for a well-defined stress distribution in the sample and to avoid deformation concentrations at the crack-tips [99]. The prepared samples are then inserted in a Gold nanoparticles suspension. This is for the purpose of positioning the nanoparticles on the surface of the samples which will serve as fiducial markers.
The prepared samples are ultimately glued on copper grids which can be fitted in the specimen holders. A high strength alumina adhesive is used for this purpose whose maximum grip is achieved at about 370°C. This whole sample preparation is performed in a way that the grain boundary plane forms a 45° angle with respect to the straining axis of the holder. By doing so, a maximum resolved shear stress parallel to the grain boundary plane is achieved.

2.1.2 Experiment description

A home-made heating straining holder (figure 2.1a) is used for in situ experiment in JEOL 2010. The straining mechanism (figure 2.1b) consists of a mobile and a fixed jaw and a micromotor which displaces the mobile jaw. The specimen is anchored on the initial positions of the jaws and is strained by their relative displacements. The heating is done by radiation of a resistor wire wound in an alumina multibore tube. The temperature is a function of the current intensity applied to the resistor. The relation between temperature and current is determined experimentally by melting in-situ metals of known melting point [99].
Once the specimen is mounted on the holder and the holder loaded on the microscope the

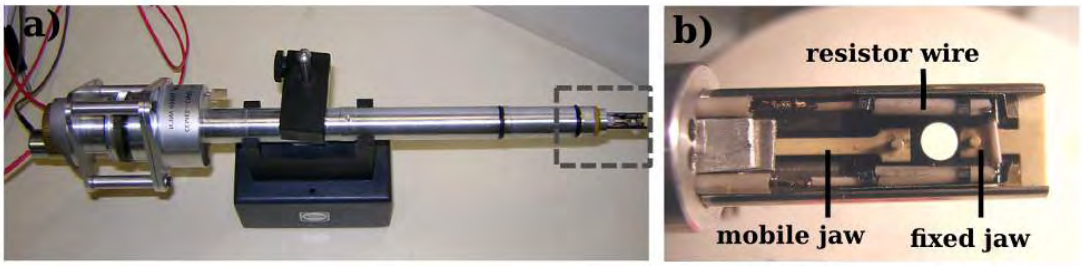

Figure 2.1: Set-up of for the in-situ TEM straining experiments. a) the heating straining sample holder ; b) the straining mechanism

experiment can be started by heating up to the desired temperature i.e about 400-450°C. This approximately corresponds to $0.7T_m$, with T_m the melting temperature of Al. In order to avoid any deformation due to thermal drifts, the heating and cooling steps should be performed as slowly as possible. The mobile jaw is then moved to kill the gap between the sample grip and the holder so that the sample to be under load. At this point the straining is started slowly by applying increments of strain and observing the sample response. The maximum applied stress in the sample corresponds to the region where the hole rim is parallel to the straining axis [100]. Also in the zones with preexisting cracks on the hole rim there is more tendency to trigger the deformation in response to stress application.
Selected area diffraction is used, whenever needed for the crystallographic identification of the zones of interest in the sample. The dynamic observation is recorded by a DVD/HD recording

using a 25 fps video rate MEGAVIEW III CCD camera. The video tracks are then analyzed frame by frame and the representative sequences and images are cropped.
The image quality and contrast is enhanced by image processor computer programs. Image correlation is used to qualitatively and quantitatively study the grain boundary migration in the observed zones. To do so, two images taken before and after grain boundary migration are superimposed using the fiducial markers on the surface of one (reference) of the grains. In order to obtain a precise superposition of two images their contrasts are subtracted. The relative displacement of a grain compared to the reference one corresponds to the non-superposition of the markers in that grain.

2.2 Results

2.2.1 Grain boundary dislocation step motion

Observation of elementary grain boundary dislocation steps

During the in-situ straining experiments with the bicrystalline samples, several very small steps were observed along the grain boundary. Once the sample was under stress due to straining, these steps had shown sometimes reactive either by moving parallel to the grain boundary plane or by small amplitude oscillations.
Figure 2.2 shows bright field micrographs taken during an experiment with the bicrystalline samples heated up to 400°C. The grain boundary between grains G_1 and G_2 is seen here edge-on, i.e. along the $< 001 >$ direction. The straining axis, (T), is indicated by an arrow in figure 2.2a. A 2 nm height step, labelled s in figure 2.2a can be clearly seen along the grain boundary. Though they do not appear in the figure, several other steps of this height have also been observed along the grain boundary.
Under stress, the step has been observed to move over 25 nm along the grain boundary toward

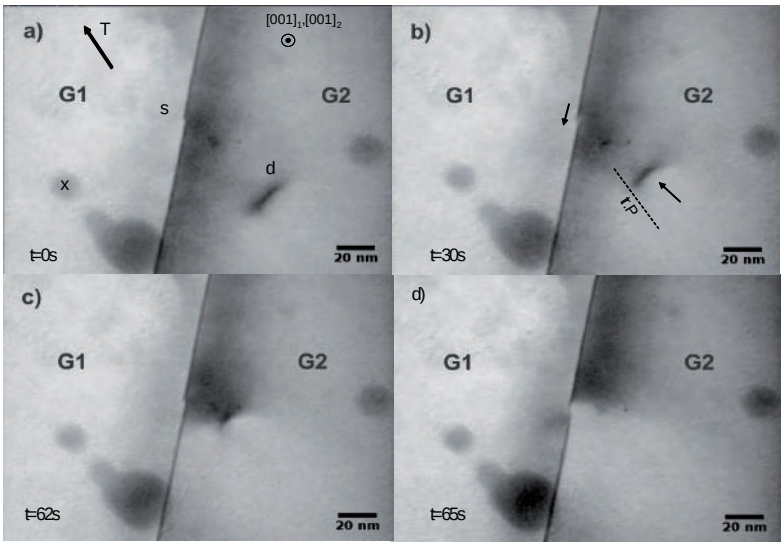

Figure 2.2: Motion of grain boundary dislocation steps, along 76.4° $\langle 001 \rangle$ *grain boundary in an Al bicrystal at* $400^\circ C$. *Time and scales are reported on each picture. The straining axis (T) is indicated by an arrow. x is a fixed point.*

the nanoparticle X at a maximum speed of few angstroms per second (figure 2.2 b and c). In the meantime, a lattice dislocation, labelled d in figure 2.2(b), glides in a $\{111\}$ plane of G_2 : the trace of the glide plane has been reported as tr.P in figure 2.2b. The dislocation d then eventually interacts with the grain boundary dislocation step (figure 2.2d). The step then remains immobile suggesting that the interaction has led to the formation of a sessile grain boundary dislocation step.
The simultaneous motion of the step and the lattice dislocation suggests that the step has a dislocation character, i.e. it is sensitive to an external applied and/or an elastic strain field due to the presence of the dislocation d in its vicinity. As a consequence, the step is identified as a grain boundary dislocation step i.e. a disconnection.

2.2.2 Macro-step formation

Besides the mentioned elementary steps, other steps with a few tens of nm height were observed along the grain boundary. These Macro-steps also move in response to an external load inducing the migration of the grain boundary.
Figure 2.3 reports the results of a straining experiment on a bicrystal presenting a macro-step. The initial configuration evidencing a plane grain boundary is shown in figure 2.3a. The straining axis (T) is indicated by an arrow in figure 2.3a.
After 548 s, a first step, labelled s_1 of height h_1=95 nm, moves at a speed of about 4 μm/s along the grain boundary toward the marker X2 (figure 2.3b) and eventually stops close to X2. The step height h_1 is around 50 times the elementary grain boundary dislocation step height, suggesting that this macro-step is composed of elementary steps. Later on, at t = 789 s, a second step s_2 of height h_2 = 50 nm, initially immobile, is observed close to the marker X1 (figure 2.3c). Two seconds later, a third step s_3 of height h_3 = 100 nm arriving from the thicker area of the sample meets s_2 where it stops (figure 2.3d). A single step s_4 of height h_4=150 nm is then formed. At t = 835s, the step s_4 starts moving rapidly at about 4 μm/s along the grain boundary (figure 2.3(e)) before being definitely blocked close to the marker X2. In the meantime, s_4 absorbs s_1.
Simultaneously to the blocking of s_4, a dislocation activity in G_1 is noticed. The motion of one or several other steps eventually occurs leading to the formation of the step s_5 of a height h_5 = 250 nm after 1309 s (figure 2.3f) and finally to a 2 μm high step s_f after several minutes (Figure 2.3g). Note also in figure 2.3g, the large number of slip traces in both grains, indicating that part of the strain is also relaxed by intragranular plasticity.
The blocking of the step s_4 motion is attributed to the presence of a surface defect, most likely an aggregate of nanoparticles that pins the step at the sample surface.
In addition, a careful analysis of figure 2.3d shows that : i) the shape of s_2 and s_3 can still be distinguished in the step s_4 and that ii) the height of s_4 is approximately equal to the sum of the heights of the steps s_2 and s_3. Similarly, the profile of the grain boundary in figure 2.3f can be interpreted as a stack of macro-steps. Figure 2.3h provides a sketch of the four different steps that accumulated to form the macro-step s_f .
From these observations, we conclude that the grain boundary migration occurs via the collective motion of elementary steps that progressively stack until forming macro-steps. Indeed, because of the impossibility of passing, faster steps will eventually pile up against immobile or slowest ones while they are temporarily slowed down or blocked, resulting in the slowing down of the migration process.

2.2.3 Measurements of the coupling factor

From figure 2.3, it is possible to extract and measure some characteristics (including the coupling factor) of the displacements associated to the grain boundary migration. These dis-

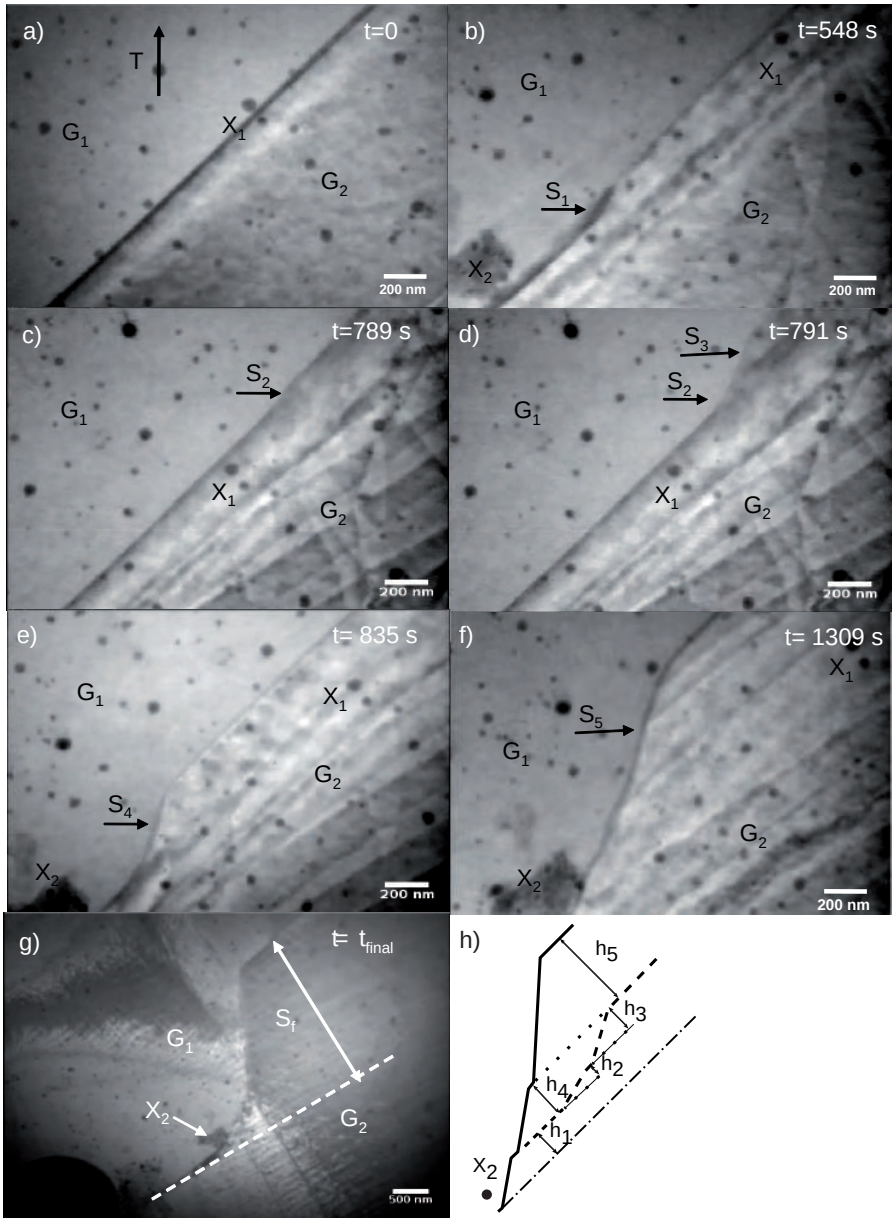

Figure 2.3: (a)-(e) Motion of macro-steps along the grain boundary. It consists first in the motion of s_1 (a-b) followed by the motion of s_3 which absorbs the immobile step s_2 (c-d) forming a step s_4 that eventually moves toward X2 (d-e). (f-g) are configurations after the motion of several other steps. The final step s_f which has largely grown is about 2 μm high. (h) is a sketch of different steps and their corresponding heights.

placements are deduced from image correlations as it is explained before. The subtraction of the pictures from the same zone before and after the grain boundary migration is performed by superimposing of markers in G_2. Because of the shear-migration coupling, the markers in grain G_1 do not superimpose : the markers appear with black and white contrasts. The relative

displacements of the markers compared to grain G_2 are deduced from these contrasts.
Figure 2.4a,b and c provide the differences between figures 2.3b and a, between figures 2.3e and b and between figures 2.3f and e, respectively.
As it was shown before, the shear displacement is expected to depend linearly on the migration distance in the area swept by the grain boundary migration, and is then constant above the grain boundary.
The motion of the step s_1, characterized in figure 2.4a is now detailed. The displacements of one marker noted X1 located in the area swept by the grain boundary and six markers noted X2 to X7 located above the area swept by the grain boundary is indicated by arrows in figure 2.4a. The grain boundary migration distance is m1. As expected, the norms of displacements of X2-X7, noted d2-d7 are equal, and their directions characterized by the angles γ_2-γ_7 between the displacement vector and the grain boundary plane are also equal $\gamma_i = \gamma \approx 20°$ (for i = 1 to 7). The coupling factor is deduced :

$$\beta_{\parallel} = \frac{d_i \cos\gamma}{m1} \approx 25 \pm 2\% \tag{2.1}$$

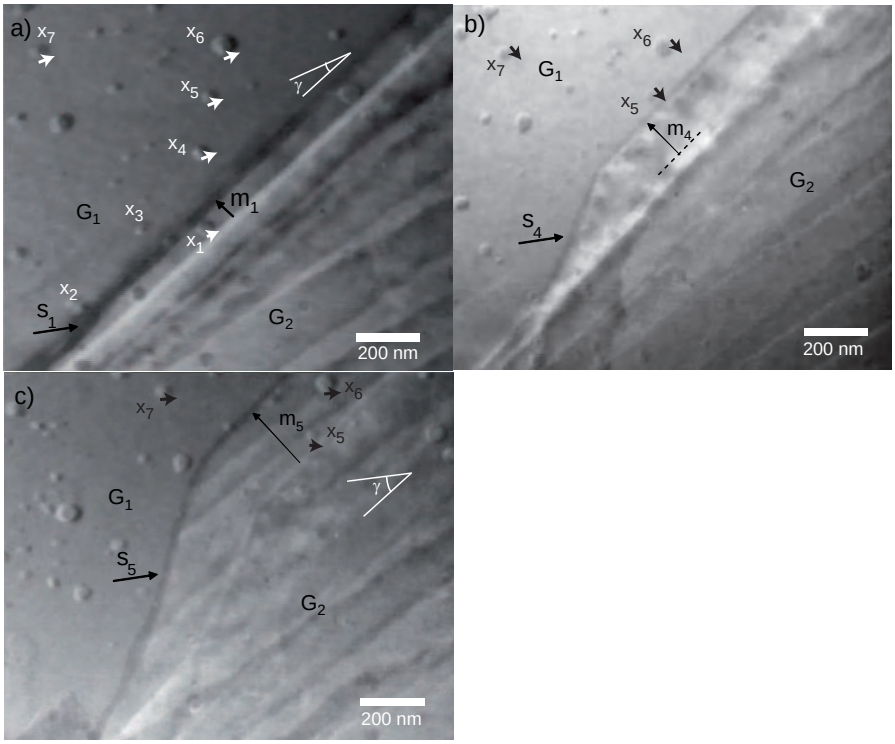

Figure 2.4: Image difference obtained by subtracting the contrast of images taken before and after the motion of step s_1(a), s_4 (b) and s_5 (c). When superimposing the markers in G_2, a shift in the markers position in G_2 is observed in all cases indicating the deformation has occurred. The coupling factor has both components parallel and perpendicular to the grain boundary.

This coupling factor is close to the value obtained by macroscopic tests on the same bicrystals [88, 76]. Besides, the migration of the step produces not only a shear strain (parallel to the grain

boundary plane) but also a displacement perpendicular to the grain boundary plane. We characterize the markers, displacements perpendicular to the grain boundary plane by the coefficient : $\beta_\perp = \frac{d_i \sin\gamma}{m1} = 6 \pm 2\%$ (i = 2 to 7), corresponding to a deformation perpendicular to the grain boundary.
Analyzing figure 2.4b, the coupling factor related to the motion of s_4 is estimated to be $\beta_\parallel \approx 0 \pm 2\%$ whereas the displacements perpendicular to the grain boundary plane is characterized by :

$$\beta_\perp = \frac{d_5 \sin\gamma}{m_4} = \frac{d_6 \sin\gamma}{m_4} \approx 6 \pm 2\% \tag{2.2}$$

Finally, figure 2.4c related to the formation of the macro- step s_5 is considered. The displacement of three markers in G_1, two below the step (X5 and X6) and one above (X7), are analyzed. Again, the displacement of the markers is not purely parallel to the grain boundary. Surprisingly, even in the area not swept by the step, markers displacement can also be noted. Moreover, the markers displacement profile in front of the step is similar to the one behind the step.
As expected, the markers displacement in the area swept by the grain boundary is not constant but increases with the distance to the initial position of the grain boundary. The coupling factor due to the motion of s_5 can again be estimated :

$$\beta_\parallel = \frac{d_7 \cos\gamma}{m_5} \approx 7 \pm 2\% \tag{2.3}$$

and the analysis of the displacements perpendicular to the grain boundary plane gives :

$$\beta_\perp = \frac{d_7 \sin\gamma}{m_5} \approx 6 \pm 2\% \tag{2.4}$$

The displacements perpendicular to the grain boundary plane, observed in all analyzed grain boundary motions, were not expected from the pure coupling mode and the motion of the step is supposed to involve climb processes, i.e. long-range diffusion, which are enabled by the high temperature.

2.2.4 Grain boundary motion with no induced deformation

The motion of the macro steps along the grain boundary is not always attributed to shear-coupled grain boundary migration. Indeed, we have observed some grain boundary migration in bicrystal and polycrystalline samples without measurable deformation in the zone swept by the grain boundary.
Figure 2.5 reports images taken during straining of the bicrystal sample at 450°C. An initially fixed grain boundary step marked with S_p at t=0s is shown in figure 2.5a. The step does not have a uniform height along the grain boundary and most probably is composed of several other steps. The maximum height of the step in the image is $h_p = 65nm$.
The position of the grain boundary is pointed with respect to the marker X on the sample. The sample is then slightly strained (the straining direction T is indicated by an arrow in Figure 2.5. The step S_p moves at a speed of $35nm/s$ upward along the grain boundary plane. A slight contrast change during the step motion is visible at the edge of the boundary however it was not possible to be characterized. Figure 2.5b reports the grain boundary observed after the passing of the step and figure 2.5c is the image difference between figures 2.5a and b, superimposed using the marker X as a reference. Figure 2.5c shows the complete superposition of the fiducial markers on both grains suggesting no induced deformation on the grains due to grain boundary migration. The observed macro-step hence can be associated to a combination of several pure steps moving in response to applied stress by shuffling mechanism.

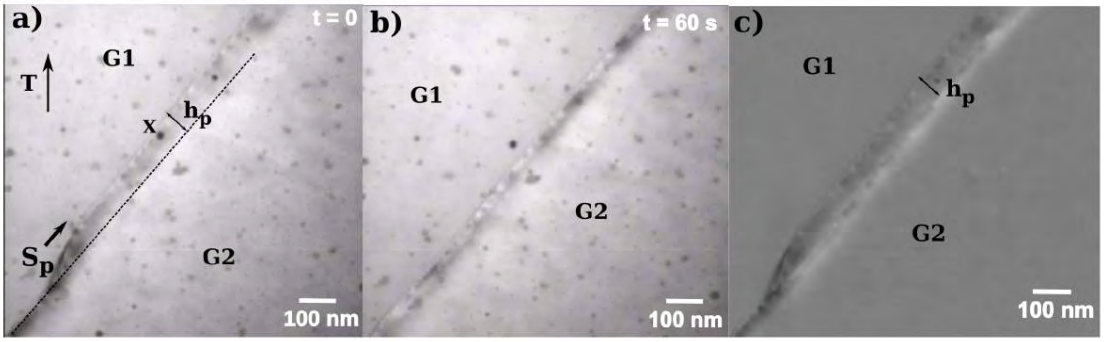

Figure 2.5: a)-b) Motion of the macro-step S_p of height h_p along the grain boundary due to straining the bicrystal at 450°C. The sense of the step motion is indicated by an arrow and X is a fiducial marker on the surface of the sample. c) The image difference between (a) and (b) shows complete superpositions of the both grains.

Grain boundary migrations with no coupled deformation were also observed during the straining of polycrystalline samples. Figure 2.6 reports three micrographs taken during straining of a polycrystalline sample at 420°C in which the straining direction (T) is indicated. Five grains G1-G5 are visible in figure 2.6a and TJ1, TJ2 and TJ3 are the triple junctions between grains (G1, G2, G4), (G2, G3, G4) and (G3, G4, G5) respectively. The exact position of the interface between G1 and G5 and the corresponding triple junction (G1, G4, G5) are not clearly visible in this contrast. In the following, the notation GB_{ij} refers to the grain boundary between grains i and j. The straining triggers the motions of GB_{14}, GB_{24}, GB_{15}, GB_{34} and GB_{35} in the directions indicated by arrows in figure 2.6a. GB_{45} remains fixed during the experiment. The collective grain boundary motion causes the grain G4, with an initial area of $0.2\mu m^2$, to shrink until its total disappearance in 6 s (figure 2.6c). No interface dislocation activity is observable in either of the grain boundaries. From the image correlation in the zones swept by boundaries, no deformation is measurable due to grain boundary migration. Accordingly, the boundary motions can be associated with curvature-driven grain boundary migration to eliminate the constraints imposed by triple junctions [101]. Curvature-driven boundary migration is supposed to be attributed to atomic shuffling processes in the vicinity of the interfaces.

2.2.5 Grain boundary dislocation nucleation

Figure 2.7 reports pictures taken during an in situ experiment in the Al polycrystal. A grain boundary between two grains G1 and G2 is initially slightly inclined with respect to the foil surface and thus exhibits a uniform black and thick contrast. The straining axis (T) is indicated by an arrow in figure 2.7a. The time origin t = 0 s is defined when two bright contrasted points S1 and S2 appear along the grain boundary (figure 2.7a). They can be attributed to the nucleation of dislocation loops at two sources S1 and S2. The two loops eventually expand (figure 2.7b) and finally impinge. In the meantime at time t = 4 s, a rapid grain boundary migration is observed in the left part of the grain boundary (figure 2.7c) the initial and final positions of the grain boundary during this migration are respectively indicated by a dashed and a solid line).
Although it was not possible to fully characterize these dislocation loops, this observation tends to indicate that a correlation exists between the nucleation of defects in the grain boundary and the migration of the grain boundary. Shortly after (t = 14 s), another dislocation source noted S3 appears in the right part of the grain boundary as reported in figure 2.7d. Figure 2.7e is a

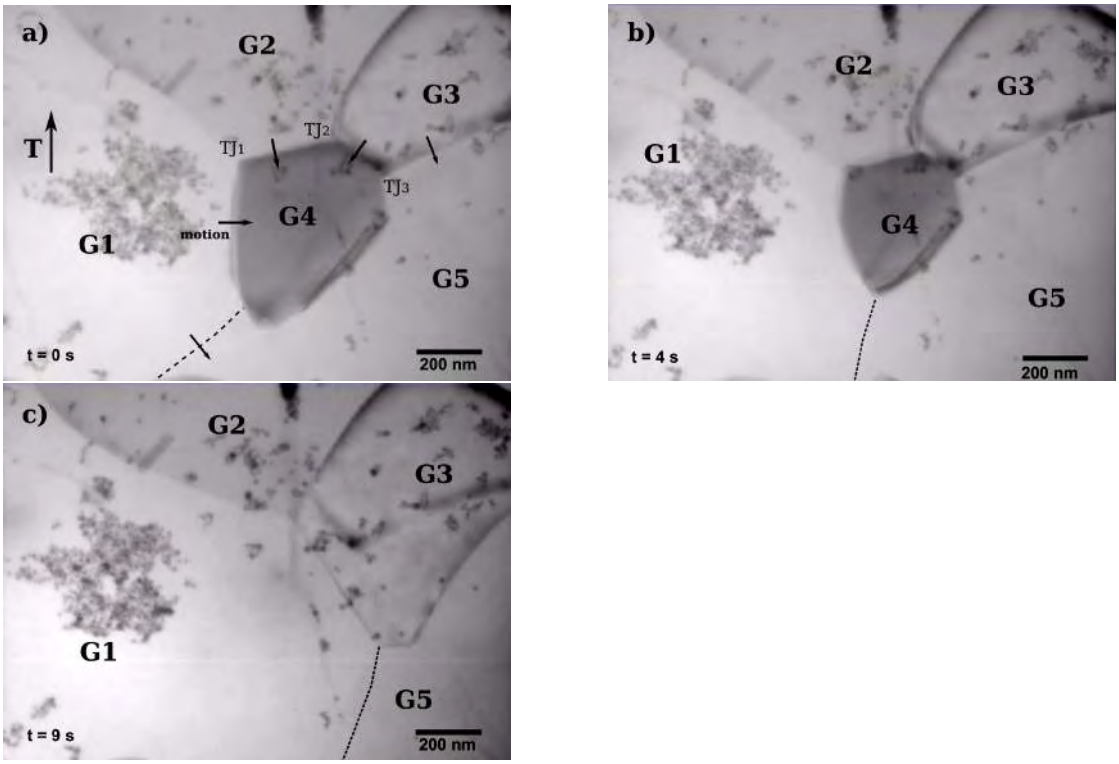

Figure 2.6: Straining of a polycrystalline sample at 420°C. a) Grains G1-G5 are visible in the image and TJ1-TJ3 are the triple junctions between grains (G1, G2, G4), (G2, G3, G4) and (G3, G4, G5) respectively. In response to straining the interface Following a-c show shrinkage and disappearance of grain G4 due to the collective motions of the boundaries GB_{14}, GB_{24}, GB_{15}, GB_{34} and GB_{35} in the indicated directions.

zoom of the source S3. Contrary to S1 and S2, it seems that several dislocation loops are emitted from S3 in G1 and G2, indicating that intragranular plastic mechanisms can also be activated in addition to stress-assisted grain boundary migration.
It is worth noting that macroscopic observations performed on Al bicrystals also revealed that the stress-induced moving boundaries can act as sources of lattice dislocations. These dislocations eventually lead to the generation and growth of new (sub)grains in the grain boundary region [77].

2.2.6 Grain boundary dislocation motion in polycrystals

Figure 2.8 reports a situation involving three grains G1, G2 and G3, and the migrations of two grain boundaries. The straining axis (T) is indicated by an arrow in figure 2.8a.
At t = 0 s, two trains of dislocations labelled d_{12} and d_{13} can be observed moving in opposite directions along the two high angle grain boundaries, GB_{12} and GB_{13}. The dislocations d_{13} have been emitted at the junction between a subgrain boundary SGB and GB_{13}. At t = 70 s reported on figure 2.8b, both GB_{12} and GB_{13} have migrated over a distance of about 400 nm, corresponding to a mean migration speed of 10 nm/s.
Figure 2.8c reports the difference between figure 2.8b and a, the markers of the grain G1 being

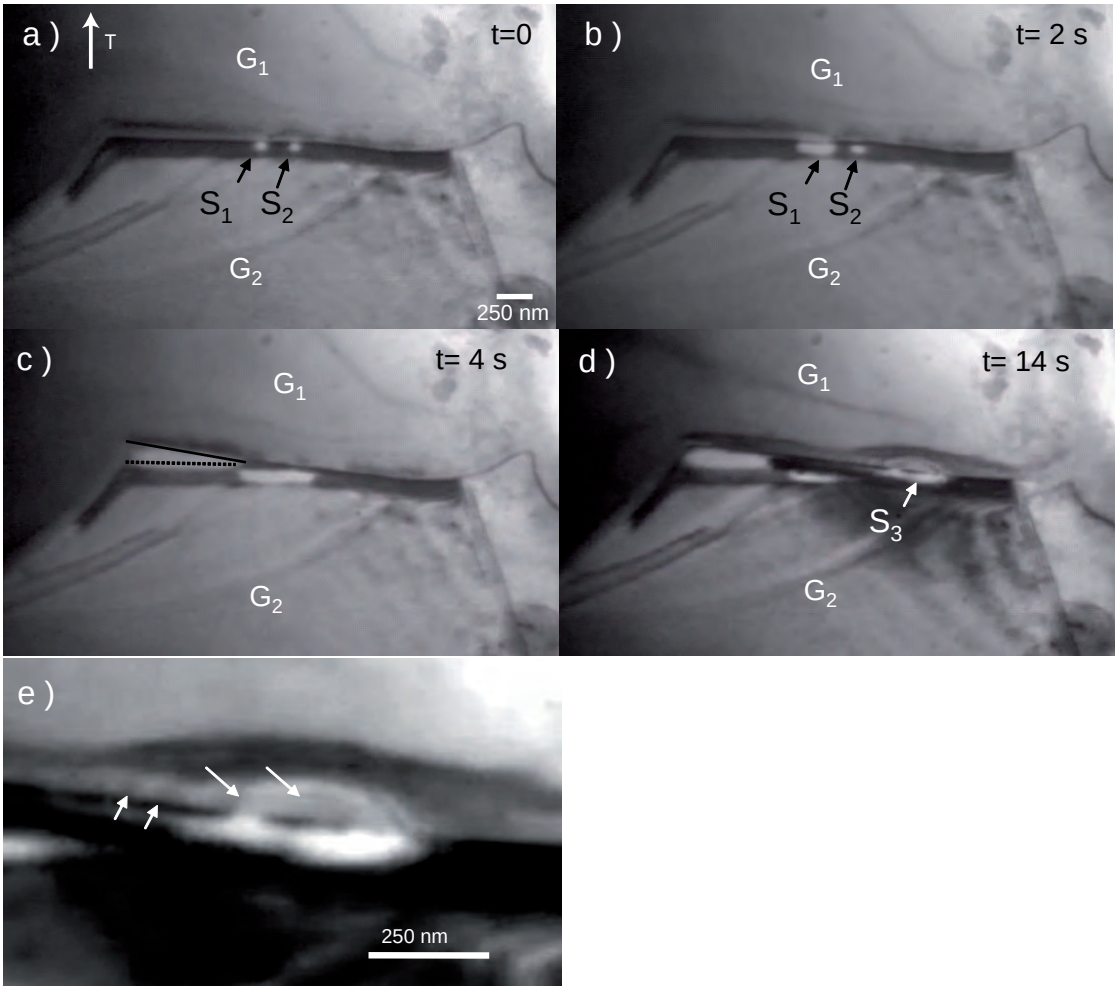

Figure 2.7: Sequence of bright field micrographs showing the emission of dislocation loops inside the grain boundary in S_1 and S_2 (a-b) followed by a grain boundary migration (c) in a polycrystal. (e) is a zoom of (d) showing the operation of the source S_3. Note in (e) the concentric dislocation loops noted by arrows emitted in G_1 and G_2.

used as a reference. The analysis of figure 2.8c shows that the markers (in G2 and G3) displacements are approximately perpendicular to the GB_{12} and GB_{13} traces. However, since the grain boundaries are inclined, part of the apparent displacement can have a shear component parallel to the grain boundary but out of the plane of the image. Figure 2.8c also reveals that the markers displacement increases with the distance from the initial position of the grain boundary in the area swept by the grain boundary.
From the measure of the displacements perpendicular to the grain boundary, one gets an apparent coupling factor $\beta_a \approx 5\%$. It is interesting to note that the markers displacements are approximately the same in both grains G2 and G3, suggesting that the same coupling mechanism operates in both grain boundaries. The grain boundary migrations can be interpreted as follows (figure 2.8d) : in GB_{12}, step dislocations d_{12} of Burgers vector $\vec{b}_{12}$ move toward the triple junction (T J in figure 2.8a, b and d), leading to an apparent marker displacement deformation.

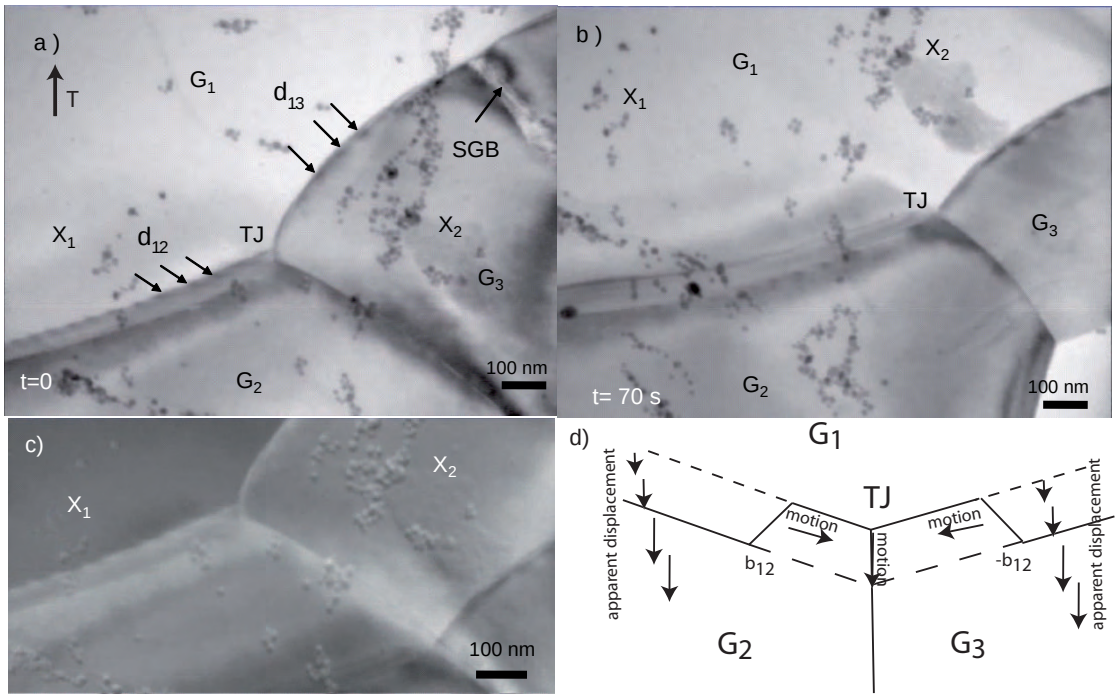

Figure 2.8: a-b)Simultaneous deformation coupled migration of two grain boundarys. Note the presence of grain boundary dislocation d_{12} and d_{13} moving in opposite direction toward the grain boundary during the grain boundary migration. (c) The difference of (a) and (b) with marker X_1 superimposed shows a shift in the markers in G_2 and G_3 (X_2 for instance). An apparent coupling factor around 5% is measured. The coupled motion is thought to occur as schematically drawn in (d).

In the meantime, in GB_{13}, step dislocations d_{13} with an opposite Burgers vector $\vec{b}_{13} = -\vec{b}_{12}$ move in the opposite direction, leading thus to the same deformation which produces the apparent displacement profile sketched in figure 2.8d. When the two-step dislocations meet at the grain boundary, they annihilate and lead to the motion of the triple junction.

2.3 Discussion

The results of the previous section evidence that stress driven grain boundary migration in the investigated bicrystals and fine grained polycrystals occurs at high temperatures (i.e. 0.7 T_m) by the rapid and repeated motion of steps (figure 2.2 and 2.3).
Indeed, each time a step moves along the entire grain boundary, it produces the grain boundary migration over a distance equal to the step height. These steps are probably composed of nanometer height elementary steps as suggested before. These elementary steps carry a plastic deformation, i.e. the steps have a dislocation character [92],[94]. This conclusion, proposed in interfacial dislocation model such as SMIG or DSC models, confirms that grain boundary dislocation steps (disconnections) operate in high angle grain boundaries similarly to their actions in twinning or martensitic transformation.
In addition, the amount of produced deformation can be different from one step to another, suggesting that several kinds of grain boundary dislocation steps can be responsible of the grain

boundary motion, or in other words, that a given grain boundary can support several coupling modes. Thus the coupling factor is a characteristic of the grain boundary defects (disconnections) rather than of the grain boundary characters (noticeably its disorientation angle).
In polycrystals, where grain boundaries are curved, the motion of the step can also be coupled to capillarity forces (see figure 2.8 and 2.6). When capillarity forces are the only driving force, the grain boundary migration is supposed to occur without deformation as it has been also observed experimentally [92],[88], presumably by the pure shuffling mechanism.

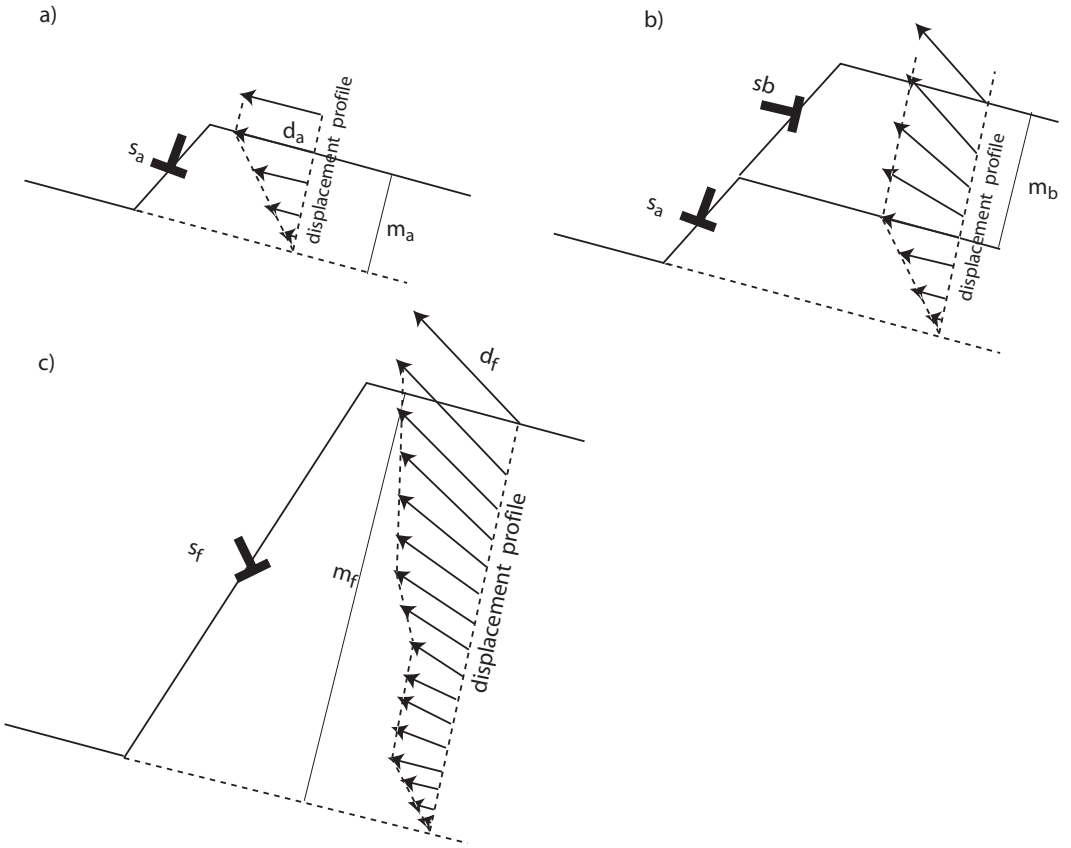

Figure 2.9: The combination of several steps of different heights carrying different amounts of deformation (a-b) is responsible for the observed final displacement profile (c).

2.3.1 Step combination and coupling factor

In this paragraph, we explain the former observations introducing a model involving the combination of steps of different heights and different Burgers vectors. These steps can also be considered as disconnections or group of disconnections.
Let's consider the motion of a first step, for instance a step s_a producing a pure shear strain parallel to the grain boundary plane : a sketch of this situation is proposed in figure 2.9a. In this case, according to the pure coupling model, the markers displacement profile linearly increases with the migration distance in the area swept by the grain boundary migration, and is then constant above the grain boundary.

If a second step s_b coupled to a strain perpendicular to the grain boundary plane, stacks to the former step s_a, the displacement profile will be modified as shown in figure 2.9b. The total markers displacements induced by both steps s_a and s_b will be characterized by a coupling factor $\beta_{\parallel} = \frac{d_a}{m_a+m_b}$ and a coefficient $\beta_{\perp} = \frac{d_b}{m_a+m_b}$, where m_a and m_b are the s_a and s_b step heights and d_a and d_b are the strain carried by the steps. If several steps of different heights carrying different

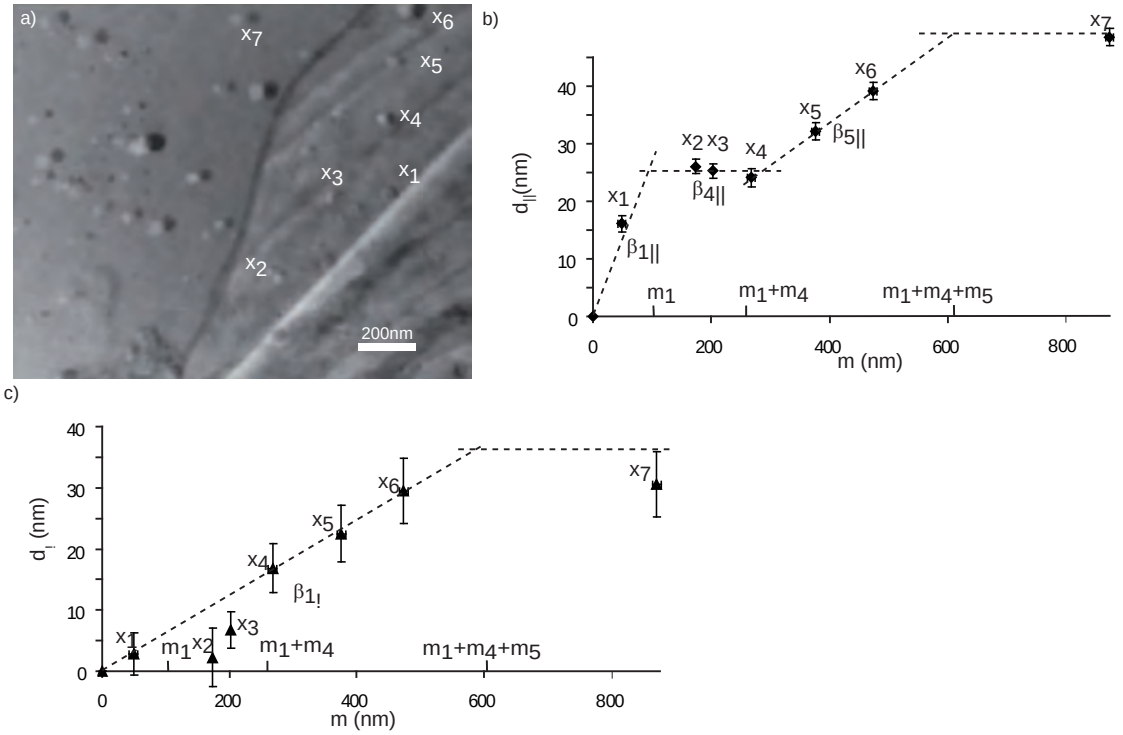

Figure 2.10: From an image difference between the initial and final position of a grain boundary due to formation of the macro-step s_5 (a), the markers displacement profile parallel and perpendicular to the grain boundary can be drawn (b) and (c). The different slopes in the curved correspond to the different coupling factors associated to the step motion.

amount of deformation (and not only shear) move along the grain boundary and eventually pile up as sketched in figure 2.9c, the observed average coupling factor will be :

$$\langle \beta_{\parallel} \rangle = \frac{\Sigma_i d_i \cos \gamma_i}{\Sigma_i m_i} \tag{2.5}$$

and for the average coefficient $\beta_{\perp}$:

$$\langle \beta_{\perp} \rangle = \frac{\Sigma_i d_i \sin \gamma_i}{\Sigma_i m_i} \tag{2.6}$$

Where γ_i is the angle between the strain direction carried by the step and the grain boundary plane.
This explanation will help us to interpret the markers displacement observed in the previously described experiments.
Figure 2.10a shows the plot of the difference between figure 2.3f and 2.3a, using the markers in

grain G2 as a reference : it thus characterizes the displacement induced by the macro-step s_5.
The displacement of seven markers x_i is analyzed. Figures 2.10b and c plot the markers displacements respectively, parallel $d_{\parallel}$ and perpendicular $d_{\perp}$ to the grain boundary plane as a function of their distances m from the initial position of the grain boundary plane.
In the first part of the curve corresponding to the motion of s_1, i.e. for $0 < m < m_1$ with $m_1 = 100nm$, both curves $d_{\parallel}$ and $d_{\perp}$ show a linear increase with m. The respective slopes of these curves are $\beta_{\parallel 1} \approx 25\%$ and $\beta_{\perp 1} \approx 6\%$. These quantities are coherent with the coupling factor $\beta_{\parallel}$ and coefficient $\beta_{\perp}$ measured from figure 2.4a i.e. from the displacements induced by step s_1 only.
For $m_1 < m < m_1 + m_4$ $m_1 + m_4 \approx 260nm$, the curve $d_{\parallel}$ (Figure 2.10b) shows a plateau while $d_{\perp}$ linearly increases (Figure 2.10c). The respective slope of these curves are $\beta_{\parallel 4} \approx 0\%$ and $\beta_{\perp 4} \approx 6\%$. These values are consistent with the coupling factors measured from figure 2.4b while analyzing the displacements induced by step s_4 .
For $m_1 + m_4 < m < m_1 + m_4 + m_5$ with $m_1 + m_4 + m_5 = 610nm$, both curves $d_{\parallel}$ and $d_{\perp}$ show a linear increase with slopes $\beta_{\parallel 5} \approx 6\%$ and $\beta_{\perp 5} \approx 6\%$. Again, this result is in agreement with the values found from Figure 2.4c while analyzing the displacement induced by the steps forming the step s_5.
Since $\beta_{\perp 1} \approx \beta_{\perp 4} \approx \beta_{\perp 5}$, the curve $d_{\perp}$ (Figure 2.10c) does not show any slope change in the range $0 < m < m_1 + m_4 + m_5$.
For $m > m_1 + m_4 + m_5$, both parallel and perpendicular displacements $d_{\parallel}$ and $d_{\perp}$ present a plateau : see marker X7 in figure 2.10b and c. They correspond to the overall displacements induced by the set of steps s_1 to s_4 , or equivalently by the macro-step s_5.
Finally, the overall coupling factor $\langle \beta_{\parallel} \rangle$ and coefficient $\langle \beta_{\perp} \rangle$ can be retrieved from these curves according to Equation 1 and 2 : $\langle \beta \rangle \approx 6.8\%$ and $\langle \beta_{\perp} \rangle \approx 6.4\%$.

2.3.2 Grain boundary dislocation step origin

Some elementary grain boundary dislocation steps were found prior to deformation and were probably inherent defects in the structure of the grain boundary itself. However, because grain boundary steps are deeply related to the grain boundary migration under stress, they have to be nucleated at a certain rate as the grain boundary migrates. Intrinsic grain boundary sources of dislocations steps have been observed (see figure 2.7) during their operation.
Atomistic simulations have also shown the nucleation and expansion of a disconnection loop in a grain boundary to account for the shear response of a tilt grain boundary in Ni [102], and disconnection sources have also been identified in $\{10\bar{1}2\}$ twin in hcp metals [103].
Grain boundary dislocations can also be nucleated from a sub-grain boundary intersecting a grain boundary (figure 2.8). Although the detailed nucleation mechanism is unknown, the operation of a source can take its origin from a spiral source formed by lattice dislocations trapped in a grain boundary. Indeed, a disconnection of Burgers $\vec{b}_s$ can result from the interaction between two lattice dislocations of Burgers vector $\vec{b}_1$ and $\vec{b}_2$ according to : $\vec{b}_s = \vec{b}_1 + \vec{b}_2$.
If the two lattice dislocations are sessile, they can act as a fixed arm around which the disconnection can spin under the shear stress [104]. Every turn, a disconnection is nucleated. Such a source cannot however last since the grain boundary migrates perpendicularly in the meantime.

2.3.3 Step motion and pinning and intragranular plasticity

Steps have been frequently found to be pinned by localized obstacles during their motion. Because steps cannot pass each other, the accumulation of elementary grain boundary dislocation steps on a pinning point forms the observed macro-steps. Some of these steps like the step s_1 can produce a large amount of deformation as observed in macroscopically deformed bicrystalline

samples [88, 76, 77].
However, in contrast to these cited studies where the tensile stress is maintained below the single crystal elastic limit, the control of both the intensity and the homogeneity of the applied stress level is difficult in our TEM experiments : an intragranular plastic stress relaxation may hence occur.
Grain boundary dislocation steps have been shown to be frequently impeded by obstacles during their motion. These obstacles can be some defects of the grain boundary structure, like lattice dislocations trapped in the grain boundary, or can be related to a defect at the sample surface. This latter type of obstacles is expected to play a crucial role for the step motion in TEM thin foils. The blocking of the steps prevents the propagation of the deformation (Figure 2.11a). Because steps are supposed to be composed by several elementary grain boundary dislocation steps, they probably develop a large long-range stress/strain field. When permanently blocked, this stress/strain field may relax through intragranular plasticity. This situation may explain

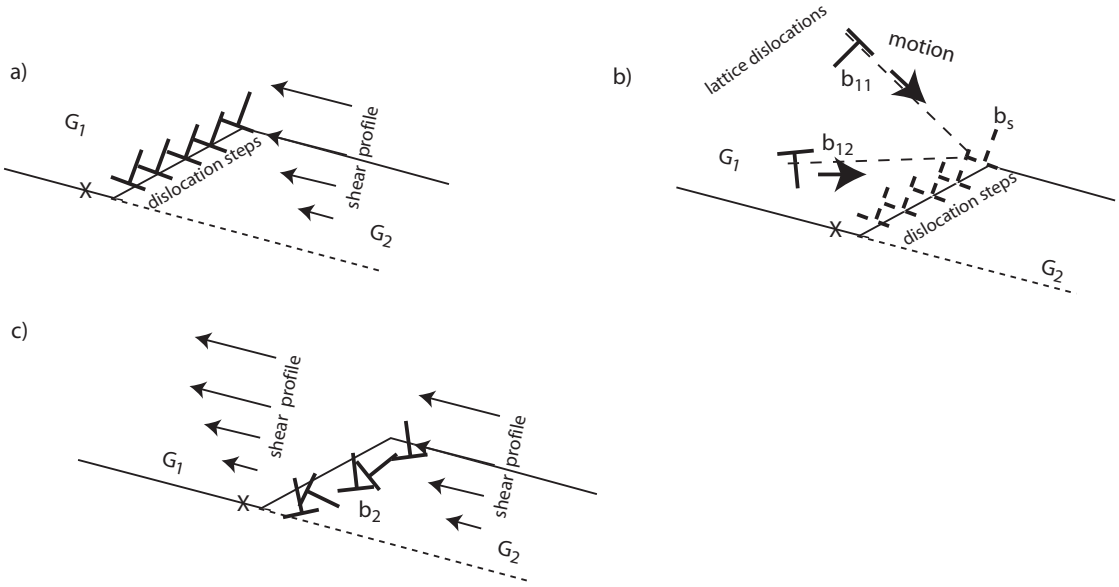

Figure 2.11: the pinning of a grain boundary dislocation step along the grain boundary (a) provokes the nucleation and glide of lattice dislocations in front of the step in order to release the strain produced by the shear-coupled motion (b). The lattice dislocation glide propagates the shear strain in front of the step. The interaction between the lattice dislocation and grain boundary dislocation produces dislocations in G_2. This may leave the step with a lower dislocation content (c).

why the markers displacements, i.e. the deformation profile perpendicular to the grain boundary, observed below and in front of the final step s_f in figure 2.4 are similar. Indeed, when the disconnections of Burgers vector $\vec{b}_s$ are stopped, the shear can be efficiently transferred in front of the step in G1 by the glide in different planes of lattice dislocations of Burgers vector $\vec{b}_{11}$ and $\vec{b}_{12}$ as schematically represented in Figure 2.11b. In this case, these dislocations are supposed to be nucleated inside G1. This mechanism is supported by the observation of a plastic deformation in front of the step in figure 2.3g.
The interaction between lattice dislocations from G1 and grain boundary dislocations can lead to the decomposition of the grain boundary dislocation step and to the formation of lattice

dislocations in G2 according to $\vec{b}_s = \Sigma_i \vec{b}_{1i} + \Sigma_j \vec{b}_{2j}$.
This decomposition may thus lead to a less energetic step and ultimately to a pure step with no dislocation (Figure 2.11c).
This interpretation is similar to the theory of emissary slip developed by Sleeswyk [105] to explain the plastic accommodation in front of a growing twin. In this theory, the very high stress and strain produced in the vicinity of a deformation twin can be relaxed by the decomposition of a twin dislocation into a slip dislocation (an emissary dislocation) that is eventually emitted in front of the twin and a so-called complementary twin partial. Emissary dislocations have been observed in various metals as reported in [106].

2.3.4 Step mobility

The very fast step motion suggests that the grain boundary mobility is controlled not only by the propagation of the grain boundary dislocation step itself but also by the nucleation of the grain boundary dislocation steps and their pinning by defects along the grain boundary. Such pinning has already been found to decrease the mobility of pure tilt grain boundaries during recrystallization processes [107]. However, little is known about the energy required to nucleate such disconnections : as reported in chapter 4, we will show that atomistic simulations can provide some structural and energetic information on the nucleation of these steps.
In contrast, the mobility of disconnections has been extensively discussed in the general case in [108]. As revealed by computer simulations for twins, the motion of grain boundary dislocations step with small Burgers vectors and small step height is favoured [103]. Indeed, long-range elastic strains decrease when Burgers vectors are small, and less shuffled atoms are implied when the step height is small.
However, grain boundary dislocation steps with small Burgers vector and/or large step height, i.e. leading to smaller coupling factor, are also probably mobile with the help of the thermal activation when small strains have to be achieved in order to reduce strain incompatibilities in polycrystals. The present study reports also that the dislocation step can carry a significant climb component (figure 2.4c and d) which also implies long-range diffusion processes that are strongly thermally activated.

2.4 Conclusion

The results presented in this chapter lead to the following conclusions :

- Shear-coupled grain boundary migration has been observed in Al bi- and poly-crystals at 400°C.
- The grain boundary migration occurs through the nucleation and the propagation of steps along the grain boundary.
- These steps carry a plastic deformation, hence the steps are grain boundary dislocation steps, also called disconnections.
- A migrating grain boundary can support different dislocation steps, each of them producing their particular deformation.
- In addition to ideal shear-migration coupling, the deformation can have a component perpendicular to the grain boundary plane.
- In polycrystalline Al, the collective motion and annihilation of these step dislocations are supposed to account for grain boundary stress assisted migration.

These results, which highlight the complexity of stress-assisted grain boundary migration mechanisms, indicate the difficulty to predict coupling modes by a purely geometrical approach. It also gives a completely different perspective on coupling motion. Locally, at the nanoscale, the deformation produced by such a mechanism is dependent on the nucleation and propagation of several kinds of grain boundary defects and on their local density. Macroscopically, however, the collective motion of grain boundary step dislocations may lead to a coupling factor representing an average value over all possible elementary coupling factors. Next chapter of this manuscript will be devoted to the identification of elementary defects in the $\Sigma 41(540)$ grain boundary.

3 DISCONNECTIONS AND THEIR POSSIBLE CREATION THROUGH LATTICE DISLOCATION INTERACTIONS

In the previous chapter, the lateral motion of individual disconnections along the grain boundary and their eventual accumulation creating macro-steps, has been shown to be the elementary mechanism responsible for the shear-coupled grain boundary migration. The different measured coupling factors suggest the possibility of different kinds of disconnections for a given grain boundary. These disconnections can either pre-exist in the samples before the loading or can be produced (nucleated) during the straining.
Several possible mechanisms of disconnections sources are reported in the literature. There are some evidence that disconnections can be emitted in the grain boundary either close to triple junctions in twin grain boundaries [109] or near grain boundary grooves [58]. In the pole mechanism for twinning [110], the source is composed of three dislocations, two sessile ones in the two adjacent crystals and a glissile one in the grain boundary. Upon stress, the glissile dislocation decomposes and spirals around the sessile dislocations, thus achieving the twin growth. This idea assumes however the existence of sessile dislocations in the grain boundary, shifting then the problem of the shear-coupled grain boundary migration to the problem of the origin of the sessile dislocation itself.
Serra and Bacon [103] have proposed that sessile disconnections in an hcp twin can act as a twinning disconnection source moving as the twin advances.
To that respect, initial defects and the defects arising from interactions between lattice dislocations and the grain boundary have to be considered as potential sources of disconnections.
In this chapter, the nature of the pre-existing structural defects is investigated by High Resolution TEM (HRTEM). This method allows us to determine the nature of the disconnections, i.e. with both step and dislocation character, at atomic scale.
In a second part, the experimental evidence of interactions between lattice dislocations and grain boundaries during the in-situ TEM straining experiments on the Al bicrystal samples are reported. Finally, the possible dislocation decomposition mechanisms in the grain boundary are investigated theoretically on the basis of observed interactions. The disconnections resulting from the decomposition of the dislocations in the grain boundary can lead to different coupling modes that will be discussed and compared in the light of experimental results, presented in the previous

chapter and in the literature.

3.1 HRTEM analysis of grain boundary defects

HRTEM observations were used to analyze the bicrystal presenting a nearly Σ41{540} grain boundary. The sample preparation has been described in the chapter 2.
HRTEM observations were performed on a TECNAI-F20 and a Hitachi HF3300-I2TEM microscopes operating at 200 kV and 300 kV. On both microscopes, the spherical aberration coefficient (C_s) and defocus was set to zero thanks to an aberration corrector. Images were obtained on a [001] zone axis. In this condition, the grain boundary plane is positioned edge on.

3.1.1 Grain boundary atomic structure

HRTEM observations report various grain boundary structures. They correspond either to the compact structure of the Σ41{540} grain boundary with a narrow core and well defined structural units (figure 3.1a-b) or to the arrangements of well separated partial dislocations leading to a wide grain boundary core structure (figure 3.1c-d).

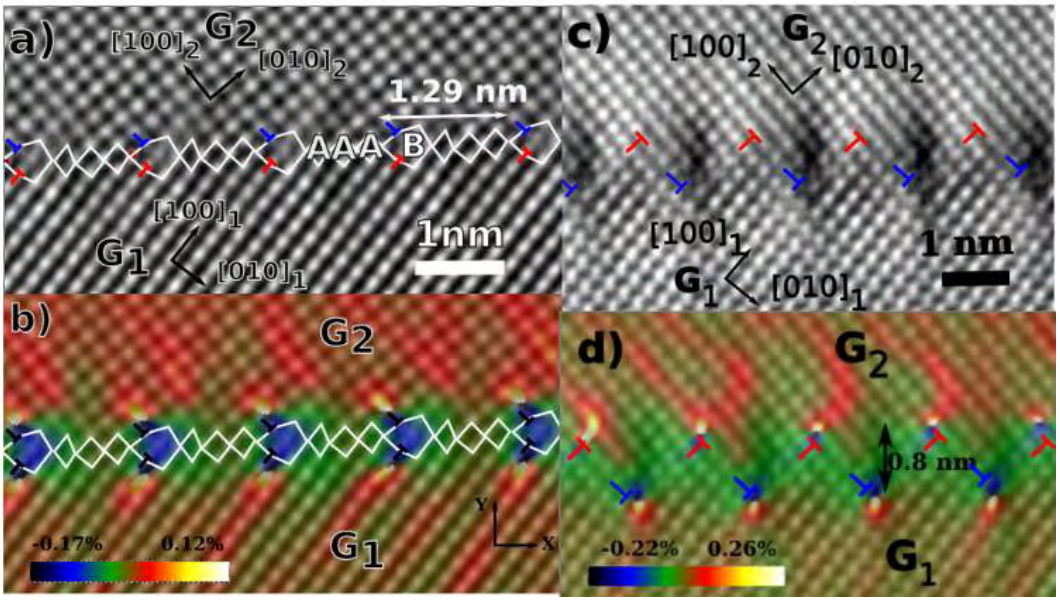

Figure 3.1: a) Compact core grain boundary structure represented by sequences of A and B structural units as |AAAB.AAAB|. The grain boundary period is composed of two coincidence sites and is 2 × 1.293 nm. Two partial dislocations from each grain, $\frac{a}{2}\langle 0\ \bar{1}\ 0\rangle_{G_1}$ and $\frac{a}{2}\langle 0\ 1\ 0\rangle_{G_2}$ shown by blue and red colors arrive together at B structural units. b) is the previous image (a) superimposed with the strain field map ϵ_{xx} (x parallel to $[4\ 5\ 0]_{G_2}$), obtained using the Geometric Phase Analysis (GPA) method. The positions of the partial dislocations are confirmed by singularities in the strain field that correspond to dislocation dipoles. c) Image of a grain boundary with wide core structure composed of separated dislocations from each grain. d) is the previous image (c) superimposed with the strain field map showing the alternately distributed dissociated dislocations along the interface. Here the dissociation distance is 0.8 nm.

The compact structure of the Σ41{540} grain boundary can be defined as a sequence of

$|AAAB.AAAB|$ structural units. A units are strained units of the perfect crystal and the B unit corresponds to the core of an edge primary dislocation with a Burgers vector $\frac{a}{2}\langle 1\ \bar{1}\ 0\rangle_{G_1}$ (using the grain 1 lattice directions). The equivalent atoms in each half period $|AAAB|$ are displaced along the tilt axis by $\frac{a}{2}[001]$. The grain boundary period between two coincidence sites is 2.58 nm. The dislocations in units B are situated at the termination of pairs of extra (200) planes and are shown in figures 3.1a and b. Thus, the B unit can also be seen as composed of two partial dislocations of Burgers vectors $\frac{a}{2}\langle 0\ \bar{1}\ 0\rangle_{G_1}$ and $\frac{a}{2}\langle 1\ 0\ 0\rangle_{G_1}$. The presence of the dislocations is highlighted in figure 3.1b by using a strain field map ϵ_{xx} (x is parallel to $[4\ 5\ 0]_{G_1}$, i.e. a direction of the plane of the grain boundary and perpendicular to the zone axis), obtained using the Geometric Phase Analysis (GPA) method [111, 109]. This method, is an image processing technique capable of resolving lattice strain with respect to an undistorted area of the crystal (taken here far from the interface).
The grain boundary wide core structure is reported in figure 3.1c and d. Figure 3.1c presents an example of alternating grain boundary structures with a wide core, composed of well separated dislocations with projected Burgers vectors equal to $\frac{a}{2}\langle 0\ \bar{1}\ 0\rangle_{G_1}$ and $\frac{a}{2}\langle 1\ 0\ 0\rangle_{G_1}$. Figure 3.1d reports the corresponding strain field map ϵ_{xx} calculated using the GPA method, and clearly shows the dissociation of the dislocations alternately distributed with a dissociation distance of $0.8nm$. This latter structure agrees with the atomistic simulations of Smith et al. [112]. This gives a grain boundary structure composed of an area of alternating ribbons of strained single crystal and stacking faults. More recent atomistic simulations of low angle grain boundary in Al indicate that fluctuation in the position of dislocations in the grain boundary can appear during the solidification process and thus may explain the concomitant presence of two grain boundary structures [113].
In the following and in agreement with Chapter 1, the dislocations described above and in the characteristics of the compact or wide core structures are referred as primary dislocations.
After this description of the grain boundary, the next section is devoted to the investigation of defects that break the compact or wide core structures, i.e. either secondary or extrinsic dislocations.

3.1.2 Grain boundary defects analysis

Several types of structural defects have been observed in the grain boundary. The first one corresponds to a dislocation that perturbs the spacing of primary dislocations (i.e. the structural unit B in figure 3.1a) They are known as spacing defects in grain boundary structure [114]. They will be described in Sect. 3.1.2a. The second group of structural defects corresponds to the steps distributed along the grain boundary. They will be evidenced and described in Sect. 3.1.2b.

a) Spacing defect

Disconnections without step character : Figure 3.2a reports the HRTEM observation of the grain boundary with a compact structure presenting a interfacial defect. The position of the defect is indicated by a full red circle. This defect induces a spacing between two B units dislocations larger than half the grain boundary periodicity.

To identify this structural defect, a method known as circuit mapping [115] is applied. This method is analogous to a Burgers circuit around a lattice dislocation, except that here the reference lattice has to be chosen in the dichromatic pattern corresponding to the perfect grain boundary structure.

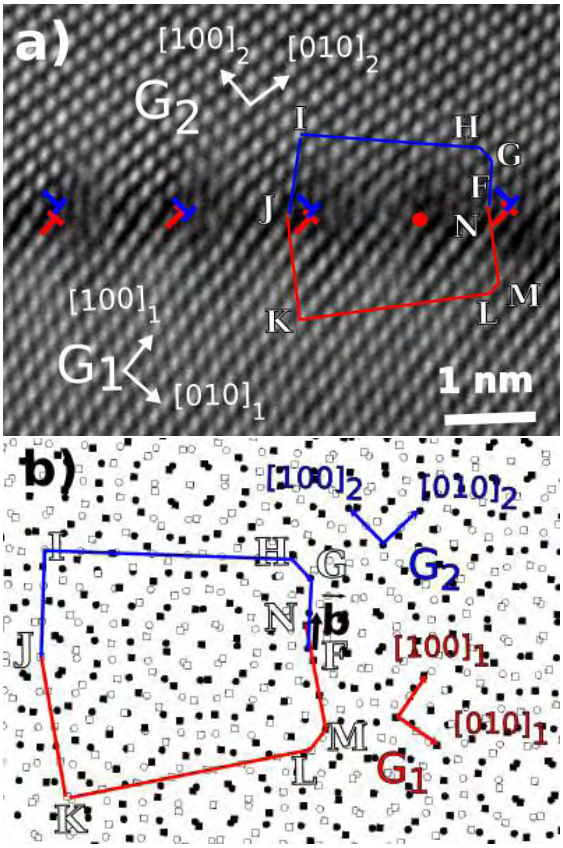

Figure 3.2: a) Grain boundary with compact dislocation cores structure. The partial dislocations in each crystal are shown with different colors. A defect is present in the right side of the image, marked by a red circle, corresponding to spacing defect between two dislocations. Circuit mapping method is used to characterize this defect : A circuit composed of the translation vectors (FGHIJ) in the upper crystal G_2 and in the lower crystal G_1 (JKLMN), are drawn around the defect. b) The same circuit is repeated in the dichromatic pattern of the grain boundary in which □ symbols correspond to lattice sites of grain G_1 and ◯ symbols represent the lattice sites of grain G_2. Filled symbols correspond to positions at $z = 1/2$. The closure defect of the circuit in dichromatic pattern is associated to a DSC dislocation $\vec{b} = \frac{3}{41}[5\ \bar{4}\ 0]_{G_1}$.

In this method, the Burgers vector of the defect is determined by [1] :

$$\vec{b}(G_1) = \vec{t}(G_1) - P\vec{t}(G_2) \tag{3.1}$$

where $\vec{t}(G_1)$ and $\vec{t}(G_2)$ are translation vectors in the lower (G_1) and the upper (G_2) crystals respectively [39]. The transformation matrix P relates the G_2 coordinate system to the G_1 system. Translations vectors are defined below.
Applying the circuit mapping to the cited defect, figure 3.2a reports the vectors JN(G_1) and JF(G_2) that join two equivalent lattice sites common to crystals G_1 and G_2. The choice of the equivalent sites is often critical but can be accurately defined with the position of the dislocation cores at the grain boundary. Here in figure 3.2a, the path in G_2 is FGHIJ, and the path in G_1

1. in the following the notation will be defined in the G_1 crystal

is JKLMN, J being common to the two crystals. In figure 3.2a, FGHIJKLMN is a closed circuit so that F and N coincide and are common to both grains. The circuit is then reproduced in the dichromatic pattern of the perfect Σ41(540) as indicated in figure 3.2b. In the dichromatic pattern, □ symbols correspond to lattice sites of grain G_1 and ◯ symbols represent the lattice sites of grain G_2. Filled symbols show positions at $z = 1/2$ (z-axis along the [001] direction). the FGHIJ (JKLMN) part of the circuit is reproduced using the G1(G2) lattice sites, J being a coincident site. Two vectors $\vec{JF}$ and $\vec{JN}$ in figure 3.2a correspond to the translations vectors $\vec{t}(G_1)$ and $P\vec{t}(G_2)$ in the dichromatic pattern.
A Burgers vector $\vec{b} = \frac{3}{41}[5\ \bar{4}\ 0]_{G_1}$ perpendicular to the grain boundary plane is attributed to this defect.

To any grain boundary defect, one can associate a step height defined by [94]

$$h_{G_1} = \vec{n}_{G_1} \cdot \vec{t}_{G_1} \tag{3.2}$$

$$h_{G_2} = \vec{n}_{G_2} \cdot \vec{t}_{G_2} \tag{3.3}$$

$$h = \frac{h_{G_2} + h_{G_1}}{2} \tag{3.4}$$

where h_{G_1} and h_{G_2} are step heights in each grain lattice, $\vec{n}_{G_1}$ and $\vec{n}_{G_2}$ are unit vectors normal to the grain boundary plane in each lattice and $\vec{t}_{G_1}$ and $\vec{t}_{G_2}$ are the translation vectors. In the present case for the defect reported in figure 3.2a, it can be easily checked that $h_{G_1} = -h_{G_2}$ so that no step is associated to the spacing defect. The defect reported in figure 3.2a corresponds to the insertion of an edge dislocation with no step in the grain boundary and thus to a spacing defect.

b) Grain boundary steps

Pure step : Several steps were observed, randomly distributed along the grain boundary. Generally the steps in grain boundaries with wide grain boundary core structure display smaller widths ($\approx 10nm$) compared to the one in grain boundaries with compact structure ($\approx 16nm$). In a separated core structure, the step corresponds in fact to a (9 1 0) grain boundary facet that reproduces well the equilibrium structure found by simulation [112]. Figure 3.3a reports an example of the steps in a wide grain boundary core structure. The $\frac{a}{2}\langle 0\ 1\ 0\rangle$ dislocations shown in blue and red correspond to G_2 and G_1 lattices respectively. In the transition zone of the step, the grain boundary structure is perturbed and the periodicity of the dislocations is not conserved. The circuit mapping is applied around this step between two equivalent sites of the interface. The same circuit in the dichromatic pattern (figure 3.3b) shows that no Burgers vectors is associated to this step, i.e. the circuit connects two coincident sites (A and B on Figure 3.3b). The step height associated to this defect can however be determined following Eq. 3.4 : the grain boundary step is a pure step of height :$h = -\frac{a}{2}\sqrt{41} = -1.29$ nm

General disconnection : Figure 3.4a presents another example of step in grain boundaries with wide grain boundary core structure. The same colors as in the previous example are used to mark the dislocation cores for each grain. In this example the dissociation distance between the dislocations varies from the right to the left of the step. The circuit mapping method is applied to this defect. The equivalent sites of the circuit around the step are selected according to the positions of the dislocations in the G_1 lattice. The circuit in the dichromatic pattern presented in figure 3.4b shows a closer defect : a Burgers vector $\vec{b} = \frac{a}{82}[910]_{G_1}$ and step height $h = \frac{45.5a}{2\sqrt{41}} = 1.43$ nm is associated to this step, a general disconnection.

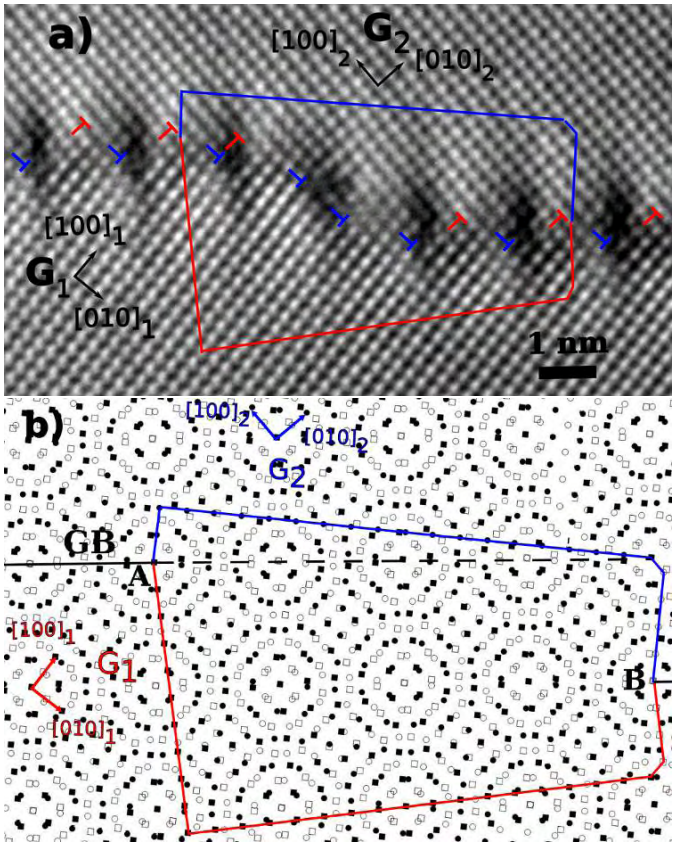

Figure 3.3: a) A step in the grain boundary with separated dislocation core. The blue signs correspond to the dislocation cores of the G_2 lattice and the red ones are those of the G_1 lattice. The blue and red translation vectors encircle the step and connect two equivalent lattice sites at the interface together. b) The circuit repeated in the dichromatic pattern of the grain boundary connect two coincidence sites together so there is no dislocation corresponding to this step and it is a pure step.

Pure step constituted of two disconnections : Finally, figure 3.5a and b show an example of a wide step and its analysis in a grain boundary with a compact structure. As in figure 3.3, the overall circuit around the step shows no closure defect and a height $h = \frac{-41a}{2\sqrt{41}}$ (figure 3.5b), i.e. the defect is a pure step, but the circuits connecting the intermediate equivalent sites in the zone between two sides of the step (1-2, 3-4) show existence of two defects with opposite Burgers vectors $\vec{b}_{1-2} = \frac{a}{82}[12\ 15\ 41]_{G_1} = -\vec{b}_{3-4}$ and different step heights ($h_{1-2} = \frac{-7a}{2\sqrt{41}}$,$h_{3-4} = \frac{-34a}{2\sqrt{41}}$) as depicted schematically in figure 3.5c.

Finally table 3.1 groups all different cases of defects that were identified during the analysis of grain boundary structure in the $\Sigma 41(540)$ bicrystals. In this table the Burgers vector $\vec{b}$ associated to each defect, lengths of the parallel and perpendicular components of the Burgers vector according to the grain boundary plane and the step heights are reported. It is worth noting that the disconnections observed often have a perpendicular component. The disconnection observed in figure 3.4 exhibits a step height close to the height of a pure step (figure 3.3). It is possible

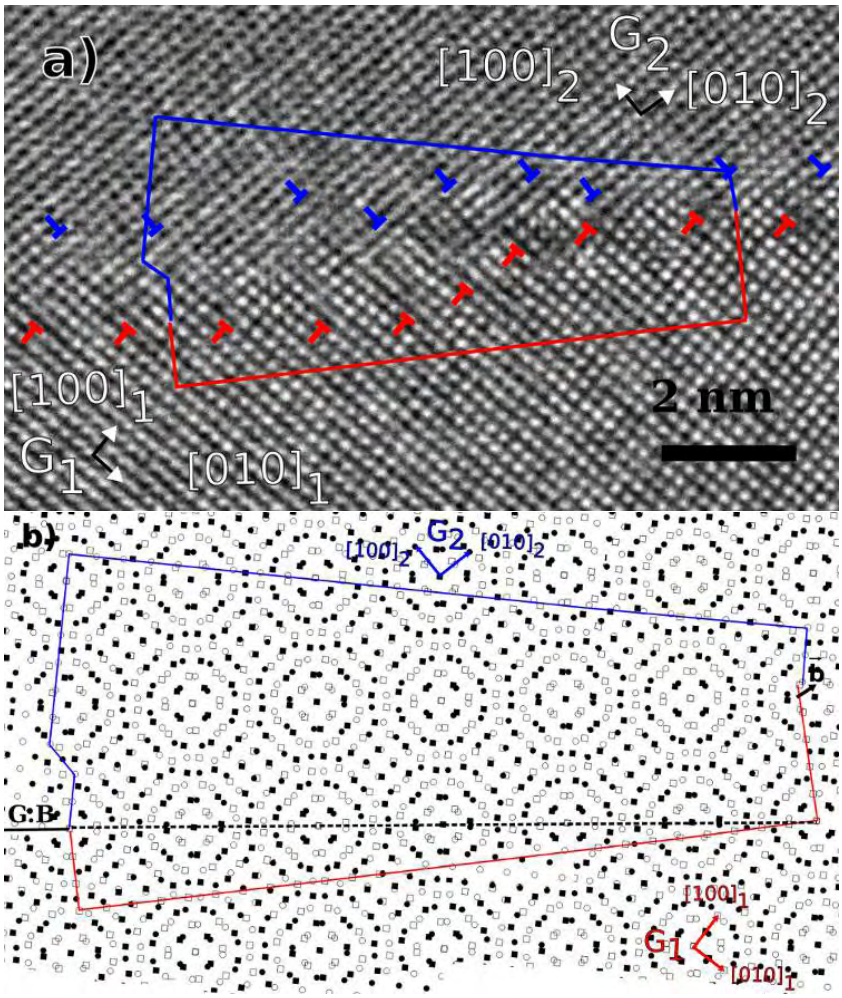

Figure 3.4: a) A grain boundary step in the dissociated dislocations structure. The blue signs indicate the dislocations cores corresponding in G_2 and the red signs show the dislocations cores in G_1. The circuit encircles the step between two equivalent crystal sites at the interface. These sites are selected according to the periodicity of the dislocations in G_1. b) The circuit in the dichromatic pattern of the grain boundary shows an associated dislocation with Burgers vector of $\vec{b} = \frac{a}{82}[910]_{G_1}$ and a step height $h = \frac{45.5a}{2\sqrt{41}}$.

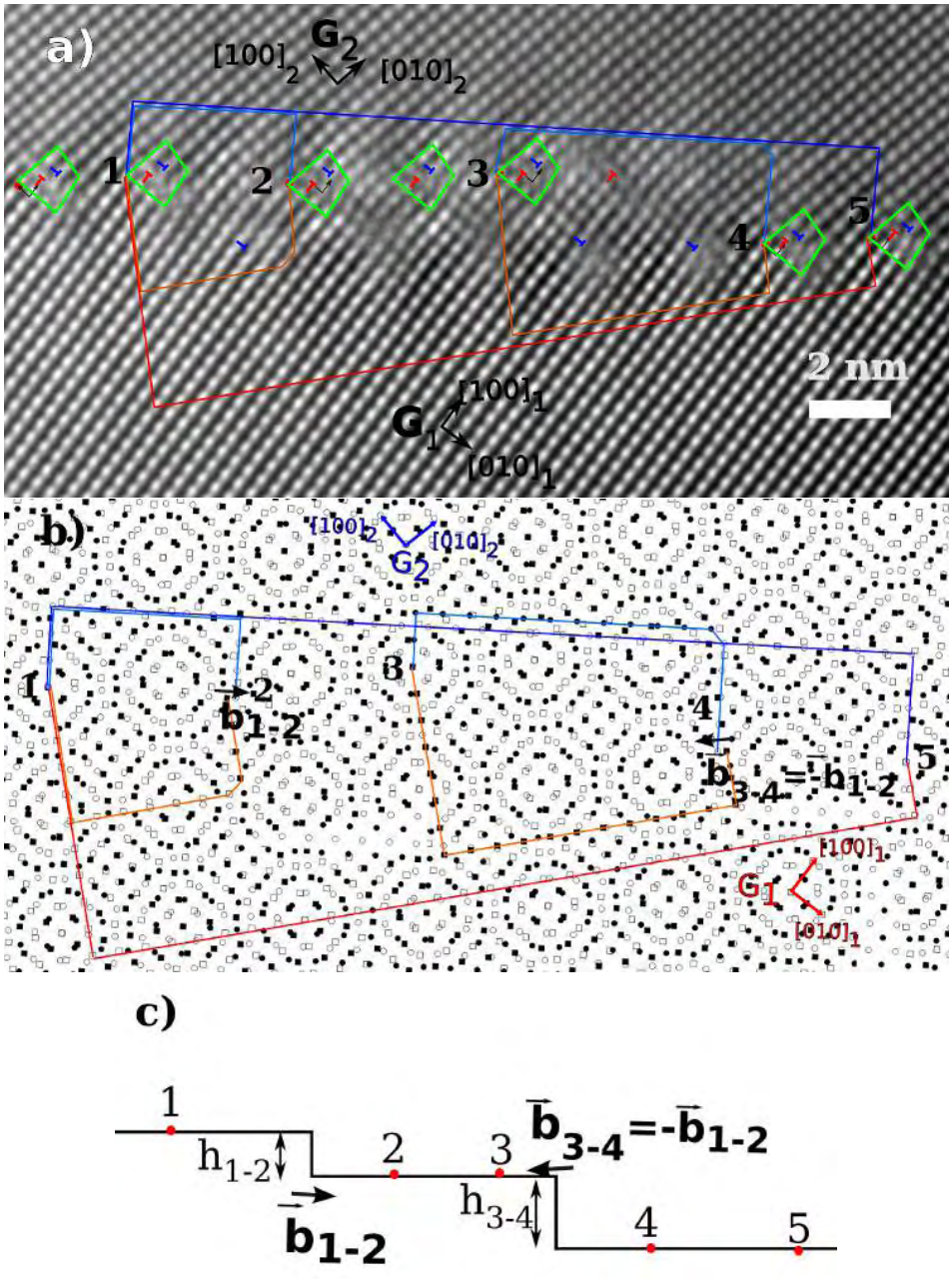

Figure 3.5: a) Grain boundary step in the compact core structure. The structural units show the position of intrinsic grain boundary dislocations along the interface. Circuits of translations vector connect the equivalent crystal sites at interface together passing from each grain. (1-2,3-4,1-5) b) The 1-5 circuit in the dichromatic pattern of the grain boundary shows no closure defect, suggesting a pure step. However the intermediate circuits between 1-2 and 3-4 points reveal two defects with opposite Burgers vectors and different step heights. c) A schematic representation of the the overall and intermediate steps and their associated defects and heights.

that this defect result from the combination of a pure step and a disconnection with a small step. This result will be discussed later to interpret possible low coupling factor.
Except for pure steps that can accommodate local variation of the grain boundary from the (540) planes, these extrinsic disconnections are thought to originate from interactions between lattice dislocations during elaboration. Indeed, triggering intragranular dislocation activity is usually inevitable during the in-situ experiments presented in the chapter 2. Interaction of gliding lattice dislocations with the grain boundary can cause structural defects in the grain boundary that can contribute to intergranular plasticity. Possible interactions studied by in-situ TEM are reported in the next section of this chapter.

Figure	$\tilde{\mathbf{b}}$	$\mathbf{b}_{\parallel}$	$\mathbf{b}_{\perp}$	$\mathbf{h}$
Fig.3.2	$\frac{3a}{41}[5\ \bar{4}\ 0]_{G_1}$	0	$\frac{3a}{\sqrt{41}}$	0
Fig.3.3	0	0	0	$-\frac{41a}{2\sqrt{41}}$
Fig.3.4	$\frac{a}{82}[9\ 1\ 0]_{G_1}$	$\frac{a}{2\sqrt{41}}$	$\frac{a}{2\sqrt{41}}$	$\frac{45.5a}{2\sqrt{41}}$
-	$\frac{a}{41}[5\ \bar{4}\ 0]_{G_1}$	0	$\frac{4a}{\sqrt{41}}$	$\frac{40a}{2\sqrt{41}}$
Fig.3.5	0	$\vec{b}_{1-2}+\vec{b}_{3-4}=0$	0	$h_{1-2}+h_{3-4}=-\frac{41a}{2\sqrt{41}}$

Table 3.1: Different cases of interfacial defects characterized in the $\Sigma 41(540)$ *grain boundary with their associated Burgers vectors and step heights.*

3.2 In-situ TEM observations of lattice dislocations/grain boundary interactions

To study interactions between lattice dislocations and grain boundary, in-situ TEM experiment of bicrystal have been performed at ambient and 400°C. Dislocations and grain boundary have been analyzed in bright and dark field conditions, using both trace, contrast analysis and stereographic representations. More technical details on these methods can be found in the appendix.

3.2.1 Characterization of disconnections

In the following, and in order to avoid confusion in the notations, lattice dislocations will be noted by d and disconnections by GBD (for Grain Boundary Dislocation).
Figure 3.6a reports a dark field micrograph of the $\Sigma41(540)$ grain boundary taken with $\vec{g} = [\bar{1}\ \bar{1}\ \bar{1}]$ and seen inclined by -45° with respect to the tilt axis (T) parallel to the straining axis.
As it is seen inclined, the grain boundary shows two traces noted by tr_1GB and tr_2GB in figure 3.6a, corresponding to the intersections of the grain boundary with the surfaces of the specimen. Because the thin area of the sample have a wedge-like shape, with an angle $\approx 20°$, the two foil surfaces are not parallel. Thus the two surface planes, reported in the stereographic projection in figure 3.6b, cut the (540) grain boundary plane at the two locations tr_1GB and tr_2GB.
Straight GBDs are visible as parallel lines along the interface. These disconnections are not homogeneously distributed along the interface and their spacing changes between 30-180 nm. Their line vector $\vec{l}_{GBD}$ is found to be along the [001] direction perpendicular to one of the surface. This probably results from energy minimization of the GBD length.

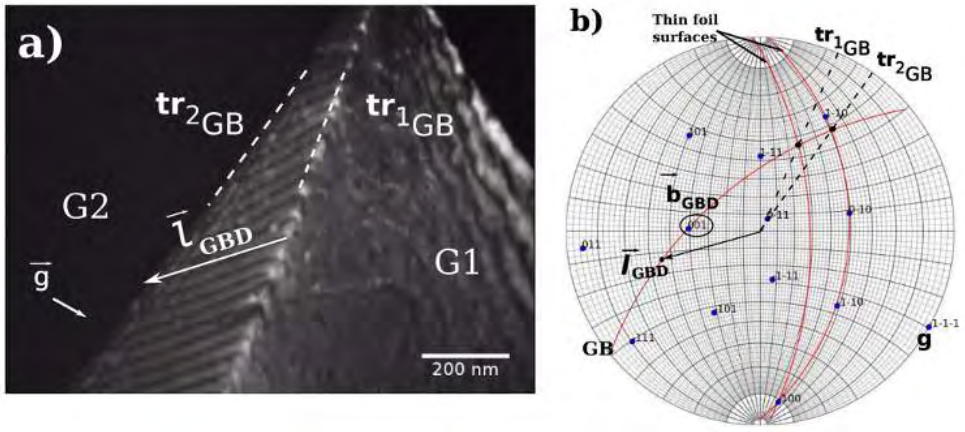

Figure 3.6: a) Dark field image from a grain boundary taken in a sample inclined by -45° with respect to the tilt axis (T). Two non-parallel grain boundary traces tr_1GB and tr_2GB, indicate a wedge-like shape of the thin foil. b) The stereographic projection of the grain G_1. The thin foil surface planes and the grain boundary plane are shown. The disconnection (GBD) are visible as parallel lines along the interface and their line is indicated by l_{GBD}.

GBDs can be further analyzed using the Marukawa and Matsubara method [116]. This method consists in analyzing the asymmetrical contrasts of the disconnections in order to determine the product vector $\vec{g} \cdot \vec{b}_{GBD}$. Figures 3.7a-c are images of GBDs for $\vec{g} = [\bar{1}\bar{1}\bar{1}]_{G_1}, [\bar{1}\bar{1}1]_{G_1}$ and $[\bar{1}00]_{G_1}$, respectively. Figure 3.7a and b show asymmetric dark (D) and light (L) contrasts

at both sides of the GBDs. The direction of the reflection vectors associated to each image are also indicated. The order of the dark and light contrasts with respect to the disconnection line oriented from the bottom to the top surface indicates $\vec{g}\cdot\vec{b}_{GBD} > 0$ in figure 3.7a and $\vec{g}\cdot\vec{b}_{GBD} < 0$ in figure3.7b. In figure3.7c, the faint and symmetric contrast is consistent with the condition $\vec{g}\cdot\vec{b}_{GBD} = 0$ and $\vec{g}\cdot(\vec{b}_{GBD}\times\vec{l}_{GBD}) = 0$. The asymmetric contrast conditions restrict the location of the Burgers vector according to the corresponding reflection vectors $\vec{g}$ in the stereographic projection of G_1 shown in figure 3.7d. The possible area for the Burgers vector according to contrast analysis of the figure 3.7a is coloured in blue. The region in red is the possible area for the Burgers vector according to figure 3.7b. Thus the Burgers vector should be in the intersecting zone of two coloured regions which is shown in violet color. Since $\vec{g}\cdot\vec{b}_{GBD} \approx 0$, this latter argument indicates that the Burgers vector ($\vec{b}_{GBD}$) is close to the [001] direction.
According to the fact that the dislocation line $\vec{l}_{GBD}$ has been found parallel to the $[001]_{G_1}$ direction (figure 3.6), they are screw disconnections.
Also considering that these GBDs are not regularly spaced tends to indicate that they are not intrinsic secondary dislocations as shown in [117], but extrinsic disconnections. Possible DSC Burgers vectors close to the [001] direction are $\frac{1}{82}[4\ 5\ 41]_{G_1}$ and $\frac{1}{82}[\bar{5}\ 4\ 41]_{G_1}$.

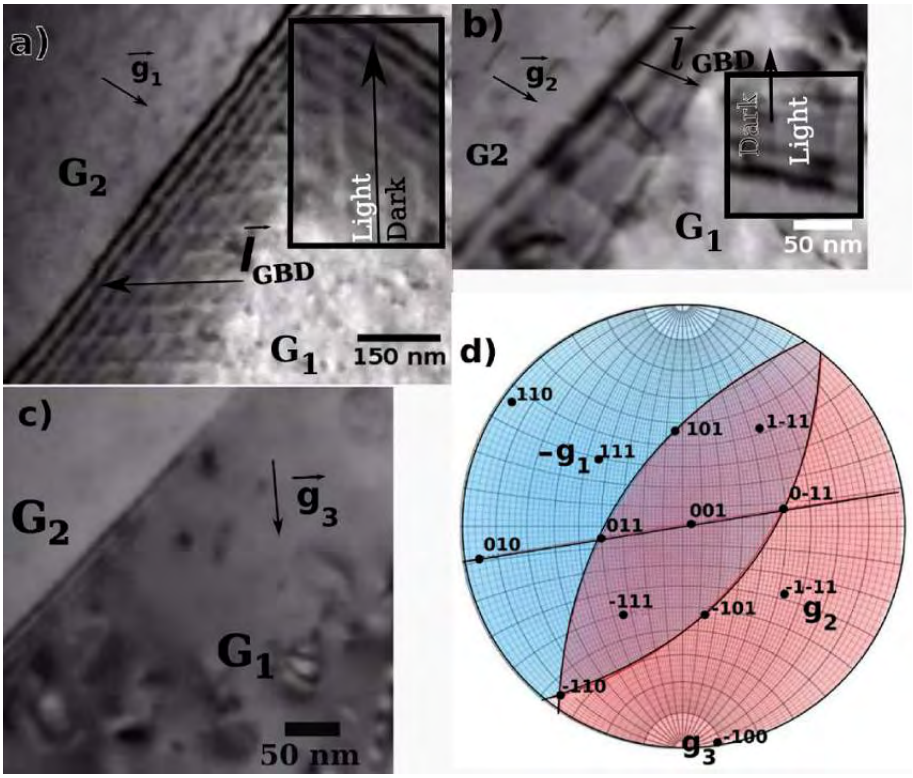

Figure 3.7: Characterizing disconnections (GBD) by Marukawa and Matsubara method. a-c) Images of dislocations for $\vec{g} = [\bar{1}\bar{1}\bar{1}], [\bar{1}\bar{1}1]$ and $[\bar{1}00]$, respectively. In a) and b) the asymmetric dark/light contrasts at two sides of the dislocations with respect to the dislocation line oriented from the bottom to the top of the grain boundary plane, indicates $\vec{g_1}\cdot\vec{b}_{GBD} < 0$ and $\vec{g_2}\cdot\vec{b}_{GBD} > 0$ c) The image with a faint and symmetric contrast of dislocations suggest $\vec{g}\cdot\vec{b}_{GBD} \approx 0$. d) These conditions shown in the stereographic projection of G_1 indicate that $\vec{b}_{GBD}$ is close to the [001].

3.2.2 Interactions between lattice dislocations and disconnections

In this section, different cases of interactions between lattice dislocations and GBDs, observed during in-situ TEM straining of Al bicrystals are presented.
Figure 3.8a is a bright field image taken with $\vec{g} = [111]_{G_1}$ of the bicrystal sample, strained along (T), at 400°C. In the image, a lattice dislocation d_1 gliding inside the grain G_1 enters into the grain boundary and the trace of its glide is marked by tr_{d1} (see the corresponding stereographic projection of G_1 in figure 3.8c).
Four [001]-type screw disconnections GBD_1, GBD_2, GBD_3 and GBD_4 are visible along the

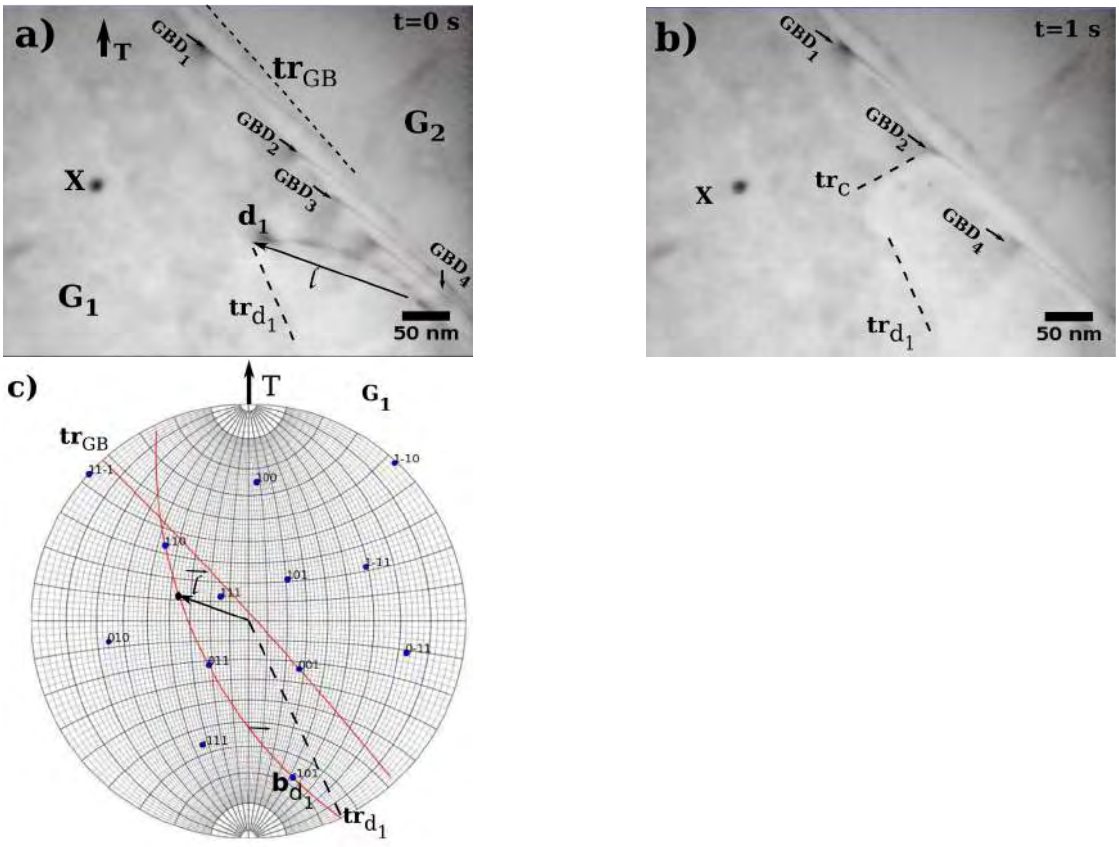

Figure 3.8: a) The sample is strained along the direction T, at 400° C. The disconnections GBD_1, GBD_2, GBD_3 and GBD_4 are visible along the interface. A fiducial marker (X) is used to locate the position of the dislocations. A lattice dislocation, d_1, moving in grain G_1, arrives into the grain boundary. The trace of the glide of the dislocation is indicated by tr_{d1}. b) GBD_3 has disappeared in the boundary as the result of its interaction with d_1. tr_c is the trace of cross-climb of d_1 into the boundary. c) is the stereographic projection of G_1 with the grain boundary and dislocation slip plane. The Burgers vector of d_1, $\vec{b_{d1}} = \pm\frac{1}{2}[\bar{1}\ 0\ 1]_{G_1}$, and its line direction $\vec{l}_{d_1}$ are also shown.

interface. The average distance between the GBDs is 61 nm. Moreover these GBDs are observed to move very slowly along the interface, in response to straining. A fiducial marker X on the surface is used to indicate the position of the GBDs.
Figure 3.8b shows a video frame taken after entrance of d_1 the grain boundary. The interaction

of d_1 with GBD_3 leaves a blank space in the place of GBD_3. In the zone where d_1 enters into the grain boundary another trace marked by tr_c is visible. The Burgers vector of the dislocation d_1 is determined as being $\vec{b}_{d1} = \pm\frac{1}{2}[\bar{1}\ 0\ 1]$. Since the line direction $\vec{l}_{d_1}$ and the Burgers vector $\vec{b}_{d_1}$ are not parallel, the dislocation motion in the plane with the trace tr_c corresponds to a motion by climb. Inspection of the interaction force between d_1 and the screw disconnection indicates that an attractive force can act as the driving force for climb close to the grain boundary [8]. This mechanism which is thermally activated probably occurs easily at 400°C. This observation indicates that a reaction between the dislocation d_1 and GBD_3 has occurred and has lead to a rapid decomposition in the grain boundary.
The interaction of d_1 with GBD_3 can be written as :

$$\frac{1}{2}[1\ 0\ \bar{1}]_{G_1} + \frac{1}{82}[4\ 5\ 41]_{G_1} \longrightarrow \frac{1}{82}[45\ 5\ 0]_{G_1} \tag{3.5}$$

which is followed by the decomposition reaction :

$$\frac{1}{82}[45\ 5\ 0]_{G_1} \longrightarrow 5\frac{1}{82}[9\ 1\ 0]_{G_1} \tag{3.6}$$

It is interesting to note that the resulting disconnections have similar types of Burgers vector as the one found in HRTEM observation (figure 3.4).
Since the Burgers vector of the 5 disconnections is small ($\|\vec{b}\| = 0.045nm$), the contrast of the resulting disconnection depending of $\vec{g} \cdot \vec{b_{GBD}} = 0.12$ is expected to be faint as observed experimentally (figure 3.8b).
Such a decomposition can occur however if the resulting disconnection can move along the grain boundary plane, i.e. if the disconnections can climb since their Burgers vectors have a component out of the grain boundary plane.
Figure 3.9 shows another example of a lattice dislocation d_2 originating from grain G1 and entering into the grain boundary along tr_{d2}. The analysis of d_2 shows that its Burgers vector is $\vec{b}_{d2} = \pm\frac{1}{2}[\bar{1}\bar{1}0]_{G_1}$ and that d_2 glides on $(1\ \bar{1}\ 1)_{G_1}$ plane (figure 3.9d). Figure 3.9a is taken 1 s before that d_2 enters the grain boundary. In figure 3.9b the dislocation d_2 enters the grain boundary at a location indicated by an arrow, close to a GBD. The contrast of the initial screw disconnection is reinforced and slightly broadened during few frames (i.e. few times 40 ms). In figure 3.9c, there is no visible difference between the initial and final contrasts of disconnection, indicating that d_2 did not interact with the initial screw the GBDs but probably decomposed rapidly into the grain boundary. This conclusion is also supported by the fact that there is no interacting force between two parallel dislocations with Burgers vectors at right angles. The expected decomposition reaction will be investigated in more details in section 3.3.

Similarly as another example of dislocations decomposition at room temperature, figure 3.10 reports the arrival and decomposition of the dislocation d_3 into the grain boundary. Figure 3.10a is a dark field image taken at $\vec{g} = [\bar{1}\ 1\ 1]_{G_2}$. Because d_3 glides into grain G_2, it is not visible until it reaches the grain boundary. The dislocation d_3 glides in the $(\bar{1}\ \bar{1}\ 1)$ plane with a Burgers vector $\vec{b}_{d3} = \frac{1}{2}[0\ 1\ 1]_{G_2}$ from the grain G2 into the boundary (marked by traces $tr_{1_{GB}}$ and $tr_{2_{GB}}$). At the moment of the interaction of d_3 with the grain boundary, the GBDs collectively reorient by an anticlockwise rotation of about 10° around an axis normal to the image plane, as shown in figure 3.10b and d. Moreover, since the line direction $\vec{l}_{d_3}$ is not at the intersection between the glide plane and the grain boundary plane, climb process should have occurred. As in the case shown in figure 3.8, elastic interactions between the GBDs and d_3 may be responsible for the observed configuration. Indeed, a configuration of two screw dislocation at 45° is a configuration with a minimum interaction elastic energy.
Ultimately after t=16 s, progressive disappearance of the contrast of d_3 dislocations indicates

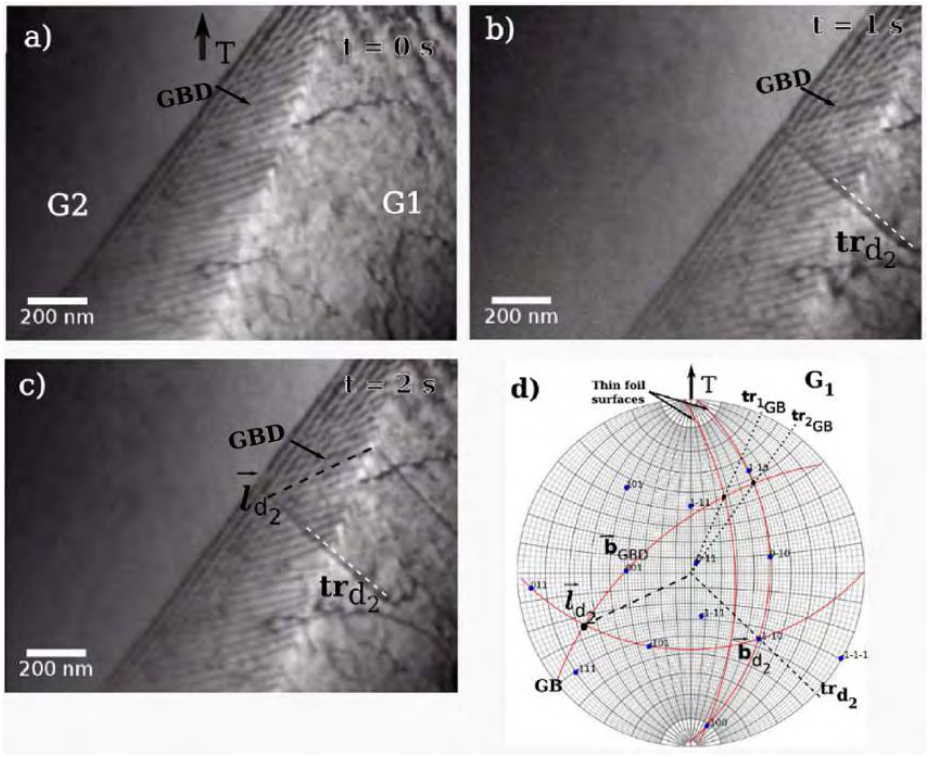

Figure 3.9: a-b) In a bicrystal sample strained at room temperature along (T), a lattice dislocation d_2 enters into the grain boundary close to the screw disconnection GBD. The glide trace is shown by tr_{d2}. c) After a short reinforcement of the contrast, the lattice dislocation contrast vanished into the grain boundary as a consequence of a decomposition. d) is the corresponding stereographic projection.

their decomposition in the boundary (figure 3.10c).
In summary, several dislocation-grain boundary interactions have been observed either at room temperature and at high temperatures. These interactions lead to decompositions into disconnections that can move eventually along the interface. In the next section, we will focus on the possible disconnection that arise from decomposition of lattice dislocations in order to evaluate possible coupling modes.

3.3 Dislocation decompositions

In the first part of this section, the theoretical conditions for dislocation decomposition are described. Applying these conditions for the dislocation decompositions observed during in-situ TEM straining and other possible lattice dislocations interacting with the grain boundary, all possible decomposition products are identified.
The potential coupling modes attributed to the resulting disconnections in the grain boundary are then reported. Finally these coupling modes are compared with measured experimental results for coupling factors in Σ41(540) grain boundary.

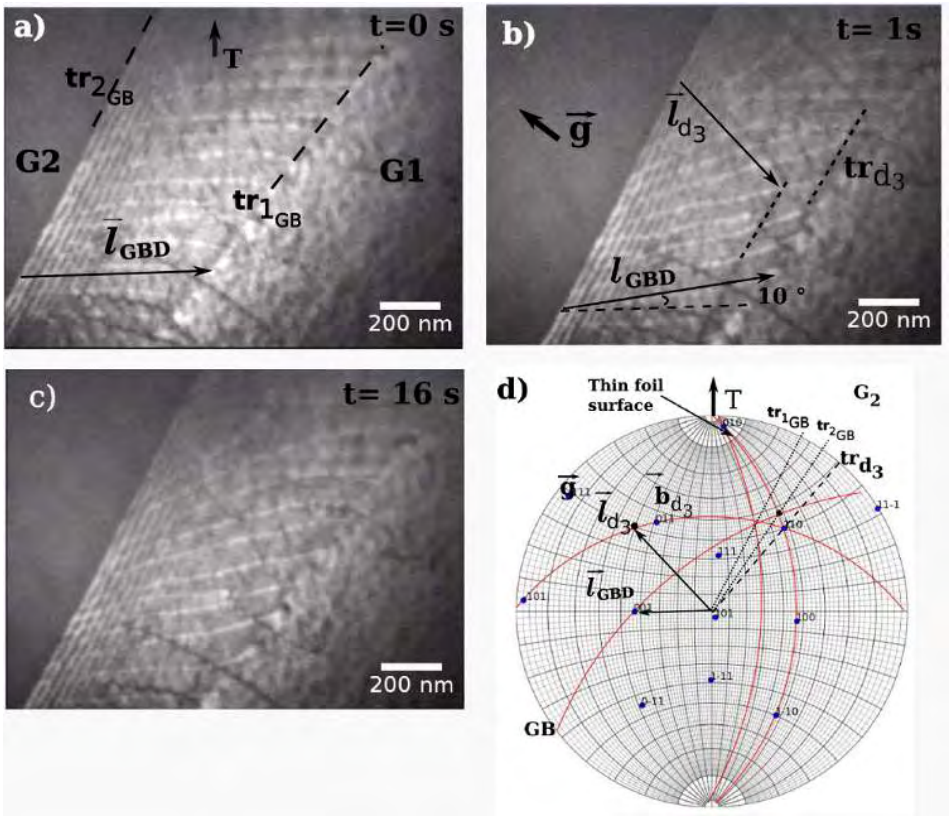

Figure 3.10: a) The sample is strained at ambient temperature. The straining direction is indicated by (T). Disconnection GBD with line vector $\vec{l}_{GBD}$ are visible. b) The lattice dislocation d_3 gliding in G2 along the indicated trace, enters into the grain boundary. Simultaneously a collective rotation of disconnections by 10°.c) The stereographic projection of G2 with grain boundary traces and the trace of the dislocation glide. The Burgers vector is $\vec{b}_{d3} = \frac{1}{2}[0\ 1\ 1]_{G_2}$. d) The contrast of d_3 dislocations disappeared progressively (after 16 s) indicating their decomposition in the boundary

3.3.1 Description of the Burgers vector in dichromatic pattern

In the following, to describe the disconnections, the notation $b_{j/k}$ will be used with j, k being the integers that indicate the position of the G_1 and G_2 lattice sites relative to a coincidence site in the dichromatic pattern of the grain boundary [103]. The step heights for each lattice are given by $h_1 = jh_0$ and $h_2 = kh_0$, and $h_0 = a/(2\sqrt{41}) = 0.08a$ is the minimum step height in lattice parameter unit, in the DSC lattice parallel to the $(5\bar{4}0)_{G_1}, (540)_{G_2}$ plane.
Figure 3.11 shows the dichromatic pattern of a Σ 41(540) grain boundary with different incident dislocations to be decomposed in the boundary, indicated.
In the section 3.2 the following dislocations were observed to interact with the grain boundary [2] : $\vec{b}_{5/0} = \pm\frac{1}{2}[1\ 0\ 1]_{G_1}$ (similar to $\vec{b}_{d1}$ and $\vec{b}_{d3}$, cf. figures 3.8 and 3.10), $\vec{b}_{1/0} = \pm\frac{1}{2}[1\ 1\ 0]_{G_1}$ (similar to $\vec{b}_{d2}$ cf. figure 3.9). Moreover, decomposition of two other lattice dislocations $\vec{b}_{9/0} = \pm\frac{1}{2}[1\ \bar{1}\ 0]_{G_1}$ and $\vec{b}_{4/0} = \pm\frac{1}{2}[0\ 1\ 1]_{G_1}$ will also be considered. The Burgers vectors of these dislocations are

2. in the following the dislocation Burgers vectors will be given in lattice parameter units

shown in the stereographic projection of G_1 presented in figure 3.12. Equivalent Burgers vectors $\vec{b}_{-5/0}$, $\vec{b}_{-4/0}$, $\vec{b}_{-9/0}$ and $\vec{b}_{-1/0}$ will not be considered.

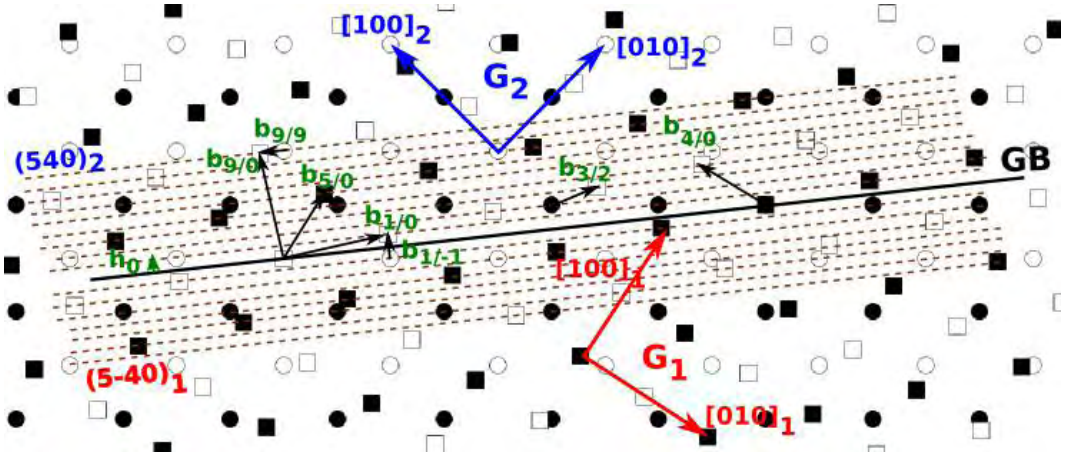

Figure 3.11: The dichromatic pattern of Σ41(540) grain boundary. The disconnections are described as $\vec{b}_{j/k}$ with j, k being integers that indicate the position of the G_1 and G_2 lattice sites relative to a coincidence site. The incident dislocations whose decomposition is studied in this chapter ($\vec{b}_{1/0}$, $\vec{b}_{4/0}$, $\vec{b}_{5/0}$ and $\vec{b}_{9/0}$) are indicated in the figure. $\vec{b}_{3/2}$ in an example of the vectors with screw component and $\vec{b}_{9/9}$) is a dislocation vector parallel to the boundary plane.

3.3.2 Conditions for dislocation decompositions

Decomposition reaction of a lattice dislocation of Burgers vector $\vec{b}$ into disconnections of Burgers vectors $\vec{b}_{DSC}$ takes the form :

$$\vec{b} \rightarrow \sum_i \vec{b}_{DSC(i)} \tag{3.7}$$

In addition to the Burgers vector conservation, the step heights counted in the two grains is conserved :

$$h_{G_1} = \sum_i h_{DSC(i)G_1} \tag{3.8}$$

$$h_{G_2} = \sum_i h_{DSC(i)G_2} \tag{3.9}$$

For the decomposition of a lattice dislocation into disconnections in the grain boundary, the total free energy should be reduced. The energy change during the decomposition can be roughly estimated by considering both the elastic energy associated to the incident and produced dislocations and the step energy.
The elastic energy of an edge disconnection is given by [8] :

$$E_e = \frac{\mu b^2}{4\pi(1-\nu)}(\ln(r_0/r_i) - 1) \tag{3.10}$$

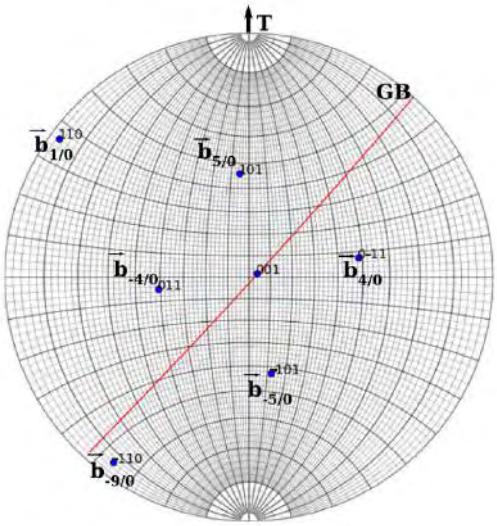

Figure 3.12: Representation of the possible Burgers vectors of the incoming dislocations interacting with the grain boundary plane (in red).

with μ the shear modulus, ν the Poisson ratio, r_0 and r_i, the outer and inner radii of the dislocation core. According to the Frank criterion, the elastic energy, proportional to b^2, is reduced during dislocation decomposition if :

$$\sum_i \left|\vec{b}_{DSC(i)}\right|^2 < \left|\vec{b}\right|^2 \tag{3.11}$$

It should be noted however that in the Frank criterion, the dislocation core energy terms and the energies of interaction between the dislocations are neglected.

According to Pond and Smith [118], the step energy, E_s, is proportional to the step height h :

$$E_s \approx h\gamma_s = nh_0\gamma_s \tag{3.12}$$

where h_0 is the minimum step height of the disconnection, n an integer, and γ_s is the grain boundary energy per unit area.
The decomposition will then be possible if the total energy $E_t = E_e + E_s$ is lowered :

$$\Delta E_t = E_{t(f)} - E_{t(i)} = \Delta E_e + \Delta E_s < 0 \tag{3.13}$$

$$-f_r E_{e(i)} + (m-n)h_0\gamma_s < 0 \tag{3.14}$$

where nh_0 and mh_0 are the net step height before and after the decomposition respectively and f_r is the relative elastic energy reduction :

$$f_r = \frac{\left|\vec{b}\right|^2 - \sum_i \left|\vec{b}_{DSC(i)}\right|^2}{\left|\vec{b}\right|^2} \tag{3.15}$$

Note here that the incident lattice dislocation introduces initially a step (of height nh_0) into the grain boundary and eventually decomposes. Taking $\mu = 25.5$ GPa, $\nu = 0.33$, $b = a/\sqrt{2}$, $r_0 = 5b$, $r_i = 1000b$, $\gamma_s \approx 0.25J/m^2$ [119], leads to the condition :

$$m - n \lesssim 200 f_r \tag{3.16}$$

Although this last inequation should not be taken as a strict criterion because of the above approximations on the evaluation of the energy, it can be used to find the solutions of equation 3.11 which preserve equations 3.8, 3.9. Figure 3.13 shows the results of the decomposition of $\vec{b}_{1/0} = \frac{1}{2}[110]_{G_1}$ (black triangles), $\vec{b}_{9/0} = \frac{1}{2}[\bar{1}10]_{G_1}$ (black squares), $\vec{b}_{5/0} = \frac{1}{2}[011]_{G_1}$ (black circles), $\vec{b}_{4/0} = \frac{1}{2}[011]_{G_1}$ (cross). Figure 3.13 reports the values of step height increase $m - n$ (in h_0 units) as a function of the elastic energy reduction f_r, calculated from equation 3.15. Equation 3.16 is also shown for $n = 0.5$ ($\vec{b}_{1/0}$), $n = 2$ ($\vec{b}_{4/0}$), $n = 2.5$ ($\vec{b}_{5/0}$), $n = 4.5$ ($\vec{b}_{9/0}$).

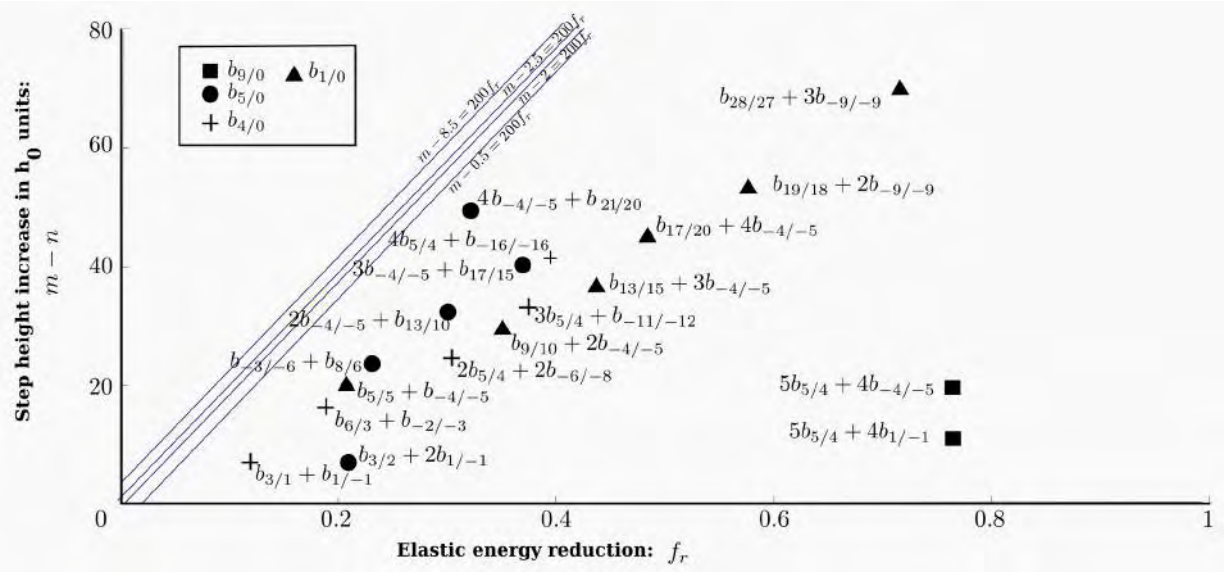

Figure 3.13: The values of step height creation $m - n$ (in h_0 units) as a function of the elastic energy reduction f_r during the lattice dislocations decomposition in a $\Sigma 41(540)$ grain boundary.

From this plot the following decompositions are possible :

Decomposition of $\vec{b}_{1/0} = \frac{1}{2}[110]_{G_1}$:
As indicated in figure 3.13, there are two groups of possible decompositions for $b_{1/0}$:

$$\vec{b}_{1/0} \rightarrow \vec{b}_{4i+1/5i} + i\vec{b}_{-4/-5} \tag{3.17}$$

$$\vec{b}_{1/0} \rightarrow \vec{b}_{9j+1/9j} + j\vec{b}_{-9/-9} \tag{3.18}$$

with $i = 1..4$ and $j = 1..3$, i.e. :

$$\vec{b}_{1/0} \to \vec{b}_{5/5} + \vec{b}_{-4/-5} \tag{3.19}$$
$$\frac{1}{2}[1\ 1\ 0] \to \frac{8}{82}[4\ 5\ 0] + \frac{1}{82}[9\ 1\ 0] \tag{3.20}$$
$$\vec{b}_{1/0} \to \vec{b}_{9/10} + 2\vec{b}_{-4/-5} \tag{3.21}$$
$$\frac{1}{2}[1\ 1\ 0] \to \frac{1}{82}[23\ 39\ 0] + \frac{2}{82}[9\ 1\ 0] \tag{3.22}$$
$$\vec{b}_{1/0} \to \vec{b}_{13/15} + 3\vec{b}_{-4/-5} \tag{3.23}$$
$$\frac{1}{2}[1\ 1\ 0] \to \frac{1}{82}[14\ 38\ 0] + \frac{3}{82}[9\ 10] \tag{3.24}$$
$$\vec{b}_{1/0} \to \vec{b}_{17/20} + 4\vec{b}_{-4/-5} \tag{3.25}$$
$$\frac{1}{2}[1\ 1\ 0] \to \frac{1}{82}[5\ 37\ 0] + \frac{4}{82}[9\ 1\ 0] \tag{3.26}$$
$$\vec{b}_{1/0} \to \vec{b}_{10/9} + \vec{b}_{-9/-9} \tag{3.27}$$
$$\frac{1}{2}[1\ 1\ 0] \to \frac{1}{82}[33\ 31\ 0] + \frac{1}{41}[4\ 5\ 0] \tag{3.28}$$
$$\vec{b}_{1/0} \to \vec{b}_{19/18} + 2\vec{b}_{-9/-9} \tag{3.29}$$
$$\frac{1}{2}[1\ 1\ 0] \to \frac{1}{82}[25\ 21\ 0] + \frac{2}{41}[4\ 5\ 0] \tag{3.30}$$
$$\vec{b}_{1/0} \to \vec{b}_{28/27} + 3\vec{b}_{-9/-9} \tag{3.31}$$
$$\frac{1}{2}[1\ 1\ 0] \to \frac{1}{82}[17\ 11\ 0] + \frac{3}{41}[4\ 5\ 0] \tag{3.32}$$

Decomposition of $\vec{b}_{9/0} = \frac{1}{2}[1\bar{1}0]_{G_1}$:
Two decompositions leading to a large elastic reduction energy can be expected :

$$\vec{b}_{9/0} \to \vec{b}_{5/4} + 4\vec{b}_{1/-1} \tag{3.33}$$
$$\frac{1}{2}[1\ \bar{1}\ 0] \to \frac{1}{82}[1\ \bar{9}\ 0] + \frac{4}{41}[5\ \bar{4}\ 0] \tag{3.34}$$
$$\vec{b}_{9/0} \to 5\vec{b}_{5/4} + 4\vec{b}_{-4/-5} \tag{3.35}$$
$$\frac{1}{2}[1\ \bar{1}\ 0] \to \frac{5}{82}[1\ \bar{9}\ 0] + \frac{4}{41}[9\ 1\ 0] \tag{3.36}$$

Decomposition of $\vec{b}_{4/0} = \frac{1}{2}[0\bar{1}1]_{G_1}$:

The most favourable reactions are :

$$\vec{b}_{4/0} \rightarrow \vec{b}_{3/1} + 2\vec{b}_{1/-1} \tag{3.37}$$

$$\frac{1}{2}[0\ \bar{1}\ 1] \rightarrow \frac{1}{82}[1\bar{0}\ \bar{3}\bar{3}\ 41] + \frac{2}{41}[5\ \bar{4}\ 0] \tag{3.38}$$

$$\vec{b}_{4/0} \rightarrow \vec{b}_{6/3} + \vec{b}_{-2/-3} \tag{3.39}$$

$$\frac{1}{2}[0\ \bar{1}\ 1] \rightarrow \frac{1}{82}[11\ 1\bar{7}\ 0] + \frac{1}{82}[1\bar{1}\ 2\bar{4}\ 41] \tag{3.40}$$

$$\vec{b}_{4/0} \rightarrow 2\vec{b}_{5/4} + 2\vec{b}_{-6/-8} \tag{3.41}$$

$$\frac{1}{2}[0\ \bar{1}\ 1] \rightarrow \frac{2}{82}[1\ \bar{9}\ 0] + \frac{1}{82}[\bar{2}\ 2\bar{3}\ 41] \tag{3.42}$$

$$\vec{b}_{4/0} \rightarrow 3\vec{b}_{5/4} + \vec{b}_{-11/-12} \tag{3.43}$$

$$\frac{1}{2}[0\ \bar{1}\ 1] \rightarrow \frac{3}{82}[1\ \bar{9}\ 0] + \frac{1}{82}[\bar{3}\ 1\bar{4}\ 41] \tag{3.44}$$

$$\vec{b}_{4/0} \rightarrow 4\vec{b}_{5/4} + \vec{b}_{-16/-16} \tag{3.45}$$

$$\frac{1}{2}[0\ \bar{1}\ 1] \rightarrow \frac{4}{82}[1\ \bar{9}\ 0] + \frac{1}{82}[\bar{4}\ \bar{5}\ 41] \tag{3.46}$$

Decomposition of $\vec{b}_{5/0} = \frac{1}{2}[1\ 0\ 1]_{G_1}$:
The most favourable reactions are :

$$\vec{b}_{5/0} \rightarrow \vec{b}_{3/2} + 2\vec{b}_{1/-1} \tag{3.47}$$

$$\frac{1}{2}[101] \rightarrow \frac{1}{82}[21\ 16\ 41] + \frac{4}{82}[5\ \bar{4}\ 0] \tag{3.48}$$

$$\vec{b}_{5/0} \rightarrow \vec{b}_{-3/-6} + \vec{b}_{8/6} \tag{3.49}$$

$$\frac{1}{2}[101] \rightarrow \frac{1}{82}[19\ \bar{7}\ 0] + \frac{1}{82}[22\ 7\ 41] \tag{3.50}$$

$$\vec{b}_{5/0} \rightarrow \vec{b}_{13/10} + 2\vec{b}_{-4/-5} \tag{3.51}$$

$$\frac{1}{2}[101] \rightarrow \frac{1}{82}[23\ \bar{2}\ 41] + \frac{2}{82}[9\ 1\ 0] \tag{3.52}$$

$$\vec{b}_{5/0} \rightarrow \vec{b}_{17/15} + 3\vec{b}_{-4/-5} \tag{3.53}$$

$$\frac{1}{2}[101] \rightarrow \frac{1}{82}[14\ \bar{3}\ 41] + \frac{3}{82}[9\ 1\ 0] \tag{3.54}$$

$$\vec{b}_{5/0} \rightarrow \vec{b}_{21/20} + 4\vec{b}_{-4/-5} \tag{3.55}$$

$$\frac{1}{2}[101] \rightarrow \frac{1}{82}[5\ \bar{4}\ 41] + \frac{4}{82}[9\ 1\ 0] \tag{3.56}$$

All these decomposition reactions yield possible disconnections that can eventually move along the grain boundary. The mobility of these disconnections and the deformation induced by their motion is discussed in the next section

3.4 Discussion

The table 3.2 reports the different disconnections studied in this chapter, in $\vec{b}_{j/k}$ notation and also in G_1 lattice, together with their step heights h. According to the angle γ between the Burgers vectors $\vec{b}_{i/j}$ and the grain boundary plane, the glide $b_g = \|\vec{b}_{i/j}\| \cos\gamma$ and the climb $b_c = \|\vec{b}_{i/j}\| \sin\gamma$ component of each disconnection are given in lattice parameter unit. We suppose that the line vector of these disconnections is parallel to tilt axis [0 0 1] thus the screw component b_s of the Burgers vector is also determined by its projection along the tilt axis of the boundary. If the grain boundary migration occurs by the movement of any of these disconnections along the boundary, shear deformations and/or long-range diffusion would be induced in the material according to the corresponding Burgers vector. The glide component b_g would be responsible for a shear deformation parallel to the boundary plane whereas the screw component b_s can potentially induce a deformation along the tilt axis i.e. out of the foil plane. On the other hand the disconnections with Burgers vectors having perpendicular component to the grain boundary plane require climb mechanism to move [89]. The potential deformations parallel $\beta_{\parallel} = b_g/h$ and perpendicular $\beta_{\perp} = b_c/h$ to the boundary and the one along the tilt axis $\beta_s = b_s/h$ are reported, for each disconnection resulting from the above decomposition, in the table 3.2.

$\vec{b}_{DSC}$	$\vec{b}_{G_1}$	b_g	b_c	b_s	h	$\beta_{\parallel}$	$\beta_{\perp}$	β_s
$b_{9/9}$	$\frac{1}{41}[\bar{4}\ \bar{5}\ 0]$	$-2/2\sqrt{41}$	–	–	$9h_0$	-0.222	–	–
$b_{1/-1}$	$\frac{1}{82}[5\ \bar{4}\ 0]$	–	$2/2\sqrt{41}$	–	–	–	–	-
$b_{5/5}$	$\frac{8}{82}[4\ 5\ 0]$	$8/2\sqrt{41}$	–	–	$5h_0$	1.6	–	-
$b_{5/4}$	$\frac{1}{82}[1\ \bar{9}\ 0]$	$-1/2\sqrt{41}$	$1/2\sqrt{41}$	–	$4.5h_0$	-0.22	0.22	-
$b_{3/2}$	$\frac{1}{82}[21\ 16\ 41]$	$4/2\sqrt{41}$	$1/2\sqrt{41}$	1/2	$2.5h_0$	1.6	0.4	2.5
$b_{8/6}$	$\frac{1}{82}[22\ 7\ \bar{4}1]$	$3/2\sqrt{41}$	$2/2\sqrt{41}$	$-1/2$	$7h_0$	0.42	0.28	-0.9
$b_{13/10}$	$\frac{1}{82}[23\ \bar{2}\ 41]$	$2/2\sqrt{41}$	$3/2\sqrt{41}$	1/2	$11.5h_0$	0.17	0.26	0.55
$b_{-16/-16}$	$\frac{1}{82}[\bar{4}\ \bar{5}\ 41]$	$-1/2\sqrt{41}$	–	1/2	$-16h_0$	0.0625	–	-0.4
$b_{6/5}$	$\frac{1}{82}[73\ 81\ 0]$	$17/2\sqrt{41}$	$1/2\sqrt{41}$	–	$5.5h_0$	3.09	0.18	–
$b_{3/1}$	$\frac{1}{82}[\bar{1}0\ \bar{3}3\ 41]$	$5/2\sqrt{41}$	$2/2\sqrt{41}$	1/2	$2h_0$	2.5	1	3.2
$b_{6/3}$	$\frac{1}{82}[11\ \bar{1}7\ 0]$	$-1/2\sqrt{41}$	$3/2\sqrt{41}$	–	$4.5h_0$	-0.22	0.66	–
$b_{-11/-12}$	$\frac{1}{82}[\bar{3}\ \bar{1}4\ 41]$	$-2/2\sqrt{41}$	$1/2\sqrt{41}$	1/2	$-11.5h_0$	0.17	-0.08	0.55
$b_{28/27}$	$\frac{1}{82}[17\ 11\ 0]$	$3/2\sqrt{41}$	$1/2\sqrt{41}$	–	$27.5h_0$	0.109	0.03	–
$b_{19/18}$	$\frac{1}{82}[25\ 21\ 0]$	$5/2\sqrt{41}$	$1/2\sqrt{41}$	–	$18.5h_0$	0.27	0.05	–
$b_{17/20}$	$\frac{1}{82}[5\ 37\ 0]$	$5/2\sqrt{41}$	$-3/2\sqrt{41}$	–	$18.5h_0$	0.27	-0.16	–
$b_{13/15}$	$\frac{1}{82}[14\ 38\ 0]$	$6/2\sqrt{41}$	$-2/2\sqrt{41}$	–	$14h_0$	0.42	-0.14	–
$b_{9/10}$	$\frac{1}{82}[23\ 39\ 0]$	$7/2\sqrt{41}$	$-1/2\sqrt{41}$	–	$9.5h_0$	0.73	-0.105	–
$b_{17/15}$	$\frac{1}{82}[14\ \bar{3}\ 41]$	$1/2\sqrt{41}$	$2/2\sqrt{41}$	1/2	$16h_0$	0.0625	0.125	0.4
$b_{21/20}$	$\frac{1}{82}[5\ \bar{4}\ 41]$	–	$1/2\sqrt{41}$	1/2	$20.5h_0$	–	0.049	0.31

Table 3.2: The products of lattice dislocations decomposition in a Σ41(540) grain boundary. The associated glide (b_g) and climb (b_c) components of the disconnections, along with their step heights are also reported. The motion of these disconnections in the grain boundary can induce deformations parallel $\beta_{\parallel} = b_g/h$ and perpendicular $\beta_{\perp} = b_c/h$ to the grain boundary that are described in the table as well. b_s in the table corresponds to the screw component of some disconnections that can potentially induce a deformation along the tilt axis of the grain boundary (β_s).

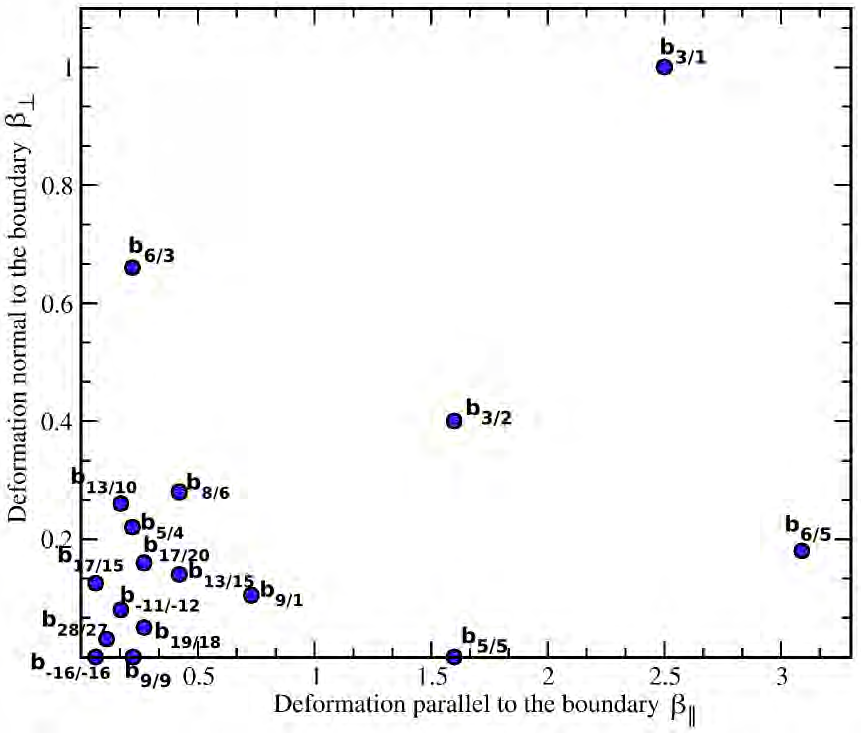

Figure 3.14: Schematic representation of all possible deformation modes associated to the disconnections resulting from decomposition of lattice dislocations in the boundary.

Figure 3.14 gives a schematic representation of different possible deformation modes associated to the disconnections reported in table 3.2 for the grain boundary Σ41(540). Each point in the diagram represents a disconnection for which horizontal and vertical coordinates correspond to the associated deformation parallel $\beta_{\parallel}$ and perpendicular $\beta_{\perp}$ to the grain boundary.

3.4.1 Mobility of disconnections

According to Serra and Bacon [103], disconnections with small Burgers vectors parallel to the boundary plane and with non-null step heights involve a minimal atomic shuffling and hence are likely to be mobile.
The disconnection with Burgers vector perpendicular to the boundary on the other hand, move by climb. If a disconnection of a length l and step height h with a Burgers vector having a climb component (b_c) moves over a distance δx, the change in the number of atoms δN transferred between grains G_1 and G_2 during the diffusive flux of material is given by [94] :

$$\delta N = l b_c X(G_1/G_2)\delta x \tag{3.57}$$

where $X(G_1/G_2)$ is the number of atom per unit volume of the material transferred between G_1 and G_2. Thus the motion of sessile defects depends directly to the climb component of its Burgers vector b_c.
The velocity of a lattice climbing dislocation v_c by lattice diffusion process in response to an

applied stress τ can be estimated by [120] :

$$v_c = \frac{D_{sd}}{b_c}\frac{\tau\Omega}{kT} \tag{3.58}$$

where D_{sd} corresponds to the bulk vacancy self-diffusion coefficient, Ω the atomic volume, k the Boltzmann constant and T the absolute temperature. The equation 3.58 corresponds to the climb velocity of dislocations under high temperatures and low stresses and thus is applicable to roughly estimate the disconnection climb velocity in our case.
According to equation 3.58 there is an inverse relationship between the climb velocity of dislocations and their climb component. Thus, the velocity of $\vec{b}_{28/27}$ corresponding to minimum climb components in table 3.2 ($b_c = a/2\sqrt{41}$) would be three times larger than the velocity of $\vec{b}_{6/3}$ ($b_c = 3a/2\sqrt{41}$).
Taking $D_{sd} = 3.5 \times 10^{-6}\exp(\frac{-1.25eV}{kT})m^2/s$ [121] and $\Omega = 2.52 \times 10^{-29}m^3$ as the atomic volume of Al, the climb velocity v_c of $\vec{b}_{28/27}$ under a shear stress of τ=10 MPa (Yield strength of pure Al [122]) at T=400°C gives 1.33 μm/s. This velocity is in the range of the observed step motion in the chapter 2 ($\sim 4\mu$m/s). It should be underlined that this estimation is strongly effected by the value of the vacancy self-diffusion coefficient. More accurate estimation of D_{sd} for disconnections climb should take into account the diffusion along grain boundaries.
This result indicates that although long range diffusion is required for moving GBDs with a component out of the grain boundary plane, their motion may be possible provided they have a small climb component and temperature/diffusion coefficient is sufficiently high.

As grain boundary migration results from the motion of disconnections, the ones with the largest climb component are then expected to control the mobility of grain boundary, by playing the role of obstacle to the motion of disconnections with a higher mobility (in particular the purely glissile ones). Indeed since they are expected to be the slowest disconnections, faster ones will pile up against them, presumably explaining the creation of macro-steps. If the mobility of the slowest dislocation is comparable to the mobility of the fastest ones, then the mobility of the grain boundary will be controlled by the collective motion of all the disconnections. This situation can be favoured at high temperature in thin foils because vacancy diffusion is enhanced due to the presence of close free surface [123]. At low stress and lower temperature however, the difference in mobility can be much higher and then the slowest disconnections can be viewed as strong obstacles. This situation favours then their overcoming/elimination by purely glissile disconnections (such as $\vec{b}_{9/9}$). Observation of macro-step locking and unlocking along the grain boundary may be the result of this process. The resulting coupling factor is thus expected to depend on the relative mobility of the disconnections. The evaluation of these coupling factors is discussed below.

3.4.2 Evaluation of the coupling factor

According to the table 3.2, the possible deformation modes attributable to disconnections in a Σ41(540) scatters within a wide range of possibilities. However according to the discussion above about the mobility, the disconnections with small Burgers vectors, step heights and small climb components are more likely to move and induce deformation. These disconnections in figure 3.14 are positioned in the lower left corner of the $\beta_\perp - \beta_\parallel$ curve.
In order to compare the coupling modes corresponding to these disconnections, experimental values of the coupling factor (both parallel and perpendicular components) are recalled in the table 3.3. The coupling mode induced by the motion of the purely glissile disconnection $\vec{b}_{9/9}$, ($\beta_\parallel = -0.22$, $\beta_\perp = 0$ and $\beta_s = 0$) is both in agreement with values obtained by MD simulations [23] and in-situ Scanning Electron Microscopy (SEM) hot deformation tests [77].

The $\vec{b}_{-16/-16}$ disconnection which corresponds disconnections with screw component, produces smaller shear in parallel direction to the boundary ($\beta_{\parallel} = 0.062$). Moreover the screw component of this disconnection can induce a deformation parallel to the tilt axis of the boundary. Grain rotation with a rotation axis perpendicular to the grain boundary plane coupled with migration, can result from the motion of this group of disconnections. Indeed the combined motion of screw disconnections producing a shear parallel to the rotation axis and disconnections with a Burgers vector producing a shear parallel to the grain boundary plane (and perpendicular to the rotation axis) can produce a rotation as reported in [97]. $\vec{b}_{-11/-12}$, $\vec{b}_{28/27}$ and $\vec{b}_{19/18}$ have climb

	$\beta_{\parallel}$	$\beta_{\perp}$	$\vec{b}_{i/j}$
in-situ SEM	0.22	0	$\vec{b}_{9/9}$
in-situ TEM (step 1)	0.25 ± 0.02	0.06 ± 0.02	$\vec{b}_{19/18}, \vec{b}_{9/9} + \vec{b}_{5/4}$
in-situ TEM (step 4)	0 ± 0.02	0.06 ± 0.02	$\vec{b}_{21/20}$, 50% $\vec{b}_{13/10}$ + 50% *Pure step*
in-situ TEM (step 5)	0.07 ± 0.02	0.06 ± 0.02	$\vec{b}_{28/27}$, $4\vec{b}_{-4/-5}$ + *Pure step*

Table 3.3: The deformations parallel $\beta_{\parallel}$ and perpendicular $\beta_{\perp}$ to the grain boundary, induced by the motion of steps, measured by in-situ TEM straining experiments. For comparison, possible disconnections $\vec{b}_{i/j}$ corresponding to the experimental values are indicated

components that will induce a deformation in normal direction to the boundary ($\beta_{\perp}$). This is consistent with the coupling modes that were observed by in-situ TEM straining experiments reported in chapter 1. The glide and climb components of $b_{19/18}$, ($\beta_{\parallel} = 0.27$, $\beta_{\perp} = 0.05$) can produce deformations that are comparably close to the coupling factors of step 1 measured by in-situ TEM.
Similarly the deformation measured for the step 5 of the table 3.3 corresponds to a coupling mode which is attributable to the disconnection $b_{28/27}$ with ($\beta_{\parallel} = 0.109$, $\beta_{\perp} = 0.03$). Moreover, other coupling factors can arise from combination between several disconnections and also pure steps as discussed below.

3.4.3 Combined motion of disconnections and pure steps

As it was concluded in the previous chapter, grain boundary migration proceeds by the formation and propagation of macro-steps. Macro-steps are considerably larger ($h \approx 60 - 100$ nm) than the disconnection step heights identified in the previous section and pure steps ($h_p = 41h_0 \approx 1.31$ nm). So it can be concluded that the macro-steps are composed of several elementary steps moving along the interface and also of pure steps. It has been found in Chapter 2 that pure steps move along the interface as well, presumably under capillarity forces. These steps also can be dragged by other moving steps. Although pure steps do not have any effect in the deformation of the material, however due to their step heights they can largely affect the coupling factor of the shear-coupled boundary migration. Figure 3.15 schematically shows the combined motion of a pure step h_p and a disconnection of step h and Burgers vector $\vec{b}$ with a glide $\vec{b}_g$ and a climb $\vec{b}_c$ component.
If f is the fraction of pure steps in the macro-step, then for the deformations $\beta'_{\parallel,\perp}$ produced in the sample, due to the motion of the macro-step, parallel and perpendicular to grain boundary

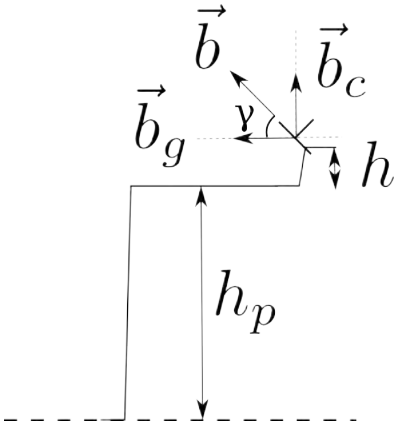

Figure 3.15: A schema of the combination of a disconnection with a step of height h with a pure step h_p along the interface. According to the angle γ between the Burgers vector $\vec{b}$ of the dislocation and the grain boundary, the glide $\vec{b}_g$ and a climb $\vec{b}_c$ components of the dislocation are indicated

plane we have :

$$\beta'_{\parallel,\perp} = \frac{(1-f)\|\vec{b}_{\parallel,\perp}\|}{f(h_p-h)+h} = \frac{(1-f)h}{f(h_p-h)+h}\beta_{\parallel,\perp} \tag{3.59}$$

$\beta_{\parallel,\perp}$ being the deformation caused by the motion of the grain boundary dislocation.

According to equation 3.59 the deformation produced by the combination, for f=0.5, of a $\vec{b}_{13/10}$ with ($\beta_{\parallel} = 0.17$ $\beta_{\perp} = 0.26$) and a pure step become : $\beta'_{\parallel} = 0.03$ and $\beta'_{\perp} = 0.05$. These values are for instance very close to the measured coupling factors for the step 4 in table 3.1 obtained by in-situ TEM straining. This example among a lot of possibilities of combination of disconnections and pure steps indicate the large variability of possible coupling factors.

3.4.4 Grain boundary migration driven by lattice dislocation incorporation

The observation of possible lattice dislocation decomposition into disconnection suggests that grain boundary migration can occur without requiring any disconnection sources but by the continuous feeding of the grain boundary by lattice dislocations as the migration proceeds.
Consider for instance a bicrystal with a dislocation density ρ. Let l the total grain boundary length and m the migration distance. The number of disconnection of step height h required is then $N_r = m/h$. This assumption supposes that the disconnections are perfectly mobile and move over the entire grain boundary. The number of available dislocations N_a can be set in a first approximation as the total number of dislocations in the bicrystal swept over the distance m, i.e for a dislocation density ρ, $N_a = \rho lm$. If the ratio $N_a/N_r = \rho lh > 1$ then the interaction and decomposition of dislocations into glissile disconnections is sufficient to pursue the shear coupled grain boundary migration. In small grain polycrystals with almost no dislocation in grain interiors, ρ and l are negligible and the above inequality cannot be fulfil. In a large bicrystal typically $l = 1mm$, the above condition can be fulfilled with a reasonable dislocation density, i.e. when $\rho \approx 10^{13}m^{-2}$, taking a typical value of $h = 0.1nm$.

At sufficiently high temperature and in work-hardened materials, this mechanism is thus expected to occur and may enhance dynamic recrystallization for instance. The role of shear-coupled grain boundary migration as a possible trigger of recrystallization have been pointed out by [23]. The authors postulate that cold-worked tilt grain boundaries susceptible to migrate and sweep intragranular dislocations can form initiation sites for new grains. Strain induced recrystallization of Al tilt grain boundary in front of intragranular slip band in annealed bicrystals can also be an evidence of grain boundary migration induced by a coupling mode [124].

3.5 Conclusion

In this chapter, the role of disconnections in the shear-coupled grain boundary migration was investigated in details. The following conclusions can be drawn :

- By means of high resolution TEM, grain boundary defects in as-grown Al bicrystals were observed and characterized. Dislocations without step character, pure steps and general disconnections were found along the interface. Conventional bright field imaging has revealed the presence of screw disconnections. All these disconnections are extrinsic presumably formed during the elaboration or the thin foil preparation.
- Different cases of interactions between lattice dislocations, activated by intragranular plasticity during in-situ TEM straining, and the grain boundary were analyzed. Rapid decomposition of lattice dislocations into disconnections were observed inside the grain boundary. (Figure 3.9 and figure 3.10).
- The theoretical examination of decomposition reactions indicates that the disconnections produced possess generally both glide and climb component.
- Completely glissile dislocations, corresponding to disconnections with a Burgers vector parallel to the grain boundary plane, and with small step heights to limit atomic shuffling are favoured. However, disconnections with a small climb component can move at a speed compatible with the observation presented in Chapter 1. The grain boundary migration mobility is then supposed to be controlled by the motion of these disconnections or by the ability of the most mobile disconnections to overcome them.
- Disconnections can also have a Burgers vector parallel to the misorientation axis and thus can produce a strain out of the foil plane. The combined motion of disconnections with Burgers vector at right angles can then explain grain migration coupled with rotation [97].
- The motion of the disconnections produced by decomposition, can explain the observed coupling factors (Table 3.2). Moreover, the large variety of combination of disconnections and pure steps can account for a large variability of the coupling factor.
- Grain boundary migration under stress may be feed by the continuous absorption of lattice dislocations as the grain advances, followed by their decomposition and motion, provided the intragranular dislocation density and temperature is sufficient high. This is supposed to have an impact on recrystallization processes.

4 ELEMENTARY PROCESSES OF THE COUPLING MECHANISM AT ATOMIC SCALE : ATOMISTIC SIMULATION

In the previous chapters, the shear-coupled migration of the grain boundary has been shown to be related to the formation and motion of grain boundary steps identified as disconnections. In this chapter, an atomistic simulation study is performed in order to understand the formation and migration of these disconnections.
Despite numerous numerical studies on the shear-coupled migration mechanisms, to our knowledge the characterization of the nucleation and migration of the disconnections has not been reported before. Indeed, most of the numerical simulations have focused on the relation between the coupling factor and the grain boundary geometry or on the stick-slip grain boundary migration under a constant shear velocity [23, 80, 125, 126] or on the temperature dependence of shear coupling [82]. Only few studies report on the observation of the formation of grain boundary steps [80, 102] though no characterization are reported. On the other hand, a recent study also reports that the migration of a grain boundary containing pre-existing disconnection is easier (i.e. requires a smaller applied shear stress) than a perfect grain boundary [127]. This latter result suggests that the migration of disconnections is easier than their nucleation.
In the present chapter aiming at identifying the elementary mechanisms of the shear-coupled migration by atomistic simulation, we propose an original procedure that consists in constructing the atomic structure of a grain boundary before and after its migration and in uncovering the reaction path between them. Section 4.1.1 describes the simulation model and the equilibrium grain boundary structure. Section 4.1.2, 4.1.3 and 4.1.4 are devoted to technical details (interatomic potential, energy minimization algorithm and stress calculation). In order to determine the reaction path between two positions of the grain boundary, the Nudged Elastic Band (NEB) method is used and will be described in section 4.1.5. Finally the section 4.2 is devoted to the study and results evidencing and characterizing the elementary mechanisms of the shear-coupled grain boundary migration.

Contrary to the experimental study dealing with aluminium, the results of the present chapter concern copper. The choice of copper was motivated by 1) the several detailed numerical studies on copper [80] providing direct available data and 2) my initially limited skills in simulations techniques. A first step of my Ph.D. work has thus been the reproduction of some already

published results as an exercise before really starting the study reported in this chapter. While we initially planned to switch to aluminium for a direct comparison with the experimental work, the study on copper and its first results results were very interesting and engaging, so that additional simulations (noticeably the size effects) were required. Finally, the copper study has gone on all over the last tree years and has not let enough time for the study on Aluminium.

4.1 Model and technical details

4.1.1 Simulation model

In this work, a Copper bicrystal containing a planar symmetric tilt grain boundary is modeled. The grain boundary is a coincident Σ13 (320). The misorientation angle between the grains, associated to this boundary is θ=67.38° and the rotation axis is parallel to [001] crystallographic direction. Figure 4.1 reports the dichromatic pattern for the Σ13(320) grain boundary in which the crystallographic axes for each grain are indicated. In this pattern the squares correspond to the atoms of grain 1, whereas circles represent the grain 2. Open and full symbols correspond to atoms in different planes in the [001] direction. The grain boundary plane (320) is shown according to the crystallographic directions of grain 1.

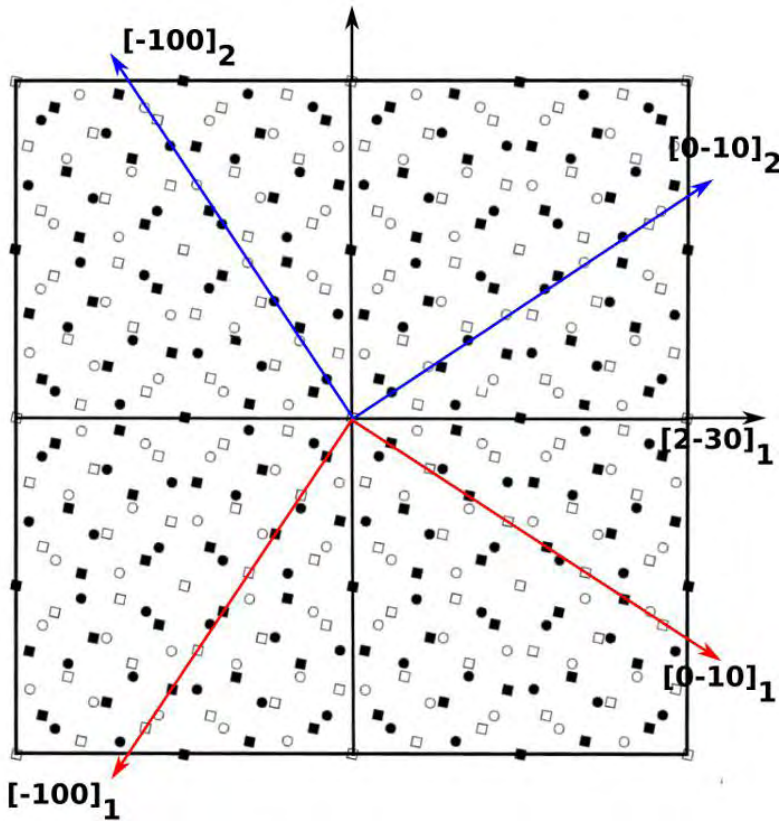

Figure 4.1: Dichromatic pattern for Σ13(320) CSL system showing 4 CSL cells. Major crystallographic directions are shown as subscripts for grain 1 and grain 2.

In order to apply a shear on the grain boundary to induce its migration, we construct a judicious simulation box. Figure 4.2a represents a sketch of the simulation cell. The simulation cell contains two symmetric grains of a perfect fcc copper crystal disorientated relatively to each other by an angle θ around the [001] direction, parallel to the Z-direction of the simulation box ; the relative position of the grains is adjusted and extra atoms are deleted in order that a symmetric coincident site lattice (CSL) tilt boundary, $\Sigma 13(320)$, results at the interface. Periodic boundary conditions are set in the directions parallel to the grain boundary plane : $[2\bar{3}0]$ (y-axis) and [001] (z-axis) directions. The cell x-size (x-axis along the [320] direction) is about 10.3 nm and remains unchanged all over the study. Two 1.5 nm thick slab regions at the top and the

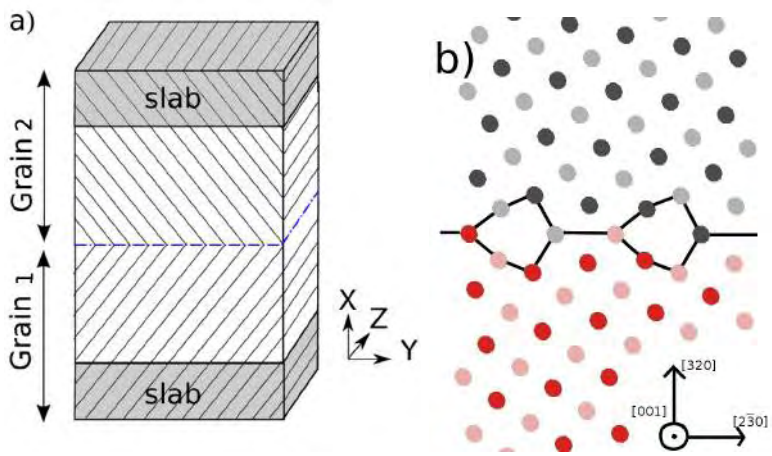

Figure 4.2: a) Sketch of the simulation cell. b) Configurations of the $\Sigma 13(320)$ *grain boundary projected in the (x,y) plane : Black (Grey) and Red (Pink) atoms belong to different grains. Black(red) and Grey(Pink) atoms have not the same z-coordinates.*

bottom of the simulation box are used to shear the bicrystal by displacing them parallel to the grain boundary plane. These slabs contain atoms with relative positions frozen to their perfect lattice positions.
Interactions between the atoms in the simulation box are defined by an Embedded Atom Method (EAM) potential function. The description of this potential function is given in the next section 4.1.2.
The simulations are performed using the Large-scale Atomic/Molecular Massively Parallel Simulator (LAMMPS) [128].

The equilibrium structure of the grain boundary is achieved by energy minimization of the system using the Conjugate gradient algorithm. This algorithm is described in the section 4.1.3. The equilibrium structure of the grain boundary is shown in figure 4.2b. Black and red circles represent the atoms in the two grains and the dark and light colors correspond to the atoms in different (001) planes. The kite-shaped structural units at the interface correspond to the stable structure of the grain boundary at 0K temperature and are characteristic of the $\Sigma 13(320)$ grain boundary [80]. The position of the grain boundary is defined as the straight line passing the median of the structural units.
In the section 4.2.1 the migration of the grain boundary is produced by shearing the bicrystal. Shearing is achieved by displacing the upper slab, parallel to the grain boundary plane along y

direction. During this procedure, each displacement of the slab is followed by minimization of the potential energy in the cell and the energy and stress variations are studied as a function of the shear displacements. The shear stress component τ_{xy} is evaluated using virial stress tensor described in the section 4.1.4.

4.1.2 Embedded Atom Method (EAM)

Due to the delocalized conduction electrons in the metallic bonds in Copper, a many-body potential is required to model the atomic interactions. The Embedded Atom Method (EAM), has shown its reliability for the atomistic simulations of metallic stressed structures and of metallic extended crystalline defects [129].
Among the different available EAM potentials for Copper ([129], [130], [131]), we have used the one provided by Mishin et al. [129] since the elasticity constants are very close to the experimental ones (See Table 4.1) and since it provides good results in modelling crystal defects ([132, 133, 134]). However it should be specified that here the experimental data corresponds to the elasticity constants of Copper measured at ambient temperature, contrarily to the theoretical values that are determined at 0 K.

	C_{11}(GPa)	C_{12}(GPa)	C_{44}(GPa)
Experimental	168.4	121.4	75.4
Simulation	168.5	122.6	76.1

Table 4.1: The elasticity constants of Copper determined by Mishin et al. EAM potential compared with experimental data [135]

In the Embedded Atom Method (EAM), the total energy $E(\vec{R})$ of N-atom system is represented as a function of atomic positions :

$$E(\vec{R}) = \sum_{\alpha}^{N} F(\bar{\rho}_\alpha) + \frac{1}{2}\sum_{\alpha\neq\beta}^{N} \phi(\vec{r}_{\alpha\beta}) \tag{4.1}$$

where $\vec{R} = \{(x_0, y_0, z_0), ...(x_{N-1}, y_{N-1}, z_{N-1})\}$ is a 3N dimension vector with $(x_\alpha, y_\alpha, z_\alpha)$ the Cartesian coordinates of atoms α ($\alpha \in (0, ..., N-1)$). $\vec{r}_{\alpha,\beta}$ is the relative position of the atom β compared to the atom α. The first term $F(\bar{\rho}_\alpha)$, is the cohesive energy part depending on the electron density $\bar{\rho}_\alpha$ of atom α.[136] The second term of the Eq.4.1 is a pair interaction potential which includes some corrections to the first term and which especially accounts for the short-distance repulsive interactions between an atom and its neighbours [1]. In this model, the atom α is embedded in the electron density $\bar{\rho}_\alpha$ created by the neighbouring atoms. $\bar{\rho}_\alpha$ is approximated by the sum of the atomic densities : each neighbour β of atom α is assumed to contribute to the host electron density by means of an atomic density $\rho(\vec{r}_{\alpha,\beta})$ depending on $\vec{r}_{\alpha,\beta}$:

$$\bar{\rho}_\alpha = \sum_{\beta\neq\alpha}^{N} \rho(\vec{r}_{\alpha,\beta}) \tag{4.2}$$

1. Actually, while the functional form of Eq.4.1 is based on the physical ideas regarding bonding in metallic systems, its two terms may practically lose their original physical meaning and be treated as some fitting functions. The only requirement is that the potential should adequately reproduce the material properties.

In the Mishin potential the pair potential $\phi(r)$ reads :

$$\phi(\vec{r}) = [E_1 M(r, r_0^{(1)}, \alpha_1) + E_2 M(r, r_0^{(2)}, \alpha_2) + \delta] \times \psi(\frac{r - r_c}{h}) - \sum_{n=1}^{3} H(r_s^{(n)} - r) S_n (r_s^{(n)} - r)^4 \quad (4.3)$$

where M is a Morse function given by :

$$M(r, r_0, \alpha) = \exp[-2\alpha(r - r_0)] - 2exp[-\alpha(r - r_0)] \quad (4.4)$$

In Eq.4.3 $H(x)$ is the unit step function and $\psi(x)$ is a cutoff function defined as $\psi(x) = 0$ if $x \geq 0$ and $\psi(x) = \frac{x^4}{1+x^4}$ if $x < 0$.
The electron density function is taken as :

$$\rho(\vec{r}) = [a \exp(-\beta_1 (r - r_0^{(3)})^2) + \exp(-\beta_2 (r - r_0^{(4)})) \times \psi(\frac{r - r_c}{h}) \quad (4.5)$$

and the embedding function is represented by a polynomial :

$$F(\bar{\rho}) = F^{(0)} + \frac{1}{2} F^{(2)} (\bar{\rho} - 1)^2 + \sum_{n=1}^{4} q_n (\bar{\rho} - 1)^{n+2} \; for \; \bar{\rho} < 1 \quad (4.6)$$

and

$$F(\bar{\rho}) = \frac{F^{(0)} + \frac{1}{2} F^{(2)} (\bar{\rho} - 1)^2 + q_1 (\bar{\rho} - 1)^3 + Q_1 (\bar{\rho} - 1)^4}{1 + Q_2 (\bar{\rho} - 1)^3} \; for \; \bar{\rho} < 1 \quad (4.7)$$

The above equations contain 20 fitting parameters : E_1, E_2, a, $F^{(0)}$, $F^{(2)}$, q_1, q_2, q_3, q_4, Q_1, Q_2, $r_0^{(1)}$, $r_0^{(2)}$, $r_0^{(3)}$, $r_0^{(4)}$, α_1, α_2, β_1, β_2, δ, r_c, h, and $\{r_s^{(n)}, S_n\}_{n=1,2,3}$. The potential is optimized by minimizing the weighted mean squared deviation of selected properties of Cu, taken from experimental data or ab-initio calculations. The properties of Cu taken from experimental data consist in : the equilibrium lattice constant a_0, the cohesive energy E_0, the bulk modulus B, the elastic constants c_{ij}, the phonon frequencies $v_L(X)$ and $v_T(X)$ at the zone-boundary point X, the relaxed vacancy formation (E_f) and migration energies E_m, the thermal expansion factors, the equilibrium bond energy E_d of Cu dimer and the intrinsic stacking fault energy γ_{SF}.
The ab initio part include the excess energies of the hcp and bcc structures over fcc. The optimized values of parameters are given in [129].

4.1.3 Energy minimization

In this section, the Conjugate Gradient (CG) algorithm is described. This algorithm is used to find the minimum of a many-variable function. In our atomic simulations, it is used to find the minimum of the potential energy $E(\vec{R})$ and thus to find the equilibrium structure of the bicrystal.
The CG procedure to minimize the function $E(\vec{R})$ is an iterative process consisting of an initial choice of an atomic configuration, the finding of a suitable direction in order to displace atoms leading to a less energetic configuration.

The detailed CG algorithm is the following :
– Initialization : a initial judicious configuration $\vec{R}^1$ is selected.
– Iterative Procedure : the system is in the configuration $\vec{R}^j$

1. The search direction $\vec{d^j}$ is set to be

$$\vec{d^j} = -\vec{\nabla}E^j + \varepsilon^j \vec{d}^{j-1} \text{ for } j \neq 1 \quad (4.8)$$
$$= -\vec{\nabla}E^j \text{ for } j = 1 \quad (4.9)$$

where :

$$\varepsilon^j = \frac{\vec{\nabla}E^{j\,T}(\vec{\nabla}E^j - \vec{\nabla}E^{j-1})}{\vec{\nabla}E^{j-1\,T}\vec{\nabla}E^{j-1}} \quad (4.10)$$

The search direction at step j is perpendicular to the one at step $j-1$. Equation 4.10 corresponds to Polak-Ribiere [137] version of the CG algorithm.

2. $\vec{R}^{j+1}$ is found according to :

$$\vec{R}^{j+1} = \vec{R}^j + s^j \cdot \vec{d^j} \quad (4.11)$$

Where the step length s^j in the direction $\vec{d^j}$ is optimized by minimizing the function $E(\vec{R}^j + s^j \cdot \vec{d^j})$ compared to the variable s^j :

$$\frac{dE(\vec{R}^j + s^j \cdot \vec{d^j})}{ds^j} = 0 \quad (4.12)$$

3. Check if the convergence criteria are satisfied. If not go to step 1. If yes end the procedure

– Convergence Criteria are met if one of the following conditions is fulfilled :

1. the energy difference between two consecutive iterations is smaller than a selected energy tolerance ϵ_e : $|\frac{E(\vec{R}^{j+1}) - E(\vec{R}^j)}{E(\vec{R}^j)}| \leq \epsilon_e$
2. the global force vector acting on atoms is weak : the norm $|-\vec{\nabla}E(\vec{R}^{j+1})|$ of the gradient of the potential energy is smaller than a selected force tolerance ϵ_f : $|-\vec{\nabla}E(\vec{R}^{j+1})| \leq \epsilon_f$.
3. the line search fails because the step distance s^j backtracks to 0.0
4. The number of iterations exceeds a selected number

In these simulations, the tolerances for the energy difference and global force acting on atoms were set as 10^{-16}.

4.1.4 Stress calculation

The stress tensor is calculated using virial formulation. For an atom α, the virial stress tensor component $\sigma_{AB,\alpha}$ reads [138] :

$$\sigma_{AB,\alpha} = \frac{1}{\Omega_\alpha}[-m_\alpha v_{A,\alpha} v_{B,\alpha} + \frac{1}{2}\sum_{\beta \neq \alpha} F_{A,\alpha\beta} r_{B,\alpha\beta}] \quad (4.13)$$

where $(A, B) \in (x, y, z)$. Ω_α and m_α are the volume and the mass of the atom α. In all the results of section 4.2, Ω_α has been fixed to the atomic volume in a perfect fcc copper structure. $v_{A,\alpha}$, $F_{A,\alpha\beta}$ and $r_{A,\alpha\beta}$ are the A component of the velocity of the atom α, of the force $\vec{F}_{\alpha\beta}$ and of the

relative position $\vec{r}_{\alpha\beta}$. As already mentioned, $\vec{r}_{\alpha\beta} = \vec{r}_\beta - \vec{r}_\alpha$, with $\vec{r}_\alpha$ the position vector of the atom α. Using the expression Eq. 4.1 of the EAM potential :

$$\vec{F}_{\alpha\beta} = -\vec{\nabla}_\alpha \left[\frac{1}{2} \sum_{\gamma \neq \beta} \phi(\vec{r}_{\beta\gamma}) + F(\bar{\rho}_\beta) \right] \tag{4.14}$$

The first term of Eq.4.13 corresponds to a kinetic energy contribution : in our case, as we maintain the system at 0K, this term cancels.

4.1.5 The Nudged Elastic Band (NEB) method

In this section, we describe the nudged elastic band method aimed at calculating the transition path between two stable configurations of an atomic system. In the following initial and final states respectively refer to these stable atomic configurations. The transition path, the Minimum Energy Path (MEP), is defined as the lowest energy curve that connects the initial and final states of the system.
In our simulations, the initial and final states correspond to two positions of the grain boundary before and after the migration of the grain boundary.

In the NEB method, intermediate configurations of the system between the initial and final states are introduced. A set also referred as a band in this case, of m replicas (images) of the system defined by their atomic configuration $\vec{R}^i$ with $i \in (0, ..., m-1)$ forms an extended phase space. Replica 0 and m-1 are respectively the initial and final states. For a N-atom system, each vector $\vec{R}^i$ has 3N coordinates.

The NEB method consists in the minimization of a judicious Hamiltonian (described below) by an iterative process in the extended phase space : the Hamiltonian is constructed so that its minimum corresponds to the replica being along the MEP.

Based on the analogy that an elastic string linking two minima on a 2D surface roughly follow the MEP, the sum of the total potential energies of each replica contributes to this Hamiltonian. In addition, a spring interaction (spring constant K) between adjacent replicas is added to model the elastic string, ensure the continuity of the path and prevent that the minimization drive the intermediate replica to the initial and final states. The above analogy suggests thus to minimize the following Hamiltonian :

$$H = \sum_i E(\vec{R}^i) + \sum_{i=0}^{m-2} \frac{1}{2} K(\vec{R}^{i+1} - \vec{R}^i)^2 \ for\ i > 1, i < m-1 \tag{4.15}$$

Unfortunately, the direct minimization of H does not yield the MEP. Indeed, let $\vec{\tau}^i$ be the tangent to the path at replica i estimated from the two adjacent replicas, $\vec{R}^{i+1}$ and $\vec{R}^{i-1}$:

$$\vec{\tau}^i = \frac{\vec{T}^i}{|\vec{T}^i|} \tag{4.16}$$

$$\vec{T}_i = \frac{\vec{R}^i - \vec{R}^{i-1}}{|\vec{R}^i - \vec{R}^{i-1}|} + \frac{\vec{R}^{i+1} - \vec{R}^i}{|\vec{R}^{i+1} - \vec{R}^i|} \text{ for } 0 < i < m-1 \tag{4.17}$$

$$\tag{4.18}$$

The definition of the tangent for replica 0 and $m-1$ are not required in the NEB method.

The spring forces on replica i have a parallel and perpendicular component to the tangent $\vec{\tau}^i$. The perpendicular components tend to prevent the band from following a curved MEP and thus can drag the replica out of the MEP. In the NEB method, H is thus minimized taking into account only the parallel component of the spring forces.

The forces derived from the energy potential on replica i have also a parallel and perpendicular component to tangent $\vec{\tau}^i$. The parallel component drives the replica towards the closest minimum. In order to approximately keep the same spacing between replica, in the NEB method the minimization of H is performed taking into account only the perpendicular component.

Finally, the force (a 3N-coordinates vector) acting on replica i used during iterative minimization process is :

$$\vec{F}^i(R^i) = \vec{F}^i_{pot}|_\perp + \vec{F}^i_{spring}|_\parallel \tag{4.19}$$

Where

$$\vec{F}^i_{pot} = -\vec{\nabla}_{\vec{R}^i} E(\vec{R}^i) \tag{4.20}$$

$$\vec{F}^i_{pot}|_\perp = \vec{F}^i_{pot} - (\vec{F}^i_{pot}.\vec{\tau}^i)\vec{\tau}^i \tag{4.21}$$

and

$$\vec{F}^i{}_{spring} = K(\vec{R}^{i+1} - \vec{R}^i) - K(\vec{R}^i - \vec{R}^{i-1}) \tag{4.22}$$

$$\vec{F}^i_{spring}|_\parallel = \left[\left(K(\vec{R}^{i+1} - \vec{R}^i) - (\vec{R}^i - \vec{R}^{i-1})\right).\vec{\tau}^i\right]\vec{\tau}^i \tag{4.23}$$

By this force projections, referred as "nudging", the spring forces only control the spacing of the images along the band and do not interfere with the convergence of the elastic band to the MEP.
The minimization is performed following an iterative procedure using the "quickmin" algorithm[139], a damped dynamics method. Once the convergence is reached (following a convergence criteria), the replicas are on the MEP. However, none of the replica lands at the saddle point.

The Climbing Image-NEB extends the NEB method to determine the saddle point on the MEP.

The replica i_{max} with the highest energy at the end of the regular NEB is identified. CI-NEB is identical to the NEB, except that the acting force $\vec{F}^{i_{max}}$ on the replica i_{max} brings it to saddle point : $\vec{F}^{i_{max}}$ moves the image i_{max} up to the potential energy surface along the elastic band and down the potential surface, perpendicular to the band.

$$\vec{F}^{i_{max}} = -\vec{\nabla}E(\vec{R}^{i_{max}}) + 2\vec{\nabla}E(\vec{R}^{i_{max}})|_\parallel = -\vec{\nabla}E(\vec{R}^{i_{max}}) + (2\vec{\nabla}E(\vec{R}^{i_{max}}).\vec{\tau}^i)\vec{\tau}^i \tag{4.24}$$

This force is not affected by spring forces and mainly depends on the potential energy of the replica i_{max} (and the tangent $\vec{\tau}_i$).

Once the MEP, including the saddle point is obtained, it is convenient to represent the energy evolution curve along the MEP using a reaction coordinate (RC).
The reaction coordinate represents the progress of the reaction between initial and final states denoted respectively by RC=0 and RC=1. In our study, the reaction coordinate of a given replica of the system l, is defined as the cumulative distance (normalized by the total cumulative distance) between adjacent replicas. Here "distance" is defined as the length of the 3N-vector of differences in atomic coordinates, N being the number of atoms in the system :

$$RC^l = \frac{\sum_{i=0}^{l-1} |\vec{R}^{i+1} - \vec{R}^i|}{\sum_{i=0}^{m-1} |\vec{R}^{i+1} - \vec{R}^i|} \tag{4.25}$$

4.2 Results

As already mentioned, in order to identify the elementary mechanisms of the shear-coupled grain boundary migration, the atomic structures of the grain boundary, before and after migration should be constructed. Since in the NEB method all atoms in a given replica are distinguishable, section 4.2.1 presents a procedure to produce the atomic structure of the grain boundary, before and after migration. Using these atomic structures as initial and final configurations in the NEB method, the MEP during the grain boundary migration is analyzed in section 4.2.2 : both energetic and structural studies are performed. Finally, the dependence of the results on the simulations size box is analyzed in section 4.2.3. Finally, an interpretation of the MEP using the elasticity theory results in a energetic characterization of the elementary mechanisms of the grain boundary migration.

4.2.1 Stick-Slip motion

In order to shear the grain boundary, the slabs are translated relatively to each other in the y direction by small increments and the potential energy is minimized at each step.

The variation of shear stress τ and the potential energy of the system during the shearing process is reported in figure 4.3 (a) and (b), as a function of the relative displacement, d, of the slabs. The simulation cell y and z sizes are $L_y = 1L_{[2\ \bar{3}\ 0]}$ and $L_z = 1L_{[0\ 0\ \ 1]}$ with $L_{[2\ \bar{3}\ 0]} = 1.3$nm and $L_{[0\ 0\ \ 1]} = 1.4$nm, the CSL periods in the $[2\bar{3}0]$ and $[0\ \ 0\ \ 1]$ direction. The simulation cell contains 1664 atoms.

Starting from d = 0 in figure 4.3a, the shear stress (black curve) increases linearly with the relative displacement d of the slabs. This is coherent with the quadratic variation of the potential energy with the displacement d (figure 4.3b) and is characteristic of the elastic regime. In this regime the position of the grain boundary, relative to its initial position is unchanged.
At a critical value of the relative displacement of the slabs, $d_c = 0.365nm$, there is an abrupt stress drop from $\tau \approx 1.4GPa$ down to $\tau \approx 1GPa$. The visualization of the atomic configurations during this process shows that this stress drop coincides with the migration of the grain boundary. From this point ($d > d_c$), any additional increase in the shear displacement, d (red curve) produces again a linear increase of the shear stress until the next grain boundary migration at $d = 0.46nm$. This behaviour creates a sawtooth stress-displacement curve representing the stick-slip movement of the grain boundary in which each stress drop is associated to a spontaneous migration of the grain boundary [80, 84].
On the other hand, after the first grain boundary migration at $d = d_c$, decreasing the relative distance d between the slabs, the shear stress decreases (red curve for $d < d_c$). Similarly to the black curve the variations of stress and energy are linear and quadratic respectively. During this decrease, the grain boundary configuration remains unchanged in its final position after the first migration. Here, contrary to the black curve, the stress does not cancel for a zero slab displacement $d = 0$, but for a displacement $d_1 = 0.1nm$. This displacement d_1 corresponds to the shear deformation induced by the grain boundary migration. Dividing the deformation value by the grain boundary migration distance m = -0.25 nm, the coupling factor of the migration is obtained $\beta = \frac{d1}{m} = -0.40$. The grain boundary migration distance m is measured from the direct inspection of the grain boundary configurations. The coupling factor $\beta = -0.40$ is in agreement with previous theoretical studies which describe the coupling factor as a function of the misoreintation angle : $\beta_{<110>} = 2\tan(\frac{\pi}{4} - \frac{\theta}{2})$ [23].
While the grain boundary migrates at 0 K for $d = d_c$ and since the grain boundary migration is expected to be a thermally activated process, the grain boundary may migrate for $d < d_c$

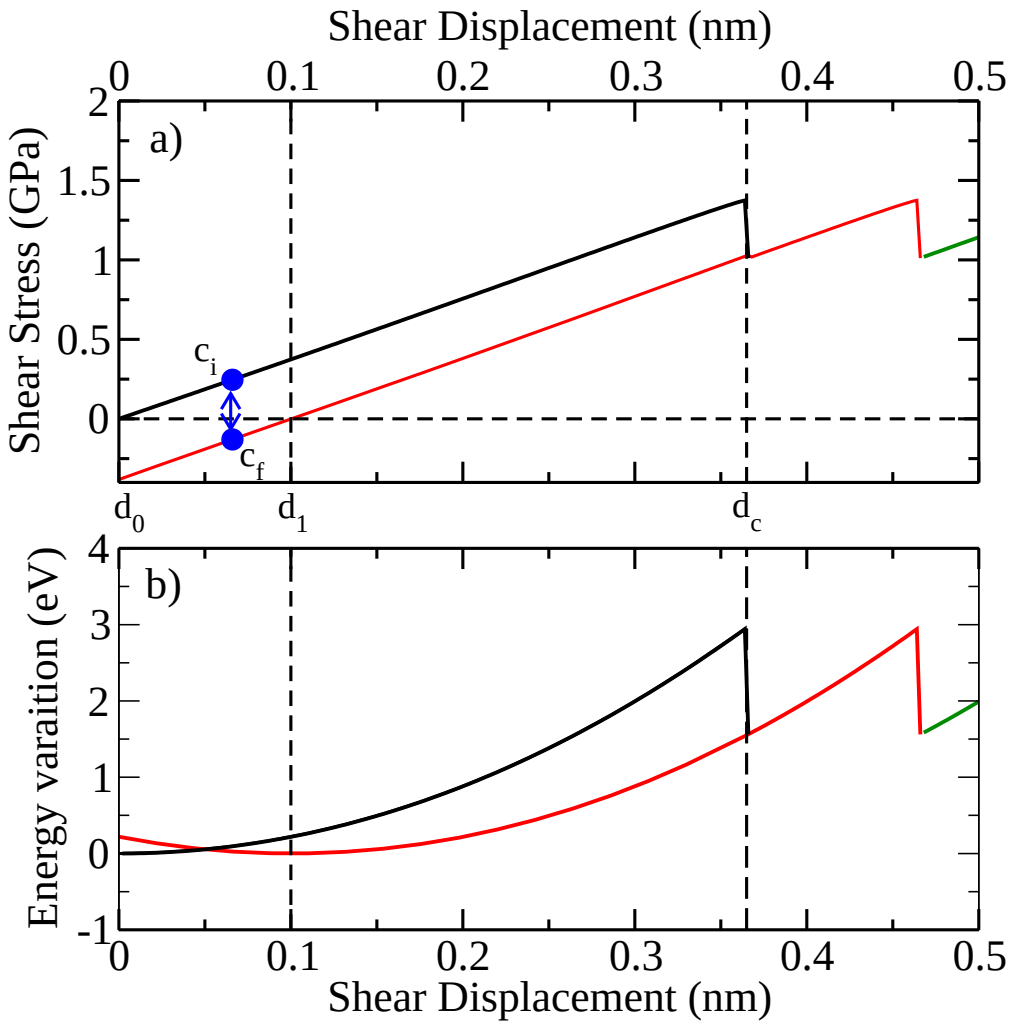

Figure 4.3: a) Shear stress and b) potential energy variation (black, red and green) as a function of the shear displacement. The black and red curves correspond to the initial and final configurations of the grain boundary. Dashed lines are guide to the eyes. The cell y- and z-sizes are 1.3 nm and 1.4 nm.

at finite temperature. To investigate this expected thermally activated migration, the configurations of the system before and after the grain boundary migration obtained at 0 K for a given external parameter d are used as the initial and final configurations in the NEB method. These configurations are well suited to the NEB method (for which atoms are distinguishable) since they result from the modifications of the same initial equilibrium configuration.
By the above procedure, the configurations of the system corresponding to two positions of the grain boundary, before and after the migration, are obtained for different displacements $0 \leq d \leq d_c$. For instance at $d = 0.066nm$, the NEB is performed between the system configurations (reported on figure 4.3a) corresponding to initial c_i and final c_f positions of the grain boundary.

4.2.2 Grain boundary migration transition path

The NEB method is used to determine the Minimum Energy Path (MEP) of the grain boundary migration for 15 values of the slab displacements d between $0 \leq d \leq d_c$. 40 replicas of the system are used in each NEB calculation. Note that when the MEP shows some metastable state, NEB calculations are repeated using these states as initial and final configurations. RC=0 and RC=1 correspond to the initial and final positions of the grain boundary.

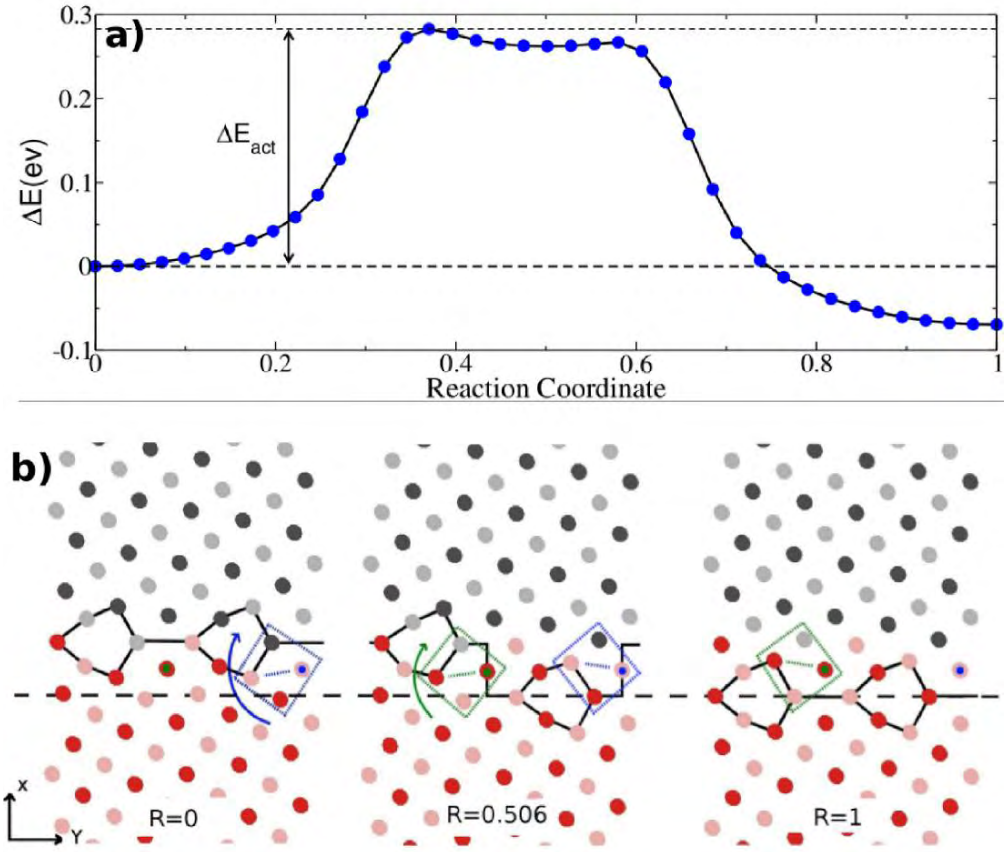

Figure 4.4: a) The MEP curve between the initial and final states of the system during the grain boundary migration corresponding to initial and final positions of the boundary respectively. The vertical axis corresponds to the energy change in the system and the horizontal axis is the reaction coordinates (RC). b) Structural evolution of the grain boundary along the MEP projected in the x-y plane. (See the color code in figure 4.2). Blue and green squares display the atoms that rotates and bring the structural units to its next position. The cell y- and z-sizes are 1.3 nm and 1.4 nm.

Energetic evolution during migration

Figure 4.4a reports the MEP energy curve for the displacement d = 0.066 nm, a representative MEP among those obtained for different values of d. The MEP presents two local maxima for RC = 0.37 and 0.58 and a local minimum for RC = 0.506. The energy difference between energies of

the initial state (E= -5845.049 eV) and the highest energy maximum (E= -5844.766 eV) is the energy barrier for the grain boundary migration : $E_{act} = 0.283eV$.

Structural evolution during migration : disconnections

By visualizing the evolution of the atomic configuration of the system along the MEP, the structural evolution of the grain boundary during shear-coupled migration for a given displacement d can be revealed. The figure 4.4b reports the configurations along the MEP for the initial RC=0, the metastable RC=0.506 and the final states RC=1. For RC=0 and RC=1, the two structural units lie in the same plane marking the initial and final positions of the grain boundary. For RC=0.506, corresponding to the metastable state of the MEP, one of the structural units have been displaced evidencing two opposite grain boundary steps schematically reported in figure 4.4b.

The displacements of the structural units mainly happen by the clockwise rotation of four atomic columns around the z-direction, suggesting a shuffling mechanism [92, 62]. These columns are enclosed in the blue (RC = 0 $\longrightarrow$ 0.506) and green squares (RC = 0.506 $\longrightarrow$ 1) in figure 4.4b and the rotation axes nearly coincide with the columns depicted by the blue and green points.

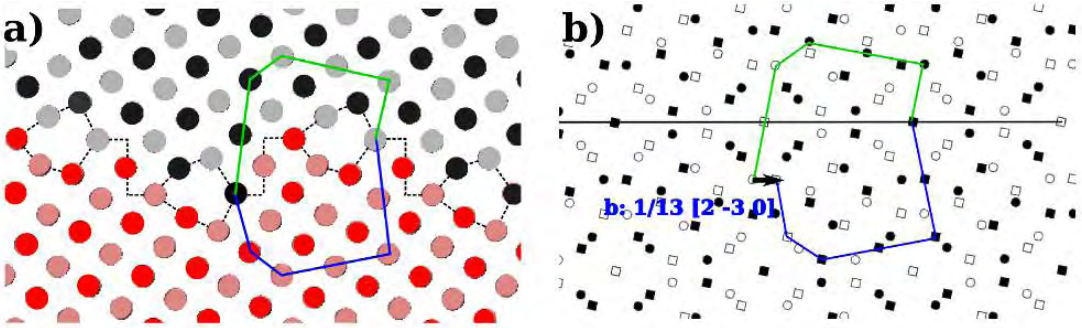

Figure 4.5: a) Circuit mapping to connect two equivalent coincident sites on the grain boundary enclosing the step. b) The same circuit on the dichromatic pattern of the Σ13(320). The closure defect appears in this second circuit. It corresponds to a dislocation with the burgers vector of $\vec{b_1} = \frac{a_0}{13}[2\ \bar{3}\ 0]$*, parallel to grain boundary plane.* a_0 *here stands for the lattice parameter of Copper.*

In order to characterize these grain boundary steps, the circuit mapping technique is used. Two coincident positions on the grain boundary are connected to each other by a closed circuit, passing from each grain and encircling one of the steps as indicated in figure 4.5a. This circuit is then repeated in the dichromatic pattern of the coincident Σ13(320) grain boundary(figure 4.5b). The closure defect of the Burgers circuit is the Burgers vector. $\vec{b_1} = \frac{a_0}{13}[2\ \bar{3}\ 0]$ (a the lattice parameter) and $\vec{b_2} = -\vec{b_1}$ are associated to the left and right steps. $\vec{b_1}$ and $\vec{b_1}$ are parallel to the grain boundary plane.

Such grain boundary steps, presenting a dislocation character and a normal displacement (the step height) are disconnections [39]. The ratio between the shear component $\vec{b}$ and the step height is the grain boundary coupling factor :

$$\beta = \frac{|\frac{a_0}{13}[2\bar{3}0]|}{-0.25nm} = -0.40 \tag{4.26}$$

This coupling factor is identical with the one previously obtained from the stick-slip motion of the grain boundary at 0 K. This result shows that the coupling factor β is a characteristic of the nucleated disconnection rather than that of the grain boundary.

Activation energy

Repeating the NEB method for different values of the displacement $0 \leq d \leq d_c$, figure 4.6 reports the energy barrier E_{act} for the grain boundary migration as a function of the displacement d.
The energy barrier E_{act} decreases with d : displacing the slabs requires a positive work given to the system. The energy barrier cancels for $d = d_c = 0.365nm$, corresponding to the spontaneous displacement of the grain boundary at T=0 K.

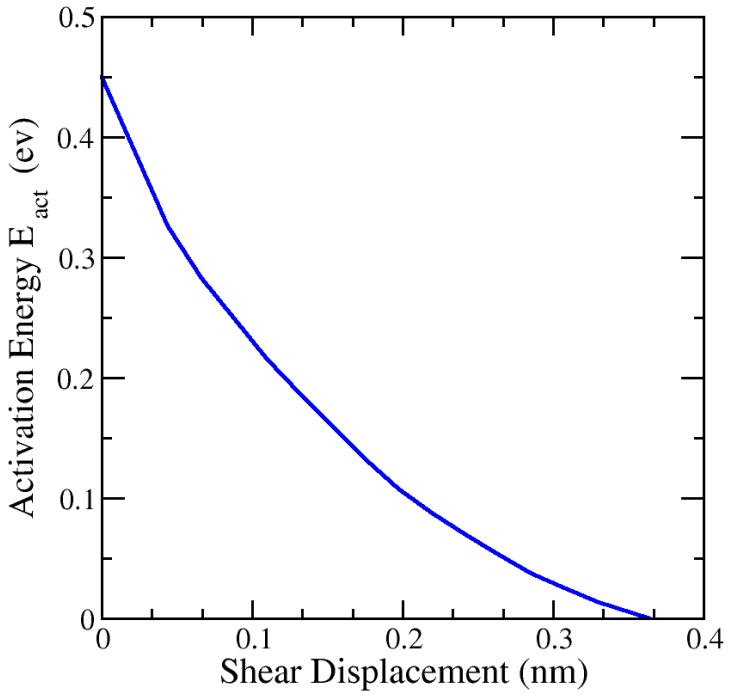

Figure 4.6: a) Variation of the energy barrier E_{act} for the grain boundary migration as a function of the shear displacement d.

4.2.3 Size effects

In the direction parallel to the shearing (y), there are elastic interactions between the disconnections due to their dislocation character. These elastic interactions does not only exist between disconnections in the cell, but also between the ones in the image cells produced by the periodic boundary conditions. These elastic interactions depend on the distances between the disconnection [8]. The size of the cell is thus highly important in the interpretation of the MEP.
In order to study the size effect contribution to the MEP, simulations were performed changing the cell y-sizes from $1L_{[2\ \bar{3}\ 0]}$ to $5L_{[2\ \bar{3}\ 0]}$. The dimension of the simulation cell normal to the grain boundary plane, (the x-direction of the cell), was kept constant all through simulations.

In the table 4.2 the different simulations cells and their corresponding sizes and atomic populations are reported. The left column of the table reports the denominations used in the following for these simulation cells.

Cell	L_x(nm)	L_y(nm)	L_Z (nm)	No. of Atoms	L_y (CSL units)	L_z (CSL units)
Y1Z1	10.3	1.3	1.4	1664	$1L_{[2\bar{3}0]}$	$1L_{[001]}$
Y2Z1	10.3	2.6	1.4	3328	$2L_{[2\bar{3}0]}$	$1L_{[001]}$
Y3Z1	10.3	3.9	1.4	4992	$3L_{[2\bar{3}0]}$	$1L_{[001]}$
Y4Z1	10.3	5.2	1.4	6656	$4L_{[2\bar{3}0]}$	$1L_{[001]}$
Y5Z1	10.3	6.5	1.4	8320	$5L_{[2\bar{3}0]}$	$1L_{[001]}$
Y2Z2	10.3	2.6	2.8	6656	$2L_{[2\bar{3}0]}$	$2L_{[001]}$
Y2Z3	10.3	2.6	4.2	9984	$2L_{[2\bar{3}0]}$	$3L_{[001]}$

Table 4.2: Simulation cells used in this study with their dimensions, atomic populations and numbers of CSL periods in the directions parallel to grain boundary plane.

Size effects on the MEP

This section reports the results of the simulations performed in cells $Y1Z1$, $Y2Z1$,...,$Y5Z1$. In order to compare the MEP resulting from simulations with different y-sizes, figure 4.7 reports the MEP per unit area $\Delta e = \frac{\Delta E}{A}$ (with A being the grain boundary area) as a function of RC for the displacement d = 0.066 nm. As expected, we checked that Δe for the initial and final

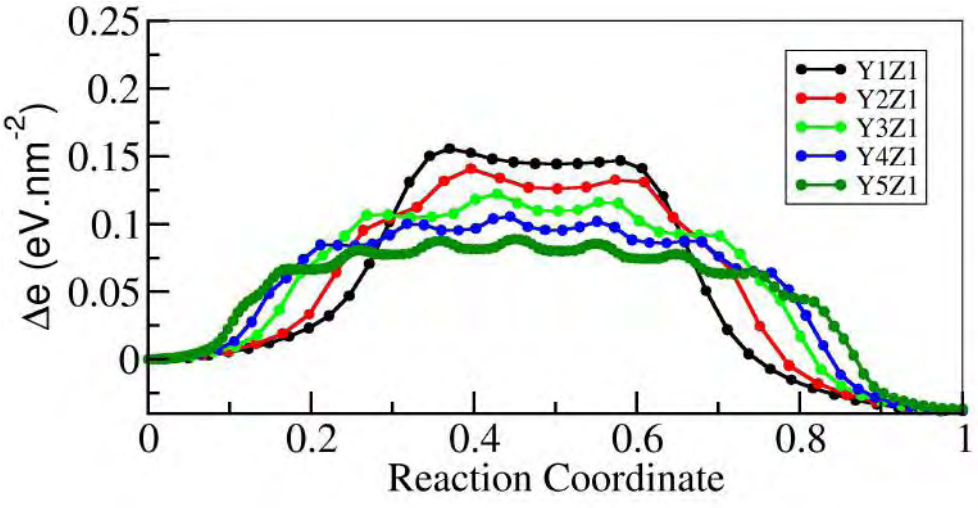

Figure 4.7: Minimum Energy Path per unit area as a function of the RC for $d = 0.066$ nm for 5 different cell y-sizes. The legend reports the simulation cells used for the calculations.

configurations (RC=0 and RC=1) do not depend on the cell y-size. However, the number of the local extrema in the MEP increases with the simulation cell y-size. In order to understand the physical meaning of these extrema, the atomic configurations corresponding to local minima of the MEP in the simulation cell $Y5Z1$ are analyzed.

Figure 4.8 reports the MEP per unit area for $d = 0.066nm$ in the Y5Z1 simulation cell. The MEP per unit area presents 7 local minima corresponding to metastable states, labelled c, d, ... i on figure 4.8 and two shoulders corresponding to unstable states labelled b and j. The states a and l are the initial and final configurations. The atomic configurations corresponding to all these states, as well as their associated reaction coordinate are reported in figure 4.8. The Y5Z1 simulation cell contains 10 structural units.

The configuration c presents two structural units that have shifted downward to the level of the final position of the grain boundary. Two grain boundary steps are hence generated from state a to c. From the state c to d, the distance between the two steps is widened by an additional structural unit shifted downward. The distance between the steps increases along the MEP : each local minimum of the MEP corresponds to an integer number of the structural units that have shifted downward. This process ends with the complete migration of the grain boundary for RC=1.

The states b and j are unstable while they present a structural unit that have been shifted. The elastic interactions between disconnections are very strong due to the very short distance between the disconnections and thus destabilize these states.

Examination of configurations along the MEP for cells Y2Z1, Y3Z1 and Y4z1 are similar, except that the number of structural units in the cell is smaller, leading to smaller number of metastable states.

The above structural analysis evidences that the grain boundary migration occurs through the formation and motion in opposite directions of two opposite disconnections per cell regardless the cell y size.

Interpreting the MEP using the elasticity theory

Below, the disconnection formation is shown to be the limiting step of the migration. To this aim, the MEP curves are interpreted within the elasticity theory.

In the following, the energy quantities denoted by ζ refer to energies per unit disconnection length.

The excess energy ζ due to the presence of two opposite parallel disconnections separated by a distance a in the simulation cell reads [127] :

$$\zeta(a) = 2\zeta_{form}(r_c) + \zeta_{inter}(a, r_c) + \zeta_{stress}(a) \tag{4.27}$$

Where $\zeta_{form}(r_c)$ is the disconnection formation energy, with r_c the core radius of the disconnection, $\zeta_{inter}(a, r_c)$ is the elastic interaction energy between the disconnections and finally $\zeta_{stress}(a)$ is the work of internal forces during the disconnection motion in absence of disconnection interactions.

The elastic interaction energy, $\zeta_{inter}(a, r_c)$, includes the interaction $\zeta^{cell}_{inter}(a, r_c)$ between the disconnections in the simulation cell, and their interaction $\zeta^{image}_{inter}(a, r_c)$ between the disconnections in the image cells due to the periodic boundary conditions in the y-direction :

$$\zeta_{inter}(a, r_c) = \zeta^{cell}_{inter}(a, r_c) + \zeta^{image}_{inter}(a, r_c) \tag{4.28}$$

The figure 4.9 shows a schematic representation of the disconnections in the simulation cell n=0 and image cells $n = \pm 1, ...$

Figure 4.8: Minimum Energy Path per unit area for the grain boundary migration for $d = 0.066$ nm in the Y5Z1 simulation cell. The z-size is $1L_{[001]}$ and atomic configurations corresponding to remarkable states (Same projection and color code as figure 4.2.

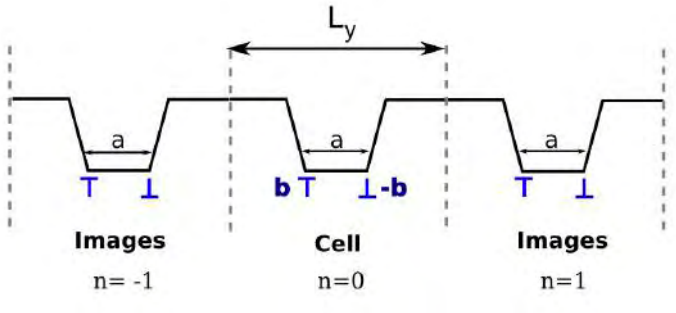

Figure 4.9: Schematic representation of two opposite disconnections of $\vec{b}$ and $-\vec{b}$ Burgers vectors by a distance a from each other in the simulation cell of width L_y. Considering periodic boundary conditions the main cell is numerated by n=0 and the image cells are represented by $n = \pm 1, ...$

According to linear elasticity theory the elastic interaction of two disconnections characterized by $\vec{b}_1$ and $\vec{b}_2$ separated by the distance a in an infinite medium with no external stress(or strain), $\zeta_{inter}^{cell}(a, r_c)$, is : [8]

$$\zeta_{inter}^{cell}(a, r_c) = \frac{\mu \vec{b}_1 \cdot \vec{b}_2}{2\pi(1-\nu)} \ln(\frac{a}{r_c}) \tag{4.29}$$

with ν and μ the Poisson's ratio and the shear modulus respectively .
To determine $\zeta_{inter}^{image}(a, r_c)$, the interaction energies of each disconnection of the simulation cell with each of the image cells, are summed together. The interaction energies between two disconnections belonging to different cells contribute for half to the energy of each of these cells.

According to the figure 4.9, $\zeta_{inter}^{image}(a, r_c)$ is hence given by :

$$\zeta_{inter}^{image}(a, r_c) = \frac{1}{2} \sum_{n=1}^{+\infty} \frac{-\mu {b_1}^2}{2\pi(1-\nu)} \ln(\frac{nL_y}{r_c}) + \frac{-\mu {b_1}^2}{2\pi(1-\nu)} \ln(\frac{nL_y}{r_c}) + \frac{\mu {b_1}^2}{2\pi(1-\nu)} \ln(\frac{nL_y + a}{r_c}) + \frac{\mu {b_1}^2}{2\pi(1-\nu)} \ln(\frac{nL_y - a}{r_c}) \tag{4.30}$$

$$+ \frac{1}{2} \sum_{n=-1}^{-\infty} \frac{-\mu {b_1}^2}{2\pi(1-\nu)} \ln \frac{|n|L_y}{r_c} + \frac{-\mu {b_1}^2}{2\pi(1-\nu)} \ln \frac{|n|L_y}{r_c} + \frac{\mu {b_1}^2}{2\pi(1-\nu)} \ln(\frac{|n|L_y + a}{r_c}) + \frac{\mu {b_1}^2}{2\pi(1-\nu)} \ln(\frac{|n|L_y - a}{r_c}) \tag{4.31}$$

The equation can be simplified as :

$$\begin{aligned}\zeta_{inter}^{image}(a,r_c) &= \frac{1}{2}\sum_{n=1}^{+\infty}\frac{\mu {b_1}^2}{2\pi(1-\nu)}\ln(\frac{(nL_y-a)(nL_y+a)}{n^2{L_y}^2}) \\ &+ \frac{1}{2}\sum_{n=-1}^{-\infty}\frac{\mu {b_1}^2}{2\pi(1-\nu)}\ln(\frac{(|n|L_y-a)(|n|L_y+a)}{|n|^2{L_y}^2}) \\ &= \sum_{n=1}^{+\infty}\frac{\mu {b_1}^2}{2\pi(1-\nu)}\ln(1-\frac{a^2}{n^2{L_y}^2})\end{aligned} \tag{4.32}$$

According to [140], the last series is equal to :

$$\zeta_{inter}^{image}(a,r_c) = \frac{\mu {b_1}^2}{2\pi(1-\nu)}(\ln(\sin(\frac{\pi a}{L_y})) - \ln(\frac{\pi a}{L_y})) \tag{4.33}$$

Summing the ζ_{inter}^{cell} and ζ_{inter}^{image} the total elastic interactions of the disconnections in the cell becomes :

$$\zeta_{inter}(a,r_c) = \frac{\mu {b_1}^2}{2\pi(1-\nu)}\ln\left[\frac{L_y}{\pi r_c}\sin(\frac{\pi a}{L_y})\right] \tag{4.34}$$

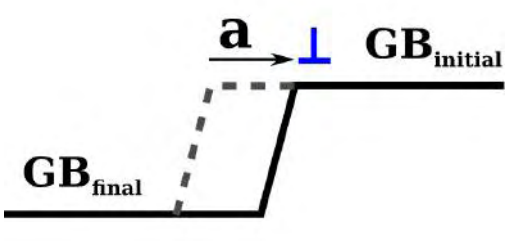

Figure 4.10: Schematic representation of the motion of a disconnection in an infinite bicrystal, from left to right by a distance a.

To determine the work of internal forces $\zeta_{stress}(a)$, the displacement by a distance a of a single disconnection in an infinite bicrystal is considered. This case is schematically represented in figure 4.10. Here $GB_{initial}$ and GB_{final} refer to the semi-infinite grain boundaries on the right and left of the disconnection. The displacement a of the disconnection to the right respectively increases and decreases the areas of the semi-infinite grain boundaries GB_{final} and $GB_{initial}$. Since the elastic displacement field induced by the disconnection is just translated with no modification, the energy change in the system due to this displacement only depends on the energies per unit area of $GB_{initial}$ and GB_{final} :

$$\zeta_{stress}(a) = (e_{final} - e_{initial})a \tag{4.35}$$

Here e_{final} and $e_{initial}$ are the energy per unit area of the system corresponding to the final and initial positions of the grain boundary. $e_{final} - e_{initial}$ can be determined from figure 4.3b.

Finally the excess energy of two disconnection separated by a distance a, $\zeta(a)$ becomes :

$$\zeta(a) = 2\zeta_{form}(r_c) + K \ln\left[\frac{L_y}{\pi r_c}\sin(\frac{\pi a}{L_y})\right] + (e_{final} - e_{initial})a \tag{4.36}$$

where $K = \frac{\mu {b_1}^2}{2\pi(1-\nu)}$.
The equation 4.36 only applies for the metastable configurations along the MEP. Since the MEP is plotted as a function of the reaction coordinates in figure 4.8 and the excess energy equation 4.36 is given as a function of the distance a between the disconnections, the distances a between the disconnections are measured for each metastable configurations along the MEP and are plotted as a function of the reaction coordinates. a linearly varies with RC : $a = L_y RC$

Figure 4.11 reports the MEP as a function of the RC (green solid curve) for the displacement $d = 0.066$ nm, calculated in the larger cell(Y5Z1) and the fit (dashed curve) of the metastable configurations curve by equation 4.36. The values of $\zeta_{form}(r_c) = -0.053\text{eV.nm}^{-1}$ and $K = 0.3059\text{eV.nm}^{-1}$ are deduced. r_c has been fixed as the lattice parameter of Copper. Though the expression $\zeta_{inter}(a)$ is established in an externally unstressed infinite medium, its application to the present case is satisfactory.
Figure 4.11b reports $\zeta_{motion}(RC)$ the subtraction of the equation 4.36 (dashed curve) from the MEP. All metastable configurations present the same value of ζ_{motion} . Between two successive metastable configurations, ζ_{motion} presents an energy barrier $\Delta\zeta_{act}^{disc}$ associated to the motion of the disconnection. From figure 4.11b averaging over the disconnections motion we found $\Delta\zeta_{act}^{disc} \approx 52 \pm 4\ meV.nm^{-1}$.
The energy barrier $\Delta\zeta_{act}^{disc}$ for the motion of the disconnections is about 11 times smaller than the energy barrier for grain boundary migration $\Delta\zeta_{act}^{GB}(5L_{[2\bar{3}0]}) = 578\ meV.nm^{-1}$ where $\Delta\zeta_{act}^{GB}$ is defined in figure 4.11a.
This result agrees with the simulation results from Khater et al. [127] : the stress required to induce the migration of a grain boundary containing pre-existing disconnections is smaller than the stress required to induce the migration of a perfect grain boundary.
From the above analysis, the migration rate of a perfect grain boundary is essentially controlled by the formation of a critical nucleus composed of two disconnections.

The energy barrier per unit disconnection length, $\Delta\zeta_{act}^{GB}(\infty)$ to form such a critical nucleus can be estimated from Eq.4.36 :
In the limit $L_y \to \infty$:

$$\lim_{L_y \to +\infty} \zeta(a) = 2\zeta_{form}(r_c) + K \ln(\frac{a}{r_c}) + (e_{final} - e_{initial})a \tag{4.37}$$

which is stationary for $a_c = -\frac{K}{e_{final} - e_{initial}}$.
So the grain boundary migration mechanism presents a critical nucleus only if $a_c > 0$ i.e. $e_{final} - e_{initial} < 0$ or from figure 4.3, $d > 0.05nm$. For d = 0.066 nm, $\Delta\zeta_{act}^{GB}(\infty) = 748 meV.nm^{-1}$ is found.

This result can be compared to the energy barriers $\Delta\zeta_{act}^{GB}(L_y)$ measured for different cell y-sizes. Figure 4.12 reports the variation of the energy barriers $\Delta\zeta_{act}^{GB}(L_y)$ for different cell y-sizes as a function of the displacement d. For all cell sizes, $\Delta\zeta_{act}^{GB}(L_y)$ decreases with displacement d as already was discussed in figure 4.6. For a given applied displacement d, $\Delta\zeta_{act}^{GB}(L_y)$ increases with cell y-size. For $d < 0.05nm$, $\Delta\zeta_{act}^{GB}(L_y)$ does not seem to converge with L_y as expected from the above analysis. For intermediate displacement values $0.05nm < d \lesssim 0.1 - 0.15nm$, the convergence of $\Delta\zeta_{act}^{GB}(L_y)$ with L_y is not complete as evidenced by the comparison between the energy barrier in the biggest cell $\Delta\zeta_{act}^{GB}(5L_{[2\bar{3}0]}) = 578\ meV.nm^{-1}$ and the theoretical estimation

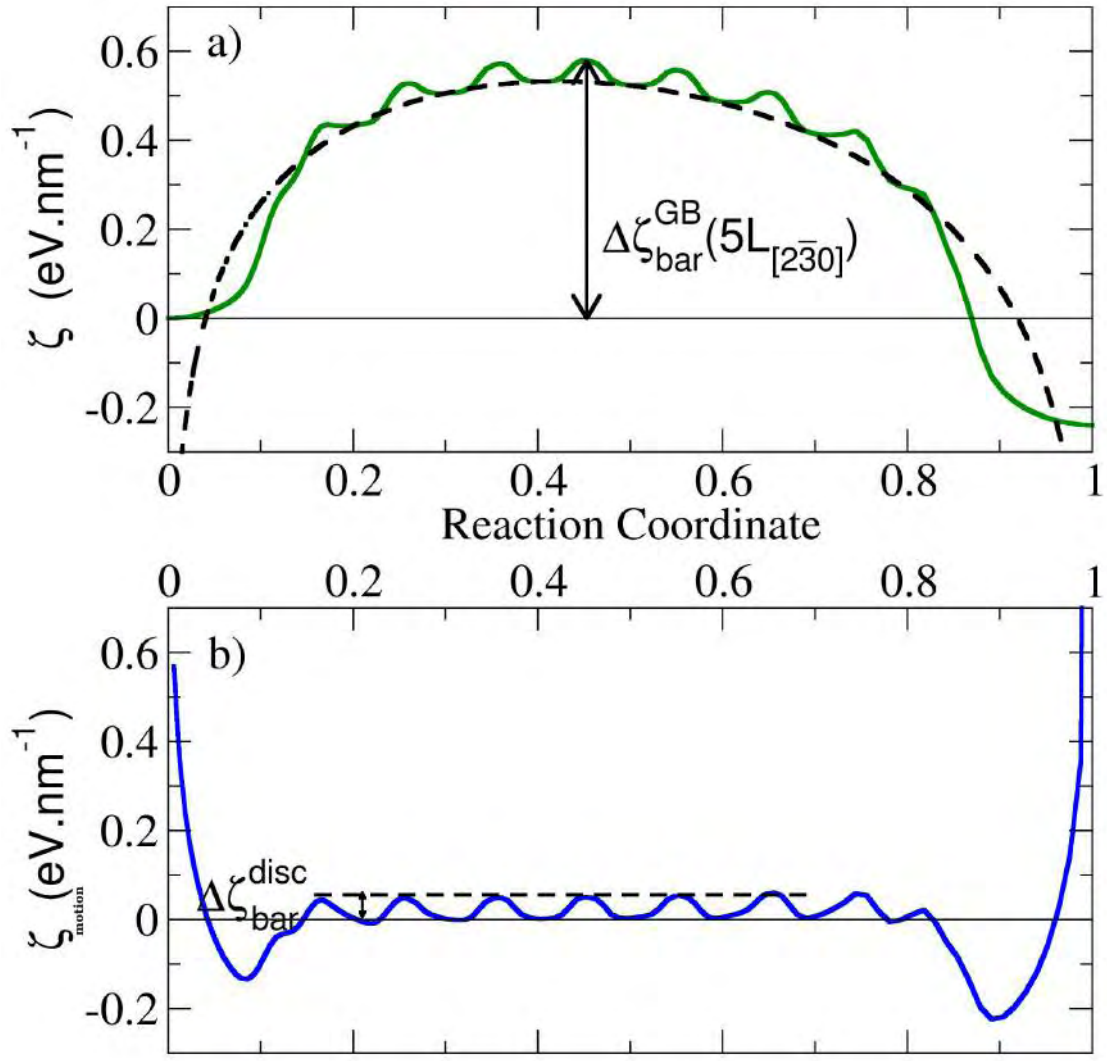

Figure 4.11: a) Minimum Energy Path (green solid line) per unit disconnection length as a function of the RC for $d = 0.066$ nm (the cell y- and z-size are 6.5 nm and 1.4 nm) and the energy variation curve (dashed curve) as fitted from equation.4.36. b) $\zeta_{motion}(RC)$:the subtraction of the energy variation curve from the MEP as a function of the RC.

$\Delta\zeta_{act}^{GB}(\infty) = 748meV.nm^{-1}$ for d = 0.066 nm. For $d > 0.1 - 0.15nm$, $\Delta\zeta_{act}^{GB}(L_y)$ seems to converge with L_y. Finally, the dependence of the energy barrier $\Delta\zeta_{act}^{disco}$ for the disconnection motion has been found to weakly vary with the shear displacement d. Regarding the incertitude on the measure of $\Delta\zeta_{act}^{disco}$, the quantitative characterization of this dependence is not possible, so that in first approximation, this energy barrier can be considered as invariant with the shear displacement.

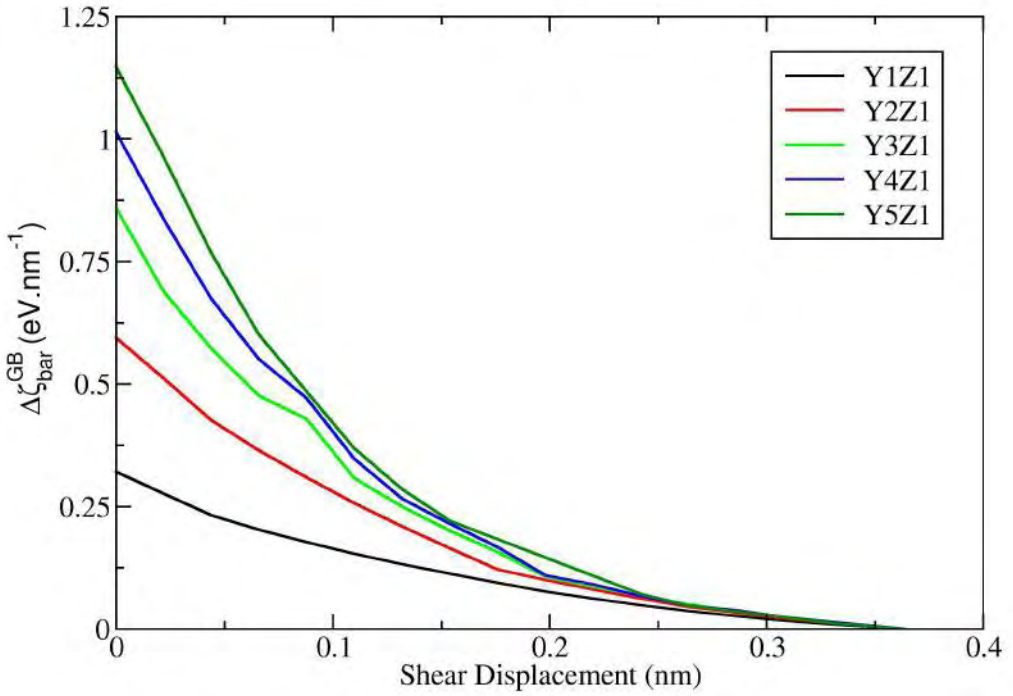

Figure 4.12: Variation of the energy barrier per unit disconnection length $\Delta\zeta^{GB}_{act}$ as a function of displacement d for different simulation cell sizes.

Effect of cell z-size on grain boundary migration

In the former analysis of the grain boundary migration, the cell z-size was small imposing to the atomic configuration a $L_{[001]}$ periodicity along the z direction. An energy barrier for the grain boundary migration per unit disconnection length was derived suggesting that the energy barrier for the grain boundary migration linearly increases with the cell z-size. Since this latter claim is unphysical, we have repeated our NEB calculation varying the cell z-size. The considered cells are Y2Z1, Y2Z2 and Y2Z3 which corresponding dimensions are reported in Table 4.2.

Figure 4.13a reports the MEP for the grain boundary migration for a displacement $d = 0.066\ nm$ for the Y2Z3 simulation cell. The MEP curve presents again a metastable state corresponding to a configuration displaying two opposite disconnections. However the analysis of the atomic configurations along the MEP shows that the nucleation and motion of the disconnections are not invariant by translation (multiple of $L_{[001]}$) along the z-direction. Figure 4.13b reports the projection in the xy-plane of the configuration of 16th replica pointed out by an arrow in figure 4.13a : a structural unit is at about half the way between its initial and final positions. Figure 4.13c reports the same configuration projected in the xz-plane where only atoms between the two dashed lines of figure 4.13b are displayed. The configuration reported in figure 4.13c evidences two disconnection kinks in the grain boundary, along the z-direction. Nevertheless no metastable state in the MEP associated to a configuration presenting some disconnection kinks have been identified during our investigation.
In addition, figure 4.14 reports the variation of the energy barrier $\Delta\zeta^{y}_{act}$ per L_y length unit as a function of the displacement d for different cell z-sizes. For a given displacement d, the gain boundary migration energy barrier $\Delta\zeta^{y}_{act}$ linearly increases with the cell z-size and thus does not

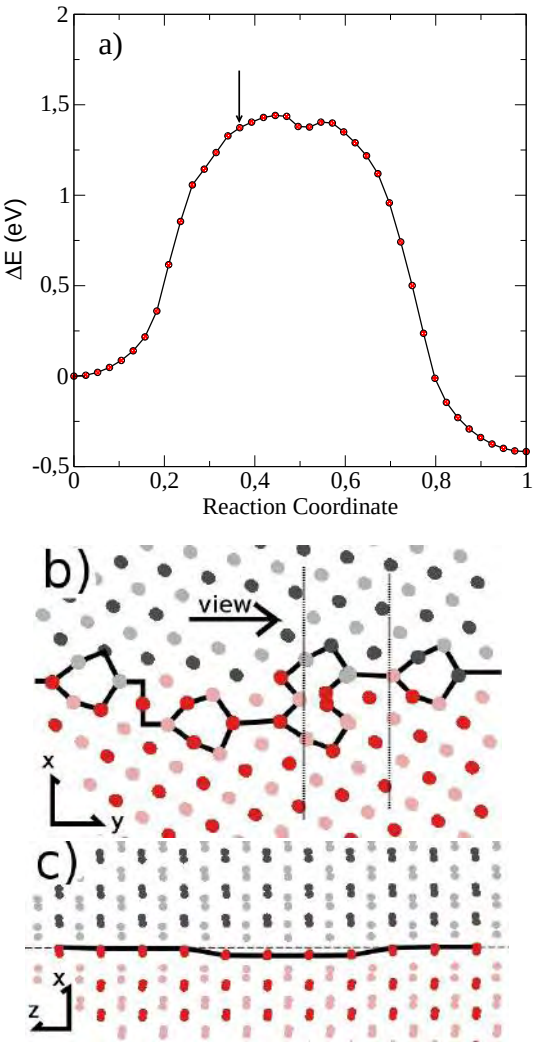

Figure 4.13: a) The MEP for a displacement $d = 0.066$ nm in the Y2Z3 simulation cell. b) and c) Configurations of the $\Sigma 13(320)$ grain boundary projected in the (x,y) and (z,x) planes. c) Only atoms between the two dashed lines of b) are displayed. Black lines are guide to the eyes.

converge with the cell z-size for the investigated sizes.
While the existence of disconnections kinks has been structurally evidenced, the investigated cell z-sizes (constrained by the computing limitations) seems to be too small to weaken the elastic interactions between disconnections kinks and to evidence their energetic signature.

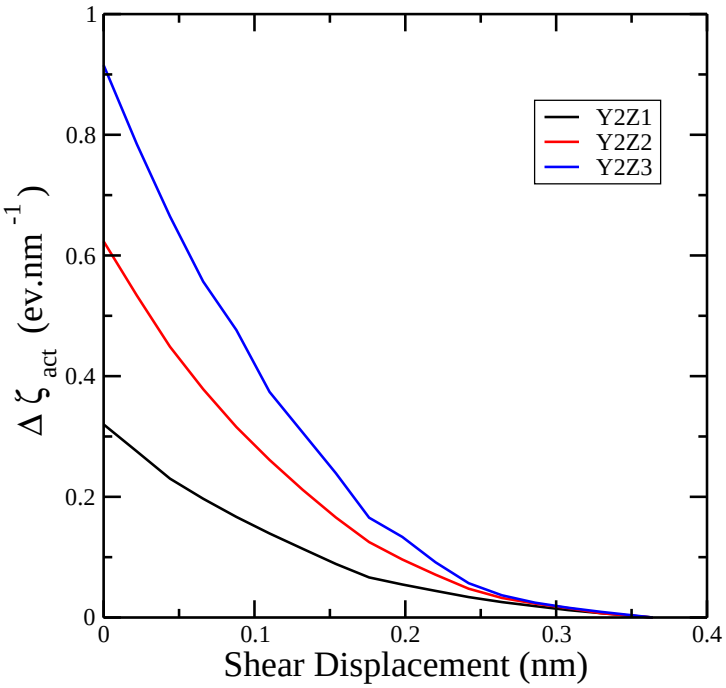

Figure 4.14: Variation of the grain boundary migration energy barrier per y-size unit $\Delta\zeta_{act}$ as a function of the displacement for three z-sizes of the cell.

4.3 Conclusion

In this chapter the elementary mechanisms of the shear-coupled grain boundary migration at 0K, in a Copper bicrystal containing a symmetrical Σ13(320) grain boundary have been evidenced. Through atomic visualization of the evolution of the system along the MEP curve corresponding to the migration, it was shown that complementary to the common stick-slip grain boundary motion, the grain boundary migration occurs through the nucleation and motion of grain boundary steps. This is in agreement with recent simulations [102] and is supported by the experimental results evidencing the formation and motion of grain boundary macro-steps presented in previous chapters.
These steps were identified as disconnections due to their dual step/dislocation character. It was seen that these disconnections contain the same coupling factor that it is found in the migration of grain boundary in stick-slip motion. This suggests that the coupling factor is a property of the disconnection rather than the grain boundary itself.
Moreover, the energy barrier for the nucleation of the disconnections and their propagation was determined. It was shown that the energy barrier for nucleation of the disconnection is nearly 11 times larger than the energy barrier for their motion. So it can be deduced that the limiting step in grain boundary migration coupled with shear deformation is the formation of a nucleus of two opposite disconnections. Although we succeeded in structurally evidencing some disconnection kinks in the z-direction, we failed to identify a metastable state, presenting such configuration.

However in a real systems with non perfect grain boundaries (containing vacancies, impurities,...) or in polycrystalline materials due to existence of triple junctions, nucleation of disconnections in grain boundaries would be easier.

5 CONCLUSION AND PERSPECTIVES

In the present work, we have investigated both experimentally and by atomistic simulations, the elementary processes underlying the shear-coupled grain boundary migration, as one of the grain boundary-mediated plasticity mechanisms.
Experimental observations consisted of high resolution transmission electron microscopy (HRTEM) observations and in situ TEM straining of Al bi-crystal and ultra-fine grain Al. Only a bi-crystal was considered for atomistic calculations.
The principal findings of this work can be summarized as follows :

- The motion of disconnections along the grain boundary is the process that carries out the grain boundary migration, in response to strain. In-situ TEM straining experiments shows that the migration occurs by collective motion of disconnections that coalesce in macro-steps of various heights.
- Measurement of the strains produced by the disconnections can be done by TEM image analysis. They reveal that several possible coupling modes operate in a given grain boundary. In addition to the ideal shear coupled grain boundary migration, the motion of disconnections can also induce a deformation perpendicular to the grain boundary plane.
- HRTEM and in-situ TEM straining revealed that disconnections can either exist along the boundary prior to straining, or they can be produced due to the interactions of the lattice dislocations with the grain boundary.
- The Burgers vectors of the disconnections resulting from the decomposition of the lattice dislocations in the boundary can have glide and/or climb components. The motion of these disconnections would thus carry a deformation respectively parallel and/or perpendicular to the boundary plane, including a possible shear along the rotation axis of the boundary.
- Atomistic calculations carried out using molecular dynamics (EAM potentials) at 0 K were used to determine the energy path of the grain boundary migration. This migration occurs through the nucleation and propagation of disconnections that constitute the elementary mechanisms of the coupling at atomic scale.
- The energy barrier for the nucleation of the disconnections and their propagation was determined. It was shown that the energy barrier for the nucleation of the disconnections is 11 times larger than the energy barrier for their motion. So in the absence of preexisting defects, the controlling mechanisms in the shear-coupled grain boundary migration is the formation of a nucleus of two opposite disconnections.

– Finally, both experiment and simulations suggest that coupling factor is a property of the disconnections rather than the grain boundary itself. This is a possible explanation why several coupling mode may exist for a given grain boundary.

Perspectives

The following perspectives can be considered as complementary to this study :

– The coupling mechanism in other coincidence grain boundaries should be investigated. Two possible directions can be followed. 1) Experimentally, the study of the coupling in high angle grain boundaries in which the atomic structure is less variant than in the Σ41 has indeed to be pursued.
2) The investigation of the coupling in asymmetrical grain boundaries would be interesting. Recent experimental and numerical results reveal different coupling factors [77, 141, 142] for an asymmetrical grain boundary, suggesting mechanisms involving different disconnections. Evidencing and characterizing these disconnections can be considered both experimentally and numerically.

– In addition to the coincidence grain boundaries, the coupling mechanisms should also be investigated experimentally for general grain boundaries where the identification and characterization of disconnections is expected to more difficult since no DSC lattice can be defined.

– For a more quantitative comparison with the experimental results, the atomistic simulations should be extended to Aluminium. Indeed the stacking fault energy in Al is higher compared to the one of Cu. Hence although the elementary mechanisms of the shear-coupled grain boundary migration are expected to be qualitatively identical in Al and Cu, quantitatively, strong differences may be expected, especially the ratio between the energies for nucleation and motion of the disconnections.

– In order to investigate several possible coupling modes in a grain boundary, we propose to analyze the energy path between two configurations obtained from the shearing of the grain boundary at high temperature. Indeed, alternative coupling modes to the one observed at 0 K, maybe thermally activated at high temperatures. Such a study would enable an energetic comparison of several coupling modes and consequently a comparison of the occurrence probabilities of these modes (using the Arrhenius law).

ANNEXE

APPENDIX

A.1 Presentation of the crystallographic features of the samples

By indexing the diffraction patterns obtained by TEM, the orientations of the grains in the samples can be identified. Here this was done by an in-house developed program that gives the Euler angles of the grains according to the diffraction patterns. The Euler angles (Φ_1, Φ, Φ_2) of individual grains correspond to the rotation of the crystallographic axes of the crystal, relative to the reference coordinates of the sample. Having the Euler angles, the orientations of the grains are presented in a stereographic projection.

The stereographic projection is a method for presentation of crystal directions and planes. The

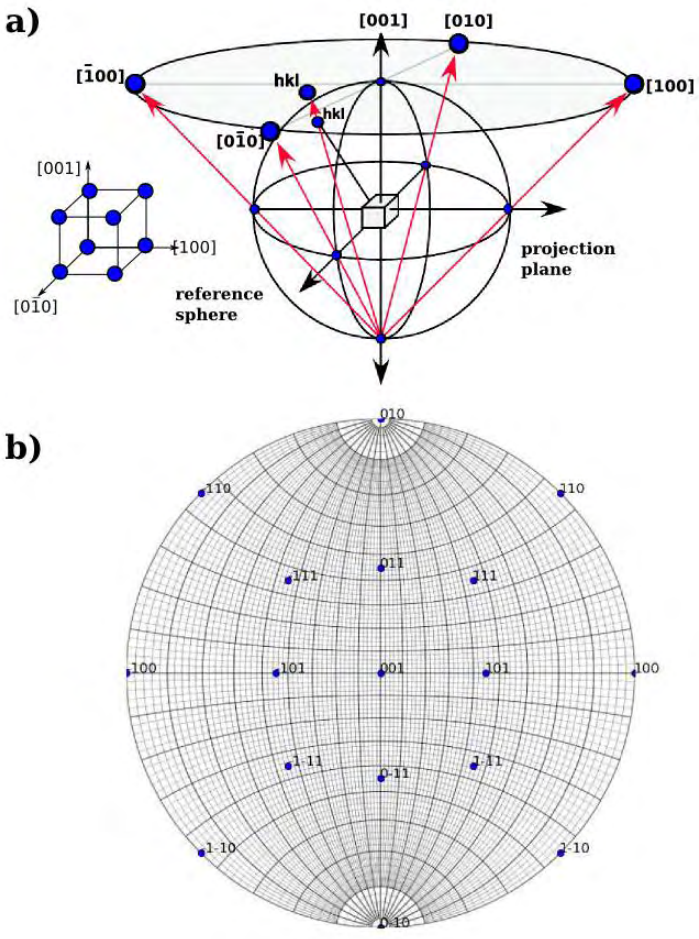

Figure A.1: a) Stereographic projection and (b) a Wulff net superimposed with the representative crystallographic directions for a primitive cubic crystal.

crystal is imagined in the center of a reference sphere and the planes and directions are projected on its equatorial plane (figure A.1a). In stereographic projections the crystal planes and directions are shown as lines and points respectively.
A Wulff net is a stereographic projection of latitude and longitude lines as in figureA.1b in which the principal directions of the cubic lattice are superimposed. The grid of latitude and longitude lines in the Wulff net serve to angular measurements between directions.

A.2 Determining a grain boundary or slip plane

A plane in the crystal is characterized by the direction of its trace and also according to the variation of its apparent width as a function of the the inclination of the plane in different tilt angles of the sample in the microscope. A trace in a TEM image is the intersection of a plane (grain boundary plane or slip plane) with two surfaces of the thin foil.
Figure A.2a represents a 3-D scheme of a bicrystal sample cut in a thin foil with parallel surfaces,

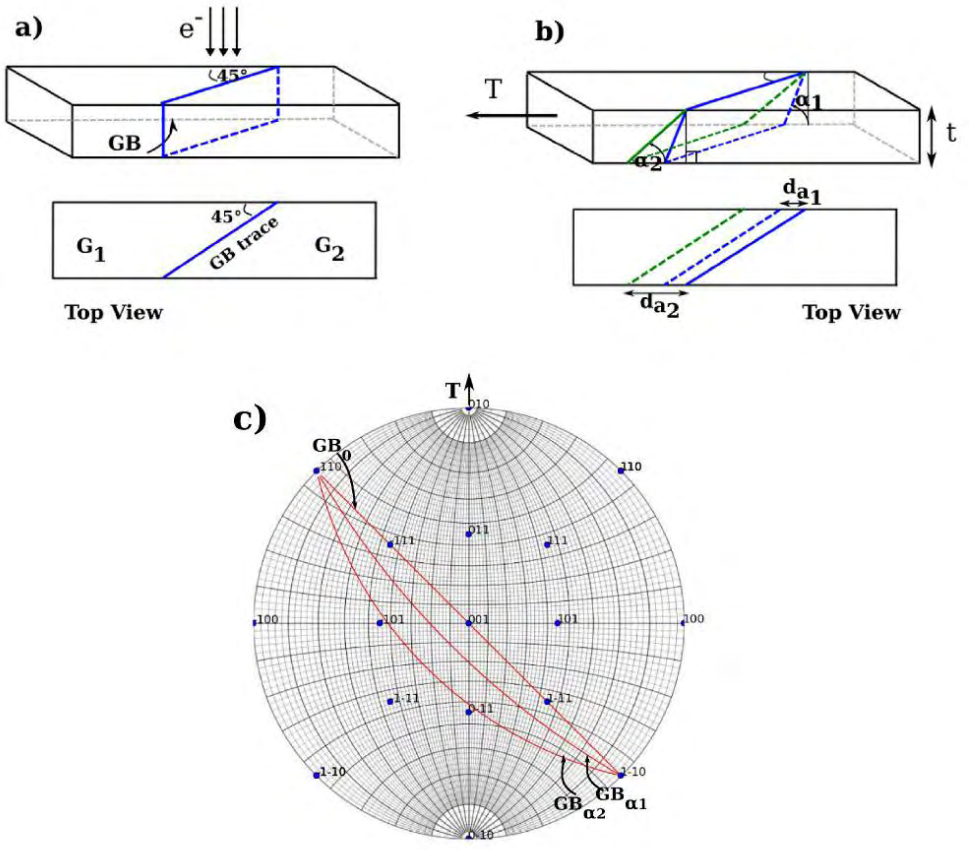

Figure A.2: a) Schematic representation of a bicrystal containing a grain boundary positioned edge-on in a thin foil with parallel surfaces. The trace of the grain boundary is indicated in the top view of the sample. b) The grain boundary represented inclined by α_1 and α_2 angle with respect to normal to the sample. d_{a1} and d_{a2} are the apparent widthsof the grain boundary plane corresponding to each inclination angle. t here is the thickness of the foil.

containing a grain boundary separating two grains G1 and G2. The grain boundary is edge-on and is positioned with 45° angle relative to the tilt axis (T). The filled blue line in the top view of the sample is the trace of the grain boundary plane. In the stereographic projection of the figure A.2c the trace is shown by GB_0.
Figure A.2b shows the grain boundary which for two tilt angles of the sample is inclined respectively by α_1 and α_2 relative to the normal direction to the foil. The apparent widths of the grain boundary plane corresponding to α_1 and α_2 are shown by d_{a1} and d_{a1}. The trace of the grain boundary plane for the tilt angles are marked by $GB_{\alpha 1}$ and $GB_{\alpha 1}$ in the stereographic projection (Figure A.2c). According to the figure A.2a following relationship holds :

$$\frac{\tan\alpha_1}{\tan\alpha_2} = \frac{d_{a2}}{d_{a1}} \tag{A.1}$$

By comparing the apparent widths of the grain boundary plane in the TEM micrographs taken in different sample tilts, the inclination of the grain boundary plane with respect to the normal direction to the foil can be estimated.

A.2.1 Thin foils with non-parallel faces

In preparation of thin films for TEM observations, generally it is very difficult to have a uniform thickness over the entire length of the sample and thus the thin observable area of the specimen usually makes a wedge shape at the edge. Consequently the grain boundary plane being cut with two non-parallel surfaces will have two non-parallel traces. This case is represented in figure A.3a where β is the angle of the wedge. Figure A.3b shows the top view projection of the planes in the observation plane where d_a is the maximum apparent width of the grain boundary plane. FigureA.3c shows the front view of the foil. The α and β angles correspond to the inclination of the grain boundary plane and the wedge angle. The thickness of the foil is marked by t and l is the distance of the grain boundary from the edge of the foil. By following equation, α and β are related to the apparent width of the grain boundary plane :

$$\tan\alpha = \frac{m}{d_a} \tag{A.2}$$

$$\tan\beta = \frac{m}{l - d_a} = \frac{t}{l} \tag{A.3}$$

$$d_a \tan\alpha = m = (l - d_a)\tan\beta \tag{A.4}$$

$$d_a \tan\alpha + d_a \tan\beta = l \tan\beta \tag{A.5}$$

$$d_a = \frac{t}{\tan\alpha + \tan\beta} \tag{A.6}$$

For determining the grain boundary plane or the slip plane of a dislocation, the apparent widths are measured for different tilt angles of the specimen. Considering the trace of the plane on the stereographic projection and by comparing the change of the apparent widths with inclination angle of planes, the orientation of the planes can be estimated.

The wedge angle β is estimated according to the distance between the thickness fringes that are generally visible for non-uniform specimen thicknesses in bright field micrographs. The thickness fringes are produced from complementary oscillations of the incident and diffracted

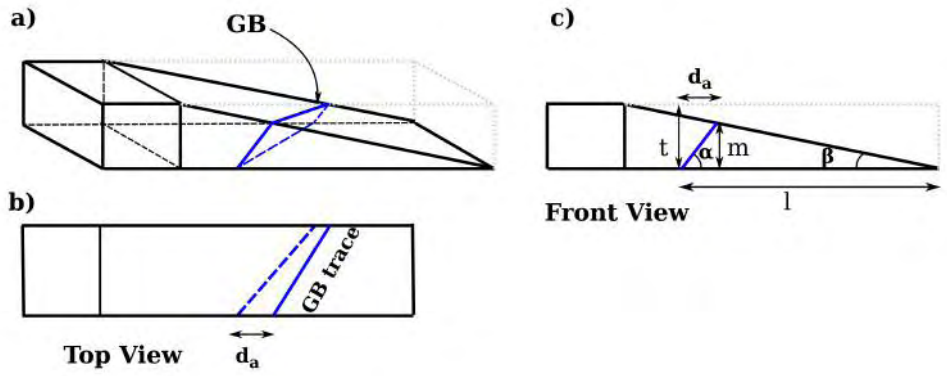

Figure A.3: a) Schema of a bicrystal with a grain boundary inclined by angle α in a thin foil with wedge shape edge. β is the wedge angle. b) The projection of the grain boundary plane in the top view of the foil where d_a is the maximum apparent width of the grain boundary plane. c) The front view of the foil with t as the maximum thickness of the foil, l is the distance of the grain boundary from the edge of the foil and m is the thickness of the foil at l.

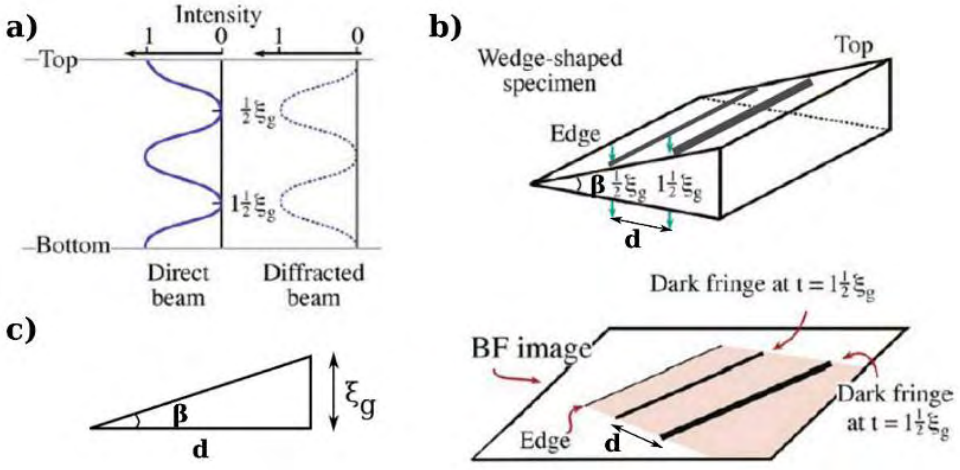

Figure A.4: a) Complementary oscillations of the incident (I_0) and diffracted (I_g) beams along the thickness of the foil. b) Thickness fringes on the bright field image of the thin foil with d being the spacing between the frineges and ξ_g extinction distance of the diffracted beam I_g. c) Geometric relation between the thickness fringes spacings (d), the extinction distance (ξ_g) and the wedge angle β (after [143]).

beams along the thickness of the foil. The normalized intensity of the Bragg diffracted beam I_g is given by [143]

$$I_g = (\frac{\pi t}{\xi_g})^2 \frac{\sin^2(\pi t S_{eff})}{(\pi t S_{eff})^2} = 1 - I_0 \tag{A.7}$$

where t is the specimen thickness, S_{eff} the effective extinction error and ξ_g is the extinction distance which is a characteristic length for the reflection $\vec{g}$.

At Bragg condition for the reflection $\vec{g}$, the intensity I_0 of the incident beam starts equal to unity, gradually decaying until zero whereas the intensity I_g of the diffracted beam gradually increases from zero until unity and the process repeats itself periodically. Figure A.4a shows this oscillation as a function of the extinction distance of the diffracted beam which is the periodicity of this oscillation. According to figure A.4b-c and having the extinction distance ξ_g and the distance d between the fringes on the surface of the foil, the wedge angle β can be estimated by :

$$\tan \beta = \frac{\xi_g}{d} \tag{A.8}$$

B :RÉSUMÉ

B.1 Introduction

Dans les métaux à gros-grains la déformation plastique s'effectue par nucléation, multiplications et interaction des dislocations entre elles ou avec la microstructure. La capacité d'un matériau à supporter une contrainte critique avant la déformation plastique (la limite d'élasticité) dépend alors de la difficulté à former et déplacer ces dislocations. Le raffinement des grains est l'une des stratégies de renforcement des matériaux car les joints de grains sont considérés comme des obstacles au mouvement des dislocations. En diminuant la taille des grains et donc en augmentant la densité des joints au sein des matériaux polycristallins, on peut augmenter leur limite d'élasticité. Cette conclusion empirique est celle à laquelle Hall et Petch [1, 2] étaient parvenus dans les années 50s. La relation de Hall-Petch s'écrit comme :

$$\sigma_y = \sigma_0 + kd^{-1/2} \tag{B.1}$$

avec σ_0 le minimum contrainte de frottement pour le mouvement des dislocations dans un grain et k le coefficient de Hall-Petch dépendant du matériaux, du taux de déformation, du type de joints de grain etc.
La loi de Hall-Petch, s'explique physiquement à partir d'empilements de dislocations contre les joints. Elle prévoie convenablement l'amélioration des propriétés mécaniques des polycristaux de petite taille de grains ($100nm < d <\sim 1\mu$ m) par rapport aux mêmes matériaux à gros grains. Pourtant en diminuant la taille des grains jusqu'à l'échelle du nanomètre, ($d <\sim$ 100nm on parle alors de matériaux nanocristallins - NC), la loi de Hall-Petch cesse d'être valide. Dans certains cas une diminution de la limite d'élasticité des matériaux peut suivre le raffinement des grains ($d <\sim$ 10nm). Dans ces matériaux le calcul des contraintes d'empilement n'est plus valable car la distance entre dislocations deviendrait trop faible. De plus, cette théorie ne parvient pas à expliquer l'inversement de la loi de Hall-Petch. En effet, les dislocations intragranulaires sont habituellement peu présentes dans les matériaux NC, ce qui peut impliquer un rôle plus important des joints des grains dans la plasticité de ces matériaux. Différents mécanismes de déformations aux joints de grains sont proposés dans les matériaux NCs : glissement des joints, fluage par diffusion, rotation des grains et migration des joints couplée à un cisaillement. Ce dernier mécanisme a attiré beaucoup d'attention car il est mis en évidence par différentes méthodes expérimentales (essais d'indentation, de compression ou de tension). Ce mécanisme consiste

à la migration de joints de grains assistée par la contrainte et produisant un cisaillement permanent. L'étude des processus élémentaires qui sous-tendent ce mécanisme constitue l'objectif principal de cette thèse dont le manuscrit est structuré comme suivant :

- Le premier chapitre est une introduction générale des concepts fondamentaux utilisés pendent cette étude. La suite du chapitre est également consacrée à un résumé bibliographique sur les mécanismes de déformations à base de joints de grains, en insistant sur le mécanisme de couplage.
- Dans le deuxième chapitre, les résultats de la caractérisation expérimentale du couplage dans des bicristaux d'Al déformés en traction in-situ en microscopie électronique en transmission (MET) sont présentés.
- Dans le 3ème chapitre, les défauts structuraux des joints de grains sont étudiés par MET en haute résolution (HRTEM). Les interactions entre dislocations de réseau et dislocation de joints qui donnent lieu aux défauts supplémentaires dans la structure du joint sont aussi abordées.
- Le dernier chapitre est consacré à la simulation atomistique du couplage.

Dans la première section de ce résumé, les défauts structuraux des joint des grains, vecteurs de la déformations dans les mécanismes de base des joints des grains sont présentés :

B.1.1 Défauts structuraux des joints de grains

Les principaux défauts structuraux des joints de grains sont appelés "disconnections" [39]. Ils sont analogues aux dislocations du réseau. En effet, comme les dislocations du réseau qui sont des perturbations d'un cristal parfait et préservent la symétrie de translation du cristal (leur vecteur de Burgers est une translation du réseau), les disconnections sont des perturbations de la structure des joints de grains qui préservent l'invariance de translations dans le joint, i.e. la coïncidence.

Le réseau de sites de coïncidence (CSL) est un réseau périodique des positions atomiques coïncidant dans deux grains voisins qui est défini pour des angles de désorientations et des plans de joints particuliers. Dans le cas de petits écarts par rapport aux angles correspondant à la coïncidence, les disconnections sont insérées dans la structure du joint pour accommoder ces déviations. Dans ce cas-là les disconnections sont aussi appelées dislocations intrinsèques secondaires des joints de grain et leurs vecteurs de Burgers appartiennent à un réseaux qui comprend toutes les translations possibles entre les positions atomiques des deux cristaux. Ce réseau est appelé réseau DSC (Displacement Shift Complete) et correspond au réseau formé par toutes les translations possibles $\vec{t} = \vec{t_1} - \vec{t_2}$, où $\vec{t}_{1,2}$ sont les vecteurs de réseau de grains G_1 et G_2 respectivement.
En revanche, les disconnections isolées, appelée aussi dislocations extrinsèques, peuvent provenir de la réaction de décomposition d'une dislocation du réseau dans le joint de grain.
Généralement une marche dans le joint de grain est aussi associé à une disconnection. Ceci est dû au fait que le vecteur de Burgers n'est pas toujours contenu dans le plan de joint. En effet, si une disconnection de vecteur de Burgers $\vec{b}$ comme indiqué sur la figure B.1, est introduite dans le plan de $(2\bar{3}0)$, l'ancienne position de coïncidence O (l'origine du vecteur de translation $\vec{t_1}$ et $\vec{t_2}$) sera déplacée vers la nouvelle position N. La hauteur des marches h, qui peut être définie dans chaque grain est alors :

$$h_{1,2} = \vec{t}_{1,2} \cdot \vec{n} \tag{B.2}$$

avec $\vec{n}$ la normale au plan de joint de grain. La hauteur totale de la marche du joint de grain

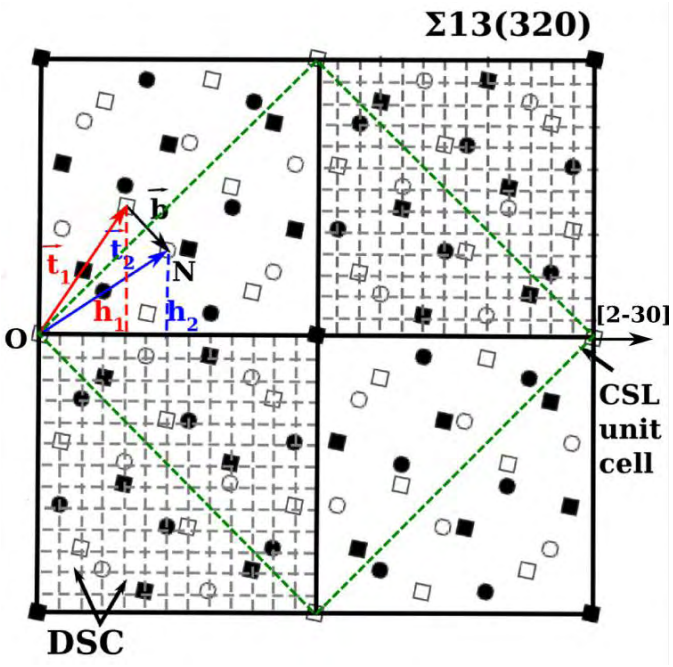

Figure B.1: Les réseaux de sites de coincidence (CSL) et DSC dans le cas d'un joint de grain Σ13(320). *Les positions des réseaux pour les grains G1 et G2 sont représentées par* □ *et* ◯ *respectivement et des formes pleines et vides représentent différentes profondeurs le long de l'axe de rotation* ([001]). $\vec{t_1}$ *et* $\vec{t_2}$ *sont des vecteurs de translation correspondant à chaque grain et* h_1 *et* h_2 *sont des hauteurs de marche associées.* $\vec{b} = \vec{t_2} - \vec{t_1}$ *est le vecteur de Burgers de la dislocation intrinsèque secondaire de la structure intergranulaire correspondant.*

sera la moyenne des hauteurs de marche mesurées dans chaque grain :

$$h = \frac{h_1 + h_2}{2} \tag{B.3}$$

A partir des relations entre les vecteurs de Burgers et les hauteurs des marches dans chaque grain, différents cas de disconnections peuvent être définis :

- Disconnection sans marche $\vec{b} \neq 0$, $h = 0$
- Marche pure $h \neq 0$, $\vec{b} = \vec{0}$
- Disconnections générales $\vec{b} \neq 0$, $h \neq 0$

B.1.2 Migration de joint de grains couplée au cisaillement

On considère traditionnellement que la croissance des grains est due aux forces de capillarité afin de réduire la surface des joints ou à la différence d'énergie élastique entre les grains, comme on l'observe au cours de la recristallisation. Les premières observations de la migration d'un joint près de Σ 5 à haute température par Babcock et Baluffi [62] avaient montré des mouvements erratiques des joints qui n'étaitent pas corrélées au mouvement des dislocations. Des expériences plus récentes sur des petit grains isolés arrondis, ont révélé que les joints de grains migrent (et s'annihilent) en absence de contrainte, sous l'effet des forces de capillarité à température élevée [63, 64]. Ce type de mouvement est attribué à un mécanisme de réarrangement atomique (shuffling) pur qui se produit par la réorganisation collective et stochastiques d'atomes du joint de

grain [65].
La migration de joints de grain sous contrainte, bien connue dans les joints de grains à faible angle de désorientations [66, 67] ou dans les macles [68], n'a par contre jamais été reconnue comme un mécanisme de plasticité dans les matériaux NC avant les récentes observations expérimentales [28] et les simulations atomistiques [69]. Depuis, la croissance des grains assistée par contrainte a été mis en évidence expérimentalement ou par des simulations de dynamique moléculaire dans différents matériaux et sous diverses sollicitations mécaniques.
Les simulations de dynamique moléculaire [23, 78] et les méthodes expérimentales, soit dans les bicristaux (voir par exemple [76]) soit dans les polycristaux [75] ont montré que le déplacement des joints de grains dans la direction normale au plan sur une distance m est habituellement accompagné par une translation relative d des grains parallèlement au plan de joint de grain. Cette migration des joints grain couplée au cisaillement est caractérisé par un facteur de couplage $\beta = \frac{d}{m}$, qui représente la déformation de cisaillement induite (figure B.2) [23, 79].

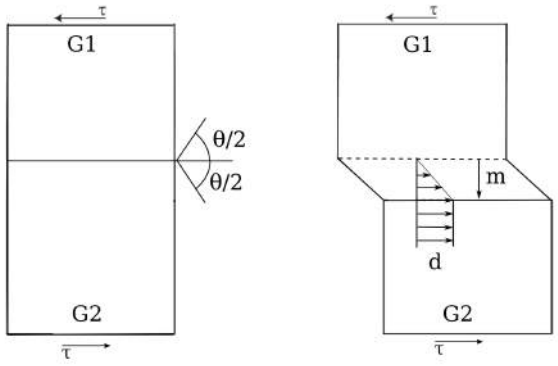

Figure B.2: Le joint entre deux grains G1 et G2 désorientés de θ est cisaillé par τ. La contrainte de cisaillement provoque le déplacement du joint de grain dans la direction perpendiculaire à son plan d'une distance m. La zone balayée par le joint est soumise à une déformation qui augmente de façon linéaire jusqu'à la prochaine position du joint. Le facteur de couplage β est le rapport entre la déformation et la distance de migration.

De nombreuses théories ont été proposées pour expliquer le mécanisme de couplage et en particulier la relation entre le facteur de couplage et la géométrie des joints de grains.

Modèle de Read et Shockley

La migration des joints de grains de flexions couplée au cisaillement a été d'abord observée expérimentalement dans les joints à faibles angles de désorientations (LAGB) dans Zn [66, 67]. Théoriquement, les LAGBs peuvent se déplacer entièrement par le mouvement simultané de leurs dislocations intrinsèques primaires [83]. Soumis à une contrainte de cisaillement uniforme τ, le travail d'une dislocation de vecteur de Burgers $\vec{b}$ déplacée de $\vec{\delta r}$ est donné par :

$$\delta W = \vec{F} \cdot \vec{\delta r} = [\tau \cdot (\vec{l} \times \vec{\delta r}]) \cdot \vec{b} \tag{B.4}$$

où $\vec{l}$ est le vecteur de ligne de la dislocation et $\vec{F}$ représente les forces Peach-Koehler. L'application d'une contrainte de cisaillement τ sur un LAGB symétrique de flexion, représentée schématiquement sur la figure B.3a, engendrera donc une force (par unité de longueur) de $\vec{F_g} = \tau\vec{b}$ exercée

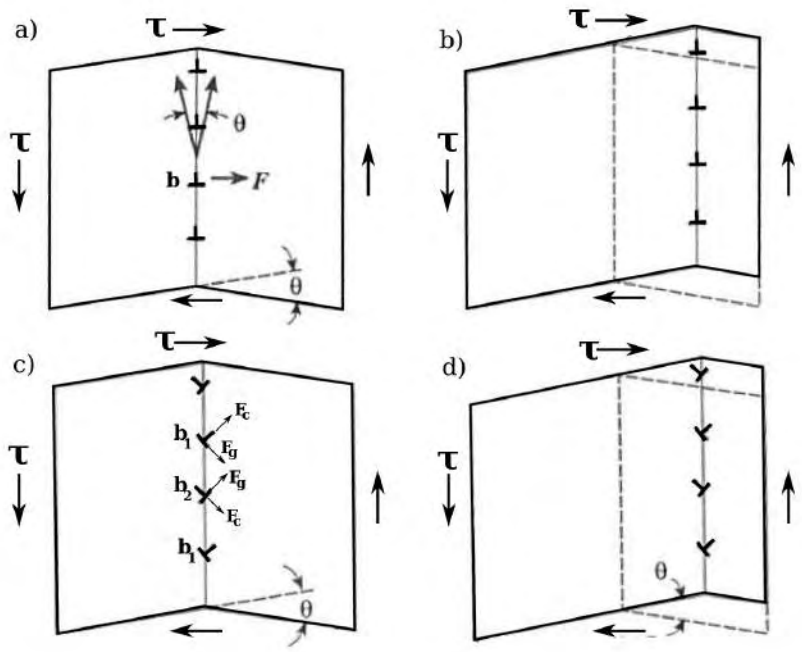

Figure B.3: Mouvement des joints symétriques à faible angle de désorientation couplés aux contraintes de cisaillement appliquées, τ, selon le modèle Read-Shockley. $\vec{F}$ est la force de glissement appliquée sur les dislocations due au cisaillement. c)- d) Mouvement d'un joint de grain constitué de deux familles de dislocations couplées au cisaillement.

sur chaque dislocation, qui la fera glisser sur son plan de glissement. Cette force entraîne le joint de grains à se déplacer vers l'avant au moyen du mouvement collectif des dislocations, sans modification de leur répartition locale. Par conséquent, le mouvement uniforme du joint va induire un changement de forme dans le bicristal (figure B.3 b). Pour un joint de grain symétrique de flexion plus complexe contenant deux familles de dislocations de vecteurs de Burgers $\vec{b}_1$ et $\vec{b}_2$, $(\vec{b} = \vec{b_1} + \vec{b_2})$, la contrainte de cisaillement appliquée exerce une force de montée $\vec{F_c}$ et une force de glissement $\vec{F_g}$ sur chaque dislocation comme indiqué dans la figure B.3c. Lors de l'application de la contrainte τ, chaque dislocation se déplacerait simultanément et normalement au plan du joint, par combinaison du glissement et de la montée alors que les forces mutuelles d'interaction imposent de garder leur répartition régulière (figure B.3 d).

Modèle de Cahn

Comme une extension du modèle de Read et Shockley , Cahn et al. le généralisent aux joints de grains symétriques et asymétriques d'angle de désorientation élevée [84, 85]. Ce modèle est purement géométrique et suppose que la migration des joints de grains induite par les contraintes appliquées ou par les forces capillaire ou toute autre forces motrices, produirait une déformation de cisaillement dans le réseau balayé par le mouvement des joints de grains [23, 86]. Dans cette théorie, le facteur de couplage β ne dépend que de la densité des dislocations, qui varie de façon continue avec l'angle de désorientation θ. En conséquence, le facteur de couplage est une fonction

continue de θ.
Selon le modèle de Cahn, la déformation de cisaillement couplée avec la migration des joints de grains comporte deux étapes : (1) la déformation plastique du réseau par le mouvement des dislocations primaires de joint (d_p) dans le plans du glissement du grain qui rapetisse, sans modifier l'orientation de réseau et (2) une rotation du réseau du grain qui rapetisse dans l'orientation du grain qui croît.
La déformation de cisaillement produite à la première étape dépend de la densité de dislocations du joint, et dans la deuxième étape, pour assurer la continuité du réseau, il y une rotation de θ qui corresponds à l'angle de désorientation du joint. L'étape de rotation dépend de la symétrie de rotation qui produit des états identiques du réseau. Pour le cas particulier des joints de flexion $< 001 >$ dans les cristaux cfc, il y a quatre joints de grains de coïncidence équivalents obtenus pour un angle de désorientation k$\pi/2 - \theta$ pour $k = 0..3$. Cela génère quatre modes de couplage possibles :

$$\beta = 2\tan(\theta/2 + \pi k/4), k = 0, 1, 2, 3 \tag{B.5}$$

Parmi les quatre facteurs de couplage possibles, deux d'entre eux, qui correspondent au plus petit $\vec{b}$, ont été mis en évidence par les simulations MD [23, 80] et aussi expérimentalement [87, 77, 88] :
Mode $< 100 >$ **:** comme c'est le cas pour un $\Sigma 13(510)$, en réponse à l'application d'un cisaillement τ, les dislocations avec des vecteurs de Burgers de $a[100]_{G_1}$ se déplacent parallèlement à $< 100 >_{G_1}$ dans le plan de glissement (100). En raison du mode de couplage, une rotation en sens inverse des aiguilles d'une montre réorganise les sites de réseaux du grain G_1 en G_2, entraînant le déplacement du joint de grain vers le haut. Le facteur de couplage dans ce mode est donné par :

$$\beta_{<100>} = 2\tan(\frac{\theta}{2}) \tag{B.6}$$

Mode $< 110 >$ **:** Ce mode de couplage correspond au mouvement des dislocations de vecteur de Burgers $a/2[110]_{G_1}$ parallèles à $< 110 >_{G_1}$ dans le plan du glissement de (110) dans le cas de $\Sigma 13(320)$. La déformation de cisaillement couplée avec le mouvement du joint dans ce mode est caractérisée par :

$$\beta_{<110>} = 2\tan(\frac{\pi}{4} - \frac{\theta}{2}) \tag{B.7}$$

Semblablement aux joints de grains à faible angle de désorientation constitués des deux familles de dislocations, la migration des joints asymétriques consiste à mouvement coopératif des deux familles de dislocations ($\vec{b_1}$ et $\vec{b_2}$).

Modèle des disconnections

Le mouvement des disconnections avec une hauteur de marche non nulle fournit un mécanisme pour la migration des joints de grains [89]. Selon l'angle entre la disconnection et le plan du joint, son mouvement peut se faire par glissement et/ou de processus de montée. Ainsi, le passage d'une rangée de disconnections le long de l'interface consiste en un cisaillement de la matrice et/ou à la diffusion à longue portée. Dans tous les cas, la continuité du réseau au cours de ce mouvement nécessite des réarrangements atomiques i.e shuffling pur simultanément au mouvement de la marche [72]. Des conclusions similaires peuvent être tirées dans le cas des macles, comme proposé par Bilby et Crocker [90] et confirmé par simulation atomistique pour Zr [91].
Ainsi selon ce modèle, le facteur de couplage induit par le mouvement des disconnections est mesurée par le rapport entre son vecteur de Burgers et la hauteur de marche h.
Toutefois, il faut souligner que les deux modèles de disconnection et de Cahn correspondent aux joints de flexions en coïncidence ou quasi-coïncidence et sont donc non-applicables aux joints de grains avec des angles de désorientation élevés et les joints généraux et non-coïncidents, comme

ceux que l'on retrouve dans les polycristaux.
Plus récemment, dans le modèle SMIG (Shear Migration Geometrical), Caillard et al. [93, 92] adoptent une approche qui permet de calculer plusieurs modes de couplage pour un joint de grain arbitraire. Dans ce modèle, les deux grains adjacents sont considérés comme deux phases différentes, mais avec des types d'atomes et un réseau identiques. Ces différentes phases peuvent être définies dans le plan perpendiculaire au plan du joint et à l'axe de rotation en sélectionnant deux motifs en forme de parallélogramme distincts avec la même aire et le même nombre de sites du réseau pour chaque grain. En trouvant des paires de valeurs de cisaillement et de rotation, une orientation de réseau peut être transférée dans l'autre grain et selon le choix de ces paires différents modes de couplage peuvent être obtenus.

B.1.3 Objectifs

Parmi les différents modèles présentés pour le mécanisme de couplage, le modèle de disconnections (et comme un cas particulier, le modèle de Cahn) a montré un bon accord avec les résultats expérimentaux sur des bicristaux dans Al [73, 88, 87], Zn [74], la zircone cubique [96] et Au [62]. Cependant, dans d'autres expériences sur des échantillons polycristallins et bicristallins d'Al [97, 32, 75], des modes de couplage beaucoup plus complexes, souvent associés aux faibles facteurs de couplage et parfois avec une rotation de grain, ont été observées.
Le modèle des disconnections permet une grande variété de défauts associés à la migration des joints couplée au cisaillement et donc plus apte à capturer plus facilement la variation des résultats expérimentaux. Bien que le modèle des disconnections explique potentiellement différents modes de couplage pour un joint de grain donné, une analyse détaillée du fonctionnement de ces mécanismes n'est pas encore disponible.
La compréhension des mécanismes à l'échelle atomique associés au fonctionnement des disconnections pendant la déformation, comme les mécanismes élémentaires du couplage est indispensable pour donner une explication détaillée des résultats observés à l'échelle microscopique et macroscopique.
En conséquence, l'objectif principal de ce projet est l'étude des mécanismes élémentaires de la migration des joints grain couplée au cisaillement par la réalisation des objectifs suivants :

- Étude de la dynamique des disconnections pendant la déformation et identification des modes de couplage :
  Cette question est traitée dans le premier chapitre de ce manuscrit où les résultats des essais de traction in-situ en MET sur Al (bicristaux et des échantillons polycristallins) sont présentés en détail.
- Étude des défauts structuraux dans les joints de grains : des défauts préexistants et ceux créés par interactions des dislocations de réseau avec le joint sont analysés dans le deuxième chapitre. Leurs relations aux modes de couplage possibles et la comparaison avec les résultats obtenus au chapitre 1 sont examinés.
- Identification des processus atomiques qui sous-tendent le couplage : Dans le dernier chapitre, la migration d'un $\Sigma13(320)$ couplée au cisaillement est modélisé à 0K dans un bicristal de cuivre. Le chemin d'énergie minimum de la migration et l'évolution structurelle correspondante sont ensuite déterminés.

B.2 Mouvements des disconnections associés à la migrations des joints de grains couplée au cisaillement

Dans ce chapitre, nous avons utilisé les essais in-situ de traction en microscopie électronique en transmission (MET) pour étudier qualitativement et quantitativement la migration des joints couplée au cisaillement dans des polycristaux et bicristaux.
Les essais de traction in-situ en MET, fournissent un moyen unique d'étudier directement les évolutions microstructurales dans les matériaux en temps réel. Ils consistent à déformer des microéchantillons par application d'un chargement uniaxial dans un MET à l'aide de porte-objets dédiés.
Depuis plusieurs années, l'utilisation des essais de traction in-situ en MET s'est avérée efficace pour sonder les mécanismes élémentaires dans les matériaux à petits grains où la plasticité intergranulaire est difficile à capter par des observations post-mortem. Toutefois, la détermination des caractéristiques des joints de grains dans les métaux NC est une tâche difficile dans le meilleur des cas, et presque impossible si plusieurs grains se chevauchent dans l'épaisseur de la lame mince. Pour éviter ce problème, nous avons utilisé une plus grande taille de grain (dans la gamme de grain ultrafin $100nm < d < 1\mu m$) et des bicristaux. Toujours dans le but d'activer préférentiellement la plasticité intergranulaire, nous avons mené des expériences à haute température.
Les bicristaux sont des matériaux modèles, permettant l'étude des mécanismes de déformation dans des joints de grain aux caractéristiques contrôlées (désorientation et plan du joint). Ils évitent la complexité d'un réseau de joints de grains courbés et des jonctions triples. En outre, leur utilisation permet une comparaison directe avec les tests de fluage in-situ effectuées dans bicristaux massifs [88].

Observation des disconnections élémentaires dans les joints de grains

Au cours des essais de traction in-situ sur les bicristaux, plusieurs très petites marches ont été observées le long du joint. Une fois l'échantillon soumis à une contrainte de traction, ces marches se sont soit déplaçées parallèlement au plan du joint ou ont montré des oscillations de petite amplitude.
La figure B.4 montre des micrographies à champ clair prises lors d'une expérience avec des bicristaux chauffés jusqu'à 400 °C. Le joint entre les grains G_1 et G_2 est vu ici debout, c'est à dire le long de la direction $< 001 >$. L'axe de traction, (T), est indiqué par une flèche sur la figure B.4a. Une marche de hauteur de 2 nm, montrée par s dans la figure B.4a peut être clairement vue le long du joint des grains. Bien qu'elles n'apparaissent pas dans la figure, plusieurs autres marches de cette hauteur ont également été observées le long du joint.
Sous contrainte, la marche s'est déplacée de plus de 25 nm le long du joint vers la nanoparticule X à une vitesse maximale de quelques Angstrœms par seconde (figure B.4 b et c). En même temps, une dislocation de réseau (d dans la figure B.4 b), glisse dans un plan $\{111\}$ de G_2 : la trace du plan de glissement est indiquée par tr.P dans la figure B.4b. La dislocation d interagit finalement avec la marche de dislocation dans le joint (figure B.4d). La marche reste alors immobile, ce qui suggère que l'interaction a conduit à la formation d'une marche sessile.
Le mouvement simultané de la marche et de la dislocation du réseau suggère que la marche a un caractère de dislocation, c'est à dire qu'elle est sensible au champ de déformation élastique appliqué ou celui dû à la présence de la dislocation d dans son voisinage. En conséquence, la marche est identifiée comme ayant une composante dislocation de joints, c'est une disconnection.

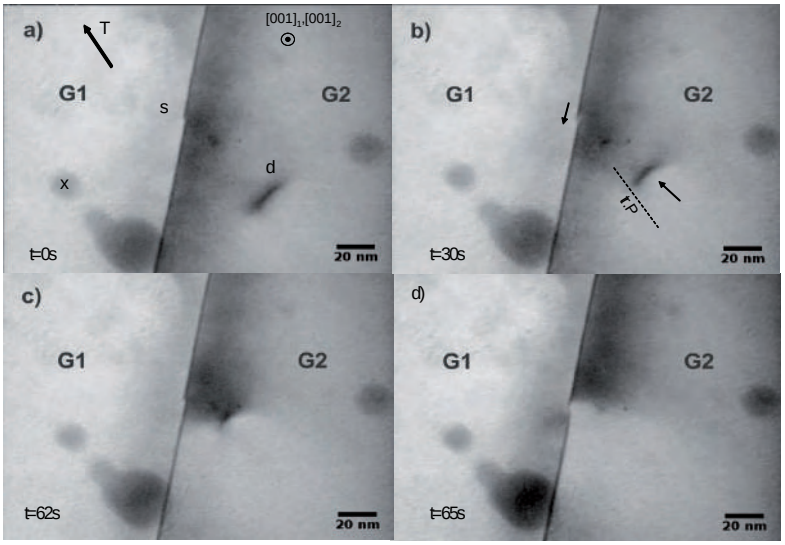

Figure B.4: Mouvement de marches le long des joints 76.4° ⟨001⟩ *dans un bicristal d'Al à 400 °C.*

B.2.1 Formation des Macro-marches

Outre les marches élémentaires mentionnées, d'autres marches de quelques dizaines de nm de hauteur ont été observées le long du joint de grain. Ces macro-marches se déplacent également en réponse à une charge extérieure induisant la migration des joints.
La figure B.5 rapporte les résultats d'un essai de traction sur un bicristal présentant une macro-marche. La configuration initiale attestant d'un joint de grain plat est montrée sur la figure B.5 (a). L'axe de traction (T) est indiqué par une flèche sur la figure B.5a.
Après 548 s, une première marche, étiquetée s_1 de hauteur $h_1 = 95$ nm, se déplace à une vitesse de 4 μm/s le long du joint vers le marqueur X2 (figure B.5b) et finit par s'arrêter près de X2. La hauteur des marches h_1 est environ 50 fois la hauteur de la disconnection élémentaire , ce qui suggère que cette macro-marche est composée de plusieurs marches élémentaires. Plus tard, à t = 789 s, une deuxième marche s_2 de hauteur $h_2 = 50$ nm, d'abord immobile, est observée à proximité du marqueur X1 (figure B.5 c). Deux secondes plus tard, une troisième marche s_3 de hauteur $h_3 = 100$ nm en provenance des zones plus épaisses de l'échantillon rejoint s_2 et s'arrête (Figure B.5d). Une seule marche s_4 de hauteur $h_4 = 150$ nm est alors formée. A t = 835 s, la marche s_4 commence à se déplacer rapidement à 4 μm/s le long du joint de grain (figure B.5e) avant d'être définitivement bloquée à proximité du marqueur X2. En attendant, s_4 absorbe s_1.
Simultanément au blocage de s_4, une activité de dislocation dans G_1 est remarquée. Le mouvement d'une ou de plusieurs autres marches se produit pour aboutir finalement à la formation de la marche s_5 d'une hauteur h_5= 250 nm après 1309 s (figure B.5f) et, enfin, à une marche s_f haute de 2 μm après plusieurs minutes (figure B.5g). A noter également sur la figure B.5G, le grand nombre de traces de glissement dans les deux grains, indiquant qu'une part de la déformation est également accommodée par de la plasticité intragranulaire.
Le blocage du mouvement de la marche s_4 est attribué à la présence d'un défaut de surface, peut-être un agrégat de nanoparticules qui fixe la marche à la surface de l'échantillon.
En outre, une analyse précise de la figure B.5d montre que : i) la forme d's_2 et s_3 peut encore être distinguée dans la marche s_4 et que ii) la hauteur de s_4 est approximativement égale à la somme des hauteurs des marches s_2 et s_3. De même, le profil du joint dans la figure B.5 f peut

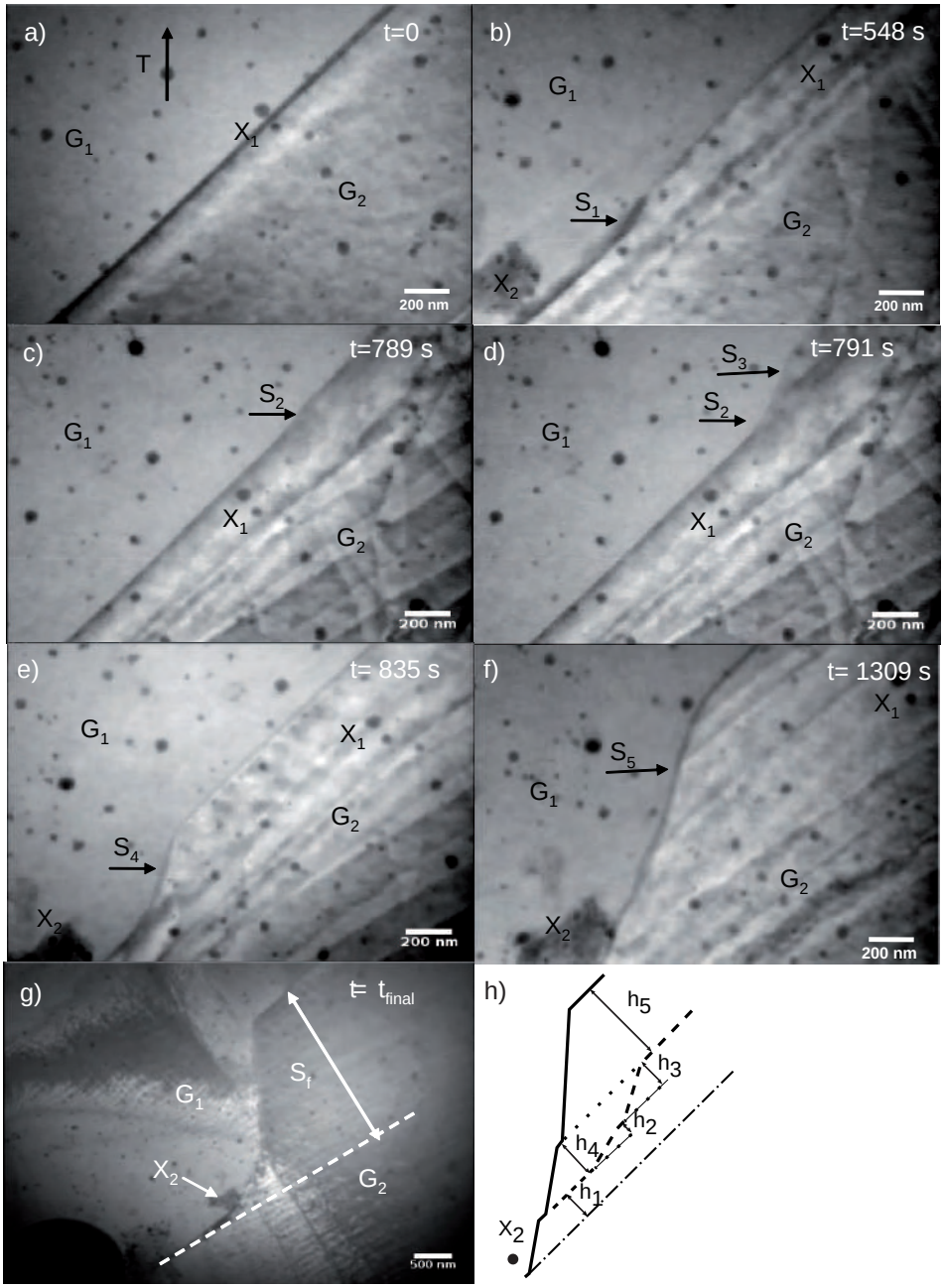

Figure B.5: (a)-(e) Mouvement de macro-marche le long du joint de grain en plusieurs étapes. Mouvement de s_1 (a-b), suivi par le mouvement de s_3 qui absorbe la marche immobile de s_2 (c-d) formant la marche s_4 qui finalement se déplace vers X2 (d-e). (f-g) sont des configurations après le mouvement de plusieurs autres marches. La dernière marche s_f voit sa hauteur largement augmentée (d'environ 2 μm). (h) est un schéma des différentes marches et de leurs hauteurs correspondantes.

être interprété comme une groupe des macro-marches. La figure B.5h fournit une esquisse des quatre marches différentes qui s'accumulent pour former la macro-marche s_f
. A partir de ces observations, nous concluons que la migration des joints de grains se fait par le mouvement collectif de marches élémentaires qui peuvent éventuellement s'empiler pour former des macro-marches.

B.2.2 Les mesures du facteur de couplage

A partir de la figure B.5, il est possible d'extraire et de mesurer certaines caractéristiques (notamment le facteur de couplage) des déplacements liés à la migration des joints de grains. Ces déplacements sont déduits des corrélations d'image. La soustraction des images de la même zone avant et après la migration des joints de grains est effectué par superposition de marqueurs dans G_2. En raison du couplage, les marqueurs dans le grain G_1 ne se superposent pas : les marqueurs apparaissent avec des contrastes noirs et blancs. Les déplacements relatifs des marqueurs par rapport au grain G_2 sont déduits de ces contrastes.
Les figures B.6a, b et c fournissent les différences entre les figures B.5 b et a, entre les figures B.5

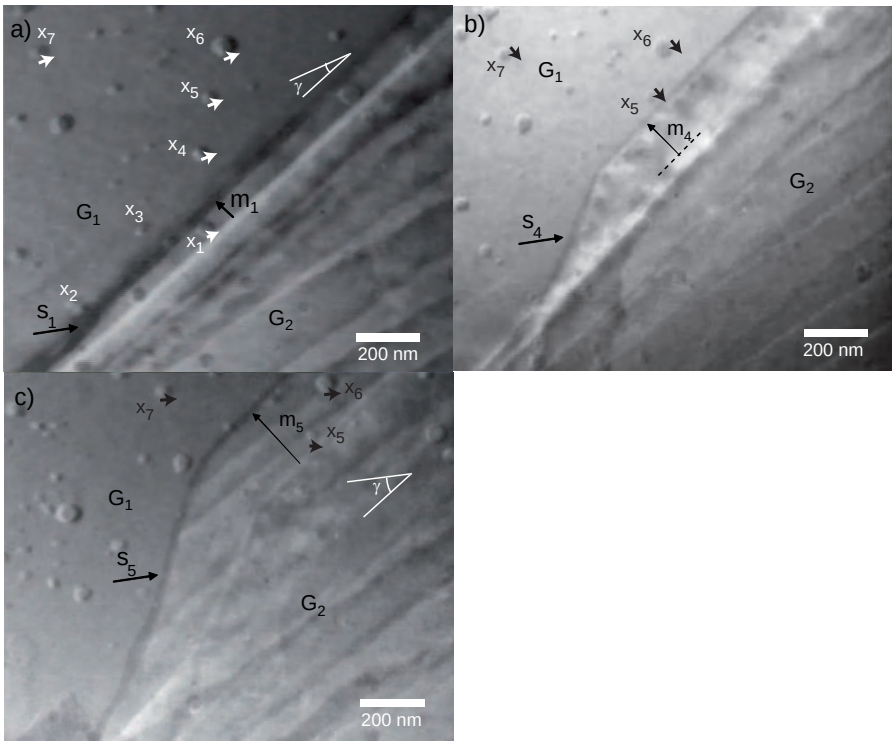

Figure B.6: Différence d'image obtenue par soustraction de contraste des images prises avant et après le mouvement de la marche s_1 (a), s_4(b) et s_5 (c). En superposant les marqueurs dans G_2, un décalage dans la position des marqueurs dans G_2 est observé indiquant la déformation produite dûe à la migration. Le facteur de couplage possède à la fois une composante parallèle et perpendiculaire au joint de grains.

e et b et entre les figures B.5f et e , respectivement
Comme indiqué précédemment, le déplacement en cisaillement doit dépendre linéairement de la distance de migration dans la zone balayée par la migration des joints de grains, puis doit être

constante au-dessus du joint.
Le mouvement de la marche s_1, caractérisé en figure B.6 est maintenant détaillé. Les déplacements d'un marqueur noté X1 situé dans la zone balayée par le joint de grain et six marqueurs notés X2-X7 situés au-dessus de la zone balayée par le joint sont indiqués par des flèches dans la figure B.6a. La distance de migration du joint est m1 . Comme prévu, les déplacements de X2 -X7 , notées par d2- d7 ont la même norme et leurs directions caractérisées par des angles γ_2 - γ_7 entre le vecteur de déplacement et le plan de joint de grain sont aussi égaux $\gamma_i = \gamma \approx 20°$ (pour i = 1 à 7). Le facteur de couplage est déduit :

$$\beta_{\parallel} = \frac{d_i \cos\gamma}{m1} \approx 25 \pm 2\% \tag{B.8}$$

Ce facteur de couplage est proche de la valeur obtenue par des essais macroscopiques sur les mêmes bicristaux [88, 76]. En outre, la migration de la marche produit non seulement un cisaillement parallèle au plan de joint mais aussi un déplacement perpendiculaire à ce plan. A l'aide des marqueurs, nous caractérisons les déplacements perpendiculaires au plan de joint par le coefficient :
$\beta_{\perp} = \frac{d_i \sin\gamma}{m1} = 6 \pm 2\%$ (i = 2 à 7) , correspondant à une déformation perpendiculaire au joint de grain.
En analysant la figure B.6b, le facteur de couplage lié au mouvement de s_4 est estimée à $\beta_{\parallel} \approx 0 \pm 2\%$, tandis que les déplacements perpendiculaires au plan du joint sont caractérisés par :

$$\beta_{\perp} = \frac{d_5 \sin\gamma}{m_4} = \frac{d_6 \sin\gamma}{m_4} \approx 6 \pm 2\% \tag{B.9}$$

Enfin, la figure B.6c liée à la formation de la macro-marche s_5 est considérée. Le déplacement de trois marqueurs dans G_1, deux au-dessous de la marche (X5 et X6) et un au-dessus (X7), sont analysés. Là encore, le déplacement des marqueurs n'est pas purement parallèle au joint de grain. Étonnamment, même dans la zone non balayée par la marche, un déplacement des marqueurs apparaît. En outre, le profil de déplacement des marqueurs devant la marche est identique à celui qui est derrière la marche.
Comme attendu, le déplacement des marqueurs dans la zone balayée par le joint de grain n'est pas constant mais augmente avec la distance par rapport à la position initiale du joint de grain. Le facteur de couplage dû au mouvement de s_5 peut être estimé :

$$\beta_{\parallel} = \frac{d_7 \cos\gamma}{m_5} \approx 7 \pm 2\% \tag{B.10}$$

et l'analyse des déplacements perpendiculaires au plan de joint de grain donne :

$$\beta_{\perp} = \frac{d_7 \sin\gamma}{m_5} \approx 6 \pm 2\% \tag{B.11}$$

Les déplacements perpendiculaires au plan de joint, observés dans tous les mouvements de joints analysés, ne sont pas prévus par le mode de couplage pur ce qui veut dire que le mouvement de la marche implique des processus de montée, i.e. de diffusion à longue portée, activée à haute température.

A partir des observations précédentes on peut considérer un modèle impliquant la combinaison des disconnections de différentes hauteurs et différents vecteurs de Burgers.
Prenons le mouvement d'une première marche, par exemple une marche s_a produisant une déformation de cisaillement pur, parallèle au plan de joint de grain : un schéma de cette situation est proposée dans la figure B.7a. Dans ce cas, selon le modèle de couplage pur, le profil de déplacement des marqueurs augmente linéairement avec la distance de migration dans la zone balayée

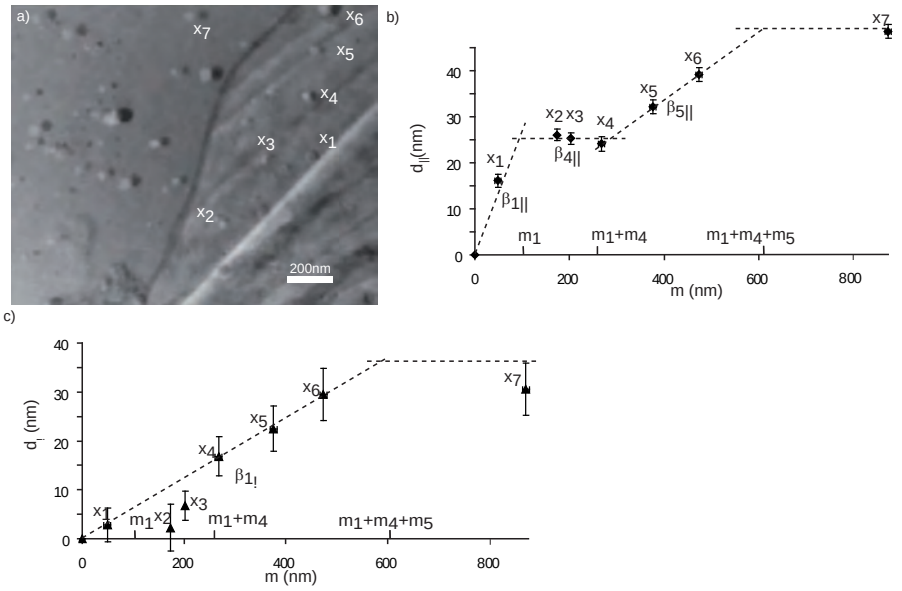

Figure B.7: Différence d'images entre la position initiale et finale d'un joint de grain, due à la formation de la macro-marche s_5 (a), le profil de déplacement des marqueurs parallèle et perpendiculaire au joint de grain peut être déduit (b) et (c) . Les différentes pentes de la courbe correspondent aux différents facteurs de couplage associés au mouvement de la marche.

par le joint de grains, puis est constante au-dessus du joint.
Si une deuxième marche s_b couplée à une déformation perpendiculaire au plan de joint de grain, s'amalgame avec l'ancienne marche s_a , le profil de déplacement sera modifié comme indiqué sur la figure B.7b . Le déplacement total des marqueurs induits par les deux marches s_a et s_b sera caractérisé par un facteur de couplage $\beta_{\parallel} = \frac{d_a}{m_a+m_b}$ et un coefficient $\beta_{\perp} = \frac{d_b}{m_a+m_b}$, où m_a et m_b sont les hauteurs des marches s_a et s_b et d_a et d_b sont la déformation induites par les marches.
Si plusieurs marches de hauteurs différentes portant des valeurs différentes de déformation (et pas seulement de cisaillement) se déplacent le long du joint de grain et finalement s'empilent comme sur le schéma de la figure B.7c, le facteur de couplage moyen sera :

$$\langle \beta_{\parallel} \rangle = \frac{\Sigma_i d_i \cos \gamma_i}{\Sigma_i m_i} \tag{B.12}$$

et pour le coefficient moyen $\beta_{\perp}$:

$$\langle \beta_{\perp} \rangle = \frac{\Sigma_i d_i \sin \gamma_i}{\Sigma_i m_i} \tag{B.13}$$

Ici γ_i est l'angle entre la direction de la déformation portée par la marche et le plan de joint de grain.
Cette explication nous aidera à interpréter le déplacement des marqueurs observé dans les expériences décrites précédemment : La figure B.7a montre la différence entre les figures B.5f et B.5a, en utilisant les marqueurs dans le grain G2 comme référence : elle caractérise ainsi le déplacement induit par la macro-marche s_5.
Le déplacement de sept marqueurs x_i est analysé. Les figures B.7 b et c reproduisent les déplacements des marqueurs respectivement, parallèle $d_{\parallel}$ et perpendiculaire $d_{\perp}$ au plan de joint de grain en fonction de leur distance m par rapport la position initiale du joint.

Dans la première partie de la courbe correspondant au mouvement de s_1, c'est à dire pour $0 < m < m_1$ avec $m_1 = 100nm$, les deux courbes $d_\parallel$ et $d_\perp$ augmentent de manière linéaire avec m. Les pentes respectives de ces courbes sont de $\beta_{\parallel 1} \approx 25\%$ et $\beta_{\perp 1} \approx 6\%$. Ces quantités sont cohérentes avec le facteur de couplage $\beta_\parallel$ et le coefficient $\beta_\perp$ mesurés à partir de la figure B.6a i.e. à partir des déplacements induits uniquement par la marche s_1.
Pour $m_1 < m < m_1 + m_4$ $m_1 + m_4 \approx 260nm$, la courbe $d_\parallel$ (Figure B.7b) montre un plateau tandis que $d_\perp$ augmente linéairement (figure B.7c). Les pentes respectives de ces courbes sont $\beta_{\parallel 4} \approx 0\%$ et $\beta_{\perp 4} \approx 6\%$. Ces valeurs sont compatibles avec les facteurs de couplage mesurés à partir de la figure B.6b, en analysant les déplacements induits par la marche s_4
. Pour $m_1 + m_4 < m < m_1 + m_4 + m_5$ avec $m_1 + m_4 + m_5 = 610nm$, les deux courbes de $d_\parallel$ et $d_\perp$ montrent une augmentation linéaire avec des pentes $\beta_{\parallel 5} \approx 6\%$ et $\beta_{\perp 5} \approx 6\%$. Encore une fois, ce résultat est en accord avec les valeurs trouvées dans la figure B.6c tout en analysant le déplacement induit par la marche s_5
Puisque$\beta_{\perp 1} \approx \beta_{\perp 4} \approx \beta_{\perp 5}$, la courbe $d_\perp$ (figure B.7c) ne présente aucun changement de la pente entre $0 < m < m_1 + m_4 + m_5$.
Pour $m > m_1 + m_4 + m_5$, les deux déplacements parallèles et perpendiculaires $d_\parallel$ et $d_\perp$ présentent un plateau : voir marqueur X7 dans la figure B.7 b et c. Ils correspondent aux déplacements globaux induits par l'ensemble des marches s_1 à s_4, ou de manière équivalente par la macro-marche s_5.
Enfin, le facteur global de couplage $\langle\beta_\parallel\rangle$ et le coefficient $\langle\beta_\perp\rangle$ peuvent être obtenus à partir de ces courbes selon l'équation 1 et 2 : $\langle\beta\rangle \approx 6.8\%$ et $\langle\beta_\perp\rangle \approx 6.4\%$.
Ces résultats montrent que la migration des joints de grains couplée au cisaillement se produit aux températures élevées (soit 0,7 T_m) par le mouvement rapide et répétitif des marches.
En effet, à chaque fois qu'une marche se déplace le long du joint, elle produit la migration du joint sur une distance égale à sa hauteur. Ces marches sont probablement composées de marches élémentaires nanométriques comme suggéré auparavant. Ces marches élémentaires produisent une déformation plastique, i.e les marches ont un caractère de dislocation [92, 94] . Cette conclusion, conforme au modèle des disconnections opèrant dans les joints de grains à forte désorientation, est semblable au mécanisme de couplage dans les macles.
En outre, la quantité de déformation produite peut être différente d'une marche à l'autre , suggérant que plusieurs types de disconnections peuvent être responsables du mouvement du joint, ou en d'autres termes, qu'un joint de grain donné peut supporter plusieurs modes de couplage. Ainsi, le facteur de couplage serait une conséquence des caractéristiques des disconnections plutôt qu'un caractère intrinsèque des joints de grains.

B.3 À propos de disconnections et leur éventuelle création à travers les interactions de dislocation du réseau

Plusieurs mécanismes possibles de sources disconnections sont rapportés dans la littérature. Il existe certaines preuves que les disconnections peuvent être émises dans le joint de grain, près des jonctions triples dans les macles [109]. Dans le mécanisme de pôle pour les macles [110], la source est composée de trois dislocations, deux sessiles dans les deux cristaux adjacents et une glissile dans le joint de grain. Sous contrainte, la dislocation glissile se décompose et tourne en spirale autour des dislocations sessiles, réalisant ainsi la croissance de la macle. Cette idée suppose toutefois l'existence de dislocations sessiles dans le joint, déplacant le problème de la migration couplée au cisaillement au problème de l'origine de la dislocation sessile.
Serra et Bacon [103] ont proposé dans les matériaux hexagonaux que des disconnections sessiles dans une macle agissent comme une source de disconnections qui se déplaceraient avec l'avancement de la macle.
A cet égard, les défauts initiaux et les défauts résultant d'interactions entre des dislocations du réseau et le joint de grain doivent être considérés comme des sources potentielles de disconnections.
Dans ce chapitre, la nature des défauts structurels préexistants est étudiée par MET en haute résolution (HRTEM). Cette méthode nous permet de déterminer la nature des disconnections.
Dans une seconde partie, les preuves expérimentales des interactions entre dislocations du réseau et joints de grains au cours de la traction in-situ en MET sur les bicristaux d'Al sont présentées.
Enfin, les possibles mécanismes de décomposition des dislocations dans le joint de grain sont étudiées théoriquement sur la base des interactions observées. La disconnection résultant de la décomposition des dislocations dans les joints peut conduire à différents modes de couplage qui seront discutés et comparés à la lumière des résultats expérimentaux présentés dans le chapitre précédent et dans la littérature.

B.3.1 Analyse HRTEM des défauts des joints de grains

Les observations HRTEM ont été utilisés pour analyser la structure du joint de grain proche de $\Sigma 41(540)$ dans les bicristaux. Ces observations montrent diverses structures du joint qui correspondent soit à une structure compacte de $\Sigma 41(540)$ avec un cœur étroit et des unités structurales bien définies (figure B.8a,b) ou à des arrangements de dislocations partielles bien séparées conduisant à une structure de cœur étendue (figure B.8c,d).

La structure compacte du joint de grain de $\Sigma 41(540)$ peut être définie comme une séquence $|AAAB.AAAB|$ des unités structurelles A et B. Les unités A sont les unités compactes du joint parfait et les unités B correspondent à une zone où se trouvent deux dislocations partielles dans chaque grain, $\frac{a}{2}\langle 0\ \bar{1}\ 0\rangle_{G_1}$ (en utilisant les directions du réseau du grains 1) et $\frac{a}{2}\langle 1\ 0\ 0\rangle_{G_1}$. Les unités B, résumant les deux dislocations partielles peuvent également être considérées comme le cœur d'une dislocation coin $\frac{a}{2}\langle 1\ \bar{1}\ 0\rangle_{G_1}$. La figure B.8a montre les unités structurales à l'interface entre les grains G_1 et G_2 . La présence de dislocations est mise en évidence sur la figure B.8b en utilisant la carte du champ de déformation ϵ_{xx} (x est parallèle à $[4\ 5\ 0]_{G_1}$, c'est à dire la direction du plan de joint de grain, perpendiculaire à l' axe de zone) , obtenu selon la méthode de l'analyse de la phase géométrique (GPA) [111, 109]. La période du joint entre les deux sites de coïncidence est 2.587 nm. Les atomes équivalents dans chaque demi-période $|AAAB|$ sont déplacés le long de l'axe de rotation par $\frac{a}{2}[001]$. Les dislocations dans les unités B sont situées à la fin des plans supplémentaires (200) et sont indiquées dans les figures B.8a et b.
La structure de cœur étendue du joint est rapportée sur la figure B.8 c et d . La figure B.8c présente un exemple de structure alternative de joint de grain avec cœur étendu, composée de

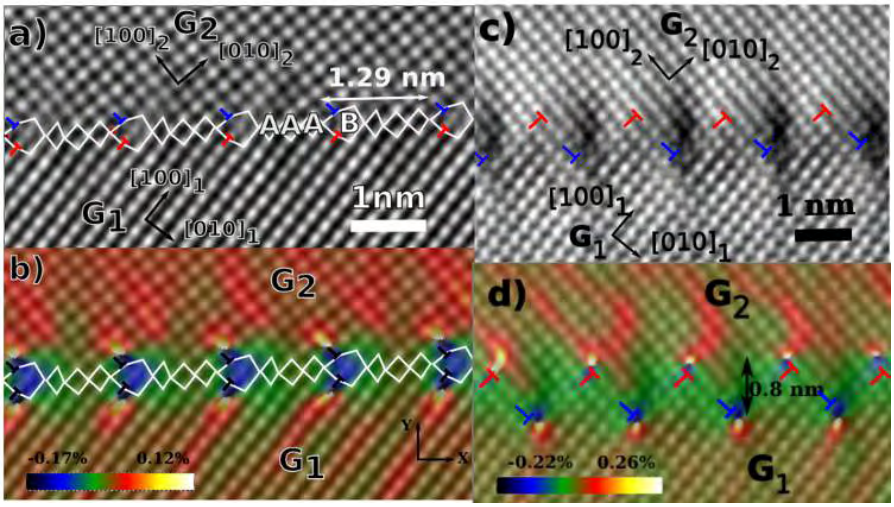

Figure B.8: a) Structure compacte de joints de grains représentée par des séquences $|AAAB.AAAB|$ des unités structurales A et B. La période de joint composée de deux sites de coïncidence est 2×1.293 nm. Deux dislocations partielles dans chaque grain, $\frac{a}{2}\langle 0\ \bar{1}\ 0\rangle_{G_1}$ et $\frac{a}{2}\langle 0\ 1\ 0\rangle_{G_2}$ (couleurs bleu et rouge) se rejoignent aux unités structurelles B. b) est l'image précédente (a) superposée avec le champ de déformation ϵ_{xx} (x parallèlement à $[\bar{4}\ 5\ 0]_{G_2}$), obtenu à l'aide de la méthode d'analyse de la phase géométrique (GPA). Les positions des dislocations partielles sont confirmées par des singularités dans le champ de déformation qui correspondent aux dipôles de dislocations. c) l'image d'un joint de grains avec une structure cœur étendue composée de dislocations séparées dans chaque grain. d) correspond à l'image précédente (c) superposée avec le champ de déformation montrant les dislocations dissociées réparties alternativementle long de l'interface.

dislocations bien séparées avec des vecteurs de Burgers projetés égaux à $\frac{a}{2}\langle 0\ \bar{1}\ 0\rangle_{G_1}$ et $\frac{a}{2}\langle 1\ 0\ 0\rangle_{G_1}$. La figure B.8d rapporte la carte du champ de déformation correspondant à ϵ_{xx} calculée avec la méthode GPA, et montre clairement la dissociation des dislocations dissociées, séparées de $0.8nm$. La section suivante est consacrée à l'étude des défauts qui perturbent les structures compactes et étendues du joint parfait que nous venons de décrire.

B.3.2 Analyse des défauts du joint de grains

Plusieurs types de défauts structuraux ont été observés dans le joint de grains. Le premier correspond à une dislocation qui perturbe l'espacement des dislocations primaires (i.e. les unité structurales B). Ils sont connus comme des défauts d'espacement dans la structure des joints de grains [144]. Le deuxième groupe de défauts correspond aux marches réparties le long du joint : **Cas général des disconnections :** La figure B.14 présente un exemple de marches dans les joints de grains avec une structure de cœur étendue. Différentes couleurs sont utilisées pour marquer les cœurs des dislocations pour chaque grain. Dans cet exemple, la distance entre les dislocations dissociées varie de la droite vers la gauche de la marche. Un procédé de "circuit mapping" (équivalent à un circuit de Burgers étendu aux cas des joints de grain) est appliqué pour ce défaut. Les sites équivalents du circuit autour de la marche sont choisis en fonction de la position des dislocations dans le réseau G_1. Le circuit, dans le modèle dichromatique présenté sur la figure B.9b, montre un défaut de fermeture : un vecteur de Burgers $\vec{b} = \frac{a}{82}[910]_{G_1}$ et une hauteur de marche $h = \frac{45.5a}{2\sqrt{41}} = 1.43$ nm sont associés à cette marche qui est une disconnection

générale.
Le tableau B.1 regroupe tous les types de défauts qui ont été identifiés lors de l'analyse de la structure des joints Σ41(540). Dans ce tableau, le vecteur de Burgers $\vec{b}$ associé à chaque défaut, les longueurs des composantes parallèles et perpendiculaires du vecteur de Burgers selon le plan de joint de grain et les hauteurs de marche sont détaillés. Mis à part les marche pures, les disconnections extrinsèques qui peuvent accommoder des variations locales du joint proviennent sans doute d'interactions avec les dislocations du réseau lors de l'élaboration. En effet, au cours des essais in-situ présentées dans le chapitre 1, l'activation de dislocations intragranulaires est généralement inévitable. L'interaction des dislocations du réseau avec le joint peut faire apparaître des défauts structurels de joints, qui peuvent à leur tour contribuer à la plasticité intergranulaire. Les interactions possibles étudiés par MET in-situ sont présentées dans la prochaine section.

$\tilde{\mathbf{b}}$	$\mathbf{b}_{\parallel}$	$\mathbf{b}_{\perp}$	$\mathbf{h}$
$\frac{3a}{41}[5\ \bar{4}\ 0]_{G_1}$	0	$\frac{3a}{\sqrt{41}}$	0
0	0	0	$-\frac{41a}{2\sqrt{41}}$
$\frac{a}{82}[9\ 1\ 0]_{G_1}$	$\frac{a}{2\sqrt{41}}$	$\frac{a}{2\sqrt{41}}$	$\frac{45.5a}{2\sqrt{41}}$
$\frac{a}{41}[5\ \bar{4}\ 0]_{G_1}$	0	$\frac{4a}{\sqrt{41}}$	$\frac{40a}{2\sqrt{41}}$
0	$\vec{b}_{1-2}+\vec{b}_{3-4}=0$	0	$h_{1-2}+h_{3-4}=-\frac{41a}{2\sqrt{41}}$

Table B.1: Différents cas de défauts caractérisés dans le joint Σ41(540) avec vecteurs de Burgers et hauteurs de marches associés.

B.3.3 Observations des interactions des dislocations de réseau avec le joint

Pour étudier les interactions entre dislocations du réseau et joints de grains, des essais MET in-situ sur les bicristaux ont été réalisées à température ambiante et à 400 °C. Dislocations et joints de grains ont été analysés dans des conditions de champ clair et champ sombre, utilisant à la fois l'analyse de trace, le contraste et la représentations stéréographique. La caractérisation des disconnections de joint (notées ici GBD pour les différencier des dislocations de réseau) montre que leur vecteur de Burgers ($\vec{b}_{GBD}$) est proche de la direction [001] et la ligne de dislocation $\vec{l}_{GBD}$ est quasiment parallèle à $[001]_{G_1}$, ce sont donc des disconnections vis. Ces GBDs ne sont pas espacées régulièrement le long de l'interface et ne sont donc pas des dislocations secondaires intrinsèques comme indiqué dans [117], mais des disconnections extrinsèques.
Différents cas d'interactions entre les dislocations du réseau et GBDs ont été observés à température ambiante ou élevée. Ces interactions conduisent à des décompositions en disconnections qui peuvent se déplacer éventuellement le long de l'interface. Dans la section suivante, nous décrirons les cas de décomposition possible des dislocations de réseau en disconnections et évaluerons les modes de couplage possibles.

B.3.4 Décomposition des dislocations

Dans la première partie de cette section, les conditions théoriques pour la décomposition des dislocations sont décrites. En appliquent ces conditions à la décomposition de dislocations observées pendant les expériences de MET in-situ ainsi qu'à d'autres dislocations de réseau qui

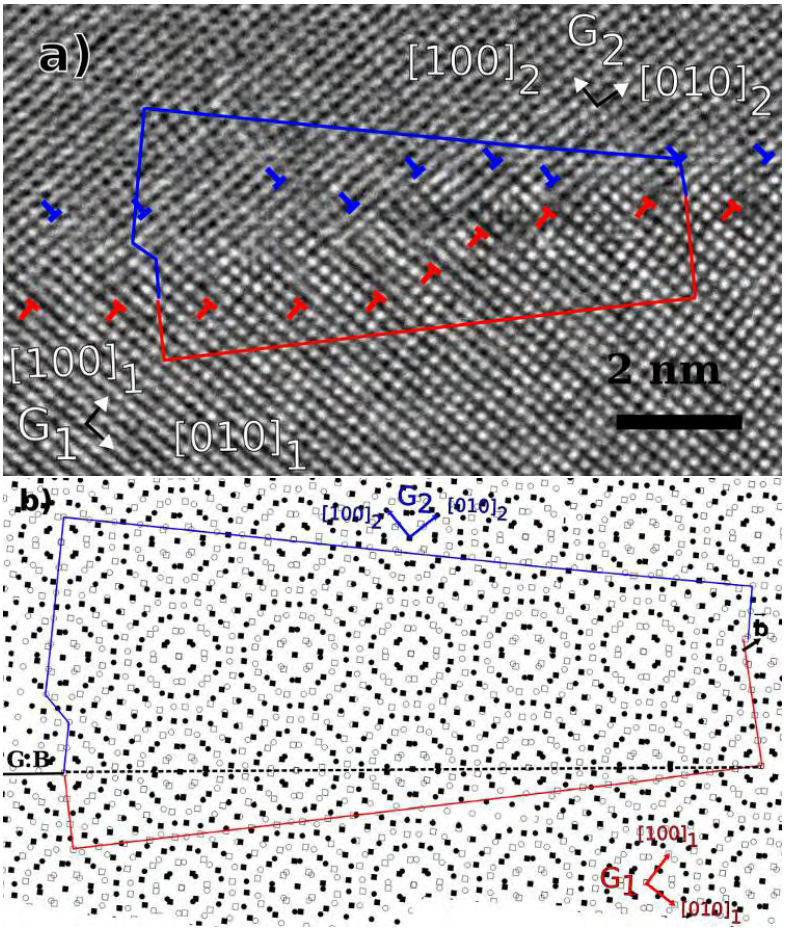

Figure B.9: a) Une marche dans une structure de joint à dislocations dissociées. Les marqueurs bleus indiquent les cœurs de dislocations correspondant à G_2 et les marqueurs rouges montrent les cœurs de dislocations dans G_1. Le circuit entoure la marche entre deux positions équivalentes du cristal sur l'interface. Ces positions sont choisies en fonction de la périodicité des dislocations dans G_1. b) Le circuit dans le réseau dichromatique du joint montre une dislocation associée à la marche avec un vecteur de Burgers de $\vec{b} = \frac{a}{82}[910]_{G_1}$ et une hauteur de marche $h = \frac{45.5a}{2\sqrt{41}}$.

interagissent potentiellement avec le joint, tous les produits de décomposition possibles sont identifiés.
Nous donnerons ensuite les modes de couplage potentiels attribués aux disconnections résultantes dans le joint. Enfin, ces modes de couplage sont comparés avec les résultats expérimentaux concernant les facteurs de couplage dans $\Sigma 41(540)$.
Le tableau B.2 reprend les différentes disconnections étudiées dans ce chapitre, avec la notation $\vec{b}_{j/k}$ présentées dans le réseau de G_1, avec leur hauteurs de marches h. Selon l'angle γ entre les vecteurs de Burgers $\vec{b}_{i/j}$ et le plan de joint, les composantes de glissement $b_g = \|\vec{b}_{i/j}\| \cos\gamma$ etde montée $b_c = \|\vec{b}_{i/j}\| \sin\gamma$ de chaque disconnection sont données dans l'unité de paramètre de maille. Nous supposons que la ligne de ces disconnections est parallèle à l'axe de rotation du joint [0 0 1] et qu'elles ont donc un caractère vis. La composante b_s du vecteur de Burgers est également déterminée par sa projection le long de l'axe de rotation.
Si la migration des joints de grains se produit par le mouvement de l'une de ces disconnections, des déformations de cisaillement et/ou de montée seront induites dans le matériau selon le vecteur de Burgers correspondant. La composante de glissement b_g serait responsable d'une déformation de cisaillement parallèle au plan du joint tandis que la composante vis b_s peut potentiellement induire une déformation le long de l'axe de rotation. D'autre part, le mouvement des disconnections avec des composantes de vecteur de Burgers normal au plan de joint de grain nécessite un mécanisme de montée pour se déplacer [89]. Les déformations potentielles parallèle $\beta_{\|} = b_g/h$ et perpendiculaire $\beta_{\perp} = b_c/h$ au joint et celle le long de l'axe de rotation $\beta_s = b_s/h$ sont rapportés pour chaque disconnection résultant de la décomposition ci-dessus, dans le tableau B.2.

$\vec{b}_{DSC}$	$\vec{b}_{G_1}$	b_g	b_c	b_s	h	$\beta_{\parallel}$	$\beta_{\perp}$	β_s
$b_{9/9}$	$\frac{1}{41}[\bar{4}\ \bar{5}\ 0]$	$-2/2\sqrt{41}$	–	–	$9h_0$	-0.222	–	–
$b_{1/-1}$	$\frac{1}{82}[5\ \bar{4}\ 0]$	–	$2/2\sqrt{41}$	–	–	–	–	-
$b_{5/5}$	$\frac{8}{82}[4\ 5\ 0]$	$8/2\sqrt{41}$	–	–	$5h_0$	1.6	–	-
$b_{5/4}$	$\frac{1}{82}[1\ \bar{9}\ 0]$	$-1/2\sqrt{41}$	$1/2\sqrt{41}$	–	$4.5h_0$	-0.22	0.22	-
$b_{3/2}$	$\frac{1}{82}[21\ 16\ 41]$	$4/2\sqrt{41}$	$1/2\sqrt{41}$	1/2	$2.5h_0$	1.6	0.4	2.5
$b_{8/6}$	$\frac{1}{82}[22\ 7\ \bar{4}1]$	$3/2\sqrt{41}$	$2/2\sqrt{41}$	$-1/2$	$7h_0$	0.42	0.28	-0.9
$b_{13/10}$	$\frac{1}{82}[23\ \bar{2}\ 41]$	$2/2\sqrt{41}$	$3/2\sqrt{41}$	1/2	$11.5h_0$	0.17	0.26	0.55
$b_{-16/-16}$	$\frac{1}{82}[\bar{4}\ \bar{5}\ 41]$	$-1/2\sqrt{41}$	–	1/2	$-16h_0$	0.0625	–	-0.4
$b_{6/5}$	$\frac{1}{82}[73\ 81\ 0]$	$17/2\sqrt{41}$	$1/2\sqrt{41}$	–	$5.5h_0$	3.09	0.18	–
$b_{3/1}$	$\frac{1}{82}[\bar{10}\ \bar{33}\ 41]$	$5/2\sqrt{41}$	$2/2\sqrt{41}$	1/2	$2h_0$	2.5	1	3.2
$b_{6/3}$	$\frac{1}{82}[11\ \bar{17}\ 0]$	$-1/2\sqrt{41}$	$3/2\sqrt{41}$	–	$4.5h_0$	-0.22	0.66	–
$b_{-11/-12}$	$\frac{1}{82}[\bar{3}\ \bar{14}\ 41]$	$-2/2\sqrt{41}$	$1/2\sqrt{41}$	1/2	$-11.5h_0$	0.17	-0.08	0.55
$b_{28/27}$	$\frac{1}{82}[17\ 11\ 0]$	$3/2\sqrt{41}$	$1/2\sqrt{41}$	–	$27.5h_0$	0.109	0.03	–
$b_{19/18}$	$\frac{1}{82}[25\ 21\ 0]$	$5/2\sqrt{41}$	$1/2\sqrt{41}$	–	$18.5h_0$	0.27	0.05	–
$b_{17/20}$	$\frac{1}{82}[5\ 37\ 0]$	$5/2\sqrt{41}$	$-3/2\sqrt{41}$	–	$18.5h_0$	0.27	-0.16	–
$b_{13/15}$	$\frac{1}{82}[14\ 38\ 0]$	$6/2\sqrt{41}$	$-2/2\sqrt{41}$	–	$14h_0$	0.42	-0.14	–
$b_{9/10}$	$\frac{1}{82}[23\ 39\ 0]$	$7/2\sqrt{41}$	$-1/2\sqrt{41}$	–	$9.5h_0$	0.73	-0.105	–
$b_{10/9}$	$\frac{1}{82}[33\ 31\ 0]$	$7/2\sqrt{41}$	$1/2\sqrt{41}$	–	$9.5h_0$	0.73	0.105	–
$b_{17/15}$	$\frac{1}{82}[14\ \bar{3}\ 41]$	$1/2\sqrt{41}$	$2/2\sqrt{41}$	1/2	$16h_0$	0.0625	0.125	0.4

Table B.2: Produits de la décomposition des dislocations de réseau dans le joint $\Sigma 41(540)$ *incluant les composantes de glissement et de montée des disconnections associées, ainsi que leurs hauteurs de marche. Le mouvement de ces disconnections dans les joints de grains peut induire des déformations parallèles* $\beta_{\parallel} = b_g/h$ *et perpendiculaires* $\beta_{\perp} = b_c/h$ *au joint.*

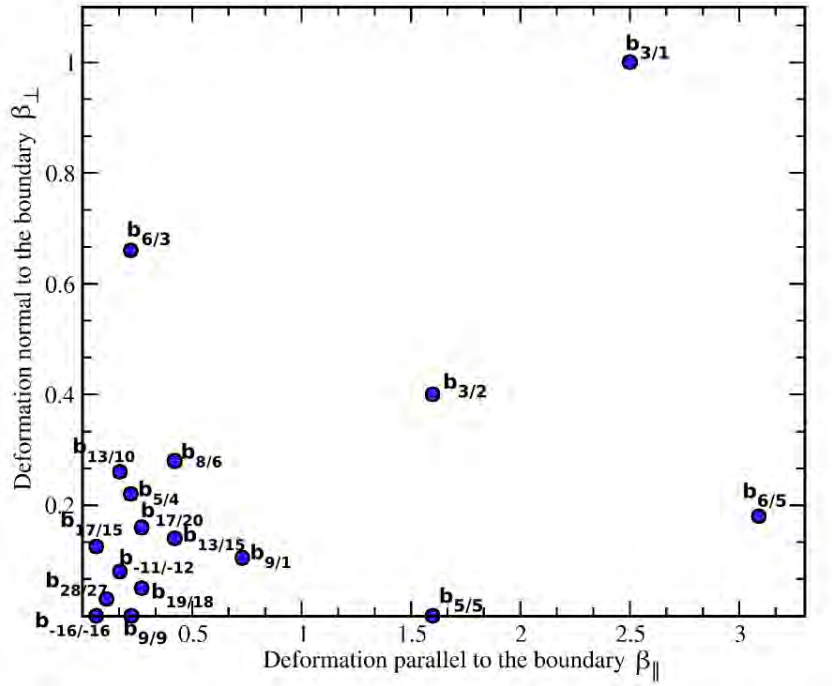

Figure B.10: Représentation schématique de l'ensemble des modes de déformation possibles associés aux disconnections résultantes de la décomposition des dislocations de réseau dans le joint de grain.

La figure B.10 donne une représentation schématique des différents modes possibles de déformation associés aux disconnections rapportées dans le tableau B.2 pour le joint $\Sigma 41(540)$. Chaque point du diagramme représente une disconnection dont les coordonnées horizontales et verticales correspondent à la déformation associée parallèle $\beta_\parallel$ et perpendiculaire $\beta_\perp$ au joint de grain.
Selon Serra et Bacon [103], les disconnections avec de petits vecteurs de Burgers parallèles au plan du joint et à hauteur de marches non-nulles impliquent un réarrangement atomique minimal et sont donc susceptibles d'être mobiles. Pour les disconnections avec des vecteurs de Burgers perpendiculaires au joint qui se déplacent par montée, il existe une relation inverse entre la mobilité des dislocations et leur composante de montée.
Comme la migration des joints de grain résulte du mouvement des disconnections, les disconnections avec la plus grande composante de montée sont censés contrôler la mobilité des joints de grains. Ces disconnection jouent le rôle d'obstacle au mouvement des disconnections plus mobiles (en particulier celles qui sont purement glissiles). En effet, les disconnections rapides vont s'accumuler contre ces disconnections plus lentes, ce qui explique la création des macro-marches. Ce blocage de marches à composante de montée peut être moindre à haute température dans les films minces, car la diffusion de lacunes est renforcée par la présence de surfaces libres [123]. À basse contrainte et faible température cependant, la différence de mobilité peut être beaucoup plus élevée, et les disconnections les plus lentes peuvent alors être considérés comme des obstacles importants. Leur élimination par des disconnections purement glissiles est alors possible. L'observation du verrouillage et du déverrouillage des macro-marches le long des joints peut être

le résultat de ce processus. On s'attend donc à ce que le facteur de couplage résultant dépende de la mobilité relative des disconnections.

B.3.5 Évaluation des facteurs de couplage

Selon le tableau B.2, les modes de déformation possibles attribuables aux disconnections dans un $\Sigma 41(540)$ offrent une large gamme de possibilités. Toutefois, comme discuté ci-dessus, une disconnection à petit vecteurs de Burgers, faible hauteur de marche et faible composant de montée devrait avoir une mobilité plus importante. Ces défauts seront susceptibles de se déplacer plus facilement et d'induire une déformation. Ces disconnections de la figure B.10 sont placées dans le coin inférieur gauche de la courbe de $\beta_\perp - \beta_\parallel$.

Le mode de couplage induit par le mouvement de la disconnection purement glissile $\vec{b}_{9/9}$ ($\beta_\parallel = -0.22$, $\beta_\perp = 0$ et $\beta_s = 0$) est à la fois en accord avec les valeurs obtenues par simulations de dynamique moléculaire [23] et les essais de déformation in-situ à chaud par microscopie électronique à balayage (MEB) [77].

Le vecteur $\vec{b}_{-16/-16}$ qui correspond à la disconnection vis observée, produit un cisaillement plus faible dans la direction parallèle au joint ($\beta_\parallel = 0.062$). De plus, la composante vis de cette disconnection peut induire une déformation parallèle à l'axe de rotation du joint de grain. Le mouvement combiné de deux familles de disconnections avec des vecteurs de Burgers à 90° dans le plan du joint provoque une rotation et une migration du grain (disconnections vis produisant un cisaillement parallèle à l'axe de rotation et disconnections à cisaillement parallèle au plan de joint de grains mais perpendiculaire à l'axe de rotation). Cet effet est expliqué dans [97].

$\vec{b}_{-11/-12}$, $\vec{b}_{28/27}$ et $\vec{b}_{19/18}$ ont des composantes de montée qui vont induire un déformation dans la direction normale au joint ($\beta_\perp$). Ceci est cohérent avec les modes de couplage qui ont été observés par des essais de traction in-situ en MET du chapitre 1. Les composantes de glissement et de montée de $b_{19/18}$ ($\beta_\parallel = 0.27$, $\beta_\perp = 0.05$) peuvent produire des déformations qui sont relativement proches des facteurs de couplage de la marche 1 mesurées par MET in-situ.

En outre, d'autres facteurs de couplage peuvent provenir de la combinaison entre plusieurs disconnections et des marches pures.

B.4 Simulation atomistique

Ce chapitre porte sur l'étude théorique des mécanismes élémentaires qui se produisent au cours de la migration de joints de grains, couplée à un cisaillement, à basse température. En utilisant des simulations atomistiques basées sur la méthode NEB (Nudged Elastic Band), nous montrons que la migration couplée au cisaillement se produit à travers la nucléation et le mouvement des disconnexions [94]. Les caractéristiques structurelles et énergétiques de ces mécanismes élémentaires sont décrites. Ces résultats montrent que la migration de joint de grain, généralement considéré comme un simple processus activé du mouvement stick-slip, est une succession de processus élémentaires activés, en accord avec les observations expérimentales des disconnections [23, 102].

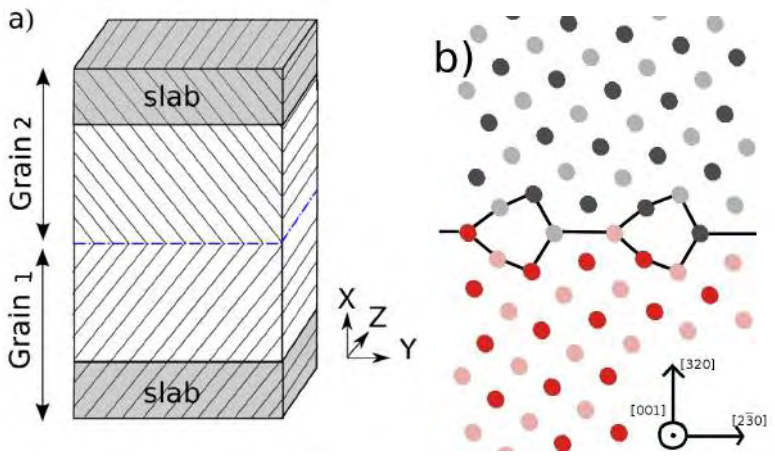

Figure B.11: a) Schéma de la cellule de simulation. b) Configuration du joint de grain de Σ13(320) *projeté dans le plan (x, y) : les atomes noir (gris) et rouge (rose) appartiennent aux différents grains.*

La migration d'un joint de grain symétrique de flexion en réponse à une déformation de cisaillement externe est étudiée dans un bicristal de cuivre en utilisant la simulation atomistique et la suite de programmes de simulation LAMMPS [128]. La figure B.11 montre un schéma du système étudié. La cellule de simulation contient deux grains symétriques d'un cristal parfait de cuivre désorientés l'un par rapport à l'autre, par un angle de $\theta = 67.38°$ autour de la direction [001] : c'est un joint symétrique de flexion, en coïncidence Σ13(320) à l'interface. Les conditions aux limites périodiques sont appliquées dans les directions parallèles à [$\bar{3}$02] (l'axe y) et [001] (l'axe z). La cellule mesure 10,3 nm selon x (l'axe x correspond à la direction [320]). Dans ce qui suit, $L_{[2\bar{3}0]}$ ($L_{[001]}$) renvoie à la période du réseau de coïncidence le long de la direction [2$\bar{3}$0]([001]).
Les interactions entre les atomes de cuivre sont modélisées en utilisant un potentiel EAM (Embedded Atom Methods) [129]. Deux blocs d'épaisseur de $1.5nm$, au dessus et en bas de la cellule contiennent des atomes avec des positions relatives gelées dans les positions d'un cristal parfait, sont utilisés pour imposer une contrainte de cisaillement sur le joint.
Le couplage est étudié à 0K : le bloc supérieur est déplacé par rapport à l'autre dans la direction y par petits incréments. L'énergie potentielle est minimisée lors de chaque étape à l'aide d'une méthode de gradient conjugué. Les figures B.12a et b montrent la variation de la contrainte de cisaillement (calculée en utilisant le viriel généralisé pour le tenseur des contraintes) et la

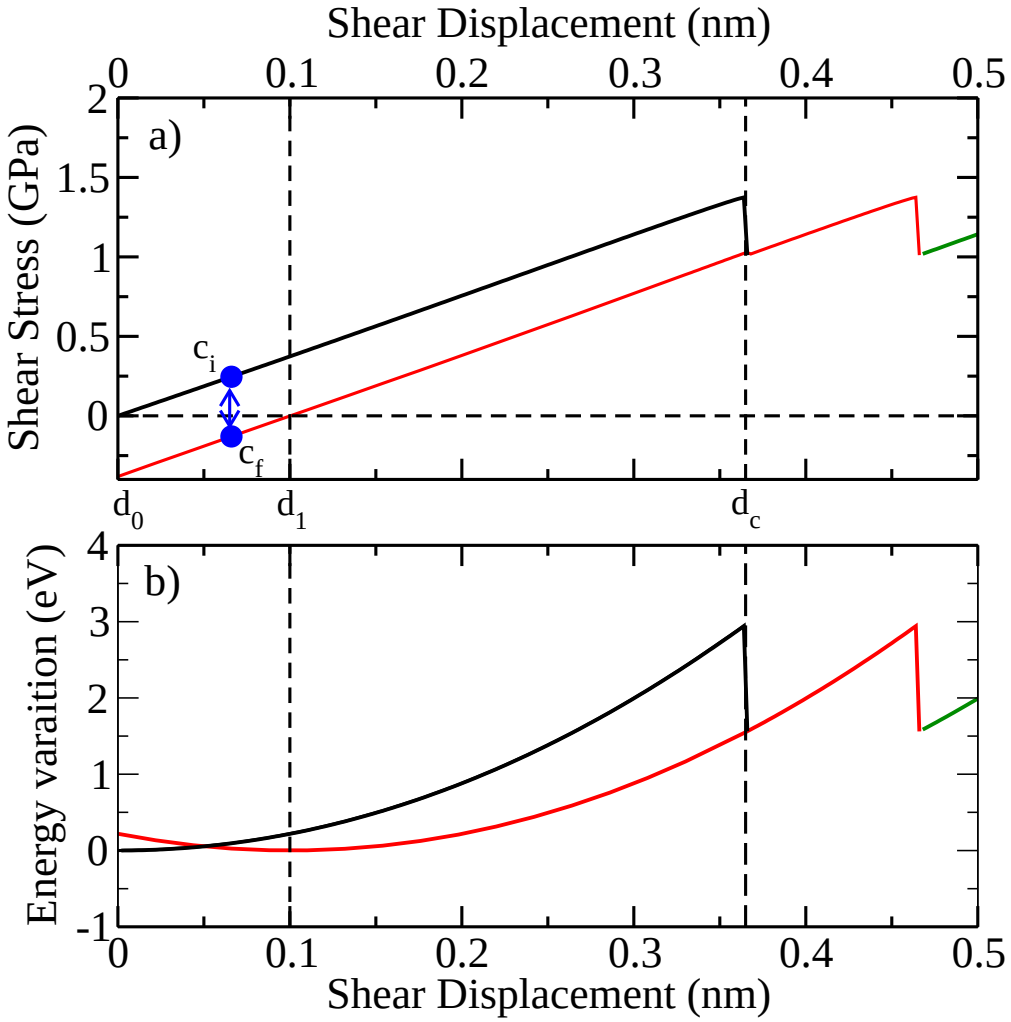

Figure B.12: Variation de a) la contrainte de cisaillement et b) de l'énergie potentielle en fonction du cisaillement. Les courbes noires et rouges correspondent aux configurations initiale et finale du joint de grains.

variation d'énergie potentielle en fonction du déplacement relatif d du bloc. Ces résultats sont donnés pour une cellule de simulation de 1664 atomes de dimensions 1,3 nm et 1.4 nm selon y (1 $L_{[2\bar{3}0]}$) et z (4 $L_{[001]}$). A partir de la configuration initiale $d_0 = 0$ dans la figure B.12, la contrainte de cisaillement croît de façon linéaire (et l'énergie potentielle de façon quadratique), ce qui est représentatif d'un régime élastique qui laisse la position du joint inchangée par rapport à sa position initiale (courbes noires). Ce régime s'arrête en $d_c = 0.365nm$ où la contrainte de cisaillement diminue à cause de la migration du joint. En augmentant le déplacement d à partir de ce point $d > d_c$, on observe une augmentation linéaire (courbe rouge) de la contrainte de cisaillement jusqu'à la prochaine migration du joint, ce qui résulte en un comportement qualifié de "stick-slip" [80]. Diminuer le déplacement d de $d > d_c$ (courbes rouges) se traduit par la diminution linéaire de la contrainte de cisaillement (et quadratique en énergie potentielle) : ce qui traduit un nouveau régime élastique où le joint est immobile par rapport à la configuration

finale atteinte après la première migration.
La contrainte de cisaillement s'annule et l'énergie potentielle est minimisée à la position d'équilibre finale du joint $d_1 = 0.1$ nm. La migration du joint sur une distance $m = -0.25nm$ (mesurée à partir de la simulation) est accompagnée par le cisaillement $\Delta d = d_1 - d_0$. Le facteur de couplage est donc $\beta = -0.40$, en accord avec des études précédentes [80].

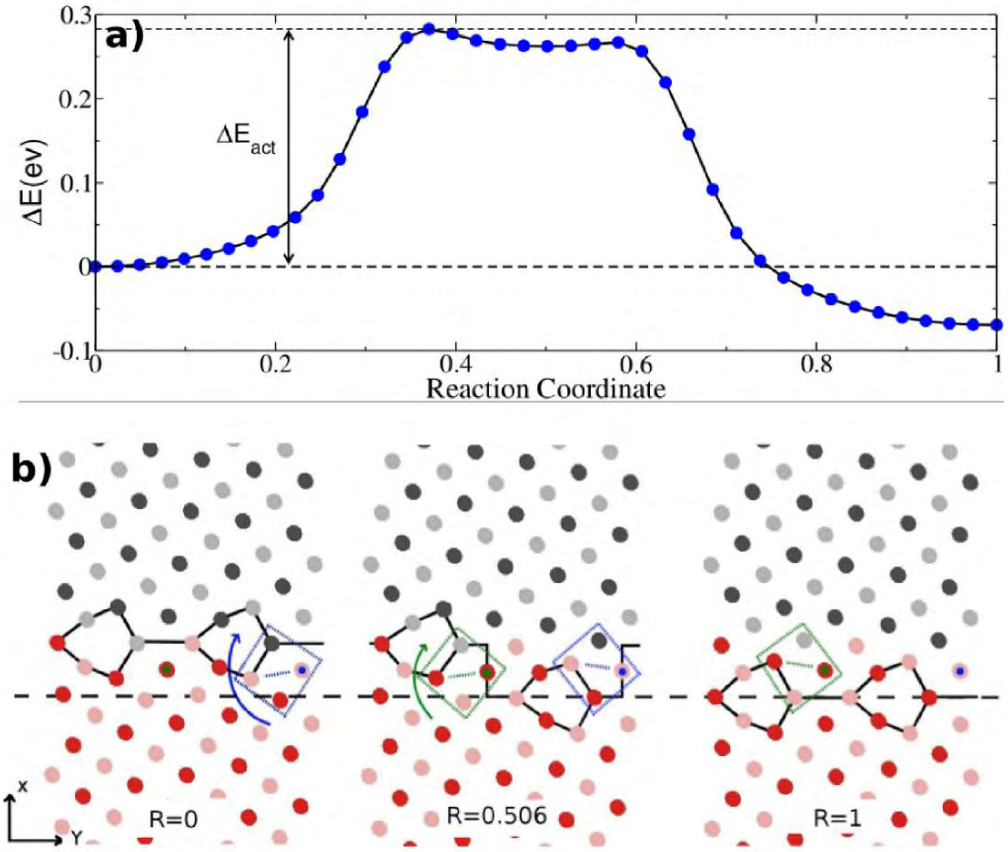

Figure B.13: a) Courbe de MEP (Minimum Energy Path) obtenue pour la migration des joints de grains entre les états initial et final du système. L'axe vertical correspond à la variation d'énergie dans le système et l'axe horizontal représente les coordonnées de réaction (RC). b) Évolution structurelle du joint le long de la MEP projeté dans le plan x-y. Les carrés bleu et vert affichent les atomes qui tournent et modifient les unités structurales à la position suivante. Les tailles de la cellule dans les directions y et z sont 1.3 nm et 1.4 nm.

Ici, le joint migre à $0K$ pour un déplacement en cisaillement de $d = d_c$, alors qu'à température finie, il peut migrer pour $d < d_c$ [80]. Pour étudier cette migration, les configurations du système avant et après la migration du joint, obtenue à 0K pour un déplacement donné de d, sont utilisées comme configurations initiales et finales dans la méthode NEB [145]. Par exemple , pour $d = 0.066nm$, la NEB est effectuée entre les configurations initiales c_i et finale c_f rapportées sur la figure B.12a. La méthode NEB permet de déterminer le chemin d'énergie minimum (MEP-Minimum Energy Path) pour une migration du joint de grain correspondant à

chaque valeur de d. Le MEP est typiquement présenté en fonction des coordonnées de réactions (RC) qui sont ici la distance cumulée (normalisée par la distance totale cumulée) entre les images successives du système dans l'espace des configurations. RC est considéré comme un indicateur de l'état d'avancement de la migration. Les configurations initiales et finales correspondent à $RC = 0$ et $RC = 1$. La figure B.13a) est un exemple représentatif de la variation de l'énergie potentielle ΔE le long de le MEP pour un déplacement en cisaillement $d = 0.066\ nm$, parmi ceux obtenus pour différents d . Le MEP présente deux maxima locaux pour $RC = 0.37$ et 0.58 et un état métastable pour $RC = 0.506$. La barrière d'énergie pour la migration du joint est déduite $\Delta E_{act}^{GB} = 0.283$ eV.
La figure B.13b montre en projection les configurations initiale, métastable et finale du joint dans le plan (x,y). La configuration métastable représente une unité structurale déplacée, et inclue deux marches opposées sur le joint. L'exécution d'un circuit de Burgers dans le plan (x,y), montrent que les vecteurs de Burgers $\vec{b}_1 = \frac{l_{[2\bar{3}0]}}{13}\vec{u}_y$ et $\vec{b}_2 = -\vec{b}_1$ sont associés aux marches de gauche et de droite. Ces marches, qui présentent une composante de cisaillement et un déplacement normal (la hauteur de la marche), sont des disconnections [94]. Le rapport entre la composante de cisaillement et la hauteur de la marche correspond au facteur de couplage. L'apparition et la disparition des disconnections sont principalement induits par la rotation de quatre colonnes atomiques autour de la direction z suggérant un mécanisme de shuffling [62, 92] : Ces colonnes sont contenues dans les carrés bleus ($RC = 0$ à 0.506) et verts (RC = 0.06 à 1) dans la figure B.13b. L'axe de rotation coïncident presque avec les points bleus et verts.

Des simulations supplémentaires sont effectués dans des cellules avec des tailles selon y allant linéairement de 1.3 nm ($1L_{[2\bar{3}0]}$) à 6.5 nm ($5L_{[2\bar{3}0]}$), correspondant à 1664 à 8320 atomes dans la cellule (les tailles x et z étant 10.3 nm et 1.4 nm). La figure B.14a rapporte l'évolution de le MEP par unité de surface $\Delta E = \frac{\Delta E}{A}$ (avec A la surface du joint) au cours de la migration du joint de grain en fonction de RC pour des tailles de cellule selon y différentes et pour un déplacement en cisaillement $d = 0.066\ nm$. Le MEP par unité de surface présente un nombre croissant d'extrema locaux en fonction de y (dimension de la cellule de simulation). L'analyse structurale montre que la migration du joint se produit à travers la formation et le mouvement en sens inverse de deux disconnections opposées, indépendamment de la taille de la cellule. À titre d'exemple, dans la cellule plus grande (taille-Y 6.5 nm) contenant dix unités structurelles, les configurations où les unités structurelles ont été déplacées successivement correspondent soit à un minimum ou un maximum local (à RC = 0.13, 0.79 et 0.84) dans le MEP.
Pour caractériser la formation des disconnections et leur mouvement, les courbes MEP sont interprétés dans la théorie de l'élasticité.
Dans la suite, toutes les quantités désignées par ζ se réfèrent aux énergies par unité de longueur de disconnection. L'excès d'énergie ζ en raison de la présence de deux disconnections parallèles et opposées, séparées par une distance a est donnée par [127] :

$$\zeta(a) = 2\zeta_{form}(r_c) + \zeta_{inter}(a, r_c)) + \zeta_{stress}(a) \tag{B.14}$$

$\zeta_{form}(r_c)$ est l'énergie de formation de la disconnection (r_c est le rayon du cœur de la disconnection). $\zeta_{inetr(a)}$ est l'énergie élastique d'interaction entre les disconnections et leurs images en raison des conditions de périodicité dans la direction y. Les calculs analytiques en utilisant l'élasticité linéaire en un milieu infini sans aucune contrainte externe (ou déformation), donnent : $\zeta_{inter}(a) = \frac{\mu b_1^2}{2\pi(1-\nu)} \ln\left[\frac{L_y}{\pi r_c}\sin(\frac{\pi a}{L_y})\right]$
$\zeta_{stress}(a)$ est le travail des forces internes au cours du mouvement des disconnections en l'absence d'interaction élastique, i.e. le changement de l'énergie produite par le déplacement a d'une seule disconnection dans une interface infinie : $\zeta_{stress} = (e_{final} - e_{initial})$ où e_{final} ($e_{initial}$) est

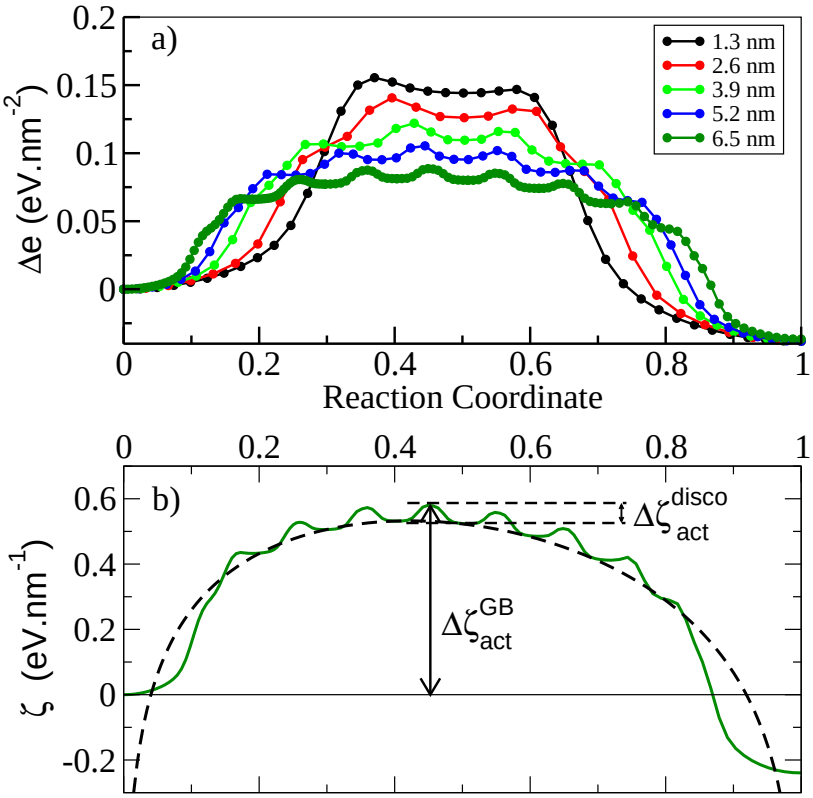

Figure B.14: a) Chemin d'énergie minimum -MEP-(ligne pleine) par unité de surface en fonction de RC pour $d = 0.066$ nm pour 5 cellules de tailles différentes selon y, allant de 1 à 5 périodes de joint de grain (la taille selon z est de 1.4 nm). b) Chemin d'énergie minimum -MEP- par unité de longueur de disconnection en fonction de RC pour $d = 0.066$ nm (cellule de 6.5 nm et 1.4 nm de long selon y et z) et variation de l'énergie (ligne en pointillés) selon la théorie de l'élasticité et Eq. (4.27).

l'énergie par unité de surface d'un système avec le plan du joint dans sa position finale (initial). $e_{final} - e_{initial}$ se déduit de la figure B.12b. En vérifiant les configurations métastables le long du MEP, la distance entre les disconnections a varie linéairement avec RC : $a = L_y RC$.
La figure B.14b) rapporte l'excès d'énergie ζ provenant des calculs NEB (courbe pleine) dans la plus grande cellule (6,5 nm taille-y) et la courbe (en pointillés) qui est ajustée par rapport aux configurations métastables par l'expression : $\zeta(a) = 2\zeta_{forme}(Rc) + K \ln\left[\frac{a}{Rc}\text{sinc}(\frac{\pi a}{L_y})\right] + (e_{final} - e_{initial})a$. Les valeurs de $\zeta_{forme}(Rc) = -0.143\text{eV.nm}^{-1}$ et $K = 0.3059\text{eV.nm}^{-1}$ (en utilisant $r_c = |\vec{b_1}| = 0.1\text{nm}$) déduit.
Par soustraction du MEP de l'équation Eq B.14, la moyenne d'énergie d'activation du mouvement d'une disconnection est déduit $\Delta\zeta_{act}^{disco} \approx 52 \pm 4\text{meV.nm}^{-1}$. La barrière d'énergie $\Delta\zeta_{act}^{disco}$ pour déplacer une disconnection est environ 11 fois plus petite que la barrière d'énergie de nucléation $\Delta\zeta_{act}^{GB}$ (pour la migration du joint dans la plus grande cellule, en accord avec les récents résultats des simulations [127]. Donc le taux de migration des joints de grains est essentiellement contrôlée par la formation (ou nucléation) d'un noyau critique composé de deux disconnections.
Pour conclure, les mécanismes élémentaires de la migration des joints de grains à basse température dans un bicristal de cuivre ont été mis en évidence. En complément du mouvement stick-slip, la migration d'un joint initialement parfait se fait par la nucléation et le mouvement de diconnections, en accord avec des simulations récentes [102]. Ces mécanismes élémentaires sont soutenues par des résultats expérimentaux récents attestant la formation des macro-marches.

B.5 Conclusion

Dans le présent travail, nous avons étudié expérimentalement et par simulation atomistique, les processus élémentaires qui sous-tendent la migration des joints de grains couplée au cisaillement. Ce mécanisme est un des mécanismes de plasticité basé sur les joints de grains.
Les observations expérimentales en microscopie électronique en transmission à haute résolution (HRTEM) et en traction in-situ en MET ont été réalisées sur des bicristaux et des polycristaux d'aluminium.
Les conclusions principales de ces travaux peuvent être résumées par :

- Le mouvement des disconnections le long des joints de grains est le processus par lequel la migration des joints de grains est réalisée, en réponse à une contrainte externe. Les essais de traction in-situ en MET montre que la migration se produit par le mouvement collectif des disconnections qui fusionnent en macro-marches de différentes hauteurs.
- La mesure des déformations produites par les disconnections peut être réalisée en analysant les image de MET. Ces images montrent plusieurs modes de couplage possibles fonctionnant dans un joint de grains donné. Outre le facteur de couplage idéal (cisaillement le long du joint), le mouvement des disconnections peut également induire une déformation perpendiculaire au plan de joint.
- HRTEM et traction in-situ en MET révèlent que les disconnections peuvent soit exister le long du joint avant la traction, soit être produites par des interactions de dislocations de réseau avec le joint de grains.
- Les vecteurs de Burgers des disconnections résultantes de la décomposition des dislocations de réseau dans le joint peuvent avoir des composantes de glissement et/ou de montée. Le mouvement de ces disconnections entraînera donc une déformation parallèle et/ou perpendiculaire au plan du joint y compris un cisaillement possible le long de l'axe de rotation du joint.
- Les calculs atomistique effectués à 0K ont été utilisés pour déterminer le mécanisme élémentaire de la migration d'un joint parfait. Cette migration se fait par la nucléation et la propagation de disconnections qui correspondent donc au couplage à l'échelle atomique.
- Les barrières d'énergie pour la nucléation des disconnections et pour leurs propagation ont été déterminées. Il a été montré que la barrière d'énergie pour la nucléation des disconnections est 11 fois plus grande que la barrière d'énergie pour leur mouvement. Ainsi, en l'absence de défauts préexistants, le mécanisme qui contrôle le couplage est la formation d'un noyau de deux disconnections opposées.
- Enfin, expériences et simulations suggèrent que le facteur de couplage est plutôt une propriété des disconnections que du joint de grain lui-même. C'est une explication possible de l'existence de plusieurs modes de couplage pour un joint de grain donné.

ABSTRACT - EN

Contrary to conventional coarse-grained metals where plastic deformation is carried out by intragranular dislocation motion, specific grain boundary-based mechanisms are involved in deformation of nanocrystalline metals. Among them, the shear-coupled grain boundary migration, i.e. the motion of the grain boundary perpendicular to its plane in response to a shear strain, has been found to be efficient to accommodate the deformations observed in several small-grained metals and under different mechanical solicitations.
Despite many experimental and theoretical efforts in recent years, the elementary mechanisms of the shear-coupled grain boundary migration are still poorly known. The major purpose of the present work is thus to investigate these elementary processes both experimentally by transmission electron microscopy (TEM) and theoretically by atomistic simulations.
In-situ TEM straining experiments on Al bicrystal at 400°C show the migration of a $\Sigma41\langle001\rangle\{540\}$ grain boundary by the collective motion of macro-steps moving along the interface. These macro-steps are characterized by measuring the deformation (related to the coupling factor) that they induce by their motion. This deformation can include both parallel (shear-coupled migration) and perpendicular (involving climb) components to the interface. Moreover, different macro-steps carry different deformations indicating the multiplicity of the possible coupling modes for a given grain boundary. Moving elementary steps, presumably composing the macro-steps are also observed in the grain boundary.
By high resolution TEM (HRTEM) observations the elementary steps are identified as disconnections and are characterized by their step heights and Burgers vectors. The TEM in-situ straining experiments at ambient and 400°C show also the rapid decompositions of lattice dislocations in the grain boundary, suggesting a possible mechanism for the creation of disconnections. The possible decomposition reactions are hence considered in order to determine the nature of the produced disconnections. The disconnections with small step heights and Burgers vectors and small climb components are thought to be mobile and the potential deformation that they would carry is in agreement with the experimentally measured coupling factors.
The shear-coupled grain boundary migration is studied by atomistic simulation in a Cu bicrystal containing a symmetrical $\Sigma13\langle001\rangle\{320\}$ grain boundary, at 0 K. The minimum energy path (MEP) of the grain boundary migration is determined by the Nudged Elastic Band (NEB) method. The structural evolution of the grain boundary along the MEP shows that the grain boundary migration occurs through the nucleation and motion of grain boundary steps, identified as disconnections, in agreement with experimental observations. The energy barrier for the nucleation of the disconnections is found to be about 11 times larger than the energy barrier for their motion. Hence, in the absence of pre-existing disconnections in the grain boundary, the nucleation of the disconnections is the limiting step of the shear-coupled grain boundary migration.

ABSTRACT - FR

La déformation plastique des matériaux est généralement induite par le déplacement de dislocations. Cependant dans les matériaux nanocristallins, ces déplacements sont inhibés et les mouvements des joints de grains jouent alors un rôle important dans la plasticité. La migration des joints de grains couplée au cisaillement est un mécanisme efficace mis en évidence lors de sollicitations mécaniques dans différents matériaux : le joint de grains se déplace perpendiculairement a son plan en réponse a une contrainte de cisaillement.

Malgré de nombreux efforts expérimentaux et théoriques ces dernières années, les mécanismes élémentaires de la migration des joints de grains couplée au cisaillement restent méconnus. Le présent travail se propose d'étudier expérimentalement par microsopie électronique en transmission (MET) et théoriquement par simulation atomistique ces mécanismes élémentaires.

Des expériences de traction in-situ en MET portant sur des bicristaux d'Aluminium chauffés à 400°C montrent qu'un joint de grains $\Sigma 41\langle 001\rangle\{540\}$ se déplace par le mouvement collectif des macro-marches le long de l'interface. Ces macro-marches sont caractérisées par la mesure de leur déformation. Cette déformation peut comporter à la fois une composante parallèle (couplée au cisaillement) et une composante perpendiculaire à l'interface (montée). Différentes macro-marches caractérisées par différentes déformations ont été observées sur un même joint de grains : différents modes de couplage peuvent ainsi permettre à un joint de grains de migrer. Des marches élémentaires, composant vraisemblablement les macro-marches ont été également observées.
L'observation par MET haute résolution de ces marches élémentaires a permis de les identifier comme des disconnections. Elles sont caractérisées par leurs hauteurs et leurs vecteurs de Burgers. Des expériences de traction in-situ en MET montrent que des dislocations du réseau se décomposent dans le joint, suggérant un mécanisme possible de création de ces disconnections. Les réactions de décomposition les plus probables ont été analysées pour déterminer la nature des disconnections produites. Les disconnections produites ayant des hauteurs de marches faibles et de faibles Vecteurs de Burgers, si elles sont supposées mobiles, sont caractérisées par des facteurs de couplage en bon accord avec les facteurs de couplage mesurés expérimentalement.
La migration des joints de grain couplée au cisaillement est étudiée par simulation atomistique dans un bicristal de Cuivre contenant un joint de grains symétrique $\Sigma 13\langle 001\rangle\{320\}$. Le chemin de moindre énergie lors de la migration est déterminé en utilisant la méthode Nudged Elastic Band. L'évolution du joint de grains lors de sa migration montre la nucléation et le déplacement des marches, identifiées comme des disconnections, en bon accord avec les résultats expérimentaux. La barrière d'énergie pour la nucléation des disconnections est environ 11 fois plus élevée que le barrière d'énergie pour leur déplacement. Ainsi, en l'absence de disconnection pré-existante dans le joint, la nucléation des disconnections est l'étape limitante de la migration du joint de grains couplée au cisaillement.

BIBLIOGRAPHIE

[1] E.O. Hall. *Proc. Phys. Soc.*, B64 :747, 1951.

[2] N. J. Petch. *J. Iron Steel Inst.*, 174 :25, 1953.

[3] K.S Kumar, H Van Swygenhoven, and S Suresh. Mechanical behavior of nanocrystalline metals and alloys. *Acta Materialia*, 51(19) :5743 – 5774, 2003.

[4] M.A. Meyers, A. Mishra, and D.J. Benson. Mechanical properties of nanocrystalline materials. *Progress in Materials Science*, 51(4) :427 – 556, 2006.

[5] G. I. Taylor. The mechanism of plastic deformation of crystals. part i. theoretical. *Proceedings of the Royal Society of London. Series A*, 145(855) :362–387, 1934.

[6] Egon Orowan. Zur kristallplastizität. i. *Zeitschrift für Physik*, 89(9-10) :605–613, 1934.

[7] M Polanyi. Lattice distortion which originates plastic flow. *Z. Phys*, 89(9-10) :660–662, 1934.

[8] John Price Hirth and Jens Lothe. *Theory of Dislocations*. Krieger Publishing Company, 1992.

[9] A Marikani. *Engineering Physics*. PHI Learning Pvt. Ltd., 2013.

[10] E Schmid. Yield point of crystals, critical shear stress law. In *Proceedings of the First International Congress for Applied Mechanics, Delft*, 1924.

[11] Louisette Priester. *Les joints de grains : de la théorie à l'ingénierie*. EDP sciences Les Ulis, France, 2006.

[12] A. Lasalmonie and J.L. Strudel. Influence of grain size on the mechanical behaviour of some high strength materials. *Journal of Materials Science*, 21(6) :1837–1852, 1986.

[13] AM El-Sherik, U. Erb, G. Palumbo, and KT Aust. Deviations from hall–petch behaviour in as-prepared nanocrystalline nickel. *Scripta Metallurgica et Materialia(USA)*, 27(9) :1185–1188, 1992.

[14] P.G. Sanders, J.A. Eastman, and J.R. Weertman. Elastic and tensile behavior of nanocrystalline copper and palladium. *Acta Materialia*, 45(10) :4019 – 4025, 1997.

[15] VY Gertsman, M. Hoffmann, H. Gleiter, and R. Birringer. The study of grain size dependence of yield stress of copper for a wide grain size range. *Acta metallurgica et materialia*, 42(10) :3539–3544, 1994.

[16] C.A. Schuh, T.G. Nieh, and T. Yamasaki. Hall-petch breakdown manifested in abrasive wear resistance of nanocrystalline nickel. *Scripta Materialia*, 46(10) :735 – 740, 2002.

[17] A. Giga, Y. Kimoto, Y. Takigawa, and K. Higashi. Demonstration of an inverse hall-petch relationship in electrodeposited nanocrystalline ni-w alloys through tensile testing. *Scripta Materialia*, 55(2) :143 – 146, 2006.

[18] G. Saada. Hall–petch revisited. *Materials Science and Engineering : A*, 400–401(0) :146 – 149, 2005.

[19] H. Van Swygenhoven and P. M. Derlet. Grain-boundary sliding in nanocrystalline fcc metals. *Phys. Rev. B*, 64 :224105, Nov 2001.

[20] J. Schiotz, F.D. Di Tolla, and K.W. Jacobsen. Softening of nanocrystalline metals at very small grains. *Nature*, 391 :561, 1998.

[21] V. Yamakov, D. Wolf, S.R. Phillpot, and H. Gleiter. Grain-boundary diffusion creep in nanocrystalline palladium by molecular-dynamics simulation. *Acta Materialia*, 50(1) :61 – 73, 2002.

[22] Diana Farkas, Som Mohanty, and Joshua Monk. Strain-driven grain boundary motion in nanocrystalline materials. *Materials Science and Engineering : A*, 493(1) :33 – 40, 2008.

[23] J. W. Cahn, Y. Mishin, and A. Suzuki. Coupling grain boundary motion to shear deformation. *Acta Mater.*, 54(19) :4953–4975, November 2006.

[24] M. Jin, A.M. Minor, E.A. Stach, and J.W. Morris Jr. Direct observation of deformation-induced grain growth during the nanoindentation of ultrafine-grained al at room temperature. *Acta Materialia*, 52(18) :5381 – 5387, 2004.

[25] Kai Zhang, JR Weertman, and JA Eastman. Rapid stress-driven grain coarsening in nanocrystalline cu at ambient and cryogenic temperatures. *Applied Physics Letters*, 87(6) :061921–061921, 2005.

[26] D. Pan, S. Kuwano, T. Fujita, and M. W. Chen. Ultra-large room-temperature compressive plasticity of a nanocrystalline metal. *Nano Letters*, 7(7) :2108–2111, 2007.

[27] S. Brandstetter, Kai Zhang, A. Escuadro, J.R. Weertman, and H. Van Swygenhoven. Grain coarsening during compression of bulk nanocrystalline nickel and copper. *Scripta Materialia*, 58(1) :61 – 64, 2008.

[28] D.S. Gianola, S. Van Petegem, M. Legros, S. Brandstetter, H. Van Swygenhoven, and K.J. Hemker. Stress-assisted discontinuous grain growth and its effect on the deformation behavior of nanocrystalline aluminum thin films. *Acta Materialia*, 54(8) :2253 – 2263, 2006.

[29] G.J. Fan, L.F. Fu, H. Choo, P.K. Liaw, and N.D. Browning. Uniaxial tensile plastic deformation and grain growth of bulk nanocrystalline alloys. *Acta Materialia*, 54(18) :4781 – 4792, 2006.

[30] Marc Legros, Daniel S. Gianola, and Kevin J. Hemker. In situ tem observations of fast grain-boundary motion in stressed nanocrystalline aluminum films. *Acta Materialia*, 56(14) :3380 – 3393, 2008.

[31] T. J. Rupert, D. S. Gianola, Y. Gan, and K. J. Hemker. Experimental observations of stress-driven grain boundary migration. *Science*, 326(5960) :1686–1690, 2009.

[32] F. Mompiou, D. Caillard, and M. Legros. Grain boundary shear-migration coupling-i. in situ tem straining experiments in al polycrystals. *Acta Materialia*, 57(7) :2198 – 2209, 2009.

[33] Lazar Simkhovich Shvindlerman. *Grain boundary migration in metals : thermodynamics, kinetics, applications*, volume 9. CRC PressI Llc, 1999.

[34] W. T. Read and W. Shockley. Dislocation models of crystal grain boundaries. *Phys. Rev.*, 78 :275–289, May 1950.

[35] J Hornstra. Models of grain boundaries in the diamond lattice i. tilt about i 10. *Physica*, 25(1) :409–422, 1959.

[36] A. P. Sutton and V. Vitek. On the structure of tilt grain boundaries in cubic metals i. symmetrical tilt boundaries. *Philosophical Transactions of the Royal Society of London. Series A, Mathematical and Physical Sciences*, 309(1506) :1–36, 1983.

[37] RC Pond. Line defects in interfaces. *Elsevier Science Publishers, Dislocations in Solids.*, 8 :1–66, 1989.

[38] W Bollmann. Crystal defects and crystalline interfaces. 1970.

[39] R.C. Pond. {TEM} studies of line defects in interfaces. *Ultramicroscopy*, 30(1-2) :1 – 7, 1989.

[40] J.P. Hirth. Dislocations, steps and disconnections at interfaces. *Journal of Physics and Chemistry of Solids*, 55(10) :985 – 989, 1994.

[41] Alexander H King. Step heights associated with grain boundary dislocations in cubic crystals. *Acta Metallurgica*, 30(2) :419–427, 1982.

[42] J.W. Christian and S. Mahajan. Deformation twinning. *Progress in Materials Science*, 39(1) :1 – 157, 1995.

[43] Vesselin Yamakov, Dieter Wolf, Simon R Phillpot, Amiya K Mukherjee, and Herbert Gleiter. Dislocation processes in the deformation of nanocrystalline aluminium by molecular-dynamics simulation. *nature materials*, 1(1) :45–49, 2002.

[44] V. Yamakov, D. Wolf, S.R. Phillpot, and H. Gleiter. Deformation twinning in nanocrystalline al by molecular-dynamics simulation. *Acta Materialia*, 50(20) :5005 – 5020, 2002.

[45] Mingwei Chen, En Ma, Kevin J. Hemker, Hongwei Sheng, Yinmin Wang, and Xuemei Cheng. Deformation twinning in nanocrystalline aluminum. *Science*, 300(5623) :1275–1277, 2003.

[46] X. Z. Liao, F. Zhou, E. J. Lavernia, D. W. He, and Y. T. Zhu. Deformation twins in nanocrystalline al. *Applied Physics Letters*, 83(24) :5062–5064, 2003.

[47] X. Wu, Y.T. Zhu, M.W. Chen, and E. Ma. Twinning and stacking fault formation during tensile deformation of nanocrystalline ni. *Scripta Materialia*, 54(9) :1685 – 1690, 2006.

[48] RL Coble. A model for boundary diffusion controlled creep in polycrystalline materials. *Journal of Applied Physics*, 34(6) :1679–1682, 1963.

[49] J. Weissmüller and J. Markmann. Deforming nanocrystalline metals : New insights, new puzzles. *Advanced Engineering Materials*, 7(4) :202–207, 2005.

[50] Gerhard Wilde. *Nanostructured materials*, volume 1. Elsevier Science, 2009.

[51] MF Ashby. On interface-reaction control of nabarro-herring creep and sintering. *Scripta Metallurgica*, 3(11) :837–842, 1969.

[52] B. Burton and G.L. Reynolds. The diffusional creep of uranium dioxide : its limitation by interfacial processes. *Acta Metallurgica*, 21(8) :1073 – 1078, 1973.

[53] Ning Wang, Zhirui Wang, K.T. Aust, and U. Erb. Effect of grain size on mechanical properties of nanocrystalline materials. *Acta Metallurgica et Materialia*, 43(2) :519 – 528, 1995.

[54] R.C. Gifkins. Grain-boundary sliding and its accommodation during creep and superplasticity. *Metallurgical Transactions A*, 7 :1225–1232, 1976.

[55] W. Beere. Grain-boundary sliding controlled creep : its relevance to grain rolling and superplasticity. *Journal of Materials Science*, 12(10) :2093–2098, 1977.

[56] Z.T. Trautt and Y. Mishin. Grain boundary migration and grain rotation studied by molecular dynamics. *Acta Materialia*, 60(5) :2407 – 2424, 2012.

[57] GR Kegg, CAP Horton, and JM Silcock. Grain boundary dislocations in aluminium bicrystals after high-temperature deformation. *Philosophical Magazine*, 27(5) :1041–1055, 1973.

[58] F. Mompiou, M. Legros, A. Boé, M. Coulombier, J.-P. Raskin, and T. Pardoen. Inter- and intragranular plasticity mechanisms in ultrafine-grained al thin films : An in situ tem study. *Acta Materialia*, 61(1) :205 – 216, 2013.

[59] S Lartigue-Korinek, C Carry, and L Priester. Multiscale aspects of the influence of yttrium on microstructure, sintering and creep of alumina. *Journal of the European Ceramic Society*, 22(9–10) :1525 – 1541, 2002.

[60] RC Pond, DA Smith, and PWJ Southerden. On the role of grain boundary dislocations in high temperature creep. *Philosophical Magazine A*, 37(1) :27–40, 1978.

[61] Louisette Priester. *Grain Boundaries and Crystalline Plasticity*. John Wiley & Sons, 2013.

[62] S.E Babcock and R.W Balluffi. Grain boundary kinetics ii. in situ observations of the role of grain boundary dislocations in high-angle boundary migratio. *Acta Metallurgica*, 37(9) :2367 – 2376, 1989.

[63] F. Mompiou, M. Legros, T. Radetic, U. Dahmen, D.S. Gianola, and K.J. Hemker. In situ tem observation of grain annihilation in tricrystalline aluminum films. *Acta Materialia*, 60(5) :2209 – 2218, 2012.

[64] T. Radetic, C. Ophus, D.L. Olmsted, M. Asta, and U. Dahmen. Mechanism and dynamics of shrinking island grains in mazed bicrystal thin films of au. *Acta Materialia*, (0) :–, 2012.

[65] K. L. Merkle, L. J. Thompson, and Fritz Phillipp. Collective effects in grain boundary migration. *Phys. Rev. Lett.*, 88 :225501, May 2002.

[66] Choh Hsien Li, E.H Edwards, J Washburn, and E.R Parker. Stress-induced movement of crystal boundaries. *Acta Metallurgica*, 1(2) :223 – 229, 1953.

[67] Douglas W Bainbridge, Hsien Li Choh, and Eugene H. Edwards. Recent observations on the motion of small angle dislocation boundaries. *Acta Metallurgica*, 2(2) :322 – 333, 1954.

[68] R Bullough. Deformation twinning in the diamond structure. *Proceedings of the Royal Society of London. Series A. Mathematical and Physical Sciences*, 241(1227) :568–577, 1957.

[69] A.J. Haslam, D. Moldovan, V. Yamakov, D. Wolf, S.R. Phillpot, and H. Gleiter. Stress-enhanced grain growth in a nanocrystalline material by molecular-dynamics simulation. *Acta Materialia*, 51(7) :2097 – 2112, 2003.

[70] J Markmann, P Bunzel, H Rösner, K.W Liu, K.A Padmanabhan, R Birringer, H Gleiter, and J Weissmüller. Microstructure evolution during rolling of inert-gas condensed palladium. *Scripta Materialia*, 49(7) :637 – 644, 2003.

[71] Pratibha L. Gai, Kai Zhang, and Julia Weertman. Electron microscopy study of nanocrystalline copper deformed by a microhardness indenter. *Scripta Materialia*, 56(1) :25 – 28, 2007.

[72] S.E Babcock and R.W Balluffi. Grain boundary kinetics—i. in situ observations of coupled grain boundary dislocation motion, crystal translation and boundary displacement. *Acta Metallurgica*, 37(9) :2357 – 2365, 1989.

[73] H. Fukutomi, T. Iseki, T. Endo, and T. Kamijo. Sliding behavior of coincidence grain boundaries deviating from ideal symmetric tilt relationship. *Acta Metallurgica et Materialia*, 39(7) :1445 – 1448, 1991.

[74] A.D. Sheikh-Ali. Coupling of grain boundary sliding and migration within the range of boundary specialness. *Acta Materialia*, 58(19) :6249 – 6255, 2010.

[75] Frederic Mompiou, Marc Legros, and Daniel Caillard. Stress assisted grain growth in ultrafine and nanocrystalline aluminum revealed by in-situ tem. *MRS Proceedings, Cambridge Univ Press*, 1086(1), 2008.

[76] Tatiana Gorkaya, Dmitri A. Molodov, and Gunter Gottstein. Stress-driven migration of symmetrical tilt grain boundaries in al bicrystals. *Acta Materialia*, 57(18) :5396 – 5405, 2009.

[77] DmitriA. Molodov, Tatiana Gorkaya, and Günter Gottstein. Dynamics of grain boundaries under applied mechanical stress. *Journal of Materials Science*, 46 :4318–4326, 2011.

[78] M. Velasco, H. Van Swygenhoven, and C. Brandl. Coupled grain boundary motion in a nanocrystalline grain boundary network. *Scripta Materialia*, 65(2) :151 – 154, 2011.

[79] Stéphane Berbenni, Bhasker Paliwal, and Mohammed Cherkaoui. A micromechanics-based model for shear-coupled grain boundary migration in bicrystals. *International Journal of Plasticity*, 44(0) :68 – 94, 2013.

[80] Y. Mishin, A. Suzuki, B. P. Uberuaga, and A. F. Voter. Stick-slip behavior of grain boundaries studied by accelerated molecular dynamics. *Phys. Rev. B*, 75 :224101, Jun 2007.

[81] Jonathan Schafer and Karsten Albe. Competing deformation mechanisms in nanocrystalline metals and alloys : Coupled motion versus grain boundary sliding. *Acta Materialia*, 60(17) :6076 – 6085, 2012.

[82] Eric R. Homer, Stephen M. Foiles, Elizabeth A. Holm, and David L. Olmsted. Phenomenology of shear-coupled grain boundary motion in symmetric tilt and general grain boundaries. *Acta Materialia*, 61(4) :1048 – 1060, 2013.

[83] A P Sutton and R W Baluffi. *Interfaces in Crysalline Materials*. Oxford University Press, 1995.

[84] John W. Cahn and Jean E. Taylor. A unified approach to motion of grain boundaries, relative tangential translation along grain boundaries, and grain rotation. *Acta Materialia*, 52(16) :4887 – 4898, 2004.

[85] J. W. Cahn, Y. Mishin, and A. Suzuki. Duality of dislocation content of grain boundaries. *Philosophical Magazine*, 86(25-26) :3965–3980, 2006.

[86] Dmitri A Molodov. *Microstructural Design of Advanced Engineering Materials*. John Wiley & Sons, 2013.

[87] Dmitri A. Molodov, Tatiana Gorkaya, and Gunter Gottstein. Migration of the sigma7 tilt grain boundary in al under an applied external stress. *Scripta Materialia*, 65(11) :990 – 993, 2011.

[88] D.A. Molodov, V.A. Ivanov, and G. Gottstein. Low angle tilt boundary migration coupled to shear deformation. *Acta Materialia*, 55(5) :1843 – 1848, 2007.

[89] CMF Rae and DA Smith. On the mechanisms of grain boundary migration. *Philosophical Magazine A*, 41(4) :477–492, 1980.

[90] BA Bilby and AG Crocker. The theory of the crystallography of deformation twinning. *Proceedings of the Royal Society of London. Series A. Mathematical and Physical Sciences*, 288(1413) :240–255, 1965.

[91] HA Khater, A Serra, and RC Pond. Atomic shearing and shuffling accompanying the motion of twinning disconnections in zirconium. *Philosophical Magazine*, 93(10-12) :1279–1298, 2013.

[92] F. Mompiou, M. Legros, and D. Caillard. Smig model : A new geometrical model to quantify grain boundary-based plasticity. *Acta Materialia*, 58(10) :3676 – 3689, 2010.

[93] D. Caillard, F. Mompiou, and M. Legros. Grain-boundary shear-migration coupling. ii. geometrical model for general boundaries. *Acta Materialia*, 57(8) :2390 – 2402, 2009.

[94] J.P. Hirth and R.C. Pond. Steps, dislocations and disconnections as interface defects relating to structure and phase transformations. *Acta Materialia*, 44(12) :4749 – 4763, 1996.

[95] R C Pond, X Ma, Y W Chai, and J P Hirth. *Dislocations in Solids*, volume 13. Elsevier, 2007.

[96] Hidehiro Yoshida, Kenji Yokoyama, Naoya Shibata, Yuichi Ikuhara, and Taketo Sakuma. High-temperature grain boundary sliding behavior and grain boundary energy in cubic zirconia bicrystals. *Acta Materialia*, 52(8) :2349 – 2357, 2004.

[97] Tatiana Gorkaya, Konstantin D. Molodov, Dmitri A. Molodov, and Günter Gottstein. Concurrent grain boundary motion and grain rotation under an applied stress. *Acta Materialia*, 59(14) :5674 – 5680, 2011.

[98] Manijeh Razeghi. *Fundamentals of solid state engineering*. Springer, 2009.

[99] Couret, A., Crestou, J., Farenc, S., Molenat, G., Clement, N., Coujou, A., and Caillard, D. In situ deformation in t.e.m. : recent developments. *Microsc. Microanal. Microstruct.*, 4(2-3) :153–170, 1993.

[100] A. Coujou, Ph. Lours, N.A. Roy, D. Caillard, and N. Clement. Determination of the local tensile axis direction in a tem in situ strained γ' single crystal—a finite element approach. *Acta Metallurgica et Materialia*, 38(5) :825 – 837, 1990.

[101] M. Upmanyu, R.W. Smith, and D.J. Srolovitz. Atomistic simulation of curvature driven grain boundary migration. *Interface Science*, 6(1-2) :41–58, 1998.

[102] Liang Wan and Shaoqing Wang. Shear response of the $\sigma 9 < 110 > 221$ symmetric tilt grain boundary in fcc metals studied by atomistic simulation methods. *Phys. Rev. B*, 82 :214112, Dec 2010.

[103] A. Serra and DJ Bacon. A new model for {10 1 2} twin growth in hcp metals. *Philosophical Magazine A*, 73(2) :333–343, 1996.

[104] Frédéric Mompiou, Marc Legros, Andreas Sedlmayr, Daniel S. Gianola, Daniel Caillard, and Oliver Kraft. Source-based strengthening of sub-micrometer al fibers. *Acta Materialia*, 60(3) :977 – 983, 2012.

[105] A.W Sleeswyk. Twinning and the origin of cleavage nuclei in α-iron. *Acta Metallurgica*, 10(9) :803 – 812, 1962.

[106] S. Mahajan and G.Y. Chin. The interaction of twins with existing substructure and twins in cobalt-iron alloys. *Acta Metallurgica*, 22(9) :1113 – 1119, 1974.

[107] D.A Molodov, P Konijnenberg, W Hu, G Gottstein, and L.S Shvindlerman. Effect of dislocation absorption on the motion of specific grain boundaries in al-bicrystals. *Scripta Materialia*, 45(2) :229 – 235, 2001.

[108] R. C. Pond and S. Celotto. Special interfaces :military transformations. 2003.

[109] M. Sennour, S. Lartigue-Korinek, Y. Champion, and M. J. Hÿtch†. Hrtem study of defects in twin boundaries of ultra-fine grained copper. *Philosophical Magazine*, 87(10) :1465–1486, 2007.

[110] N. Thompson and D.J. Millard. Xxxviii. twin formation, in cadmium. *Philosophical Magazine Series 7*, 43(339) :422–440, 1952.

[111] M.J. Hytch, E. Snoeck, and R. Kilaas. Quantitative measurement of displacement and strain fields from hrem micrographs. *Ultramicroscopy*, 74(3) :131 – 146, 1998.

[112] D.A. Smith, V. Vitek, and R.C. Pond. Computer simulation of symmetrical high angle boundaries in aluminium. *Acta Metallurgica*, 25(5) :475 – 483, 1977.

[113] Dirk Zahn, Harald Tlatlik, and Dierk Raabe. Modeling of dislocation patterns of small- and high-angle grain boundaries in aluminum. *Computational Materials Science*, 46(2) :293 – 296, 2009.

[114] J.P. Hirth, R.C. Pond, and J. Lothe. Spacing defects and disconnections in grain boundaries. *Acta Materialia*, 55(16) :5428 – 5437, 2007.

[115] R.C. Pond. On the characterisation of interfacial defects using high resolution electron microscopy. *Interface Science*, 2(4) :299–310, 1995.

[116] Kenzaburo Marukawa and Yuji Matsubara. A new method of burgers vector identification for grain boundary dislocations from electron microscopic images. *Trans. JIM*, 20, 1979.

[117] D.J. Dingley and R.C. Pond. On the interaction of crystal dislocations with grain boundaries. *Acta Metallurgica*, 27(4) :667 – 682, 1979.

[118] R. C. Pond and D. A. Smith. On the absorption of dislocations by grain boundaries. *Philosophical Magazine*, 36(2) :353–366, 1977.

[119] A. H. King and D. A. Smith. The effects on grain-boundary processes of the steps in the boundary plane associated with the cores of grain-boundary dislocations. *Acta Crystallographica Section A*, 36(3) :335–343, 1980.

[120] D Caillard, JL Martin, et al. *Thermally activated mechanisms in crystal plasticity*. Cambridge Univ Press, 2003.

[121] M. Mantina, Y. Wang, R. Arroyave, L. Q. Chen, Z. K. Liu, and C. Wolverton. First-principles calculation of self-diffusion coefficients. *Phys. Rev. Lett.*, 100 :215901, May 2008.

[122] John E Hatch. *Aluminum : properties and physical metallurgy*. ASM International, 1984.

[123] Zhiqiang Wang, Rodney J McCabe, Nasr M Ghoniem, Richard LeSar, Amit Misra, and Terence E Mitchell. Dislocation motion in thin cu foils : a comparison between computer simulations and experiment. *Acta Materialia*, 52(6) :1535 – 1542, 2004.

[124] K Kashihara and F Inoko. Effect of piled-up dislocations on strain induced boundary migration (sibm) in deformed aluminum bicrystals with originally $\sigma 3$ twin boundary. *Acta Materialia*, 49(15) :3051 – 3061, 2001.

[125] V. A. Ivanov and Y. Mishin. Dynamics of grain boundary motion coupled to shear deformation : An analytical model and its verification by molecular dynamics. *Phys. Rev. B*, 78 :064106, Aug 2008.

[126] Alain Karma, Zachary T. Trautt, and Yuri Mishin. Relationship between equilibrium fluctuations and shear-coupled motion of grain boundaries. *Phys. Rev. Lett.*, 109 :095501, Aug 2012.

[127] H.A. Khater, A. Serra, R.C. Pond, and J.P. Hirth. The disconnection mechanism of coupled migration and shear at grain boundaries. *Acta Materialia*, 60(5) :2007 – 2020, 2012.

[128] Steve Plimpton. Fast parallel algorithms for short-range molecular dynamics. *Journal of Computational Physics*, 117(1) :1 – 19, 1995.

[129] Y. Mishin, M. J. Mehl, D. A. Papaconstantopoulos, A. F. Voter, and J. D. Kress. Structural stability and lattice defects in copper : Ab initio, tight-binding, and embedded-atom calculations. *Phys. Rev. B*, 63(22) :224106, May 2001.

[130] MI Mendelev, MJ Kramer, CA Becker, and M Asta. Analysis of semi-empirical interatomic potentials appropriate for simulation of crystalline and liquid al and cu. *Philosophical Magazine*, 88(12) :1723–1750, 2008.

[131] JB Adams, SM Foiles, and WG Wolfer. Self-diffusion and impurity diffusion of fee metals using the five-frequency model and the embedded atom method. *Journal of Materials Research*, 4(01) :102–112, 1989.

[132] Seong-Woong Kim, Xiaoyan Li, Huajian Gao, and Sharvan Kumar. In situ observations of crack arrest and bridging by nanoscale twins in copper thin films. *Acta Materialia*, 60(6–7) :2959 – 2972, 2012.

[133] Shreevant Tiwari, Garritt J. Tucker, and David L. McDowell. Simulated defect growth avalanches during deformation of nanocrystalline copper. *Philosophical Magazine*, 93(5) :478–498, 2013.

[134] M. A. Tschopp and D. L. McDowell. Structures and energies of $\sigma 3$ asymmetric tilt grain boundaries in copper and aluminium. *Philosophical Magazine*, 87(22) :3147–3173, 2007.

[135] H.B. Huntington. The elastic constants of crystals. volume 7 of *Solid State Physics*, pages 213 – 351. Academic Press, 1958.

[136] Murray S. Daw and M. I. Baskes. Embedded-atom method : Derivation and application to impurities, surfaces, and other defects in metals. *Phys. Rev. B*, 29 :6443–6453, Jun 1984.

[137] Elijah Polak and Gerard Ribiere. Note sur la convergence de méthodes de directions conjuguées. *ESAIM : Mathematical Modelling and Numerical Analysis-Modélisation Mathématique et Analyse Numérique*, 3(R1) :35–43, 1969.

[138] JH Irving. Kirkwood jg. *J. Chem. Phys.*, 1950 :18, 1950.

[139] Daniel Sheppard, Rye Terrell, and Graeme Henkelman. Optimization methods for finding minimum energy paths. *The Journal of Chemical Physics*, 128(13) :134106, 2008.

[140] I. S. Gradshteyn and I. M. Ryzhik. *Table of Integrals, series, and Products*, page 47. Academic Press, San Diego, fifth edition, 1994.

[141] Z.T. Trautt, A. Adland, A. Karma, and Y. Mishin. Coupled motion of asymmetrical tilt grain boundaries : Molecular dynamics and phase field crystal simulations. *Acta Materialia*, 60(19) :6528 – 6546, 2012.

[142] SJ Fensin, M. Asta, and RG Hoagland. Temperature dependence of the structure and shear response of a $\sigma 11$ asymmetric tilt grain boundary in copper from molecular-dynamics. 2012.

[143] David B Williams and C Barry Carter. Transmission electron microscopy : a textbook for materials science. *Micron*, 28(1) :75–75, 1997.

[144] J.P. Hirth, R.C. Pond, and J. Lothe. Disconnections in tilt walls. *Acta Materialia*, 54(16) :4237 – 4245, 2006.

[145] Graeme Henkelman, Blas P. Uberuaga, and Hannes Jónsson. A climbing image nudged elastic band method for finding saddle points and minimum energy paths. *The Journal of Chemical Physics*, 113(22) :9901–9904, 2000.

ABSTRACT - EN

Contrary to conventional coarse-grained metals where plastic deformation is carried out by intragranular dislocation motion, specific grain boundary-based mechanisms are involved in deformation of nanocrystalline metals. Among them, the shear-coupled grain boundary migration, i.e. the motion of the grain boundary perpendicular to its plane in response to a shear strain, has been found to be efficient to accommodate the deformations observed in several small-grained metals and under different mechanical solicitations.
Despite many experimental and theoretical efforts in recent years, the elementary mechanisms of the shear-coupled grain boundary migration are still poorly known. The major purpose of the present work is thus to investigate these elementary processes both experimentally by transmission electron microscopy (TEM) and theoretically by atomistic simulations.
In-situ TEM straining experiments on Al bicrystal at 400°C show the migration of a $\Sigma41\langle001\rangle\{540\}$ grain boundary by the collective motion of macro-steps moving along the interface. These macro-steps are characterized by measuring the deformation (related to the coupling factor) that they induce by their motion. This deformation can include both parallel (shear-coupled migration) and perpendicular (involving climb) components to the interface. Moreover, different macro-steps carry different deformations indicating the multiplicity of the possible coupling modes for a given grain boundary. Moving elementary steps, presumably composing the macro-steps are also observed in the grain boundary.
By high resolution TEM (HRTEM) observations the elementary steps are identified as disconnections and are characterized by their step heights and Burgers vectors. The TEM in-situ straining experiments at ambient and 400°C show also the rapid decompositions of lattice dislocations in the grain boundary, suggesting a possible mechanism for the creation of disconnections. The possible decomposition reactions are hence considered in order to determine the nature of the produced disconnections. The disconnections with small step heights and Burgers vectors and small climb components are thought to be mobile and the potential deformation that they would carry is in agreement with the experimentally measured coupling factors.
The shear-coupled grain boundary migration is studied by atomistic simulation in a Cu bicrystal containing a symmetrical $\Sigma13\langle001\rangle\{320\}$ grain boundary, at 0 K. The minimum energy path (MEP) of the grain boundary migration is determined by the Nudged Elastic Band (NEB) method. The structural evolution of the grain boundary along the MEP shows that the grain boundary migration occurs through the nucleation and motion of grain boundary steps, identified as disconnections, in agreement with experimental observations. The energy barrier for the nucleation of the disconnections is found to be about 11 times larger than the energy barrier for their motion. Hence, in the absence of pre-existing disconnections in the grain boundary, the nucleation of the disconnections is the limiting step of the shear-coupled grain boundary migration.

ABSTRACT - FR

La déformation plastique des matériaux est généralement induite par le déplacement de dislocations. Cependant dans les matériaux nanocristallins, ces déplacements sont inhibés et les mouvements des joints de grains jouent alors un rôle important dans la plasticité. La migration des joints de grains couplée au cisaillement est un mécanisme efficace mis en évidence lors de sollicitations mécaniques dans différents matériaux: le joint de grains se déplace perpendiculairement a son plan en réponse a une contrainte de cisaillement.

Malgré de nombreux efforts expérimentaux et théoriques ces dernières années, les mécanismes élémentaires de la migration des joints de grains couplée au cisaillement restent méconnus. Le présent travail se propose d'étudier expérimentalement par microsopie électronique en transmission (MET) et théoriquement par simulation atomistique ces mécanismes élémentaires.

Des expériences de traction in-situ en MET portant sur des bicristaux d'Aluminium chauffés à 400°C montrent qu'un joint de grains $\Sigma41\langle001\rangle\{540\}$ se déplace par le mouvement collectif des macro-marches le long de l'interface. Ces macro-marches sont caractérisées par la mesure de leur déformation. Cette déformation peut comporter à la fois une composante parallèle (couplée au cisaillement) et une composante perpendiculaire à l'interface (montée). Différentes macro-marches caractérisées par différentes déformations ont été observées sur un même joint de grains: différents modes de couplage peuvent ainsi permettre à un joint de grains de migrer. Des marches élémentaires, composant vraisemblablement les macro-marches ont été également observées.
L'observation par MET haute résolution de ces marches élémentaires a permis de les identifier comme des disconnections. Elles sont caractérisées par leurs hauteurs et leurs vecteurs de Burgers. Des expériences de traction in-situ en MET montrent que des dislocations du réseau se décomposent dans le joint, suggérant un mécanisme possible de création de ces disconnections. Les réactions de décomposition les plus probables ont été analysées pour déterminer la nature des disconnections produites. Les disconnections produites ayant des hauteurs de marches faibles et de faibles Vecteurs de Burgers, si elles sont supposées mobiles, sont caractérisées par des facteurs de couplage en bon accord avec les facteurs de couplage mesurés expérimentalement.
La migration des joints de grain couplée au cisaillement est étudiée par simulation atomistique dans un bicristal de Cuivre contenant un joint de grains symétrique $\Sigma13\langle001\rangle\{320\}$. Le chemin de moindre énergie lors de la migration est déterminé en utilisant la méthode Nudged Elastic Band. L'évolution du joint de grains lors de sa migration montre la nucléation et le déplacement des marches, identifiées comme des disconnections, en bon accord avec les résultats expérimentaux. La barrière d'énergie pour la nucléation des disconnections est environ 11 fois plus élevée que le barrière d'énergie pour leur déplacement. Ainsi, en l'absence de disconnection pré-existante dans le joint, la nucléation des disconnections est l'étape limitante de la migration du joint de grains couplée au cisaillement.